From the Institute of Medical Engineering
of the University of Lübeck
Director: Prof. Dr. rer. nat. Thorsten M. Buzug

Field Free Line Magnetic Particle Imaging

Characterisation and imaging device up-scaling

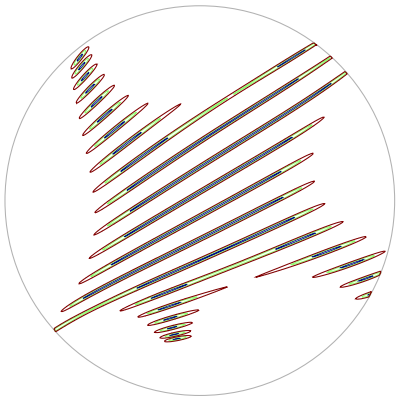

Dissertation
for Fulfilment of
Requirements
for the Doctoral Degree
of the University of Lübeck

from the Departement of Computer Sciences

Submitted by

Gaël Bringout
from Colmar, France

Lübeck 2016

First referee: Prof. Dr. rer. nat. habil. Heinz Handels
Second referee: Prof. Dr.-Ing. Alfred mertins
Date of oral examination: 20 April 2016
Approved for printing the 19 October 2016 in Lübeck.

Acknowledgement

First and foremost I would like to express my deepest appreciation to my thesis supervisor, Professor Thorsten Buzug, for giving me the opportunity to be part of his research group and for his trust and confidence in my work. Thank you very much for the freedom and the incredible support you offered me during the exploration of even the most audacious ideas.

I would like also to thank the jury, Professor Heinz Handels and Professor Alfred Mertins, who honored me by taking the time to asses my work.

The accomplishment of this endeavor would not have been possible without the scientific, moral and human support that I received. The first persons I met helped me to learn the German language and appreciate all its nuances. It started with my chanting pronunciation of my surname which was similar to a German word, which is still a good description of my experience there: *geil*. Thank you Hanne, Wiebke and Maren! I am deeply indebted to Ksenija and Dirk, for their (almost) unconditional support toward the improvement of my lexicon and their participation to my/our research, especially in the most adventurous experiments. With enough time, we could have realised our Funkbohrmaschine! The exploration of the CT and reconstruction worlds would not have been possible for me without the irradient support of Yulia, Aileen and Maik and the determination of Wolfgang and Jürgen. I am also grateful to have shared so much daily interactions with Matthias, Mandy, Christian, Matze, Klass, Martin, Jan and Corinna, as well as all the other colleagues of the institute and the university. It was for me an enjoyable source of energy and inspiration. I hope I didn't make you too anxious :) I would also like to Frau Thaler and Herr Schulz for their numerous invaluable help along those years. I did enjoy my time with all of you! Merci beaucoup!

These section would not be complete and not have been completed without the support of my loving Gaëlle and her incredible ability to make everything more enjoyable and beautiful. Finally, I would thank our families for their decisive (and) culinary support.

Abstract

First presented in 2005, magnetic particle imaging (MPI) is a new imaging modality able to acquire and reconstruct the distribution of a magnetic tracer included in a non-ferromagnetic volume. In 2009, Weizenecker et al. presented a video showing a tracer distribution flowing through the beating heart of a mouse. It was acquired in a $20.4 \times 12.0 \times 16.8$ mm^3 volume at 46 frames per seconds. The spatial encoding was done using a field free point (FFP) moved along a Lissajous trajectory. Since then, many efforts have been done to improve the technology. To further increase the sensitivity of the acquisition process, it has been proposed to replace the FFP by a field free line (FFL). In 2014, Weber et al. presented the first continuously rotating FFL scanner, acquiring and displaying 50 circular images per seconds within a Field of View (FOV) with a diameter of 25 mm.

However, to image a tracer distribution in the human body, up-scaled version of those scanners have to be realised. In this thesis, the design of two FFL scanners having a bore diameter of 173 mm and 500 mm are investigated, to highlight and investigate some of the challenges awaiting the up-scaling process.

The first part of this work defines precisely the acquisition sequence and the imaging properties of the MPI systems. It is shown that the coils designed in this work have magnetic-field topologies which cannot be considered as ideal. This, in turn, has an impact on the reconstruction of the tracer distribution. Using a model based approach which assumes perfectly straight lines, as the filtered back projection, leads to artefacts in the reconstructed images. Using a system-function reconstruction approach with properly resolved spectra suppresses those artefacts, but the acquisition rate is divided by two. To cover a larger FOV, a new FFL sequence using focus fields is introduced. It requires the use of a system function reconstruction, as no model-based reconstruction are available for a generic sequence. The first reconstruction shows artefacts, which have to be investigated in further studies.

The second part of this work is focused on safety limitations associated with MPI scanners. The main foreseen safety risk associated with an MPI scanner is the peripheral nerves stimulation (PNS). As no precise data exist on the PNS thresholds for the fre-

quencies and magnetic field-strengths usable in MPI, an approximation is proposed to evaluate the PNS risk of MPI sequences. Applying this relation to a human-sized FFL scanner imaging an FOV of 400×405 mm^2 10 times per second, it is found that the patient will probably experience PNS. Further experimental validations have to be carried out to determine more precisely the PNS thresholds for such sequences. Afterwards, the sequences may be adapted to avoid PNS in the patient. A first example of such an adjustment is also presented.

The third part of this work is focused on the construction of the electromagnets used in an FFL scanner with a bore diameter of 173 mm. A boundary element method formulation is found to be adequate to optimise all the necessary coils. A scanner design with a gradient on the line of 0.8 $T \cdot m^{-1}$ and two 15 mT drive fields has been implemented. The fields strengths are mainly limited by the cooling infrastructure available and the technical complexity associated with all the parts of the scanner. The actual design requires around 40 kW of electrical power. The rotation frequency of the line is actually limited by the filters, power factor correction elements and the shielding of the different elements.

Kurzfassung

Das in 2005 vorgestellte bildgebende Verfahren Magnetic Particle Imaging (MPI) ermöglicht die Detektierung und Visualisierung von eines magnetischen Tracers in einem nicht ferromagnetischen Volumen. Im Jahr 2009, zeigten Weizenecker et al. ein Video, in welchem eine Tracer-Verteilung durch das schlagende Herz einer Maus fließt. Es wurde in einem $20.4 \times 12.0 \times 16.8$ mm^3 großen Volumen bei 46 Bildern pro Sekunde aufgenommen. Die Ortskodierung wurde mit einer Feld Freie Punkte (FFP) realisiert, welcher entlang einer Lissajous Trajektorie bewegt wird. Seitdem wurden viele Bemühungen unternommen, um diese Technologie zu verbessern. Um die Empfindlichkeit des Akquisitionsprozesses weiter zu erhöhen, wurde vorgeschlagen den FFP durch eine Feld Freie Linie (FFL) zu ersetzen. Im Jahr 2014 präsentierten Weber et al. den ersten kontinuierlich rotierenden FFL Scanner, welcher 50 kreisförmige Bildern pro Sekunde aufnehmen konnte, innerhalb von ein Field of View (FOV) mit einem Durchmesser von 25 mm .

Jedoch muss eine hoch-skalierte Version dieser Scannertopologien realisiert werden, um die Tracerverteilung im menschlichen Körper zu bestimmen. In dieser Arbeit wird das Design von zwei FFL Scannern mit einem Bohrungsdurchmesser von 173 und 500 mm untersucht, um die Herausforderungen der Skalierung aufzuzeigen.

Der erste Teil dieser Arbeit definiert die Aufnahmesequenz und die Abbildungseigenschaften der MPI-Systeme. Es wird gezeigt, dass die Magnetfeld-Topologien der in dieser Arbeit entwickelten Spulen, nicht als Ideal angenommen werden können. Dies hat einen Einfluss auf die Rekonstruktion der Tracerverteilung. Die Verwendung eines modellbasierten Ansatzes, welcher eine gerade Linie wie in der gefilterten Rückprojektion erwartet, führt zu Artefakten in den rekonstruierten Bildern. Die Nutzung eines Ansatzes mit einer Systemfunktion, welcher die korrekt aufgelösten Spektren berücksichtigt, kann Artefakte minimieren. Jedoch teilt sich die Erfassungsrate durch zwei. Um ein größeres Sichtfeld abzudecken, wird eine neue FFL Sequenz mit Fokusfeldern eingeführt. Hier muss bei der Rekonstruktion auf die Systemfunktion zurückgegriffen werden, da keine modellbasierte Rekonstruktion für generische Sequenzen zur Verfügung steht. Die ersten Rekonstruktionen zeigen Artefakte, die in weiteren Studien untersucht werden müssen.

Der zweite Teil dieser Arbeit konzentriert sich auf Sicherheitsaspekte von MPI-Scannern. Das größte MPI-Sicherheitsrisiko, ist die periphere Nervenstimulation (PNS). Da keine genauen Daten über die PNS Schwellenwerte der in MPI genutzten Frequenzen und magnetischen Feldstärken existieren, wird eine Approximation vorgeschlagen und evaluiert. Diese Approximation für einen FFL Menschenscanner, der ein FOV von 400×405 mm^2 10 mal pro Sekunde abbildet, zeigt, dass der Patient PNS erfahren wird. Weitere experimentelle Validierungen müssen durchgeführt werden, um die PNS Schwellenwerte für solche Sequenzen genauer zu bestimmen. Danach können die Sequenzen abgestimmt werden, um PNS im Patienten zu vermeiden. Ein erstes Beispiel für eine solche Abstimmung wird in dieser Arbeit vorgestellt.

Der dritte Teil der Arbeit konzentriert sich auf die Konstruktion eines FFL Scanners mit einem Bohrungsdurchmesser von 173 mm. Eine BEM Formulierung reicht aus, um alle notwendigen Spulen zu optimieren. Ein Scanner-Design mit einem Gradient von 0,8 T$\cdot$m^{-1} und zwei 15 mT Antregungsfeldern wurde implementiert. Die Feldstärken sind vor allem durch die verfügbare Kühlungsinfrastruktur und der komplexen, technischen Realisierung beschränkt. Das tatsächliche Design erfordert ungefähr 40 kW elektrische Leistung. Die Frequenz der FFL Drehung ist durch die Filter, Leistungsfaktorkorrektur und die Abschirmungen der unterschiedlichen Elemente beschränkt.

Contents

1 Introduction

Advancements in medical imaging, medical diagnoses and medical therapies are closely related. The increased information, which can be extracted from biological processes is either obtained by the improvement of existing modalities, as magnetic resonance imaging (MRI), computed tomography (CT), and ultrasound imaging, or by the introduction of a new modality. The novelty of a modality can be defined as the use of a new or unexploited physical process, which often requires the development of dedicated hardware. The magnetic particle imaging (MPI) technique belongs to this last type. It uses the non-linear magnetisation curve of a tracer which is exposed to time and space-varying magnetic fields, including at least one low-field volume (LFV) to image its position and concentration. The first images using this modality have been published in 2005 [1]. Those first results, obtained on a small scale phantom, demonstrate that this imaging technique offers a fast and highly sensitive imaging technique, which does not rely on ionising radiation and could deliver imaging with a resolution below 1 mm. This makes MPI an excellent candidate for the improvement of pre-clinical imaging techniques and for clinical application.

Different approaches exist to realise MPI imagers. This work is focused on field-free line (FFL) scanners, which use a LFV which has the form of a cylinder in 3D or a line in 2D, and are expected to generate an MPI signal with a greater signal to noise ratio (SNR) than an field-free point (FFP) scanner [2]. This type of MPI imager was considered too

complex to be realised [2], due to the dissipated power of the coils. Knopp and al.[3, 4, 5] demonstrated that a less complex system containing only 10 coils allows the generation of a large cylindrical LFV with a dissipated power comparable to the one of an FFP scanner with an equivalent bore size. Recently, a small-sized proof of concept has been implemented [6, 5] and validated [7].

1.1 Outline of this thesis

This work focuses on the extension of the 2D FFL technique to imagers adapted to larger subjects. Indeed, up-scaling of medical technologies relying on magnetic fields is a challenging subject which covers different fields of engineering, from magnet design and optimisation to power management, imaging sequence design and safety.

To assess the performance of imagers, this work does not focus only on the dissipated power. Indeed, others aspects have to be considered to be able to compare the different imagers. Besides the dissipated power in the coils close to the subject, the analysis of the required magnetic field topology, and more particularly the influence of realistic field topologies is investigated. To complete the analysis, the safety evaluation of exposure to time-varying magnetic fields is evaluated. The covered field of view (FOV), imaging rate and the structure of the MPI signal are also added to the analysis. In order to validate the expected performance, a rabbit-sized FFL scanner was designed and the magnets close to the patient were constructed and characterized. The power signal generation and MPI signal acquisition is not treated in this work. Once assembled, the actual performance of this scanner will be evaluated.

In this work, the evaluation of different scanners is not made by comparing only the respective dissipated power and signal to noise ratio; it is done with a broader focus including patient safety and the structure of the MPI signal.

1.2 Originality of the thesis

The originality of this work can be resumed as follow:

- comparison of the parallel-pencil beam acquisition scheme to the simple FFL sequence, with an approach considering an idealised scanner made of idealised coils (ISIC),
- evaluation of artefacts introduced by using the filtered back-projection (FBP) and

the system function (SF) approaches on ISIC and realistic scanners,

- extension of the FFL sequence modelisation using homogeneous coordinates. This allows the rotation of the line around a moving point using focus fields at the same time as the projection acquisition,
- transferring the coil optimisation knowledge from the MRI community to the coils required in MPI and more particularly for FFL and single-sided scanners. An extension is introduced, which is used to estimate the influence of magnetic shields on the magnetic field topology. Moreover, different optimisation schemes have been used. The corresponding implementation has been made available to the whole community,
- derivation of a linear relation allowing the fast evaluation of peripheral nerve stimulation (PNS) risk for the most common coil topology used in MPI to generate magnetic fields with a sinusoidally time-varying amplitude,
- design, characterisation and implementation of the coils close to the patient of a rabbit-sized FFL scanner,
- design and characterisation of a human sized FFL scanner using focus fields and evaluation of the related PNS risk.

The following hypothesis is used as central thread for this work:

Up-scaling FFL 2D MPI imager allows the acquisition of circular FOV which are mainly limited by the magnetic field topology and the PNS of the subject being imaged. Rabbit-sized systems can be constructed to cover a circular fully sampled FOV of 37 mm at 10 images per second. Covering larger FOV at similar acquisition rates could be achieved on human sized 2D FFL MPI imagers.

1.3 Published work

During the course of this work, the author published works on the coil design technique [O1], on the calculation of the drive-coil shielding [O2] and on the representation of the magnetic fields [O3] in peer reviewed journal.

Moreover, coil and scanner design results [O4, O5, O6, O7], PNS specific analysis [O8, O9] and the first concept of a human sized FFL scanner [O10] have been presented at conferences.

Moreover, the author took part in many collaborations which resulted in publication in peer-reviewed journals [O11, O12, O13, O14, O15, O16, O17, O18, O19] and conferences proceedings [O20, O21, O22, O23, O24, O25, O26, O27, O28, O24, O29, O30, O31, O32, O33, O34, O35, O36, O37, O38, O39, O40, O41].

The author also took part in two applications for patents [O42, O43].

1.4 Thesis organisation

The first Chapter defines the scope of this work, as well as its goals.

The Chapter 2 goes through the main fundamentals used throughout this work.

Chapter 3 describes the existing MPI scanners and their associated sequences and performances. Following this description, the relation between parallel-pencil beam CT model and MPI is done, further studying the effect of magnetic field inhomogeneities. A new way to increase the FOV of FFL sequences is also presented.

Then, a more in depth description of the techniques used for the optimisation of air core coils and iron core coils are described in Chapter 4.

Chapter 5 introduces the notion of safety for MPI scanners. In particular, it numerically evaluates the induced electrical fields in a human model and compares them to published thresholds.

Using results from the previous chapters, two scanners are presented in Chapter 6. The coils near the subject for a rabbit-sized scanner are also implemented and their performances are evaluated. The requirements for a human-sized imager covering a large FOV are determined.

Chapters 7 and 8 will present the summary of those results, the final discussion and the outlook.

2

Basic principles

Contents

In this Chapter, the main concepts and physical principles used throughout this work are outlined. In Section 2.1, a quick overview of the principles attached to the electromagnetic phenomena exploited by the MPI technology is done. Then, in Section 2.2, the focus will be made on the Fourier transform and the relevant aspect needed in MPI, more particularly for the frequency based reconstruction and development of new scanner concepts. Finally, in Section 2.3, the fundamental aspects of the technology are presented, from the modelling of the signal generation to the reconstruction of 3D volumes.

2.1 Electromagnetism

This Section covers the four Maxwell equations used under the quasi-static approximation and the calculation of the magnetic and electrical vector and scalar potentials. Moreover, the representation of magnetic fields using spherical harmonics is presented, and

will be used throughout this thesis, in order to characterise them.

2.1.1 Maxwell equations

Electromagnetic phenomena are described for external sources in a vacuum using the four Maxwell equations [8], each known by a specific name. These are
Coulomb's law,

$$\vec{\nabla} \cdot \vec{D} = \rho_c, \tag{2.1}$$

Ampère's law:

$$\vec{\nabla} \times \vec{H} - \frac{\partial \vec{D}}{\partial t} = \vec{J}, \tag{2.2}$$

Faraday's law:

$$\vec{\nabla} \times \vec{E} + \frac{\partial \vec{B}}{\partial t} = \vec{0}, \tag{2.3}$$

and Gauss's law of magnetism:

$$\vec{\nabla} \cdot \vec{B} = 0. \tag{2.4}$$

With $\vec{D}$ the displacement, $\vec{E}$ the electric field, $\vec{H}$ the magnetic field, $\vec{B}$ the magnetic flux-density, $\vec{J}$ the current density, ρ_c the charge density and t the time. $\vec{D}$ is linked with $\vec{E}$ via the relation $\vec{D} = \epsilon\vec{E}$, with ϵ the electric permittivity. $\vec{B}$ is related to $\vec{H}$ via the relation $\vec{B} = \mu\vec{H}$, with μ the magnetic permeability.

2.1.1.1 Quasi-static approximation

Assuming that the rates of change of the electrical and magnetic fields are limited in regards to the propagation time of the field changes, the quasi-static approximation can be used for the major part of this work [8, 9, 10]. Thus, Ampère's law (2.2) becomes:

$$\vec{\nabla} \times \vec{H} = \vec{J}. \tag{2.5}$$

This approximation may lead to the omission of the skin effect. This effect is responsible for a charge density inhomogeneity in a conductor when using signals with frequencies above a few kilohertz. The charges will tend to leave the centre part of the conductor for the surface. The skin depth is defined as the depth at which the charge density falls to 1/e of its value near the surface. Thus 98 % of the charge density is found in a thickness of four times the skin depth [11]. The skin depth δ is defined as:

$$\delta = \sqrt{\frac{2\rho_e}{\omega\mu}}, \tag{2.6}$$

with ω the angular frequency and ρ_e the electrical resistivity. In this work, most of the modelling is done using the quasi-static approximation, ignoring the skin effect. In practice, this effect is either compensated for by using litz wire (see Subsection 6.1.3.1.1) or by modelling the magnetic field shielding effects of conductive surfaces (see Subsection 4.1.1.19).

2.1.1.2 Magneto-static and the continuity equation

The principles of charge conservation state that "the charge density at any point in space [is to] be related to the current density in that neighbourhood by a continuity equation" [8]. This equation is formulated as:

$$\frac{\partial \rho_c}{\partial t} + \vec{\nabla} \cdot \vec{J} = 0. \tag{2.7}$$

In the context of coil design and the study of related effects it can be assumed that, during the normal usage of the system, the rate of change of the net charge density is zero. Indeed, in each current carrying volume, there are as many charges entering the volume as there are leaving it. The system can thus be modelled as a steady state problem. The equation (2.7) thus becomes:

$$\vec{\nabla} \cdot \vec{J} = 0 \tag{2.8}$$

2.1.2 Source free volume and spherical harmonics

In a volume without magnetic field sources, that is where $\vec{J} = \vec{0}$ and without magnetisation $\vec{M} = \vec{0}$, as in the inner volume of a cylindrical coil, both magneto-static and quasi-static approximations are fulfilled. Gauss's law of magnetism (2.4) stays the same and Ampère's law can be simplified in relation (2.8), giving these two equations:

$$\vec{\nabla} \cdot \vec{B} = 0, \tag{2.9}$$

$$\vec{\nabla} \times \vec{B} = \vec{0}. \tag{2.10}$$

Using the vector formulas

$$\vec{\nabla} \times (\vec{\nabla} \times \vec{a}) = \vec{\nabla}(\vec{\nabla} \cdot \vec{a}) - \vec{\nabla}^2 \vec{a},$$

it follows that $\vec{B}$ satisfies the Laplace equation [8, 12]

$$\vec{\nabla}^2 \vec{B} = 0. \tag{2.11}$$

The solutions of the Laplace equation are known as the harmonic functions.

2.1.2.1 Spherical harmonics series expansion

Expressing the solutions in the spherical coordinates system $\vec{r} = (\rho, \theta, \varphi)$, using the Dirichlet boundary condition in a sphere with fixed radius R and requiring that the solutions are finite at the origin and periodic in φ with period 2π yields the spherical harmonic series expansion (SHSE) [13, 8, 10]:

$$B_i(\rho, \theta, \varphi) = \sum_{l=0}^{\infty} \sum_{m=-l}^{l} c_{ilm}^{R} \left(\frac{\rho}{R}\right)^{l} Y_{lm}(\theta, \varphi). \tag{2.12}$$

With $i = x, y, z$ the component directions of $\vec{B}$ in a Cartesian coordinate system, l the degree of the associated Legendre polynomial, m the order of the associated Legendre polynomial with $-l \leq m \leq l$ and c_{ilm}^{R} the spherical harmonic coefficients (SHCs) of the normed real spherical surface harmonics Y_{lm}. The spherical surface harmonics, shown in Figure 2.1, are defined by

$$Y_{lm}(\theta, \varphi) = \begin{cases} \sqrt{2} K_l^m \cos(m\varphi) P_l^m(\cos\theta) & m > 0, \\ K_l^0 P_l^0(\cos\theta) & m = 0, \\ \sqrt{2} K_l^{|m|} \sin(|m|\varphi) P_l^{|m|}(\cos\theta) & m < 0, \end{cases} \tag{2.13}$$

with P_l^m the associated Legendre polynomials and K_l^m the normalising factor defined by

$$K_l^m = \sqrt{\frac{(l-m)!}{(l+m)!}}, \tag{2.14}$$

which is the Schmidt quasi-normalisation, scaling the maximum of each spherical surface harmonics to one [14].

2.1.2.2 Normalisation

Besides the Schmidt quasi-normalisation, other normalisations could be used, but this normalisation delivers SHCs which are easily interpretable and are in good accordance with the basic description of magnetic fields used in MPI publication.

Indeed, the magnetic flux-density of homogeneous fields in a specific direction, like y, in the middle of a cylindrical coil used to generate them (in the case of y-drive coils), would correspond here to the SHC c_{y00}^{R}. Similarly, the gradient amplitude generated by cylindrical coils in their middle is often referenced; it can be calculated using a SHC of first degree $l = 1$ corresponding to the considered field direction and gradient direction. If we speak about the gradient $\frac{\partial B_x}{\partial y} = G_{xy} =$ constant, the corresponding value is obtained

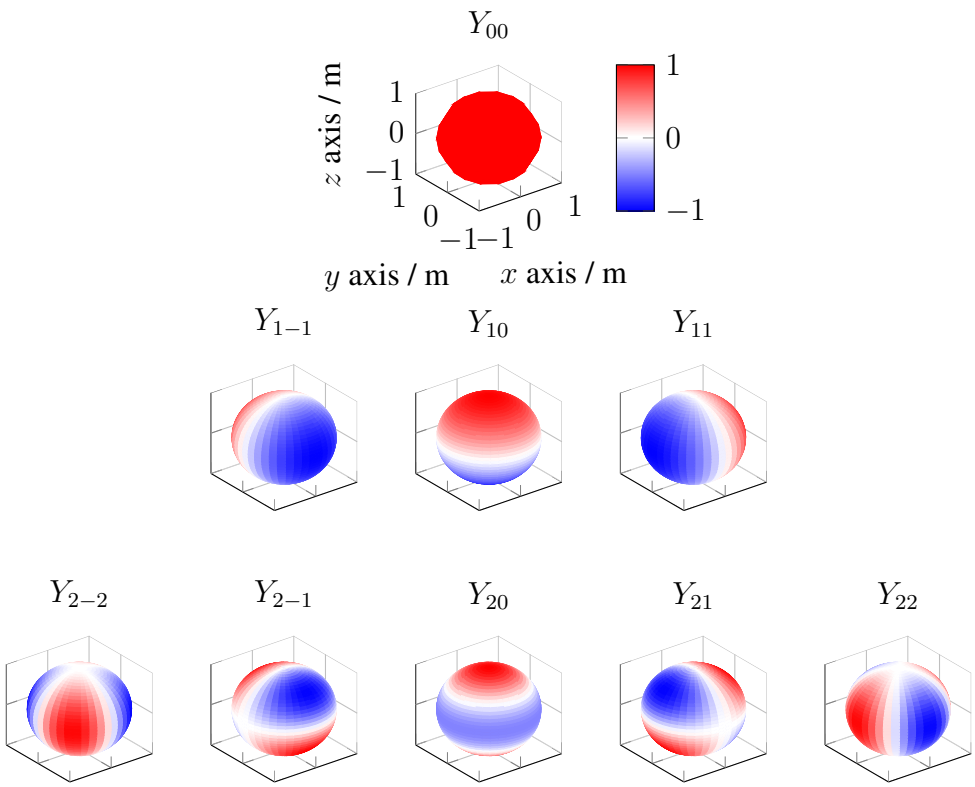

Figure 2.1: The spherical harmonics Y_{lm} with $l \leq 2$ and $-l \leq m \leq l$ are displayed on their definition sphere. Each line shows a given degree l.

as $G_{xy} = \frac{c^R_{x1\text{-}1}}{R}$ using SHSE. The in-plane visualisation proposed in Figure 2.2 aims to simplify the association of the SHC with well known field topologies used in MPI. An homogeneous field is represented at the first line. Linear gradients are represented at the second line and quadrupole fields at the third one.

2.1.2.3 Projection of an ideal magnetic flux-density

Providing to equation (2.12) any SHC set, which fulfills the Maxwell equations, allows us to obtain a 3D vectorial field which represent a magnetic field. On way to ensure that the SHCs fulfills Maxwell equations is to obtain them from magnetic fields, which can be generated by actual electromagnets. This is useful to explore and simulate different MPI scanners [O3], which can be represented as a set of different coils.

The SHCs can be calculated from the magnetic flux-density $\vec{b}$ on a sphere S via the

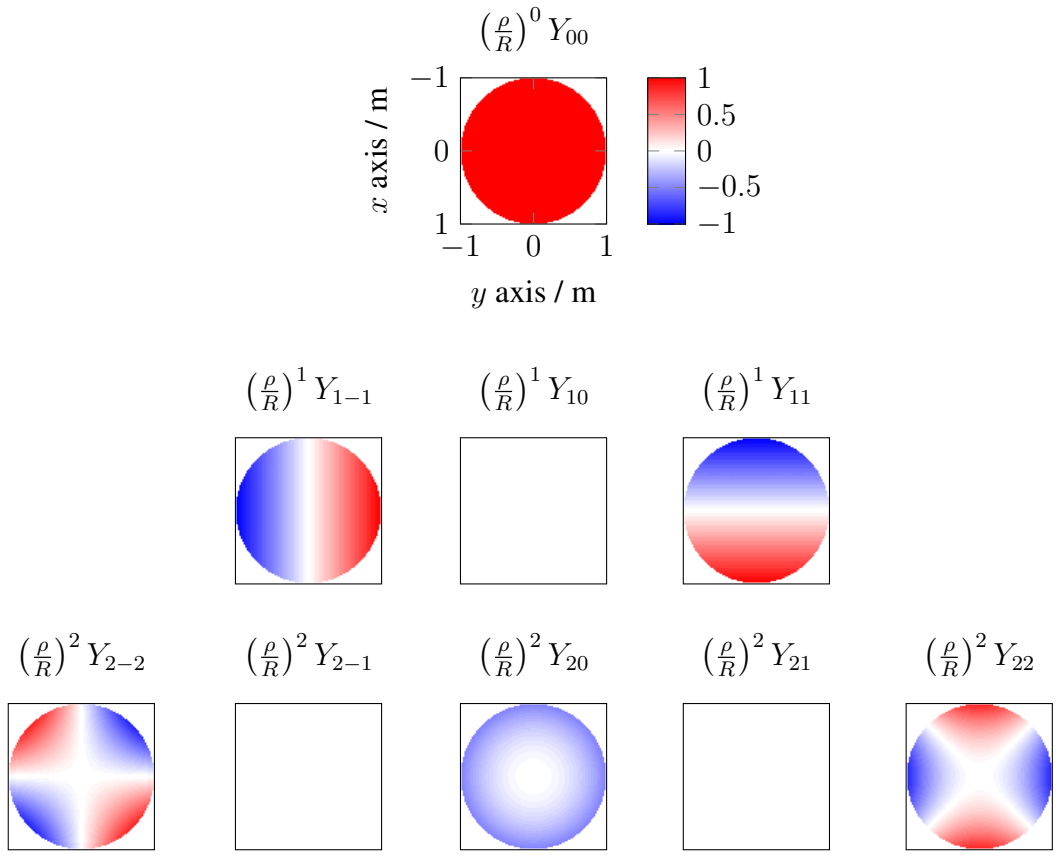

Figure 2.2: The spherical harmonics scaled in the sphere, here represented in the xy-plane. The values in the sphere are calculated using the factor $\left(\frac{\rho}{R}\right)^l$ from equation (2.12). Each line shows a given degree l.

standard scalar product [15, 16] and, as the functions Y_{lm} are orthogonal, simplified as

$$\begin{aligned} c^R_{ilm} = \frac{\langle Y_{lm}, b_i \rangle}{\langle Y_{lm}, Y_{lm} \rangle} &= \frac{1}{\|Y_{lm}\|^2} \int Y_{lm} b_i \, \mathrm{d}S \\ &= \frac{2l+1}{4\pi} \int_0^{2\pi} \int_0^{\pi} b_i(\theta, \varphi) Y_{lm}(\theta, \varphi) \sin(\theta) \, \mathrm{d}\theta \, \mathrm{d}\varphi, \end{aligned} \tag{2.15}$$

with $i = x, y, z$. One way to obtain $\vec{b}$ is to measure it at discrete positions. Equation (2.15) can then be exactly evaluated using numerical integration by

$$c^R_{ilm} = \sum_{j=1}^{N_\theta} \sum_{k=1}^{N_\varphi} \frac{2l+1}{4\pi} \omega^\theta_j \, \omega^\varphi_k \, b_i(\theta_j, \varphi_k) \, Y_{lm}(\theta_j, \varphi_k) \sin(\theta_j) \tag{2.16}$$

with N_θ and N_φ the number of measured points and ω^θ_j, ω^φ_k the weighting factor in the θ and φ directions, respectively. As θ_j and φ_k are independent from one another, the integral (2.16) can be split into two parts.

After the substitution $s_i = \cos(\theta)$ is performed, the part depending on s_i only contains the associated Legendre polynomials, which can be integrated using the Gauss-Legendre quadrature. In contrast, the part depending on φ contains only cosine and sine functions; it can be integrated with a left rectangle method. This requires N_φ points with coordinates $\varphi_k = (k-1)\frac{\pi}{N_\varphi}$ and weights $\omega_k^\varphi = \frac{\pi}{N_\varphi}$.

To be able to exactly project a magnetic field containing SHCs up to degree l_{max} and order m_{max}, only $N_\theta = l_{\text{max}} + 1$ points in the θ direction and $N_\varphi = 2m_{\text{max}} + 1$ points in the φ direction are needed [17, 18, 19].

Unfortunately, it cannot be guaranteed that the measured coil generates a magnetic flux-density containing only a finite number of low degree and order SHCs. Thus, measuring the magnetic flux-density produced by a coil will always deliver approximated results, which, besides measurement uncertainties, will depend on the field topology. Evaluation of the required number of points in order to measure the magnetic flux-density with a given precision will be done in Chapter 4.

2.1.3 Biot-Savart's law

The elemental magnetic flux-density $d\vec{B}$ generated by a current I flowing along an infinitesimally thin wire element of length $d\vec{l}$ is related to the distance between the source point $\vec{r}_{\text{s}}$ (also called the collocation point) and the target point $\vec{r}_{\text{t}}$ situated in a vacuum by the equation [8]:

$$d\vec{B}(\vec{r}_{\text{t}}) = \frac{\mu_0}{4\pi} I \frac{d\vec{l} \times \|\vec{r}_{\text{t}} - \vec{r}_{\text{s}}\|}{\|\vec{r}_{\text{t}} - \vec{r}_{\text{s}}\|^2}. \tag{2.17}$$

This experimental law was first established by Biot and Savart in 1820, and has taken their name. Note that $d\vec{l}$ should have the same direction as the current. Also, this equation follows the continuity equation (2.8) only if it is taken for a closed current carrying path, such as a circular loop.

2.1.4 Time-varying magnetisation

Faraday's law (2.3) can be used to express the electrical field generated by the time-varying magnetisation of magnetic particles. Notice that for a magnetic particle with a magnetisation $\vec{M}$, the magnetic flux-density can be written as

$$\vec{B}(\vec{r}) = \mu_0 \left(\vec{H}(\vec{r}) + \vec{M}(\vec{r}) \right), \tag{2.18}$$

The integral form of equation (2.3) for particles can be used to express the electromotive force $u(t)$ obtained at the endpoints of a volume coil made with a conductor placed on

surface ∂S covering volume V [20]

$$\begin{aligned} u(t) &= \oint_{\partial S} \vec{E}(\vec{l}, t) \cdot \mathrm{d}\vec{l} \\ &= -\mu_0 \int_V \vec{p}_q(\vec{r}) \cdot \frac{\partial}{\partial t} \vec{M}(\vec{r}, t)\, \mathrm{d}V, \end{aligned} \tag{2.19}$$

with $\vec{p}_q$ the sensitivity of a receive coil, typically obtained by calculating the magnetic flux-density of the coil using a unitary current with equation (2.17), as explained further in Section 2.3.3.2.

2.1.5 Magnetic vector and electric scalar potentials

From Gauss's law of magnetism (2.4), the magnetic vector potential field is indirectly defined though the relation

$$\vec{B} = \vec{\nabla} \times \vec{A}. \tag{2.20}$$

Then Faraday's law (2.3) can be written to express $\vec{E}$ as [21, 8]

$$\vec{E} = -\vec{\nabla}\phi_e - \frac{\partial \vec{A}}{\partial t}, \tag{2.21}$$

with ϕ_e the electric scalar potential field and $\vec{A}$ the magnetic vector potential field.

2.1.6 Gauge fixing

As seen in 2.1.5, $\vec{A}$ is indirectly defined as the curl of $\vec{B}$. The curl of the gradient of any scalar function is zero, so any gradient of a scalar function added to $\vec{A}$ will not change $\vec{B}$. But this will change the expression of $\vec{E}$, as can been seen with equation (2.21). Many ways to fully define $\vec{A}$ exist, and going from one definition to another is done using gauge transformation [22].

Various gauges are used in electromagnetism [23]. It has to be noted that most of the commonly used software like COMSOL use by default the Lorentz gauge.

In this work, the Coulomb gauge is used, which is defined as:

$$\vec{\nabla} \cdot \vec{A} = 0. \tag{2.22}$$

As will be seen in the Chapter 5, this gauge will help us to simplify the expression of ϕ_e on the boundary of a domain, thus enabling the calculation of the electric field via the equation (2.21).

2.2 Digital signal processing

In this Section, tools required to understand, study and develop concepts through the use and understanding of digital signal processing in MPI are presented. Those focus on the frequency based approach as presented by Gleich and Weizenecker in the first publication about MPI [1]. The link between the MPI signal and the discrete Fourier transform (DFT) structures, the digital signal filtering and MPI-sequence design are given.

2.2.1 Sampled signals

The sampled signal $\bar{u}$ is the result of sampling a time-continuous voltage signal u which is made band-limited through the use of a low-pass filter. Both signals u and $\bar{u}$ are shown in Figure 2.3. Assuming that besides noises any effects linked to the signal distortion are negligible, the sampled signal can be represented as a series of measurements $\bar{u}_n$ at discrete time point t_n. Those points are regularly sampled in time so that the sampling time t_n can be defined as

$$t_n = n\Delta t \tag{2.23}$$

with $n \in \mathbb{Z}$ a multiple of the sampling interval Δt [24]. The sampling frequency f_s is then given by the relation

$$f_\mathrm{s} = \frac{1}{\Delta t}. \tag{2.24}$$

The time during which the signal is acquired T_a gives the number of sampled points N_s through the relation

$$N_\mathrm{s} = T_\mathrm{a} f_\mathrm{s}. \tag{2.25}$$

The choice of the parameters f_s and T_a is closely linked to the design of MPI scanners and the choice of the reconstruction method. Those number are chosen to perfectly resolve the Fourier coefficients (FCs) obtained via the DFT of the MPI signal.

2.2.2 Discrete Fourier transform

The DFT transforms the vector with complex numbers $\bar{u}_n, n = 0, \ldots, N_\mathrm{s} - 1$ into the vector of N_s complex FCs $\hat{u}_k, k = 0, \ldots, N_\mathrm{s} - 1$ [25]. As for the SHSE different normalisations are used for the FCs. In this work, the Matlab (7.11.0, Mathworks, USA) implementation is used, which is itself based on the FFTW package [26]. The *fft* command uses the function

$$\hat{u}_k = \sum_{n=0}^{N_\mathrm{s}-1} \bar{u}_n \exp\left(-2\pi \mathrm{i} \frac{kn}{N_\mathrm{s}}\right), k = 0, \ldots, N_\mathrm{s} - 1. \tag{2.26}$$

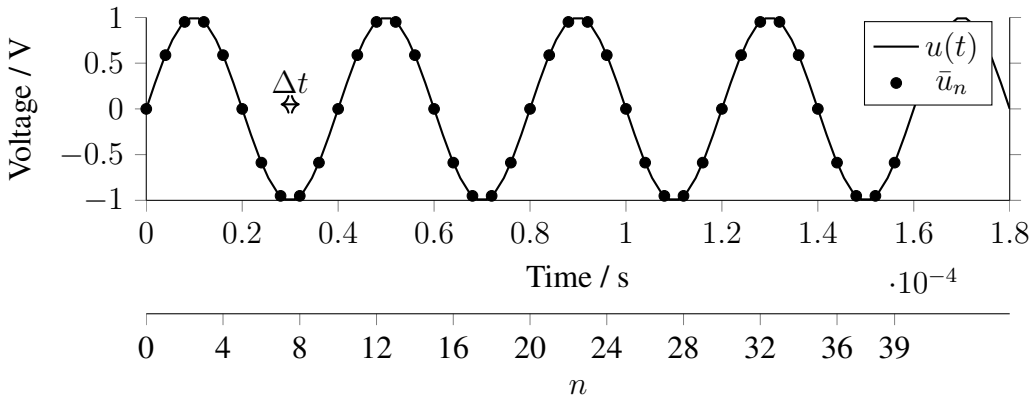

Figure 2.3: Both continuous and discrete voltage signal u and $\bar{u}$. The example of a 25 kHz signal sampled at 250 kHz is here taken. 40 points are acquired.

The output produced by the DFT of the signal shown in Figure 2.3 is shown in Figure 2.4. According to the Nyquist theorem, the maximum useful frequency f_{Ny} which can be obtained by sampling the signal is

$$f_{\text{Ny}} = \frac{f_{\text{s}}}{2}. \tag{2.27}$$

Thus, the sampling frequency should always be at least two times higher than the highest expected frequency in the signal.

The spectrum resolution Δf (also called the width of the frequency bin) is of high importance in MPI, as will be seen in the Section 2.3, and is given by the relation

$$\Delta f = \frac{f_{\text{s}}}{N_{\text{s}}} = \frac{1}{T_{\text{a}}}. \tag{2.28}$$

2.2.2.1 Properly resolved spectrum

The notion of a properly resolved spectrum can be seen from different positions. One way of seeing it is to always acquire an integer number of periods for each frequency f_k included in the original signal. This can also be fulfilled if we enforce that each f_k has to be an integer multiple of the spectrum resolution:

$$f_k = k\Delta f. \tag{2.29}$$

If this condition is not fulfilled, energy leakage will appears in the spectrum. An example is given with Figure 2.4 and 2.5.

In Figure 2.4 a $f_1 = 25$ kHz signal is sampled at $f_{\text{s}} = 250$ kHz using $N_{\text{s}} = 40$ acquisition points. The spectrum resolution $\Delta f = 6.25$ kHz can properly resolve the frequency, with $k = 25/6.25 = 4$.

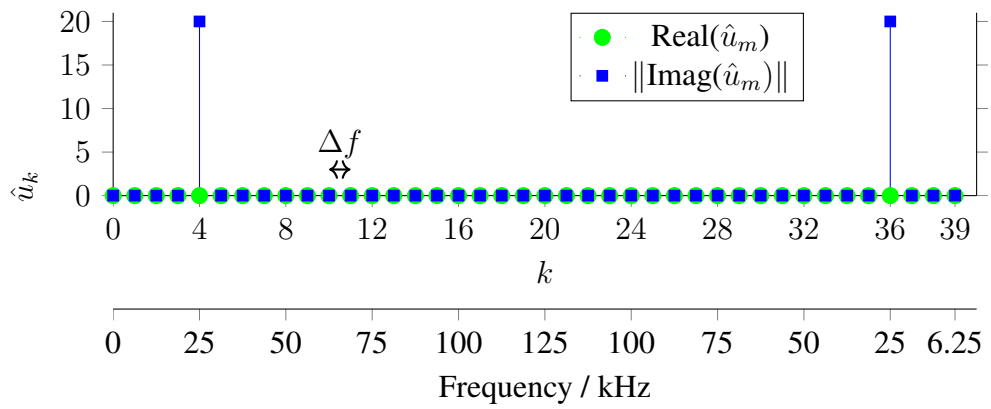

Figure 2.4: Real and imaginary parts of the DFT as described by equation (2.26) of a $f_k = 25$ kHz signal decomposed in a spectrum with $\Delta f = 6.25$ kHz. Here $k = \frac{f_k}{\Delta f} = 4$

In Figure 2.5 a slightly different frequency $f_2 = 28$ kHz is used and all the other parameters are kept the same, thus leading to $k = 28/6.25 = 4.48$, which is not an integer. It can be seen that the energy contained in the frequency is not properly resolved, thus leaking into the neighbouring bins.

If the acquisition parameters cannot be changed in order to resolve this frequency, other methods exist to correct the spectrum, such as the use of an adapted windowing function. As we are enforcing the proper resolution of spectrum in MPI, a square window will always be used, and the use of more complex ones will not be treated in this work.

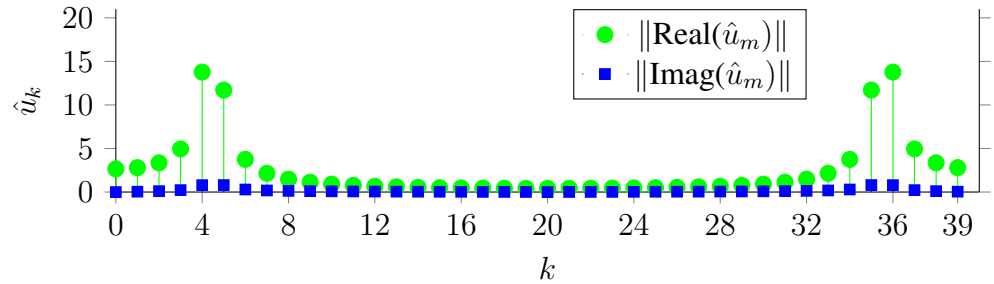

Figure 2.5: Absolute value of the real and imaginary part of the DFT as described by equation (2.26) of a $f_k = 28$ kHz signal decomposed in a spectrum with $\Delta f = 6.25$ kHz. Here $k = \frac{f_k}{\Delta f} = 4.48$.

2.2.2.2 Scaling

The FCs as defined in equation (2.26) are dependent on the number of points N_s. In order to obtain further physical meaning from the DFT, scaling functions have to be used. We first define a second series of FCs $\hat{u}^{(2)}$ as

$$\hat{u}_k^{(2)} = \frac{\hat{u}_k}{N_\mathrm{s}} \qquad k = 0, \ldots, N_\mathrm{s} - 1. \tag{2.30}$$

This scaling may be applied through the use of a window function, which in the case of a rectangular window is equivalent to the equation (2.30) [25, 24].

Assuming that N_s is even, using the symmetry properties of the FC series and keeping the energy constant, the one-sided spectrum is defined as

$$\hat{u}_k^{(3)} = \begin{cases} \hat{u}_k^{(2)} & k = 0, \\ 2\hat{u}_k^{(2)} & k = 1, \ldots, N_\mathrm{s}/2. \end{cases} \tag{2.31}$$

The power spectrum (PS) (also known as Periodogram) is then defined as

$$\mathrm{PS}_k = \|\hat{u}_k^{(3)}\|^2 \qquad k = 0, \ldots, N_\mathrm{s}/2, \tag{2.32}$$

with $[\mathrm{PS}_k] = \mathrm{V}^2$ for an sampled signal $\bar{u}$ given in volts.

The power spectral density (PSD) follows as

$$\mathrm{PSD}_k = \frac{\mathrm{PS}_k}{f_\mathrm{s}} = \frac{\|\hat{u}_k^{(3)}\|^2}{f_\mathrm{s}} \qquad k = 0, \ldots, N_\mathrm{s}/2, \tag{2.33}$$

with $[\mathrm{PSD}_k] = \mathrm{V}^2/\mathrm{Hz}$ for an sampled signal $\bar{u}$ given in volts. The amplitude spectrum (AS) is defined as

$$\mathrm{AS}_k = \sqrt{\mathrm{PS}_k} = \sqrt{\|\hat{u}_k^{(3)}\|^2} \qquad k = 0, \ldots, N_\mathrm{s}/2, \tag{2.34}$$

and the amplitude spectral density (ASD) as

$$\mathrm{ASD}_k = \sqrt{\mathrm{PSD}_k} = \sqrt{\frac{\|\hat{u}_k^{(3)}\|^2}{f_\mathrm{s}}} \qquad k = 0, \ldots, N_\mathrm{s}/2, \tag{2.35}$$

with $[\mathrm{AS}_k] = \mathrm{V}$ and $[\mathrm{ASD}_k] = \mathrm{V}/\sqrt{\mathrm{Hz}}$.

The PS and AS are typically used to display the signal amplitude, whereas the PSD and the ASD are used to display the noise spectral density. Examples of MPI-signal are given in Section 2.3.7.

2.2.3 Digital filtering

The spectrum can be modified through the direct weighting of the FCs obtained after a DFT, which is called digital filtering. This is mainly done in MPI before the reconstruction step, in order to remove the unexpected frequencies.

Besides digital filtering, the signals are also pre-processed using different analog filters, as explained in the next Sections.

2.3 Magnetic particle imaging

In this Section, the fundamentals of the MPI technology are explained in the first Sections, along with the associated limitations, hypotheses, approximations and simplifications. A simulation framework which implements the proposed model is described in detail in Appendix E. Up to 2015, the calibration based approach to reconstructing the images was the gold standard in MPI. This approach is mainly done using signals in the Fourier space. Thus, the simulations presented here are focused on the same approach to display the MPI signals. Other model-based reconstruction approaches exist, which are equivalent to the technique used here [27].

2.3.1 MPI-signal generation

Using a sample of the commercial MRI contrast agent Resovist (Bayer HealthCare Pharmaceuticals, Berlin) [28], Gleich and Weizenecker have shown that the non-linear response to an external magnetic field of the solution can be used to assess the quantity of superparamagnetic iron oxide nanoparticle (SPION) present in the sample under test. Using this principle, a specific encoding scheme and the same tracer, they also acquired a sequence of images [1]. The encoding scheme used will be explained in the next Subsection.

In Figure 2.6 is shown a widely used representation of the 0D SPION-signal generation. On the bottom right plot is represented a time-varying magnetic field with a sinusoidally time-varying strength. Directly above is the magnetisation curve of the sample under test. In the middle of the Figure is represented the time-varying magnetisation resulting from the sample magnetisation being exposed to the time-varying magnetic field shown in the first plot. Directly on the right is the signal induced by the time-varying magnetisation in the receive coil. Finally, below the induced voltage is the associated AS. It can be seen that the response of the SPION is limited to harmonics of the excitation frequency.

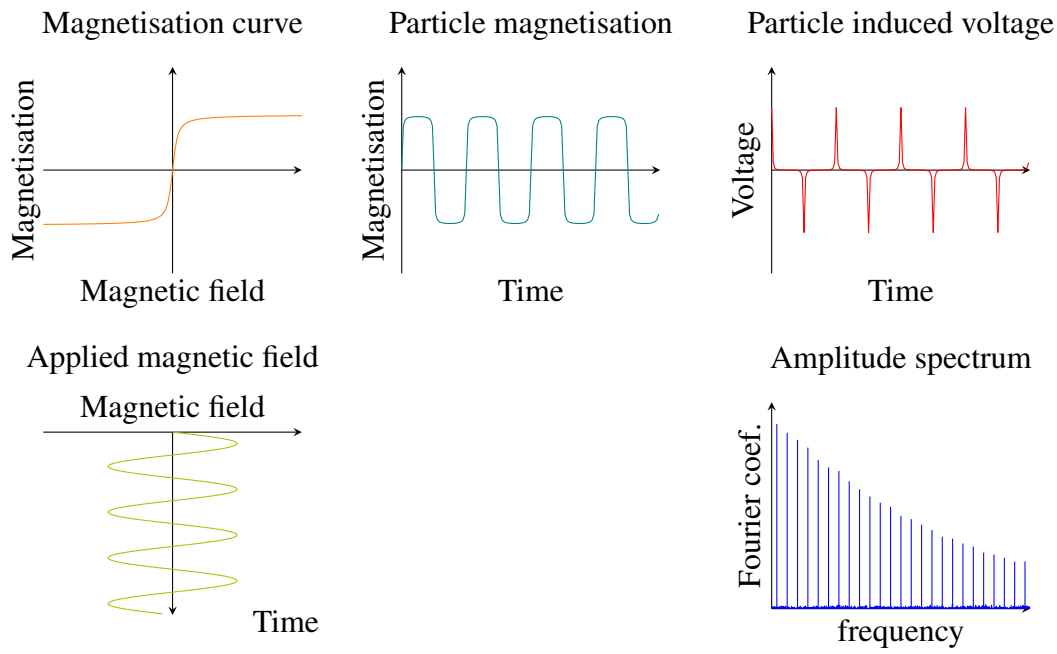

Figure 2.6: Principle of the SPION-signal generation.

This description represents only the induced voltage produced by the time-varying magnetisation of the sample. The coil generating the magnetic field will also induce a voltage in the receive coil. This voltage, which is band limited, is often 3 to 6 orders of magnitude higher than the induced signal produced by the SPION. In order to technically resolve the amplitudes of the harmonics, the voltage induced at the frequency f_0 is filtered out. This is done with analogue filters, which can damp the FC at f_0 by more than 100 dB, but could also influence the value of the FCs at $2f_0$ and $3f_0$. Thus the complete particle signal cannot be obtained and the altered signal which is acquired is called the MPI signal.

The Figure 2.7 simulates a measurement done with a spectrometer comparable to the one built by S. Biederer [29]. A field with a peak amplitude of 20 mT at a frequency $f_0 = 25$ kHz is used for the excitation signal. The solution under test is 10 μl of Resovist, which has, for the sake of this example, unknown properties.

Gleich and Weizenecker have shown in [1] that the behaviour of Resovist is well approximated by modelling the solution as one containing 3 % of the iron content of Resovist as a collection of mono-disperse magnetite (Fe_3O_4) SPIONs with a core diameter $d_{\mathrm{np}} = 30$ nm. That means that 10 μl of Resovist, having a concentration of 0.500 mol(Fe)·l^{-1}, can be modelled as a solution with an iron content of 0.015 mol(Fe)·l^{-1} of pure magnetite with a magnetisation at saturation M_{s} of 0.6 T·μ_0^{-1}. The magnetisation

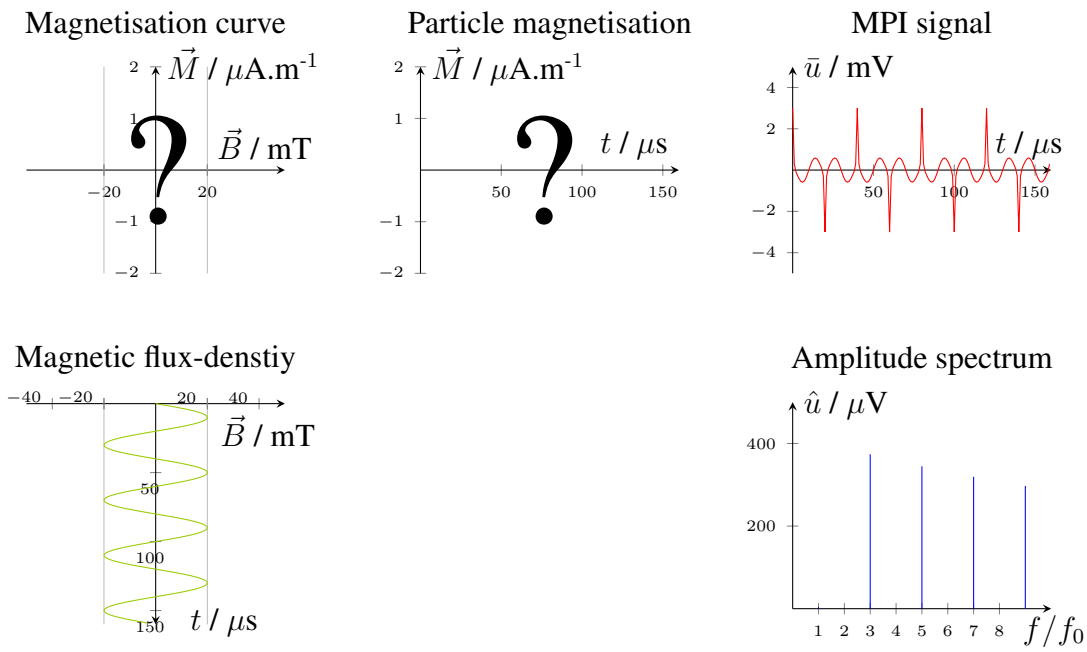

Figure 2.7: Measurement of 10 μl undiluted Resovist in a spectrometer as described in [29]. Note that the magnetisation curve and the particle magnetisation are not known.

curve of pure magnetite is approximated using the Langevin model [30, 31] as

$$\vec{M}(\vec{r},t) = c(\vec{r},t)\, M_s\, \vec{e}_{\vec{B}} \begin{cases} \coth(a) - \frac{1}{a} & \|a\| > 10^{-6}, \\ \frac{a}{3} & \|a\| \leq 10^{-6}, \end{cases} \tag{2.36}$$

with $\vec{e}_{\vec{B}}$ a unit vector in $\vec{B}$ direction, c the tracer concentration and

$$a(\vec{r},t) = \frac{\mu_s \|\vec{B}(\vec{r},t)\|}{k_\mathrm{B} T} \tag{2.37}$$

with μ_s the magnetic moment at saturation of a single SPION, k_B the Boltzmann constant and T the temperature. μ_s is calculated using the relation

$$\mu_s = \frac{1}{6}\pi d_\mathrm{np} M_\mathrm{s}. \tag{2.38}$$

Numerically the singularity present in (2.36) around $a = 0$ is removed by taking the Taylor expansion of the Langevin function. Using such a model, the magnetisation curve from our measurement can be simulated, calculating the particle magnetisation. Using relation (2.19), the receive coil sensitivity profile equivalent to the one used for the measurement, the induced voltage by the SPIONs is obtained. Then, the complete spectrum is simulated and the results are displayed in Figure 2.8.

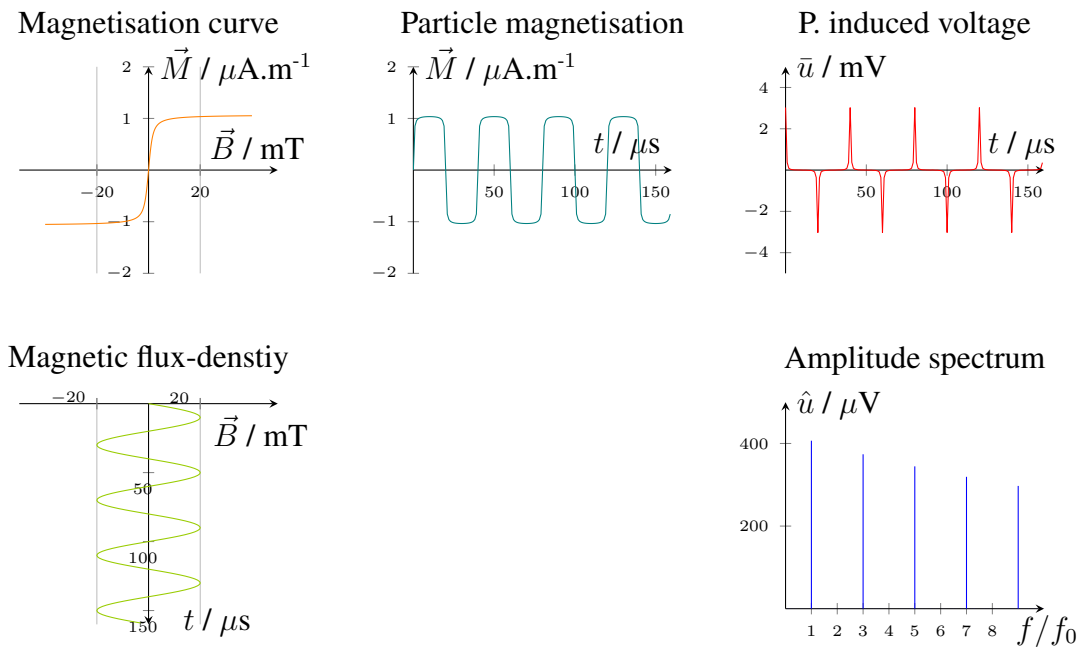

Figure 2.8: Simulation of the induced voltage of 10 μl of 30 nm Langevin particles taking into account the spectrometer characteristic, outside the filtering of the f_0 frequencies.

Comparing Figure 2.7 and 2.8, it has to be noted that the filtering of the particle signal at f_0 and the modification of the few first harmonics has a notable influence on the induced voltage shape. However, the peak voltage, required to adequately gauge the whole acquisition system, is not much influenced. This is true only if f_0 is properly filtered out.

Analysing the relation between the amplitude of the voltage or the spectrum with the particle concentration, a linear relationship has been proposed [1]. Further investigation has to be done in order to validate the different conditions required to validate this hypothesis [32, 33, 34].

Also, even if the Langevin model shows a good agreement with the measurements, more accurate models are needed to explain some aspects of the measurements. One major aspect is the influence of the relaxation time on the measurements [35]. Another one is the optimisation of new tracers. In fact, inconsistency with this model has been observed, and questions arise as to whether the Langevin model should be used to influence the syntheses of new tracer, aiming at mono-disperse solution with a given particle diameter, or if particle-particle interactions could not also be used to enhance the MPI signal [36].

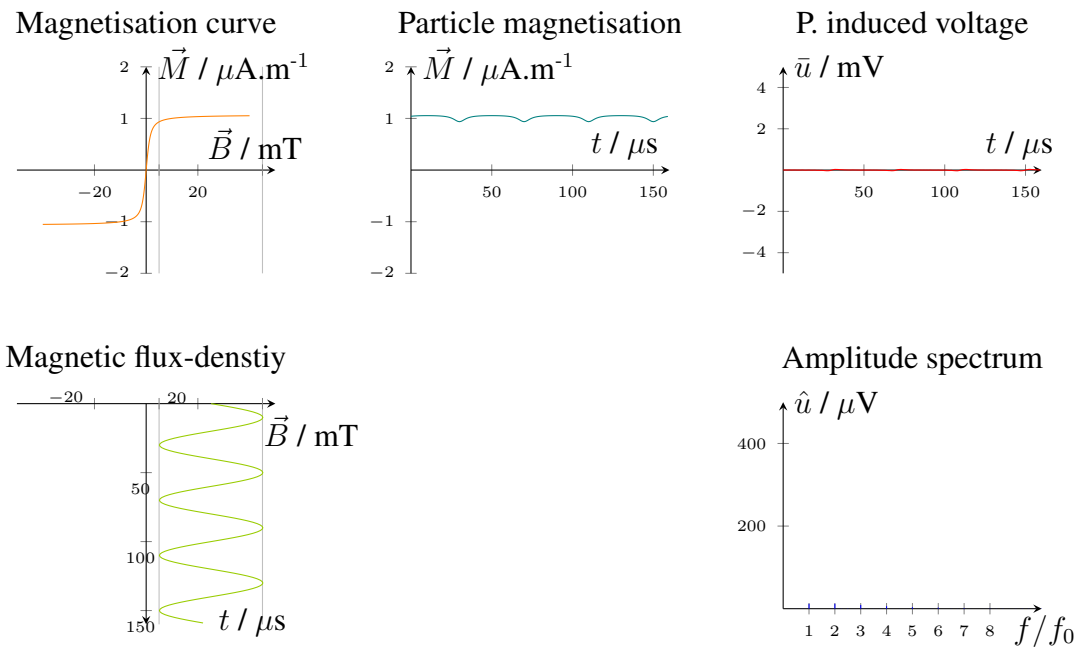

Figure 2.9: Simulation of the induced voltage of 10 μl of 30 nm Langevin particles taking into account the spectrometer characteristic, outside the filtering of the f_0 frequencies. An offset of 25 mT has been applied, thus constantly keeping the particle in saturation.

2.3.2 MPI-signal spatial encoding

The MPI signal previously generated can be described as encoding a zero-dimensional signal. The whole volume under test generates the signal. To spatially resolve the tracer distribution, only a small portion of the tracer should be able to produce signal at a given time. This can be accomplished by applying a high strength magnetic field to the other particles to saturate them, effectively reducing the MPI-signal amplitude below detectable levels. An example is given in Figure 2.9. There an offset field has been added to the magnetic field, with a strength high enough to bring the particles into saturation. The magnetisation change over time becoming smaller, the induced signal is hardly detectable.

Within any offset magnetic field, the particle will experience an asymmetric excitation, and the spectrum will not only contain odd harmonics but also even ones. This situation is represented in Figure 2.10.

In a measurement volume, most of the detectable MPI signal will originate from the position where the magnetic flux-density solely generated by the imager device is below a few milliteslas. In order to generate an MPI signal, this volume has to contain a sample of a tracer and be exposed to a time-varying magnetic flux-density with a sufficient

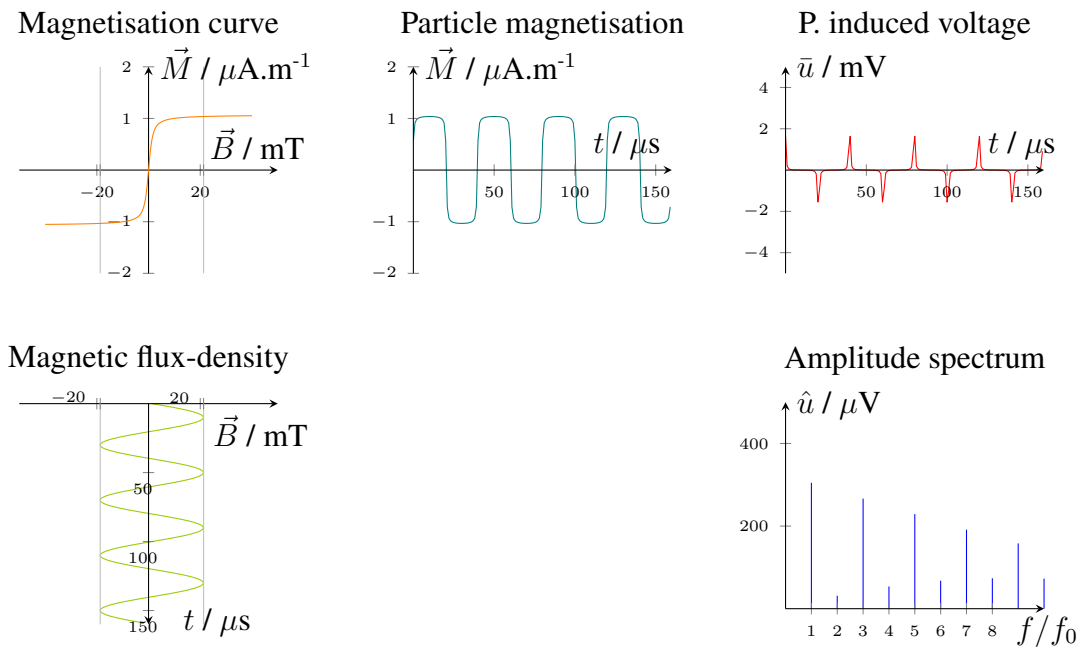

Figure 2.10: Simulation of the induced voltage of 10 μl of 30 nm Langevin particles taking into account the spectrometer characteristic, outside the filtering of the f_0 frequencies. An offset of only 1.3 mT has been applied, leading to a spectrum containing also even harmonics.

amplitude. The volume in which the MPI signal is generated is named in the literature field-free point (FFP) or field-free line (FFL), even though low-field volume (LFV) seems to be more appropriate. The distinction made between the field free point or line is originally derived from the LFV shape of the magnetic field used as offset field. In Figure 2.11, the LFV with a threshold at $\|\vec{B}\| = 3$ mT is shown as an example for ideal FFP and FFL selection fields from ideal scanners [O3]. In principle, SPIONs in the white area are in the LFV and generate the MPI signal, while the ones in the black area are mostly saturated and do not produce enough MPI signal to be detected.

In order to create the LFV a magnetic field varying in space is required. Magnetic fields varying linearly in space are mostly used, supposedly due to their easy implementation, which are the ones created by SHCs of first degrees.

Superimposing an homogeneous magnetic field onto the linearly varying magnetic field has two effects:

- the LFV is moved,
- the MPI signal in the LFV is generate,

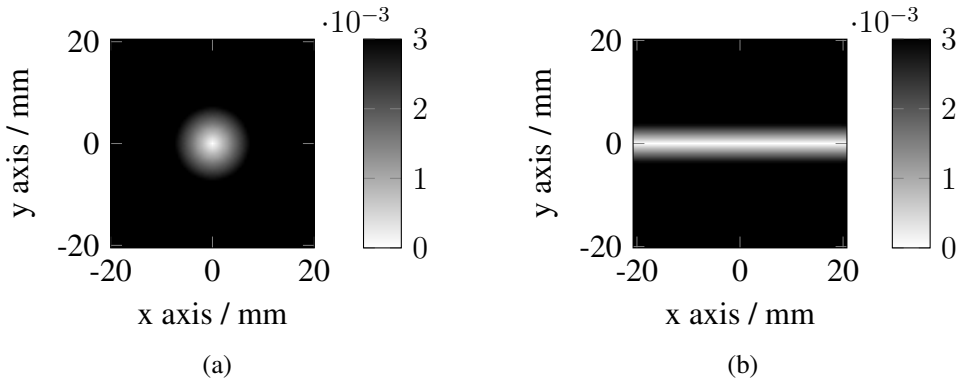

Figure 2.11: Absolute magnetic flux-density in the xy plane at $z = 0$ (in the middle of the scanner) with a black threshold at 3 mT. (a) For an ideal FFP scanner. (b) For an ideal FFL scanner.

which is a key aspect of MPI. The fields which generates the MPI signal also makes the space encoding. In this work, the relations between the spatial variation of the used magnetic fields and the time function applied to each of them will be named MPI sequences. In Section 2.3.4, the relation between a well known MPI sequence and the MPI signal structures will be presented.

2.3.3 Coils and scanners nomenclature

Up to 2015, most of the fast 2D and 3D measurements have been done on a few scanners mostly designed and operated by the technology inventors and early developers Jörn Borgert, Bernhard Gleich, Jürgen Rahmer and Jürgen Weizenecker [1, 31, 37, 38, 32]. The nomenclature used in their work to describe the different parts of the scanners is explained here and extended using the SHSE. Based on idealised coils and scanners, the notion of ISIC, or ideal scanner, is here further explained to facilitate the descriptions.

Idealised scanners are described here as an assembly of idealised coils, to which any possibly time-dependent current can be applied. As a purely computational model, the influences of derived quantities such as voltage or dissipated power have no influences. In order to model the effect of the different analogue filters, a digital filter suppressing the first frequencies (in general, up to around 1.5 times the excitation frequency) and limiting the maximum frequency to 1 to 5 MHz is applied. No further effects are taken into account.

Idealised coils are described by a small number of SHCs, which are impossible to obtain in reality. All of the idealised coils used in this work can be represented by a single

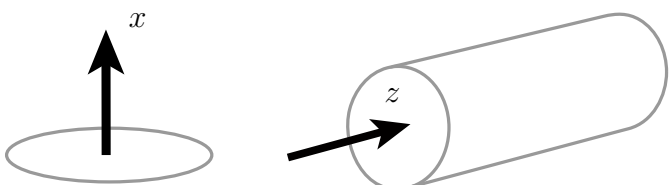

Figure 2.12: The coordinate system is defined according 2 main directions of scanners. x is described as the vertical direction and z as the direction along a cylinder.

value, which can be associated with one or several SHCs. This value, associated with a single SHC describes the main SHC. Thus, the relation between an idealised coil and its realistic pendant are the SHCs which are not included in the association with the main SHC. Aspects linked to real coils are covered in the next chapters. Note that a single real coil or coil set may combine the function of many idealised coils and *vice versa*.

Any coordinate system can be used to describe most aspects of MPI. However, to simplify further description, a right-handed Cartesian coordinate system will be assumed throughout this work. The x, y and z direction are defined as pictured in Figure 2.12. The x direction is defined relative to the single sided concept [39] as the direction perpendicular to the main flat surface of a scanner or to the vertical direction. The z direction is defined in relation to a cylindrical scanner, as the direction parallel to the rotation axis. Then, the y direction is defined following the right-hand rules.

2.3.3.1 Selection coil

The magnetic flux-density produced by a selection coil, the selection field, is used in order to produce the LFV. Common topologies only include SHCs of order 1. Besides practical limitations, this could also be generated by higher order components. Two topologies arise in the literature:

- generalised Maxwell-coil-pair, also called z-gradient,
- quadrupoles.

The generalised Maxwell coil-pair is described by the three SHC of degree $l = 1$, each in a different direction and one having a coefficient two times bigger than the other ones. For example, a Maxwell coil-pair described by the coefficients $c^R_{x1-1} = g$, $c^R_{y11} = g$ and $c^R_{z10} = 2g$ is the model for an idealised Maxwell coil-pair with the strongest gradient in the z direction [40, 41]. This could be realised by winding a solenoid around a cylinder similar to the one in Figure 2.12, and having the flowing direction of the current changing

in the middle of the cylinder. In the middle of the cylinder, in the xy plane, the LFV would appear as it is presented in Figure 2.11a. The efficiency of a selection-coil set is defined in this work using a single SHC. When the main SHCs are not all equal, the chosen coefficient has to be further specified. For example, the efficiency of a z-gradient coil is defined using its main biggest SHC, which can be described in this case as

$$\eta_{zz\text{grad}} = \frac{c^R_{z10}}{R} = \frac{2g}{R}, \tag{2.39}$$

with $[\eta_{zz\text{grad}}] = \text{T}\cdot\text{m}^{-1}\cdot\text{A}^{-1}$.

Quadrupoles are represented by only two SHC. If an FFL scanner had to be created with the Maxwell coil-pair introduced in the previous paragraph, the SHC could be chosen as $c^R_{x11} = g$ and $c^R_{y1-1} = -g$. Such a quadrupole is called Q_0 in this work. Indeed, when used along with the previously defined z-gradient coil, it produces a LFV, which is aligned with the x or y axis, depending on the magnetic field direction (or the current direction used to produce the magnetic field). Another type of quadrupole is rotated by 45 ° and is thus called Q_{45}. It is defined with the two SHCs $c^R_{x1-1} = g$ and $c^R_{y11} = g$. The efficiency of Q_0 alone is defined using its main SHC by the relation:

$$\eta_{\text{Q}_0} = \frac{c^R_{x1-1}}{R} = \frac{g}{R}, \tag{2.40}$$

with $[\eta_{\text{Q}_0}] = \text{T}\cdot\text{m}^{-1}\cdot\text{A}^{-1}$.

Using the z-gradient coil set and the Q_0 coil set previously defined with the same current, the LFV as presented in Figure 2.11b is obtained.

2.3.3.2 Drive coil and receive coil

The magnetic flux-density produced by a drive coil, the drive field, should literally drive the LFV through the space with a high velocity. The high velocity is relative to each scanner in order to differentiate the drive coils from the focus coils. The latter are introduced in the next subsection.

The drive field is a magnetic flux-density which is homogeneous in space and non-null for a single direction. It is described by a single main SHC of order $m = 0$ and degree $l = 0$. For example, three different drive coils can be used to move the LFV in 3D, using coils defined by the SHC c^R_{x00}, c^R_{y00} and c^R_{z00}.

Similarly, the same coil type could be used to receive the MPI signal either by using exactly the same coil or by making a coil with an increased number of loops in order to increase its sensitivity. Note that the concepts of efficiency $\vec{\eta}$ and sensitivity $\vec{p}$ are linked, and are taken as equivalent in MPI according to the reciprocity theorem. The first term

is nonetheless used for the coil aimed at generating a magnetic field. The second one is being used for the coil recording a magnetic field variation, as the MPI signal.

As the drive coil is mainly used in a single direction, the efficiency of such a coil is described using a single value. For example, the efficiency of a x-drive coil is defined as

$$\eta_{x\mathrm{D}} = c^R_{x00} = b, \tag{2.41}$$

with $[\eta_{x\mathrm{D}}] = \mathrm{T{\cdot}A^{-1}}$.

2.3.3.3 Focus coil

The magnetic flux-density produced by a focus-coil, the focus field, should, as for the drive coil, move the LFV in space. But the main idea here is to slowly move it, relative to the movement generated with the drive coil. Thus, the area covered by the LFV will be extended, without increasing the strength of the drive field.

This is mainly done to overcome a limitation of the drive-field strength, which is linked to the PNS in the frequency range used in MPI. This limitation will be further explained in Chapter 5. Besides safety-related aspects, the focus fields can also be used to reduce the bandwidth of the MPI signal using intermodulation techniques [42, 32] as explained in Section 2.3.4 and extended in Chapter 6. This is mainly done to overcomes a limitation of the drive-fields strength, which is linked to the PNS in the frequency range used in MPI. This limitation will be further explained in Chapter 5.

2.3.3.4 3D FFP scanner

A 3D FFP ISIC can be represented by using a Maxwell coil-pair and a drive coil in each spatial direction. This model thus required only 4 values to be fully described. Those value are summarised in Table 2.1.

Table 2.1: Representation of a 3D FFP ISIC.

Coil name	SHC		
Selection	$c^R_{x11} = -g$	$c^R_{y1-1} = -g$	$c^R_{z10} = -2g$
Drive x	$c^R_{x00} = a$		
Drive y		$c^R_{y00} = b$	
Drive z			$c^R_{z00} = c$

2.3.3.5 2D FFL scanner

A 2D FFL ISIC can be represented by using a more complex set of selection coils and two drive coils, thus generating signals in the xy plane. The selection-coil configuration is taken from [3, 4] and will be further explained in Chapter 3. To completely describe it, 5 values are required, as shown in Table 2.2. Then, to generates an FFL with those fields topologies, the current amplitude I_j associated to each coil set should be chosen so that $I_1 g_1 = I_2 g_2 = I_3 g_3$.

Table 2.2: Representation of a theoretical 2D FFL scanner.

Coil name	SHC		
Selection - Maxwell	$c^R_{x11} = -g_1$	$c^R_{y1-1} = -g_1$	$c^R_{z10} = -2g_1$
Selection - Quad$_0$	$c^R_{x11} = g_2$	$c^R_{y1-1} = -g_2$	
Selection - Quad$_{45}$	$c^R_{x1-1} = g_3$	$c^R_{y11} = g_3$	
Drive x	$c^R_{x00} = a$		
Drive y		$c^R_{y00} = b$	

2.3.4 MPI sequences

Many types of MPI sequences, also named trajectories, have emerged in the last years. In this work, the term MPI sequence is preferred to trajectory, as the latter term becomes ambiguous when several LFV are present or for the case of realistic scanners, which could have LFVs split in many parts or simply absent. Knopp et al. studied 5 different sequences in [43].

Focusing on the image acquisition rate, two types of sequences emerged. The first one aims toward a rapid space-encoding, while the second one goes for high sensitivity acquisition. As MPI-sequences and MPI-signal structures are strongly related to the scanner design, a quick review of the MPI sequences used and associated scanners is given in the Chapter 3.

In this Section, the sequences behind the first 3D MPI scan of a mouse, the FFP 2D and 3D Lissajous sequences, are explained, to better point out the differences between the developed concept of Chapters 3 and 6.

The idea behind this sequence is to quickly move the LFV along a closed Lissajous trajectory to encode a 2D slice or a 3D volume. It also provides an elegant way to transfer energy from the power sources to the coils. This aspect is further developed in Sec-

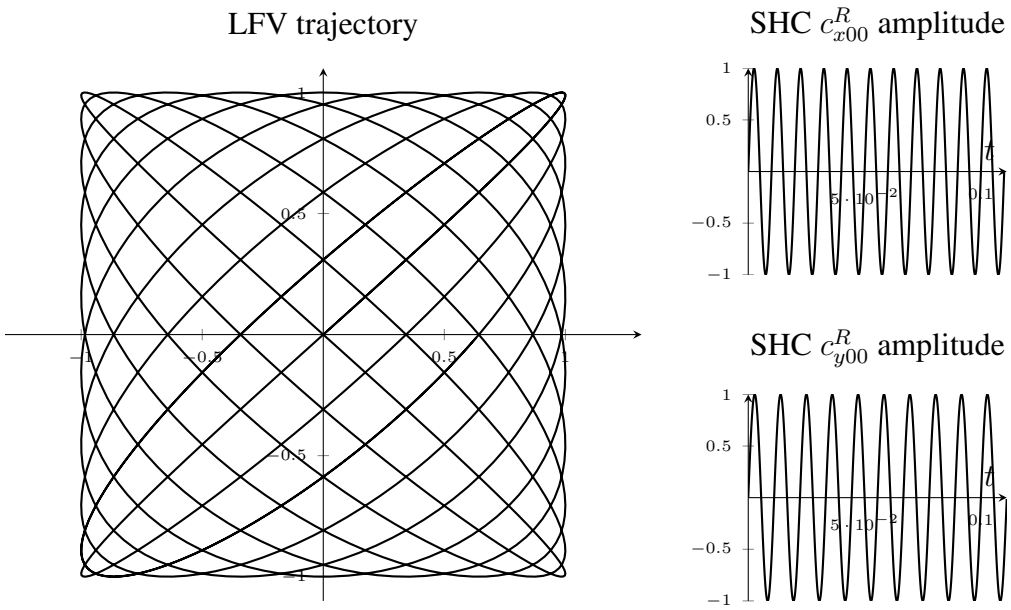

Figure 2.13: In order to move the LFV along the Lissajous trajectory, two SHCs with two different time dependent amplitudes are used. The amplitudes associated to each SHC are shown on the right. Here, frequencies $f_x = 100$ Hz and $f_y = 90$ Hz are used.

tion 2.3.6. To drive the FFP along a 2D or 3D curve two or three drive coils are used, respectively. In Figure 2.13 is an example of a closed 2D Lissajous figure. To achieve this, a sinusoidal amplitude modulation is applied to the drive-field, according to the relations

$$c^R_{x00}(t) = \sin(2\pi f_x t), \tag{2.42}$$

$$c^R_{y00}(t) = \sin(2\pi f_y t), \tag{2.43}$$

$$c^R_{y00}(t) = \sin(2\pi f_z t). \tag{2.44}$$

The frequencies f_x, f_y and f_z are chosen to be commensurable to form a closed trajectory [44] and to be almost equivalent in order to quickly acquire the target volume [20]. They are thus defined through the ratios

$$\frac{f_y}{f_x} = \frac{N_\mathrm{D}}{N_\mathrm{D}+1} \quad \text{and} \quad \frac{f_z}{f_x} = \frac{N_\mathrm{D}}{N_\mathrm{D}-1} \tag{2.45}$$

which have to exist, with the trajectory density defined by $N_\mathrm{D} \in \mathbb{N}$. The repetition time of a sequence T_Rs made of a 2D Lissajous trajectory using the frequencies f_x and f_y is given by the relation

$$T_\mathrm{Rs} = \frac{N_\mathrm{D}+1}{f_x} = \frac{N_\mathrm{D}}{f_y} \tag{2.46}$$

and for a 3D trajectory by

$$T_{\text{Rs}} = \frac{\text{lcm}(N_{\text{D}}, \text{lcm}((N_{\text{D}}+1), (N_{\text{D}}-1)))}{N_{\text{D}} f_x}, \tag{2.47}$$

with lcm(a,b) the least common multiple of numbers a and b. To facilitate the digital generation of f_x, f_y and f_z, the relation (2.45) can be rewritten as

$$a f_{\text{B}} = a N_{\text{D}} f_x = a(N_{\text{D}}+1) f_y = a(N_{\text{D}}-1) f_z, \tag{2.48}$$

with f_{B} a frequency used as a common base and $a \in \mathbb{N}$ chosen so that $a f_{\text{B}}$ matches the sampling frequency of a waveform generator.

Using $N_{\text{D}} = 24$, as used in [45] for a 2D slice, a repetition time $T_{\text{Rs}} = 1$ ms is obtained with $f_x = 25$ kHz. This very fast acquisition speed is one of the strengths of the technology.

2.3.5 System function structures

Once an MPI sequence is defined, the LFV will excite the SPION distribution in the acquisition volume Ω at different times, thus creating a characteristic induced voltage u in the receive coils. In order to reconstruct the spatial distribution of the tracer, the system response for a given set of point-like tracer distribution is required. The set of positions is commonly defined as a grid of M points covering homogeneously the wanted Ω. Neglecting the interaction between the SPION situated at different positions, a discrete linear relation between the tracer distribution and the induced voltage u can be derived [20]. This relation is named SF or system matrix. It is modeled via equation (2.19) for a known volume of tracer situated at position $\vec{r}_p$, with $p = 1, \ldots, M$. Each point response can be represented either in time or Fourier space via relations

$$\bar{u}_n^q(\vec{r}_p) = -\mu_0 \sum_{\Omega} \left(\vec{p}_q(\vec{r}) \cdot \frac{\partial \vec{M}(\vec{r}, \vec{r}_p, t_n)}{\Delta t_n} \right) \qquad n = 0, \ldots, N_{\text{s}} - 1, \tag{2.49}$$

and

$$\hat{s}_k^q(\vec{r}_p) = \sum_{n=0}^{N_{\text{s}}-1} \bar{u}_n^q(\vec{r}_p) \exp\left(-2\pi \text{i} \frac{kn}{N_{\text{s}}}\right) \qquad k = 0, \ldots, N_{\text{s}} - 1, \tag{2.50}$$

with q one of the Q receive coils available.

In this work, the SF will be always considered in the Fourier space using coefficient $\hat{s}_k^{q(3)}$

formed as

$$\underline{\underline{\hat{S}}} = \begin{pmatrix} \hat{s}_0^{1(3)}(\vec{r}_1) & \hat{s}_1^{1(3)}(\vec{r}_1) & \cdots & \hat{s}_{N_s/2}^{1(3)}(\vec{r}_1) \\ \hat{s}_0^{1(3)}(\vec{r}_2) & \hat{s}_1^{1(3)}(\vec{r}_2) & \cdots & \hat{s}_{N_s/2}^{1(3)}(\vec{r}_2) \\ \cdots & \cdots & \cdots & \cdots \\ \hat{s}_0^{1(3)}(\vec{r}_M) & \hat{s}_1^{1(3)}(\vec{r}_M) & \cdots & \hat{s}_{N_s/2}^{1(3)}(\vec{r}_M) \\ \hat{s}_0^{2(3)}(\vec{r}_1) & \hat{s}_1^{2(3)}(\vec{r}_1) & \cdots & \hat{s}_{N_s/2}^{2(3)}(\vec{r}_1) \\ \cdots & \cdots & \cdots & \cdots \\ \hat{s}_0^{q(3)}(\vec{r}_M) & \hat{s}_1^{q(3)}(\vec{r}_M) & \cdots & \hat{s}_{N_s/2}^{q(3)}(\vec{r}_M) \end{pmatrix}. \tag{2.51}$$

That is, the SF $\underline{\underline{\hat{S}}} \in \mathbb{C}^{Q \times M \times (N_s/2+1)}$ is formed by concatenating the M point responses acquired from Q receiver and all made of $N_s/2 + 1$ FCs.

The points response is simulated for a 2D FFP ISIC using a Lissajous trajectory, similar to the one used in [45]. Here, $f_\mathrm{B} = 6$ MHz, $a = 1$ and $N_\mathrm{D} = 24$ so that (2.48) becomes for a 2D case $1 \cdot 6$ MHz $= 1 \cdot 24 \cdot 25$ kHz $= 1 \cdot 25 \cdot 24$ kHz with

$$T_\mathrm{Rs} = \frac{25}{25\ \mathrm{kHz}} = \frac{24}{24\ \mathrm{kHz}} = 1\ \mathrm{ms}. \tag{2.52}$$

Acquiring a single period $T_\mathrm{a} = 1 \cdot T_\mathrm{Rs}$ at the sampling frequency $f_\mathrm{s} = 2$ MHz, a spectrum with

$$N_\mathrm{s} = T_\mathrm{a} f_\mathrm{s} = 1 \cdot 10^{-3}\ \mathrm{s} \cdot 2 \cdot 10^{6}\ \mathrm{Hz} = 20000\ \mathrm{points} \tag{2.53}$$

is acquired. With a spectrum resolution of

$$\Delta f = \frac{f_\mathrm{s}}{N_\mathrm{s}} = \frac{1}{T_\mathrm{a}} = \frac{1}{1 \cdot 10^{-3}\ \mathrm{s}} = 1000\ \mathrm{Hz}. \tag{2.54}$$

A 2D FFP ISIC with a z-gradient coil defined by $c_{y11}^1 = 5.0$ T, a x-drive coil defined by $c_{x00}^1 = 50$ mT and a y-drive coil defined by $c_{y00}^1 = 100$ mT is simulated. The drive coils are also used as receive coils. The MPI signal is acquired on an area of $\Omega = 20 \times 21$ mm^2 in x and y with a resolution of 0.5 mm, which results in 41×43 pixels. SPIONs are modelled using the Langevin model as particles with a 30 nm diameter, each voxel being filled with 1.5 mol(Fe)·m^{-3} of iron (which is equivalent to filling it with Resovist diluted 10 times with water). $\|\hat{s}_k^{(3)}\|$ for $k = 1, \ldots, 99$ are displayed in Figure 2.14 for the x-receive coil and in Figure 2.15 for the y-receive coil. The DC components ($k = 0$) are omitted and magnitudes $\hat{s}_k^{(3)}$, defined as

$$\|\hat{s}_k^{(3)}\| = \|\mathrm{real}(\hat{s}_k^{(3)}) + \mathrm{i} \cdot \mathrm{imaginary}(\hat{s}_k^{(3)})\| = \mathrm{real}(\hat{s}_k^{(3)})^2 + \mathrm{imaginary}(\hat{s}_k^{(3)})^2, \tag{2.55}$$

are normalised and plotted.

The spatial structures are not fully understood for 2D and 3D cases. Those structures have been related to Chebyshev polynomials, but a model describing their exact structure

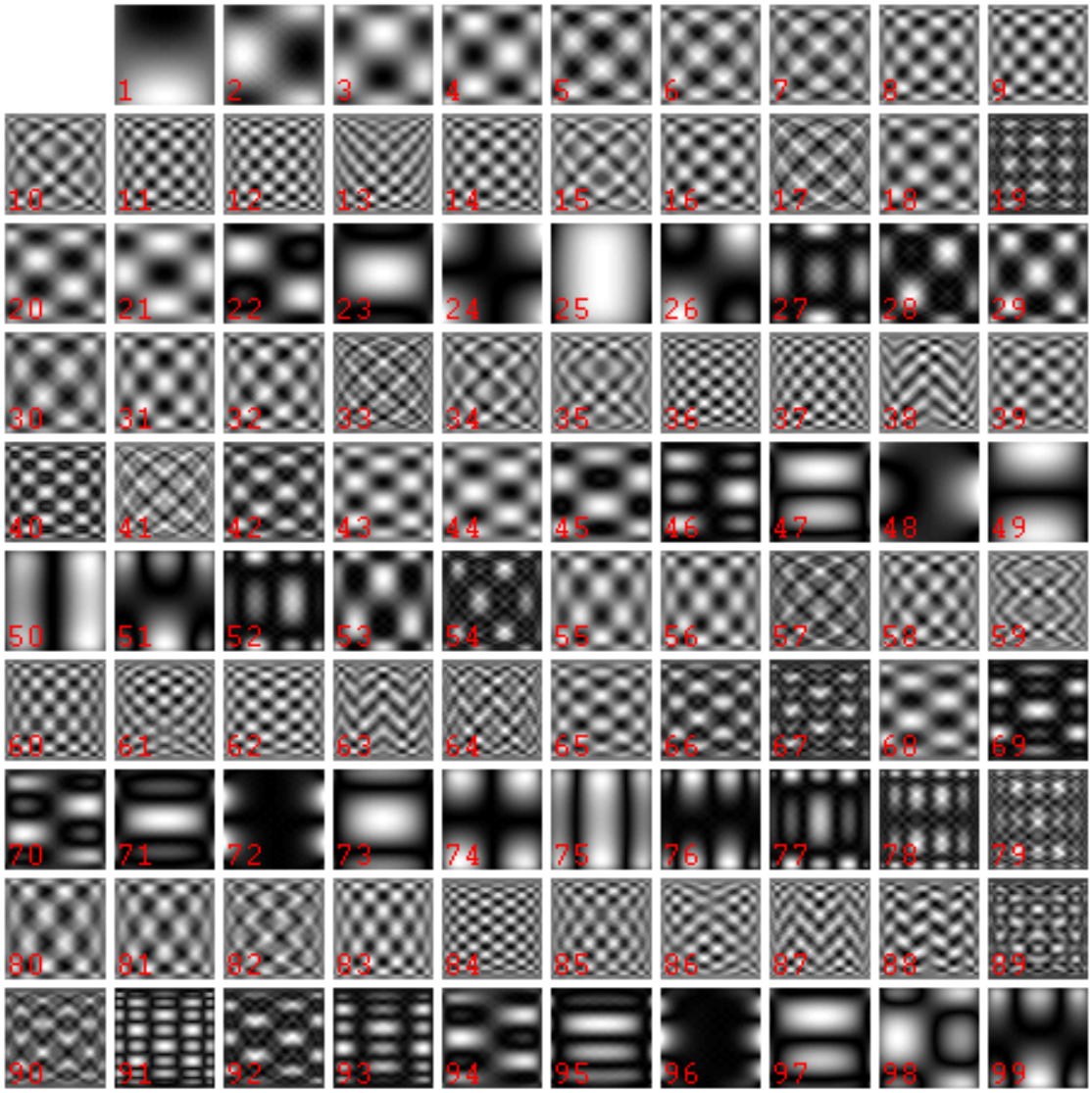

Figure 2.14: $\|\hat{s}_k^{(3)}\|$ in the x-receive coil for the whole covered area. Here, $k = 1, \ldots, 99$, with $\Delta f = 1$ kHz. The x-drive coil is used with an excitation frequency of 25 kHz. Note that the scaling is different for each image.

is still missing [45]. More precisely, the analogy to the Fourier-space could be made for pure harmonics, i.e. for $k\Delta f = nf_x$ for the x-receive coil, for example. This can be seen in Figure 2.14 for $k = 25, 50$ or 75: the spatial frequency increases with the increasing index. But looking at the intermediate components, it can be seen that the spatial frequency increases and decreases, way above the value of the pure harmonics. The same effect can be seen in Figure 2.15 for $k = 24, 48$ and 72. To further characterise those patterns, it can be seen that the energy contained in the FCs over Ω varies substantially.

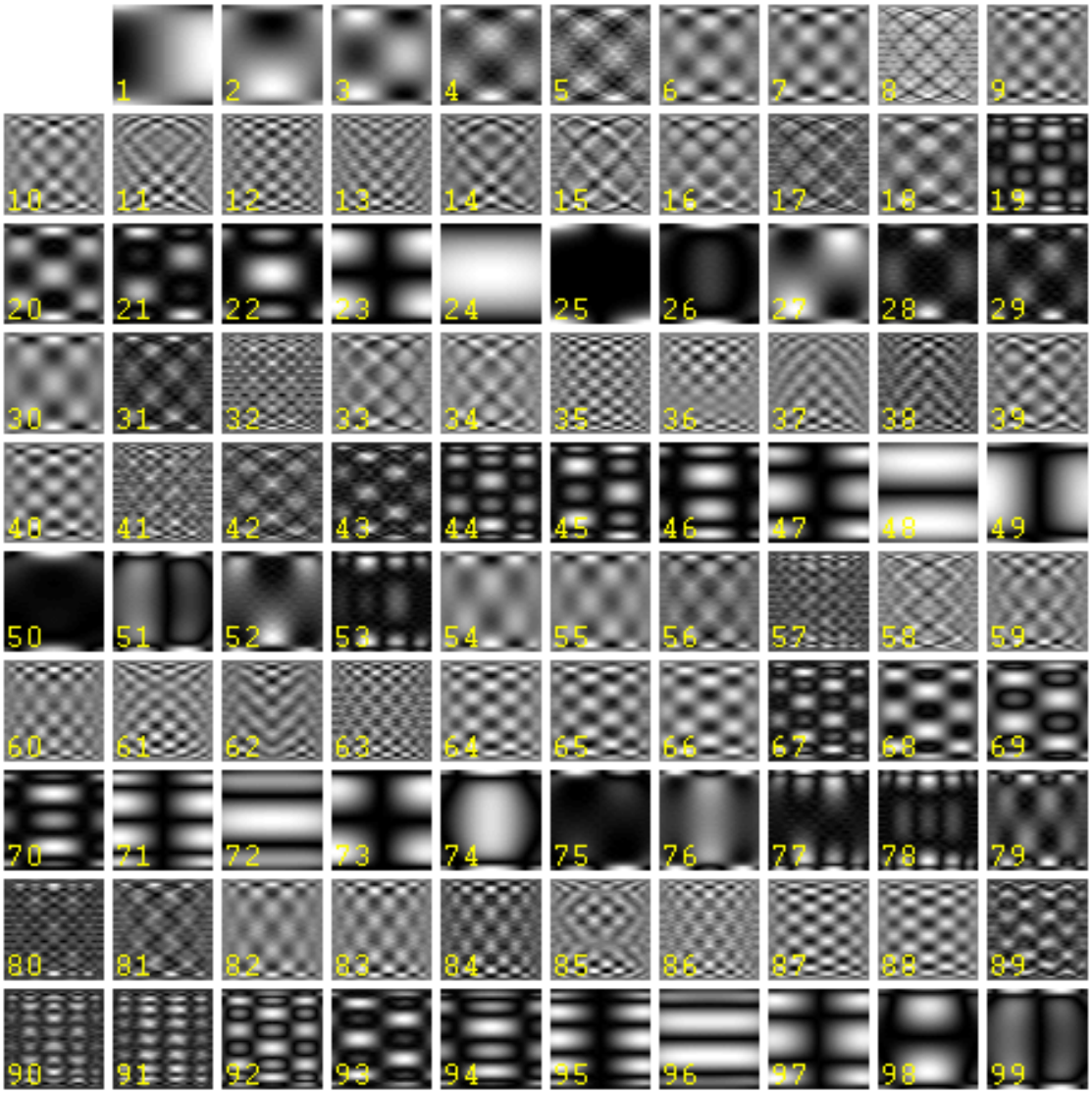

Figure 2.15: $\|\hat{s}_k^{(3)}\|$ in the y-receive coil for the whole covered area. Here, $k = 1, \ldots, 99$, with $\Delta f = 1$ kHz. The y-drive coil is used with an excitation frequency of 24 kHz. Note that the scaling is different for each image.

To represent this variation, the PS for each FC k on Ω, $\tilde{w}_k$, defined as

$$\tilde{w}_k = \sum_{p=1}^{M} \|\hat{s}_k^{(3)}(\vec{r}_p)\|^2, \tag{2.56}$$

is calculated for the same 2D FFP ISIC and shown in Figure 2.16. The power is distributed around the excitation frequency harmonics and decreases with increasing FCs, similar to inter-modulation patterns.

Those patterns appear through the non-linearity of the SPIONs, even if the fields to which

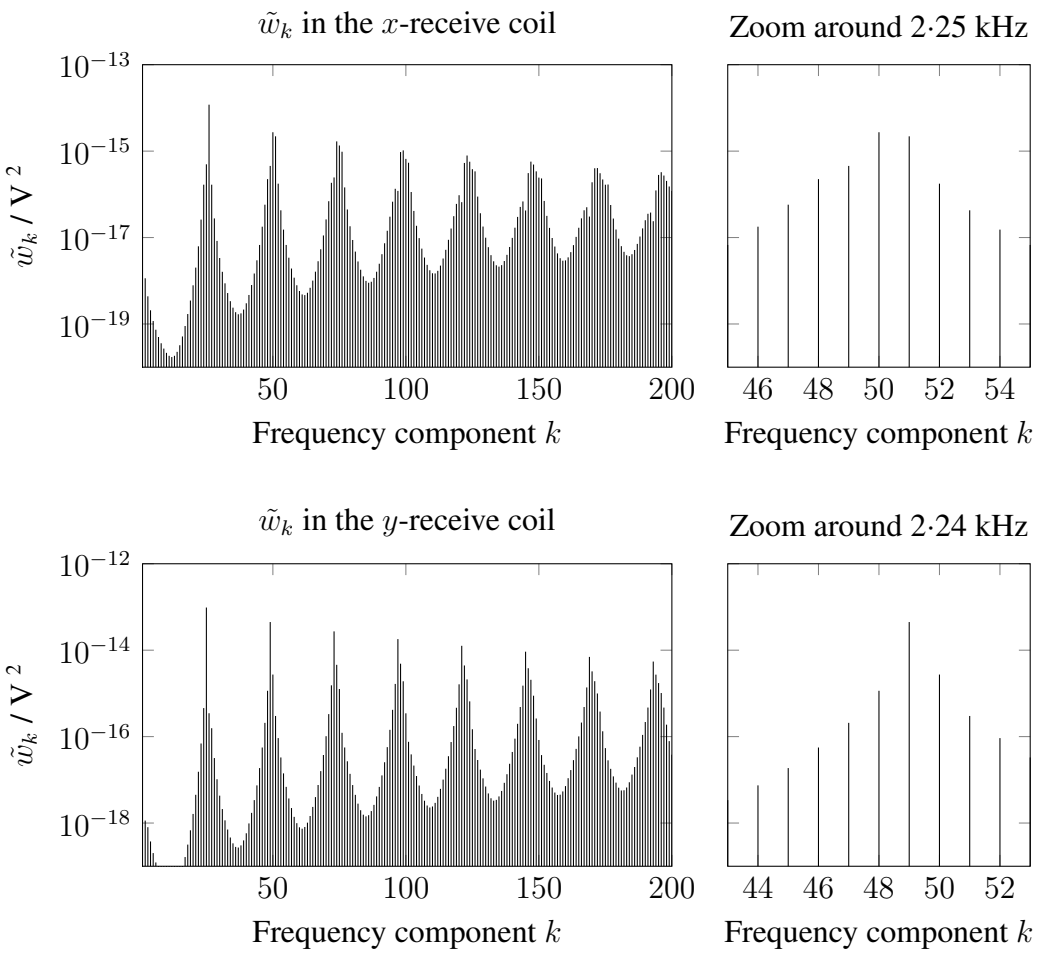

Figure 2.16: $\tilde{w}_k$ for the SF obtained in the x- and y-receive coil for an 2D FFP ISIC. The power is distributed around the excitation frequency harmonics, similar to intermodulation patterns.

the frequencies are applied are perfectly orthogonal. A 1D, 2D or 3D MPI signal can be seen as originating from a 0D excitation field with frequencies

$$\vec{B}(\vec{r},t) = \vec{B}_{\mathrm{d1}}(\vec{r})\sin(2\pi f_1\, t) + \vec{B}_{\mathrm{d2}}(\vec{r})\sin(2\pi f_2\, t) + \vec{B}_{\mathrm{d3}}(\vec{r})\sin(2\pi f_3\, t). \tag{2.57}$$

Mix-products will appear at frequencies

$$f = \|n_x f_x + n_y f_y + n_z f_z\|, \tag{2.58}$$

with n_x, n_y and $n_z \in \mathbb{Z}$ the mixing power, and amplitudes which depend on the SPIONs properties. Rahmer et al. studied the energy repartition, defined as the amplitude spectrum, in measured and simulated 3D system functions [32]. They used the intermodula-

tion structures and the mixing order, defined as

$$n_{\text{mo}} = \|n_x\| + \|n_y\| + \|n_z\|, \tag{2.59}$$

to show that most energy in the MPI signal is expected in the frequencies generated via low order mix-products, thus improving the MPI signal-truncation methods.

This approach has been followed here to compare the energy repartition of measured and simulated SFs of a 3D FFP scanner, a 3D FFP ISIC and a 0D spectrometer using the same three frequencies.

The used ISIC is made with a z-gradient defined via the main SHC $c^1_{z10} = 5.5$ T, x- y- and z-drive coils defined by $c^1_{x00} = 18$ mT, $c^1_{y00} = 18$ mT and $c^1_{z00} = 18$ mT, generating this magnetic field strength with a current of 100 A. Using $f_{\text{B}} = 2.5/3$ Mhz, $a = 3$ and $N_{\text{D}} = 33$ so that (2.48) becomes $3 \cdot 2.5/3$ Mhz $\approx 3 \cdot 34 \cdot 24.51$ kHz $\approx 3 \cdot 32 \cdot 26.04$ kHz $\approx 3 \cdot 33 \cdot 25.25$ kHz with

$$T_{\text{Rs}} \approx \frac{17952}{833333 \text{ Hz}} \approx 21.5\text{ms}. \tag{2.60}$$

Acquiring a single period $T_{\text{a}} = 1 \cdot T_{\text{Rs}}$ at a sampling frequency $f_{\text{s}} = 2.5$ MHz, three spectra with

$$N_{\text{s}} = T_{\text{a}} f_{\text{s}} = 53856 \text{ points} \tag{2.61}$$

are acquired, which are transformed into $N_{\text{s}}/2 + 1$ FCs equidistantly spaced by

$$\Delta f = \frac{f_{\text{s}}}{N_{\text{s}}} = \frac{1}{T_{\text{a}}} \approx 46.42 \text{ Hz}. \tag{2.62}$$

Ω, a volume of $16.2 \times 20.2 \times 12.0$ mm^3, is discretised in $28 \times 34 \times 20$ volume elements with an elementary volume of $0.6 \times 0.6 \times 0.6$ mm^3. A tracer with an iron content of 0.015 mol(Fe)·l^{-1}, a magnetisation at saturation of 0.6 T·μ_0^{-1} and a mono-disperse diameter distribution of 30 nm is used as a model. The 0D spectrometer used equivalent parameters without the selection coil, and is defined for a single voxel with a volume of $0.6 \times 0.6 \times 0.6$ mm^3.

Three levels of detail of the energy repartition for all FCs are offered in Figures 2.17, 2.18 and 2.19.

Looking at the global repartition in Figures 2.17, both models are able to simulate the peak and side repartition of the energy, which correspond to the frequencies obtained with low mixing orders. It has to be noted that our model is not able to accurately reproduce the energy decrease with increasing frequency of the energy envelope. The measurements show a lower energy decrease.

A closer look, shown in Figure 2.18, points to the first limitation of the 0D spectrometer model. The wave-like envelope appears narrower and more complex, whereas the 3D

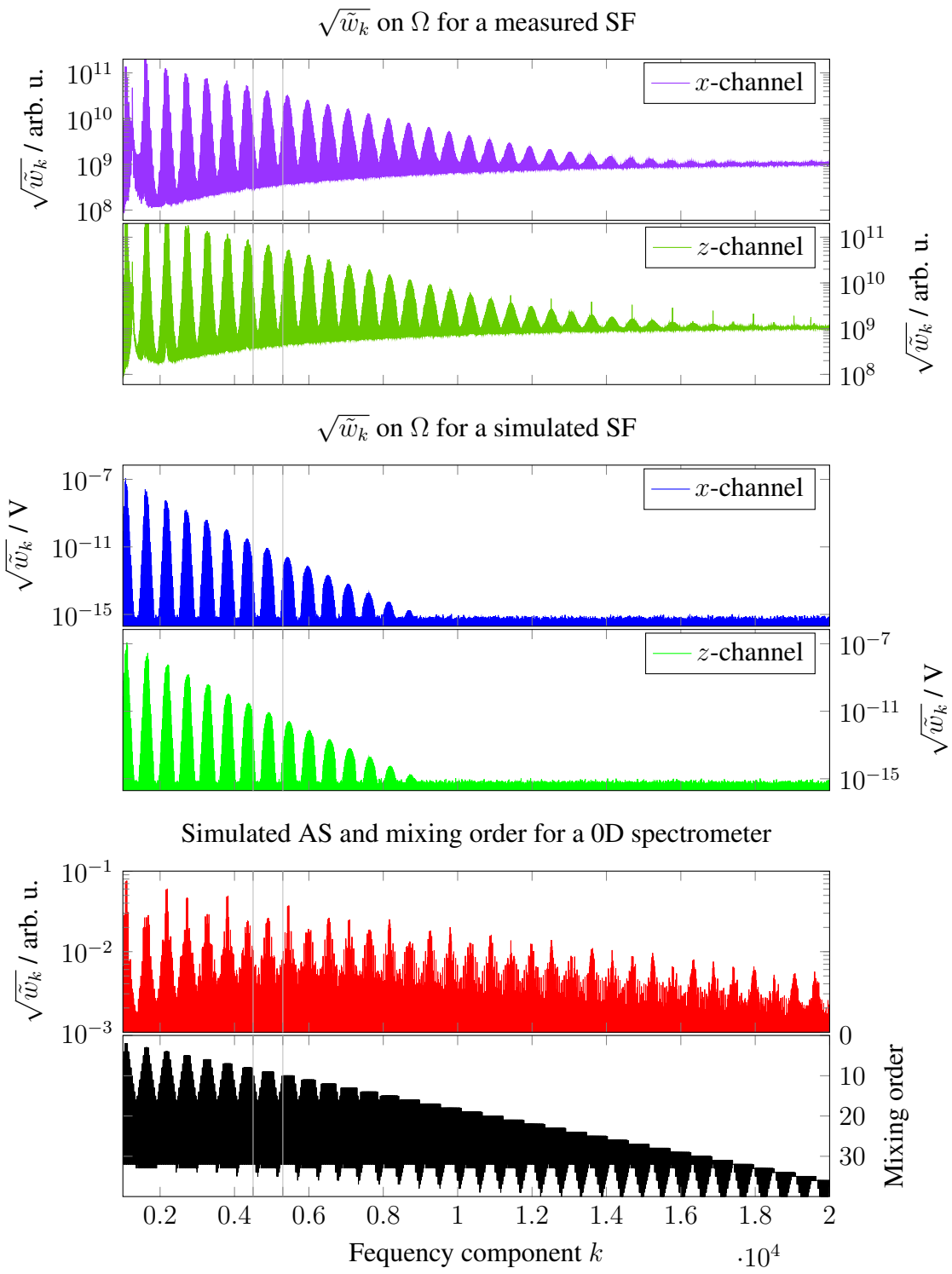

Figure 2.17: Energy structures of a measured 3D SF based on a 3D Lissajous trajectory, an equivalent ISIC and a 0D spectrometer. The energy structures appears to be correlated with the mixing order associated with each frequencies.

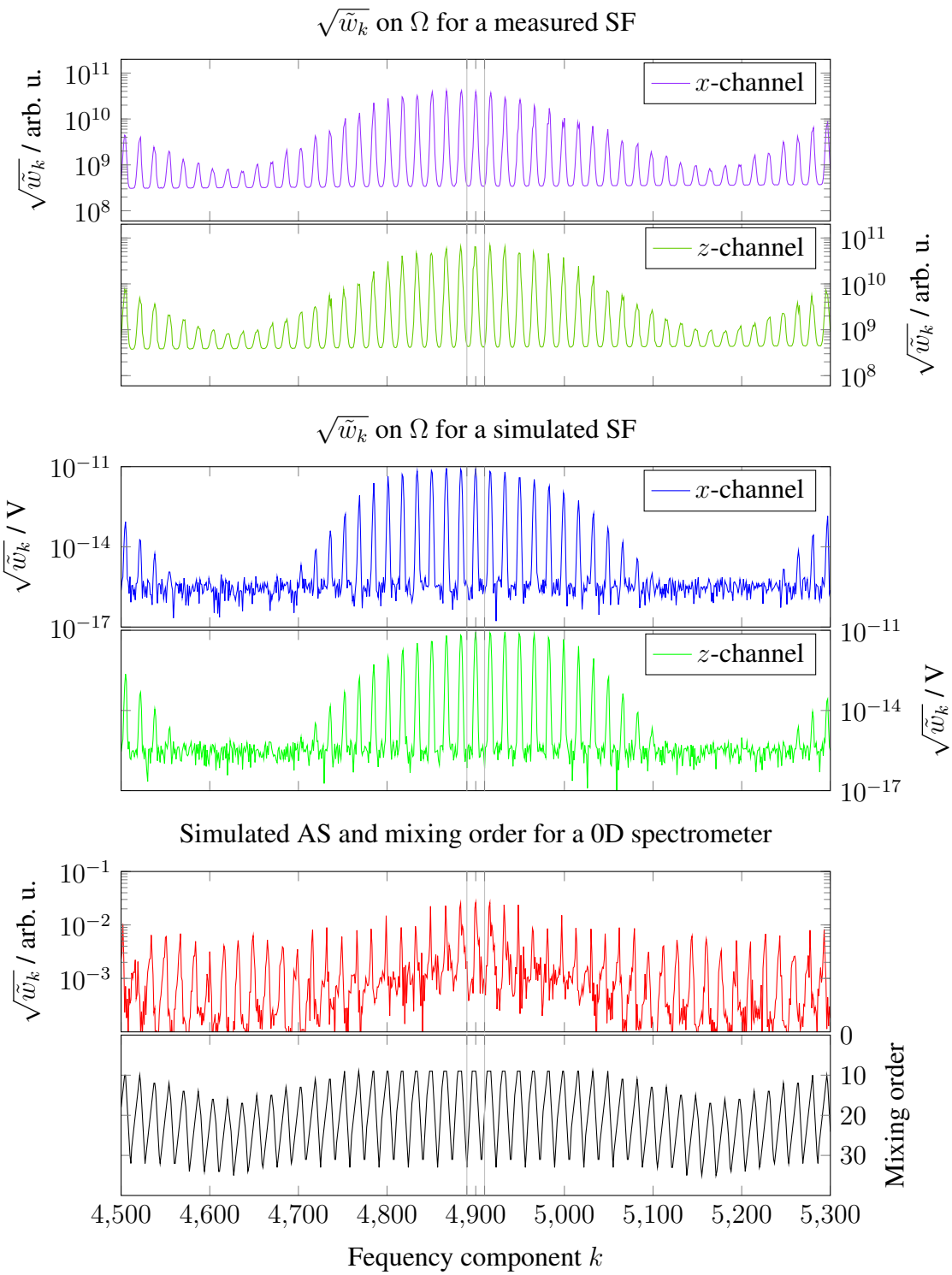

Figure 2.18: Looking between 4.5 and 5.3 kHz in the data presented in Figure 2.17, the similarities with the mixing order are still present for the SF. The 0D spectrometer energy repartition appears to be different.

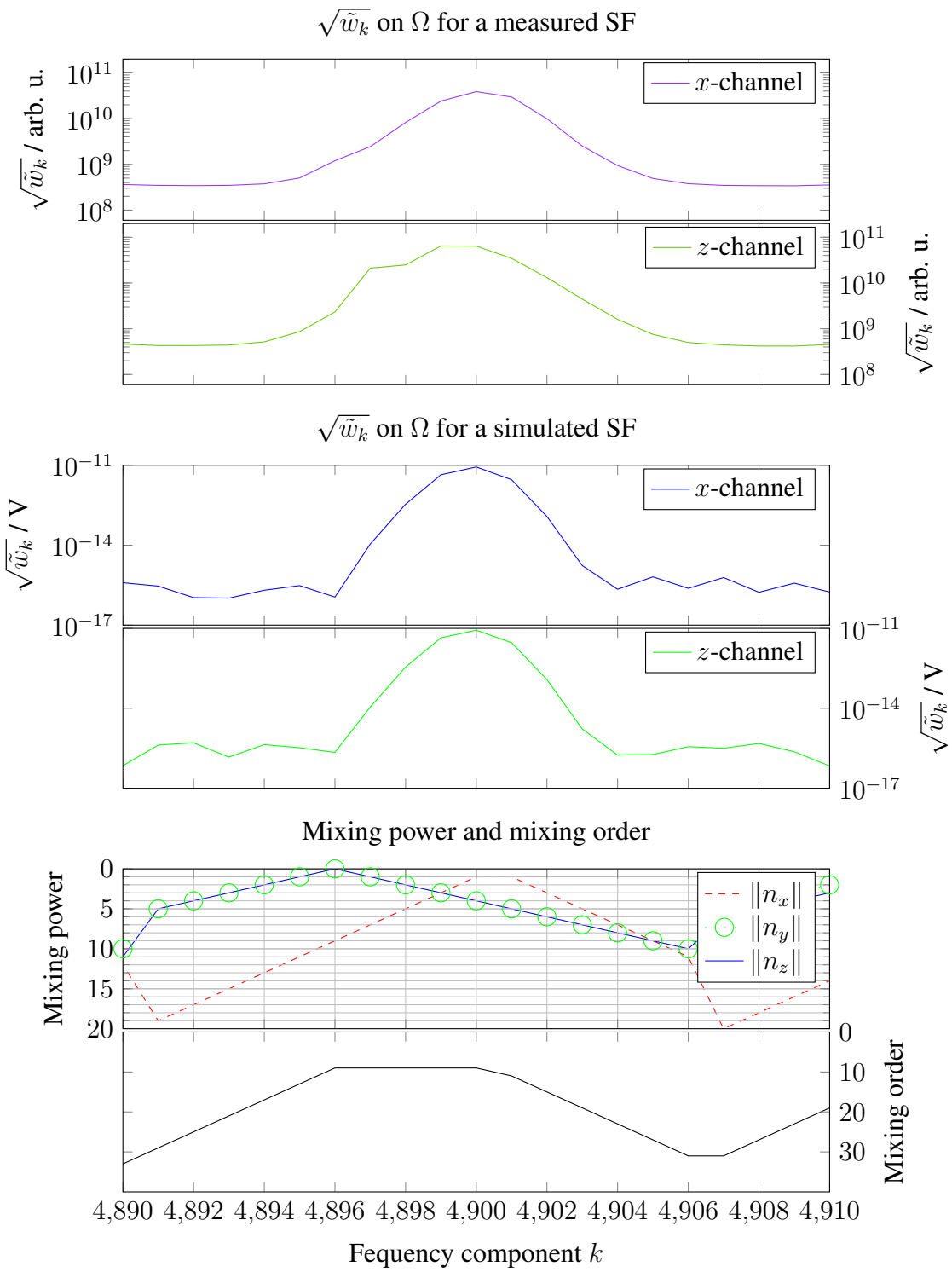

Figure 2.19: Looking between 4.5 and 5.3 kHz in the data presented in Figure 2.17, the structure of the measured and simulated SF are still similar. Decomposing the mixing order into the mixing power, it can be noted that only products of low power are present.

measurements and simulations seem to spread the plateau observed in the mixing order through the different channels. Both 3D SFs are in good agreement.

In Figure 2.19, the same behaviours are found. The structures of the 3D SFs are in good agreement, but the amplitude does not match. For example, in the measured z-channel, the ratio of the highest to the lowest value is around 10^3 when this ratio is of around 10^2 in the simulation. Looking at the mixing power $\|n_x\|$, $\|n_y\|$ and $\|n_z\|$, it can be seen that powers up to 20 are present.

This shows that a SF simulation is a good way to describe the energy repartition structures, but is not able to perfectly simulate it. Despite those differences, simulation based SFs have been used to reconstruct acquired signals, showing promising results [46]. The differences between the simulated and measured SFs are thought to come from the SPION behaviour and the precision of the magnetic field model [46].

To further assess the quality of a SF, the orthogonality of the truncated system function (tSF) can be evaluated [20]. The orthogonality is defined here as the modulus of the inner product of two normalised Fourier coefficients of the tSF as

$$\langle \hat{s}_i^{(3)}, \hat{s}_j^{(3)} \rangle = \left| \left| \sum_{p=1}^{M} \frac{\hat{s}_i^{(3)}(\vec{r}_p)}{\|\hat{s}_i^{(3)}\|} \frac{\mathrm{conj}(\hat{s}_j^{(3)}(\vec{r}_p))}{\|\hat{s}_j^{(3)}\|} \right| \right|, \tag{2.63}$$

with conj(z) the complex conjugate of $z \in \mathbb{C}$. It is common to truncate the MPI signal and the system function to keep only the Fourier coefficients which are expected to be of interest. This will be further defined in Sections 2.3.8 and 2.3.9 about the SNR and the reconstruction, respectively. One example, based on the ISIC used to obtain Figure 2.17, uses a square phantom of $5 \cdot 5$ pixel in the middle of the FOV. The drive coils are used as receive coils and acquire MPI signals in channels x and y. Noises, defined using equation (2.72) with $R_p = 0.2\,10^{-6}\ \Omega$ for the SF and $R_p = 185\,10^{-6}\ \Omega$ for the measurements, are added to the simulated signals. The orthogonality coefficients of the truncated system function FCs having a $\mathrm{SNR}^{(4)}$ greater than 6 in the phantom measurement are displayed in Figure 2.20 as a reference.

A value of 1 means that both FCs are linearly dependent, whereas a value of 0 means that both FCs are orthogonal. Ideally, only the diagonal element would have a value of 1, with all the other components having a value of 0. This shows that this tSF is not ideally formed to be inverted. Moreover, it can be seen that both receive channels are coupled, despite the perfectly orthogonal orientation of the sensitivity profiles provided by the ISIC model.

To further characterise the tSF, its singular value decomposition is studied. The ratio of the highest to the lowest singular value, named the condition number, gives a measure of

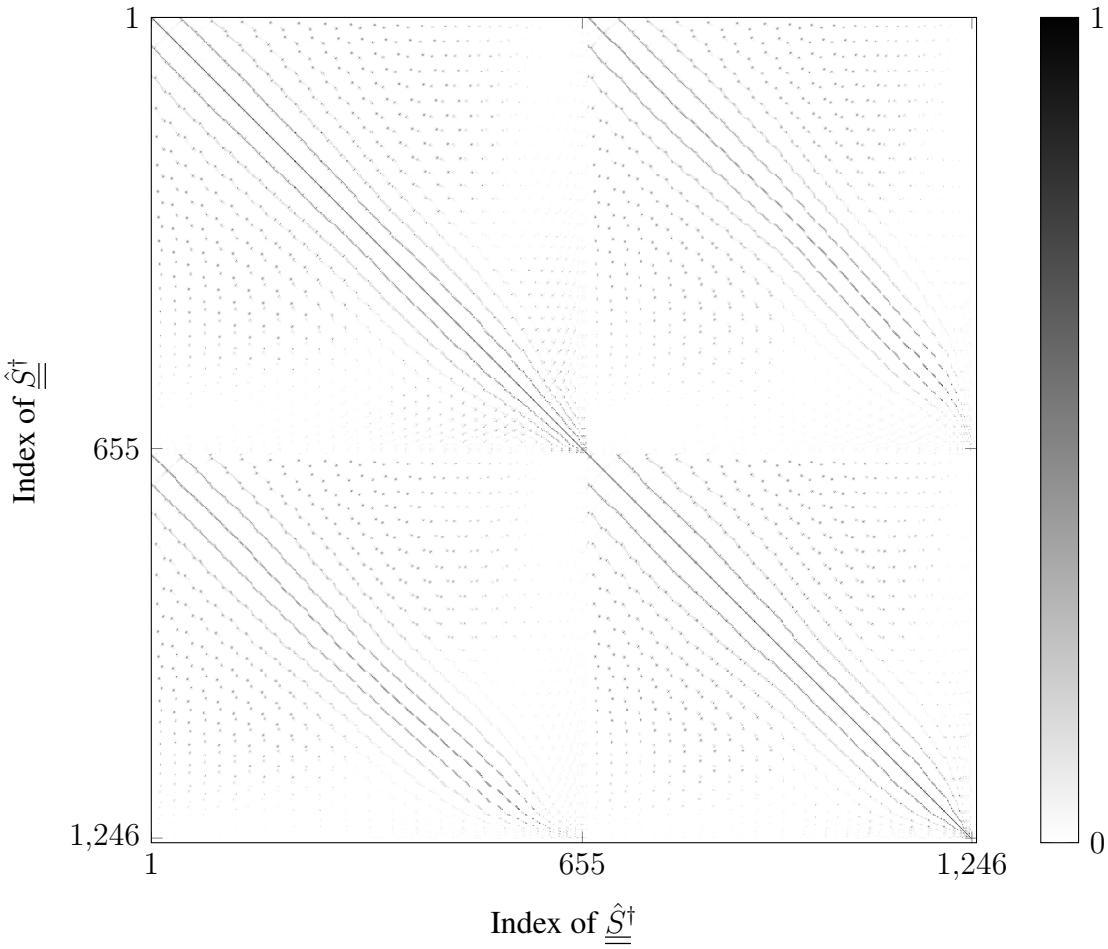

Figure 2.20: Orthogonality plot between the FCs of a tSF regrouping both receive channels. A black point means that both FCs are similar, whereas a white point means that there is no similarities between two FC.

the sensitivity of the reconstruction to the noise [47]. The lower the condition number is, the less sensitive is the problem. In the case of the tSF used to make Figures 2.20, a condition number of $7{\cdot}10^{14}$ is calculated using Matlab function *cond* (7.11.0, Mathworks, USA). The rate of decay of the singular value can also be used to further characterise the tSF. It is calculated with Matlab function *svd* and is displayed in Figure 2.21. According to Hofmann definition [47], the inversion of this tSF is a severely ill posed problem, as its sorted singular values can be approximated by a function of the form $e^{\alpha i}$, with i the index of the singular value and α the degree of ill-posedness. It has to be noted that the noise in the measured SF will change the orthogonality and the condition number of the associate tSF (by reducing it), thus making the evaluation of those two indicators less useful for a noisy measured tSF.

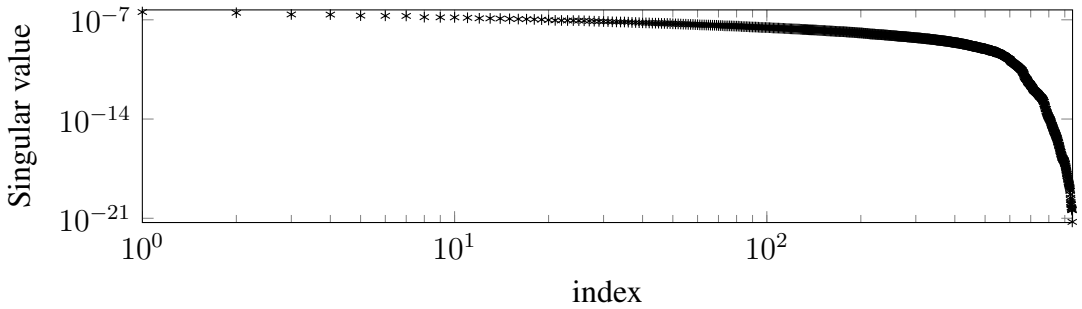

Figure 2.21: Singular values obtained from a tSF of a 2D Lissajous FFP scanner.

To influence the energy repartition in between the FCs of a SF, Goodwill and al. proposed to use a drive field which is inter-modulated with a low frequency focus field [42], using the high mixing power components of the low frequency to recover the high spatial frequencies of the signal. This should enable a reduction of the MPI-signal bandwidth which in turn would limit the noise added to the MPI signal. This in fact trades the potential high speed encoding of the system for an higher sensitivity. Using the proposed technique and associated values, an amplitude spectrum obtained in a simulated spectrometer is shown in Figure 2.22. It has to be noted that Goodwill et al. have developed this concept for a 1D MPI signal, moving the sample along another spatial dimension to acquire a second dimension. Thus, comparing this inter-modulated MPI signal to a 1D MPI signal generated with a sinusoidal excitation signal (which has a structure similar to a signal produced by a 0D spectrometer as shown in Figure 2.8), the number of available frequencies indeed increases. To date, this is implemented in several scanners and is used to increase the FOV. Further details are given in Section 3.1.1.

The influences of these modulations on the signal structure has not yet been studied. An example of scanners displaying similar properties is presented and further studied in Chapter 6. More particularly, the structure of the SF and the orthogonality of the tSF will be presented.

2.3.6 Power-signal generation

For any MPI sequences, magnets and scanners which are not completely based on permanent magnets, the magnetic fields are generated with electro magnets. The required current amplitudes to generate the magnetic fields vary from a few amperes up to several thousand amperes. For sinusoidally time-varying magnetic fields, with frequencies ranging from a few Hertz to more than 150 kHz, the required voltages vary over a wide range,

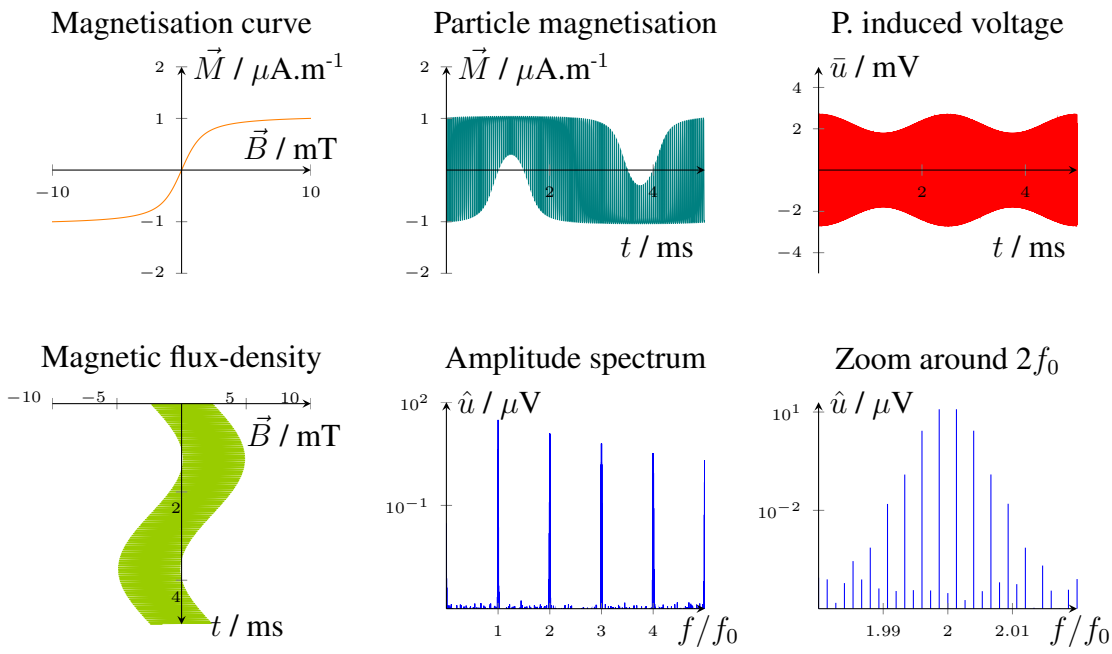

Figure 2.22: 0D example of the intermodulation of a high (150 kHz) with a low (200 Hz) frequency magnetic field, having peak strengths of 3 and 2.5 mT, respectively. The spectrum displays a large number of mixed-frequencies coming from the non-linear response of the tracer.

from a few volts to several kilovolts. No commercially available power sources are able to cover this range of frequencies, voltages, currents, precision and harmonics content. Thus, in addition to the power source, filters, power factor corrections, and/or impedance matching are required. The basic solution for those requirements are detailed here.

2.3.6.1 Band-pass and low-pass filter

Power sources cannot generate pure sinusoidal signals as distortion will always be added, due to, for example, internal non-linearity effects. A measurement of this harmonics distortion can be evaluated using the total harmonic distortion (THD) from the AS obtained via the generation of a pure sinus of frequency f_0 with a root mean square (RMS) peak amplitude V_1 , using the definition

$$\mathrm{THD}_{f_0} = \frac{\sqrt{\sum_n^{\infty} V_n^2}}{V_1}., \tag{2.64}$$

with V_n the RMS peak amplitude of the nth harmonics. The THD value depends on many more parameters, whose enumeration and specific influences are beyond the scope of the thesis [48].

For the drive coils used for the rabbit-sized FFL scanner designed during this work, linear amplifiers 7796 (AE Techron, USA) are used. Those amplifiers have a $\text{THD}_{25\text{kHz}}$ of around 1.3 %. Even if this value is really small for a high power amplifier, it is not small enough for applications in MPI. Similar problems arise for all other types of sources; thus specific analog band-pass filters are required to increase the signal purity. As an example, a Chebyshev II band-pass filter, modified to improve the buildability, can be designed to remove those distortions [49]. Those filter are built in-house, as no commercially available filters matche the requirements.

For the selection coils, which use either a DC current or frequencies around 100 Hz, commercially available low-pass filters are used.

2.3.6.2 Power factor correction and impedance matching

To transfer a maximum amount of energy from the AC sources to the load under use at a given frequency, the load impedance should be adjusted to a real value through the correction of the power factor and brought to a given value which depends on the sources [50, 20]. For the linear amplifier 7796, this is typically $\text{R}_{\text{source}} = 2\ \Omega$ per amplifier.

Different techniques are used. For frequencies around 100 Hz, as for selection and focus coils, the power factor is corrected by using a capacity in series C_s with the coil, as shown in Figure A.1. C_s is built so that the impedance at $\omega = 2\pi f_0$ of the circuit $\text{Z}^{(1)}_{f_0}$ is real, that is

$$\text{Z}^{(1)}_{f_0} = \text{R}_{\text{coil}} + \omega \text{i} \text{L}_{\text{coil}} - \frac{\text{i}}{\omega \text{C}_\text{s}}. \tag{2.65}$$

This leads to

$$\text{C}_\text{s} = \frac{1}{\omega^2 \text{L}_{\text{coil}}}. \tag{2.66}$$

For a selection coil with an inductance $\text{L}_{\text{coil}} = 474\ \mu\text{H}$ and a resistance at $f_0 = 100$ Hz of $\text{R}_{\text{coil}} = 43.5\ \text{m}\Omega$, a capacity $\text{C}_\text{s} = 5.3$ mF is required to make the impedance $\text{Z}^{(1)}_{f_0} = 321\ \text{m}\Omega$ real. In order to optimally transfer the energy from the linear amplifier to the coil, the impedance of the coil circuit has to be matched to the value required by the amplifier R_{source}. In turn, this is done with a transformer having a simplified transformer voltage ratio α defined as

$$\alpha = \frac{\sqrt{\text{R}_{\text{source}}}}{\sqrt{\text{R}_{\text{coil}}}}, \tag{2.67}$$

when all the power loss related to the transformer is neglected. In this case, a transformer with $\alpha = \sqrt{2}/\sqrt{0.043} = 6.7$ enables the transformation of the 100 V RMS 50 A RMS delivered by the amplifier into 15 V RMS 339 A RMS the circuit of the coil. This also neglects all power losses in the wiring and capacitors.

For higher frequencies, as for the drive fields varying at $f_0 = 25$ kHz, a capacitive voltage divider is designed to fulfill both the power factor correction and the impedance matching. As shown in Figure A.1 two capacities, one in series with the drive coil, $\mathrm{C_s}$, and one in parallel, $\mathrm{C_p}$, are adjusted to match the impedance $\mathrm{Z}^{(2)}_{f_0}$ of the circuits to the value required by the sources $\mathrm{R_{source}}$. The impedance is written as

$$\mathrm{Z}^{(2)}_{f_0} = \frac{1}{\frac{1}{\mathrm{R_{coil}}+\omega \mathrm{i}\mathrm{L_{coil}}-\frac{\mathrm{i}}{\omega \mathrm{C_s}}} + \omega \mathrm{i}\mathrm{C_p}}. \tag{2.68}$$

The values of $\mathrm{C_s}$ and $\mathrm{C_p}$ are obtained by solving the equation

$$\mathrm{Z}^{(2)}_{f_0} = \mathrm{R_{source}}. \tag{2.69}$$

This gives the solutions

$$\mathrm{C_s} = \frac{-1}{\omega\left(\sqrt{\mathrm{R_{coil}}}\sqrt{\mathrm{R_{source}} - \mathrm{R_{coil}}} - \omega \mathrm{L_{coil}}\right)}, \tag{2.70}$$

$$\mathrm{C_p} = \frac{-1}{\omega\left(-\frac{\sqrt{\mathrm{R_{coil}}}\,\mathrm{R_{source}}}{\sqrt{R_{\mathrm{source}}-\mathrm{R_{coil}}}}\right)}. \tag{2.71}$$

For a drive coil with an inductance $\mathrm{L_{coil}} = 26.9\ \mu\mathrm{H}$ and resistance at f_0 $\mathrm{R_{coil}} = 15.9\ \mathrm{m}\Omega$, capacities $\mathrm{C_s} = 1.57\ \mu\mathrm{F}$ and $\mathrm{C_p} = 35.56\ \mu\mathrm{F}$ are required to bring $\mathrm{Z}^{(2)}_{f_0}$ at 2 Ω. This circuit enables the transfer of the whole energy from the source to the coil circuits. This means that if 5 kW are transferred from an amplifier able to deliver 100 V RMS and 50 A RMS to the coil, a peak current of 1099 A and a peak voltage of 4661 V could be applied to the coil. This neglects all power losses in the wiring and capacities.

Those two ways to correct the power factor and match the impedance of the circuits are commonly used in MPI. They are extremely efficient but specific to a single frequency. Their good power transformation capabilities are a key of the MPI technology.

2.3.7 Small-signal acquisition

As presented in previous Sections, the MPI-signal amplitude is relatively small, in the order of a few millivolts. However, as the drive field is coupled with the particle signal, several thousand volts are generated at the excitation frequencies in the receive channel.

As the available analogues to digital converters have limited encoding capabilities, commonly in the range of $2^{16} = 65536$ to $2^{24} = 16777216$ values, the acquired signal should have a limited amplitude range. This limited range is obtained in MPI by analogically filtering out the excitation frequencies. Then, to better match the MPI-signal amplitude with the acquisition range of the digitising system, a low-noise amplifier (LNA) is used. The receive coils are often built to obtain an higher sensitivity than the drive coils, further increasing the sensibility of the acquisition. The electrical circuits for such a signal chain is shown in Figure A.2 and an acquired signal in Figure 2.23.

Another solution is to insert a band-pass filter in series with the drive coil, so that the signal situated at the drive frequencies sees a low impedance path back to the resonant circuits. Adding another band-stop filter in parallel to the band-pass filter permits the measurement of the higher frequencies, the MPI signal, without much of the energy flowing at the drive frequencies. As for the other solution, the MPI signal is then amplified with a LNA and digitised. This solution appears on bigger systems, where the integration of extra receive coils and filter is more complex than the construction of a coil with a high quality factor, L_{BPF_2} in Figure A.2. Indeed the resistance of the coil has to be kept low to limit the dissipated power losses. Both solutions and others are still investigated, as new advantages and drawbacks are found with each new improvement of the imagers.

In both cases, the measurement will be limited by the noise, which is added to the MPI signal. Many noise sources are adding energy to the MPI signal, but human-sized scanner are expected to be limited by the patient noise [51]. This noise is modelled as a resistance in which the fluctuation of electron density at a constant temperature generates a voltage. It is often referred to as Johnson noise, as it was first described by Johnson [52], and is evaluated for MPI scanners in [31]. To compensate for the actual behaviour of the patient noise, which increases with the frequency, the equivalent resistance is evaluated at 1 MHz and is used for all (smaller) frequencies. The voltage amplitude associated with the noise $\bar{u}_{\text{noise}}$ is described by the relation

$$\bar{u}^2_{\text{noise}} = 4k_{\text{B}}\, T\, BW\, R_{\text{p}}, \tag{2.72}$$

with $R_{\text{p}} = 185 \cdot 10^{-6}\ \Omega$, $\bar{u}_{\text{noise}}$ the discrete RMS voltage, T the absolute temperature of the patient (310 K) and BW the bandwidth used during the measurement. This can be simplified to obtain the noise amplitude spectral density

$$\text{ASD}_{\text{noise}} = \frac{\sqrt{\bar{u}^2_{\text{noise}}}}{\sqrt{BW}} = \frac{2 \cdot 10^{-12}\ \text{V}}{\sqrt{BW}}, \tag{2.73}$$

with $[\text{ASD}_{\text{noise}}] = \text{V}/\sqrt{\text{Hz}}$, which is a reference to compare the noise sources. Measuring with a bandwidth $BW = 1$ MHz, the patient is expected to generate $2 \cdot 10^{-9}\ \text{V}/\sqrt{\text{Hz}}$. It has

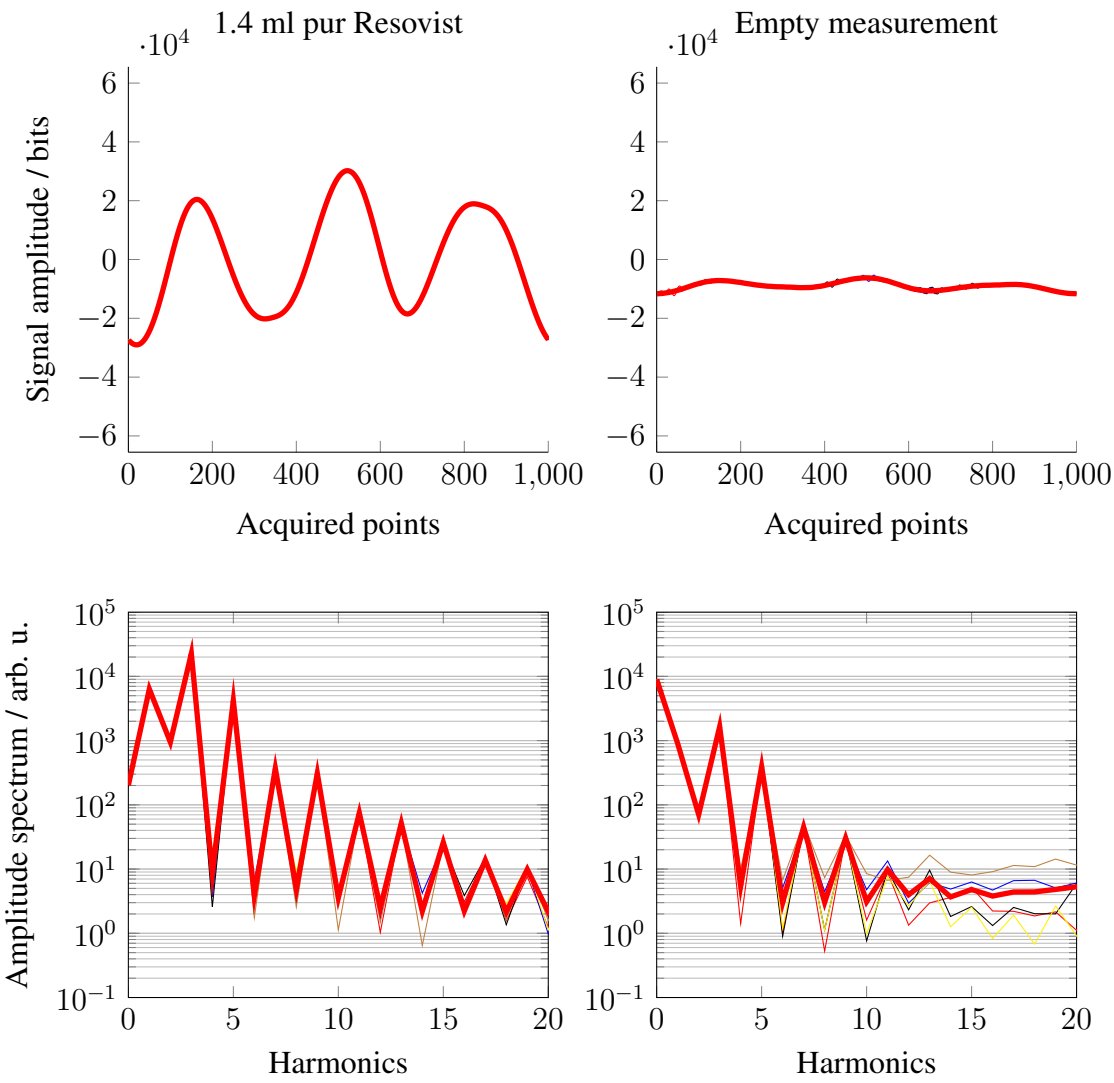

Figure 2.23: Signals recorder on a 0D spectrometer. On the top are the time signals. On the bottom are the amplitude spectra. The left part are measurements of 1.4 ml of pure Resovist. The right part are empty measurements. The red curves on each plots are the average of 1000 25 kHz periods. The other curves are randomly chosen single periods.

to be noted that the commercially available LNA, for example the model SR560 (Stanford Research Systems, USA), also add a noise amplitude spectral density of $4 \cdot 10^{-9}$ V/$\sqrt{\text{Hz}}$ to the input signal. Thus, to be only limited by the patient noise, LNA with a noise amplitude spectral density of at least 2 times lower are required.

To evaluate the preponderance of the noise over the signal, the SNR is a widely used indicator and is detailed in the next Section.

2.3.8 Signal to noise ratio

Many ways exist to determine the SNR of an MPI signal, mainly depending on which level it is looked at. The ratio can be calculated as the ratio of the signal and noise power P

$$\mathrm{SNR}_P = \frac{P_{\mathrm{signal}}}{P_{\mathrm{noise}}}, \tag{2.74}$$

making the hypothesis that both values are evaluated through the same impedance, this can be rewritten as the ratio of the amplitudes A

$$\mathrm{SNR}_A = \left(\frac{A_{\mathrm{signal}}}{A_{\mathrm{noise}}}\right)^2. \tag{2.75}$$

It can also be calculated using the signal mean or expected value μ and its standard deviation as

$$\mathrm{SNR}_{\mathrm{S}} = \frac{\mu}{\sigma} \tag{2.76}$$

with the S in $\mathrm{SNR}_{\mathrm{S}}$ standing to highlight the statistical method used. In turn, this can be evaluated using at least 5 different ways.

From these 5 ways to determine a SNR, $\mathrm{SNR}_{\mathrm{S}}^{(1)}$, based on equation (2.76), is defined for a reconstructed image. An homogeneous object is used as a phantom and the area where the homogeneous object is expected is used to determine μ. Then, σ is evaluated in a region where no signal is expected. It is notably used in [31].

$\mathrm{SNR}_{\mathrm{S}}^{(2)}$, based on equation (2.76), is defined equivalently as $\mathrm{SNR}_{\mathrm{S}}^{(1)}$, but instead of the reconstructed image, the technique is applied on the SF FCs, as the one shown in Figure 2.14 and 2.15.

$\mathrm{SNR}_{\mathrm{S}}^{(3)}$, based on equation (2.76), is defined equivalently as $\mathrm{SNR}_{\mathrm{S}}^{(2)}$, but instead of a SF FC, the discrete cosine transform (DCT) is used to reduce further the localisation of the signal, making it easier to localise the noise. An example is given in Figure 2.24, taking the unitary DCT as implemented in Matlab (7.11.0, Mathworks, USA) of the SF components 70 to 79 shown in Figure 2.14. Besides the calculation of the SNR, this can also be used for the filtering of the system function [53, 54].

$\mathrm{SNR}_{\mathrm{S}}^{(4)}$, based on equation (2.76), is defined using an empty measurement for the determination of σ. They are measured without tracers and are made of a great number of periods T_{a}. Taking the DFT of each T_{a}, σ of each FC can be calculated.

The main issue of the four SNR measurement techniques presented above is their time dependence. In each case, if there is a drift in the system, as for example a thermal instability, those estimations are going to be erroneous. To avoid that, $\mathrm{SNR}_{\mathrm{A}}^{(5)}$, based on equation (2.75), is defined using the DFT of a signal containing a great number of periods,

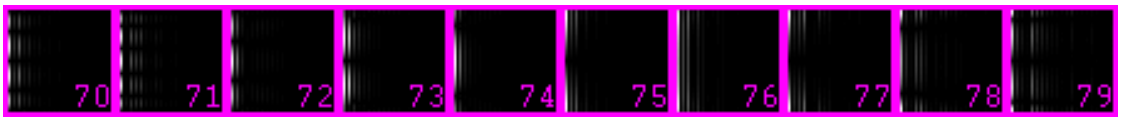

Figure 2.24: Unitary discrete cosine transform of the SF FCs 70 to 79 acquire on the x-channel of as ideal scanner using ideal coil as used for the Figure 2.14. A white intensity indicates a coefficient with a high influence on the MPI-signal structure, whereas a black intensity corresponds to a coefficient with a low influence. The MPI-signal energy is transformed towards a fewer number of coefficients, making the noise filtering easier.

that is with a spectrum having a greater spectrum resolution. The signal amplitude is determined at the position on which signal is expected, whereas the noise amplitude is averaged around those positions. This can be directly evaluated by a measurement, for example of a SF. This could reduce the maximal theoretical acquisition rate, if several T_{a} have to be acquired in order to increase the spectrum resolution.

2.3.9 Reconstruction

Once an MPI signal and a SF have been acquired, the concentration map which produces this signal has to be obtained. To calculate it, the discrete system of linear equation defined as equation (2.50) system should be inverted. In matrix-vector notation, the forward problem can be written as

$$\vec{\hat{u}} = \underline{\underline{\hat{S}}}\vec{c}, \tag{2.77}$$

where $\vec{c} \in \mathbb{C}^M$ is the vector containing the concentration of the tracer, $\vec{\hat{u}} \in \mathbb{C}^{Q \times N_s/2+1}$ is the Fourier transformed MPI signal acquired with the phantom on Q channels and M is the number of points in Ω. It should also be noted that, even if $\vec{c}$ is defined here as complex, real and positive values of concentration are expected.

The linear system (2.77) cannot be directly solved. Indeed, the measurement noise contained in $\underline{\underline{\hat{S}}}$ and $\vec{\hat{u}}$ disrupts any exact solution which may exist. Following the posedness definition by Hadamard expressed in [20, 47] as

Definition 1. *A linear system is said to be discrete well-posed, if it fulfils the following conditions:*

- *Existence: The problem has a solution,*
- *Uniqueness: The solution is unique,*
- *Stability: The system matrix has a small condition number.*

Otherwise, the linear system is said to be discrete ill-posed or ill-conditioned.

it is clear that the inverse problem associated with (2.78) is ill-posed. In this case, it is suggested to regularise the problem [47, 20] to obtain an approximate solution.

The first regularisation done is the truncation of the matrices of relation (2.78). Using the knowledge of the MPI-scanner construction, a first truncation occurs by removing the FCs which are not expected to carry relevant MPI signals due to the different filters used in the system. This is typically done by truncating the signal acquired in a bandwidth from 0 to $1.5 \cdot f_0$. Also, has it is not expected to receive MPI signal above, for example, the 30th harmonics, another truncation may happen from $30 \cdot f_0$ and $f_s/2$. Indeed, f_s tends to be oversized in comparison of the required MPI-signal bandwidth, as the exemplary limits of 30 harmonics actually depends on the imaged phantom and f_s can be set for a system in order to cover a large variation in the maximal expected frequency. Additionally, the FCs carrying too little energy, evaluated for example through SNR$^{(4)}$ values on the MPI signal coming from the phantom, are also removed. Thus, a truncated version of (2.78) is formulated as

$$\vec{\hat{u}}^{\dagger} = \underline{\underline{\hat{S}}}^{\dagger} \vec{c}, \tag{2.78}$$

with $\underline{\underline{\hat{S}}}^{\dagger}$ adn $\vec{\hat{u}}^{\dagger}$ the truncated system function and MPI signal each containing N_t FCs. N_t depends on the scanner and the acquired phantoms.

Then, a regularised least-square problem is usually formulated as a regularised weighted normal equation

$$\left(\underline{\underline{\hat{S}}}^{\dagger\mathrm{H}} \underline{\underline{W}} \underline{\underline{\hat{S}}}^{\dagger} + \lambda \underline{\underline{I}}\right) \vec{c} = \underline{\underline{\hat{S}}}^{\dagger\mathrm{H}} \underline{\underline{W}} \vec{\hat{u}}^{\dagger} \tag{2.79}$$

and solved for a given weighting matrix $\underline{\underline{W}}$ and a given regularisation parameter λ [20]. The parameter λ is here used as a numerical control parameter and therefore does not caries any physical units. The notation $\underline{\underline{\hat{S}}}^{\dagger\mathrm{H}}$ describes the complex conjugate transpose of the matrix $\underline{\underline{\hat{S}}}^{\dagger}$. Both $\underline{\underline{W}}$ and λ depend on the scanners and MPI-sequence properties and have to be experimentally chosen. It is common to use the unitary matrix or the energy of each FC as weighting matrix [55]. Moreover, λ has to be adjusted for each new MPI-signal acquisition [53]. It can be expressed as $\lambda = \lambda_{\text{rel}} \lambda_0$ with $\lambda_0 = \text{trace}(\underline{\underline{\hat{S}}}^{\dagger\mathrm{H}} \underline{\underline{W}} \underline{\underline{\hat{S}}}^{\dagger})/N_t$, which depends on the measurement, systems properties and λ_{rel}. λ_{rel} is freely chosen, with values commonly ranging from 10^{-1} to 10^{-6} [53, 31].

To solve the system described in (2.79), which can take up to several hundreds of gigabytes of memory, an iterative solver storing only a part of the tSF in memory at a time is preferred [20]. In this work, the Kaczmarz method, also known as algebraic reconstruction technique (ART), is used. Note that it introduces two additional regularisation parameters, with the number of iterations done and the relaxation parameter [56]. This

last parameter is often hard coded in the implementation. In this work, a modified implementation provided by Hansen using a fixed relaxation parameter of 1 is used [57], adding a forced non-negative constrain by settings any negative part of the solution to zero after each iteration.

The reconstruction of the tracer concentration map is named in this work image reconstruction. To obtain it, either simulated or measured tSF and MPI signal have to be used, either in full simulation [31], model-based approaches using a simulated SF and a real measurement [58] or measured SF and MPI signal [1].

In this work, extensive use of the full simulation approach will be used. The simulation framework used to this end is detailed in Appendix E and freely available at `https://github.com/gBringout/CoilDesign`.

2.3.10 Discussion

The approach taken to model the MPI-signal acquisition and image reconstruction has a number of limitations, which are summarised here to avoid over-interpretation of the simulation and measurement results.

First, the Langevin model is only a basic model, which only approximates the response of Resovist in a 0D spectrometer and in a 3D FFP Lissajous scanner by fitting the actual induced voltage with the one simulated with a modelled scanner and tracer, with a monodisperese SPION solution.

Furthermore, if the particle dispersity has to be taken into account, it raises the question of the particle-particle interactions. Those may explain the slight non-linearity of the MPI-signal strength in relation to the concentration [59].

Also, the modelisation of the different relaxation effects is particularly challenging, as further information on the particles are required but are not easily measurable [36, 35].

The way the noise is modelled, as a frequency independent process limited by the patient noise, is a confident hypothesis which is, until 2015, attained only through averaging of the signal.

The FCs selection, also named truncation and sometimes included in the weighting matrix, is of crucial importance. This process introducing previous knowledge about the MPI signal could improve the whole reconstruction process [60, 55]. Moreover, the mandatory choice of a regularisation parameter for the 3D Lissajous FFP which strongly influences the results can be seen as a limitation. In fact, an MPI scanner user will have to choose at least two parameters before reconstructing a concentration map, which could be completely erroneous. At the time, users have to know what is being imaged to judge

the quality of the regularisation parameters.

Those points make the comparison of different scanner results challenging: should scanners be modelled with a given particle diameter, iron concentration and patient noise level or should the signal SNR be adapted to match each other? Even if the first solution seems better to flatten-out the technical differences, it may be disadvantageous for MPI sequences taking advantage of non-simulated particle behaviours. Similarly, the second approach directly neglects any significant gain in SNR which may results from the design of the scanner, as is the case for FFL scanners [2].

To contribute toward the comparison of different scanners, the present work will adopt the first approach, modelling acquisition with established parameters. Indeed, as FFL scanners are expected to deliver higher SNR in specific conditions [20], adapting the SNR to other types of scanners may be unfair.

3

MPI scanners

Contents

Before the first commercial MPI scanner became available in 2014, all teams taking part in the technology development had to build their own devices. Even now, several groups work toward the improvement and the creation of new acquisition and signal encoding concepts. In this Chapter, a review of the existing MPI sequences and related imagers is given. The existing concepts are divided using the expected LFV shape of the ISIC and the used sequences.

Then, the rest of this work is focused on FFL imagers. Prioritising the fast acquisition and the acquisition of a large FOV, new and old concepts are studied. First, the analogy to CT is done, to facilitate the comparison between both modalities. Then, the influence of the magnetic field topology on the image reconstruction quality is explored. Finally, a new type of FFL sequence is proposed, increasing the covered area by moving the line rotation centre in space.

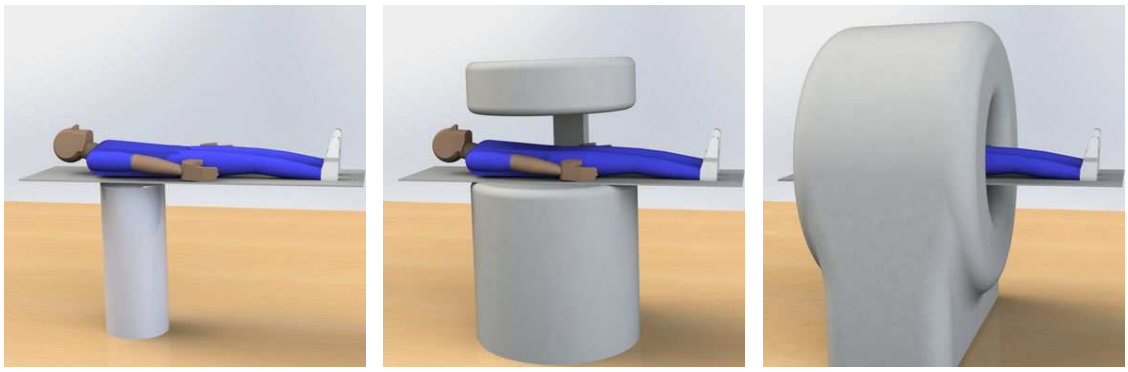

(a) (b) (c)

Figure 3.1: Different concept studies, taken as example for human sized instrument. (a) Single-sided imager. (b) Open-bore imager. (c) Closed-bore imager.

3.1 Existing topologies and sequences

The first imager created, *in-vivo* measurements and SF descriptions carried out by the Philips research team have set a cover stone to the MPI technology. Since this original work, started in 2001 [20], other groups are developing different topologies and MPI sequences, delivering simulated or measured images.

In this Section, the most recent realisations of different MPI scanners are listed; the different realisations are sorted by the type of LFV and MPI sequences they are using, as described by the definition given in Chapter 2. For each LFV, the different way to realise the spatial encoding is detailed, as this has the most influence on the scanner design and the MPI-signal structure. The actual implementation of those field shapes and MPI sequences is then implemented as three possible geometries, namely closed bore, open bore and single-sided imager, as shown in Figure 3.1. More details on the images acquired with the presented scanner can be found in [O18].

3.1.1 FFP scanners

The selection field of FFP scanners is either made with a set of permanent magnets, an electromagnet or a mix of both, with selection-coil sets producing non-isotropic gradients, with a gradient strength ranging from approximately 1 $T{\cdot}m^{-1}$ to up to 9 $T{\cdot}^{-1}$ [61]. The experimental concept of a 1D, 85 $T{\cdot}m^{-1}$ imager has also been presented [62]. All except one scanner use z-gradient coils to generate the selection field. One scanner type, named by their inventors travelling wave (University of Würzburg), uses an array of coils

to generate two FFPs [63, 64, 65].

The spatial encoding is done using 1 to 3 sinusoidally varying drive fields and up to 3 receive coils, which are orthogonally arranged. The drive coils are sometimes used at the same time as drive and receive coils. The first example of this scanner type is the first MPI scanner developed at Philips, which has imaged the beating heart [38] and the cerebral blood flow [66] of a mouse. It was described in detail in Section 2.3.5 to present the structure of a 3D SF. The FOV of this and similar scanners can be increased by adding discrete focus fields, which moves the centre of the imaging area by an offset. Philips first demonstrated this principle [67, 68]. Similar scanners, which do not always use a Lissajous trajectory, have been presented for 1D [69, 70], 2D [71, 72, 61] and 3D imaging [73, 74].

The focus fields can also be sinusoidally varied in time, using 1 [64, 75, 76, 63, 42, 77, 78], 2 [79] or 3 focus fields [65].

For the receive part, some scanners replace the 1 to 3 coils having an homogeneous sensitivity in the FOV with either gradiometer coils [72, 75, 80] or receiver array with 6 channels [64].

Linearly varying focus fields have also been implemented, in 1D [62, 81] and 2D [82, 83]. The function of a focus field is achieved in [62] by shooting the object through a 85 $T \cdot m^{-1}$ z-gradient selection generated with a permanent magnet set-up.

An MPI imager combined with an MRI imager in the same device has also been presented, combining both modalities, which can be used one after the other [84, 85]. Typically, an MRI acquisition is made, followed by the MPI tracer injection and then the MPI acquisition.

3.1.2 Single-sided scanner

A different approach of MPI imager design aims to increase the patient access by limiting the scanner construction to one single side of the imaging FOV. Those scanners use selection fields which are described with a SHSE containing non-negligible SHCs with high order and degree. Nevertheless, those imagers use 1D and 2D drive coils [86, 87, 88, 88][O19, O38].

3.1.3 FFL scanners

The FFL imagers have been presented in two variations. Both are based on a single sinusoidally time-varying drive field and perform a line rotation relative to the imaged

object. The first type of scanner makes discrete rotations, whereas the second type makes continuous rotations.

The discrete rotation of the object has been used for the imaging of blood clots and tracer phantoms [89, 80, 90], acquiring images from 20 min for a FOV diameter of 24 mm down to 80 s using additional focus fields to shift the line [91] to cover a $60 \times 60 \times 104$ mm^3 cylindrical volume. Another imager has been demonstrated covering a 25 mm diameter circular FOV in 2 minutes [7]. The mechanical rotation of the magnet has also been proposed and demonstrated for a 1D phantom, showing promising results [92]. The advantage of this approach is the simplification of the imager, which could require a single excitation chain and the absence of patient rotation, which could be problematic for *in-vivo* experiments.

The second variation of FFL scanners uses a line which is continuously rotated. This could be compared to actual modern imagers, such as CT or MRI imagers. A mouse sized scanner covering a 25 mm diameter circular FOV 50 time per seconds exists at the University of Lübeck and has already demonstrated the principle [93]. In this work, a similar scanner, covering a 180 mm diameter circular FOV is introduced, which has been presented to the community in 2015 [O4].

Furthermore, attempts to design human sized FFL scanners [94, 95] have been presented, none of them addressing the issue of limited FOV due to limited available drive-field strength and the PNS risk. Such a design has been presented by the author in [O10] and will be further developed in this work in Section 6.1. This concept overcomes the PNS limits by using a focus-field, not for shifting the lines, but for moving the rotation centre of the lines in a 2D plane. A concept covering a FOV of 400×405 mm^2 is presented in Section 6.2.

The main contribution required to develop and further optimise those two concepts are presented in the next Chapters of this work.

3.2 Contribution to topologies and sequences

During this work, three main contributions have been done in the domain of scanner topologies and sequences. First, a formal analogy is developed between FFL and CT scanners. This will help the knowledge transfer between both modalities. Then, the effects of a realistic magnetic field topology is evaluated, to assess the importance of their control on the design and implementation of an FFL scanner covering a 180 mm diameter circular FOV. Finally, the complete analytical modelling of an FFL sequence capable of moving the rotation point of the line is presented. This aims to study different

ways to increase the FOV without increasing the drive-fields strengths.

3.2.1 Analogy to CT

Both, FFL MPI ISIC using a discrete rotation and parallel pencil-beam CT imagers, use similar acquisition schemes. The comparison can be further explained by comparing Figures 3.2 and 3.3.

Parallel beam CT works using projections, which are measured on detector element ξ_i as presented in Figure 3.2a. Each element measures the intensity attenuation of the X-ray beam emitted by the source s [96]. The beams are first approximated as straight and parallel beams emitted by sources s_i, aligned along the direction ξ and targeting detector elements ξ_i. With a large number of sources and detector elements, all projections along the direction ξ can be acquired simultaneously for each rotation angle γ_j. A projection example $p_{\gamma_1}(\xi)$ for angle $\gamma = \gamma_1$ and 9 detector elements are shown in Figure 3.2a. The projections are then regrouped to form a sinogram, representing the object in the Radon space. An example of a sinogram is given in Figure 3.2b for the phantom shown in Figure 3.2a, which is generated using 128 projections between 0 and 179 ° and 250 detector elements and source positions. Using the particularities of this acquisition scheme, fast reconstruction algorithms have been developed, as the filtered back-projection (FBP).

For discrete FFL scanners, projections are also acquired. But instead of the intensity attenuation of the X-ray beam, the time dependent voltage induced in the receive-coil is used as MPI signal, as shown in Figure 3.3 and described by equations (2.19) and (2.36). The MPI signal is generated when the LFV, shown in Figure 3.3a as areas included in the red, green and blue boundaries, are moved in space. A projection is acquired when the line goes from lowest position (red boundary) to the highest position (blue boundary). A projection is equivalent to a half-period of the drive frequency f_0. As the MPI sequences used for SF are usually described as starting in the centre of the scanner (green boundary), a difference of a quarter of a period is to be expected between SF and Radon based reconstruction. As explained in [5], the sum of the absolute values of the MPI signals recorded in orthogonal receive coils are sorted to form a sinogram, as shown in Figure 3.3b. This forms the first major difference with the SF-based reconstruction, as the different channels are concatenated instead of combined.

Unlike the sinogram for CT, the ξ function depends on the time and not directly on the spacial position. After the normalisation with the LFV speed and the transformation from the time to the position space by interpolating on a evenly-spaced grid, the signal is obtained in the Radon space as shown in Figure 3.3c. It has to be noted that the

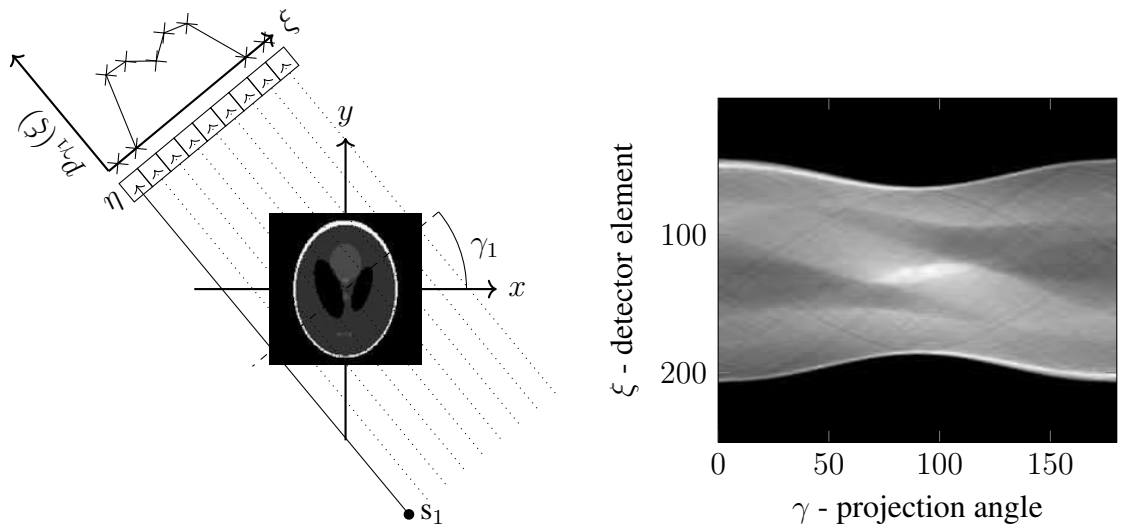

(a) (b)

Figure 3.2: Schematic of the projection principle for parallel pencil-beam CT. (a) X-rays are attenuated along the path η and the corresponding attenuation is recorded at detector elements position ξ_i for each angle γ. On this diagram, 9 elements are represented, oriented with the angle γ_1. (b) The projection integral, i.e. the summed-up attenuation along the X-ray path, are then grey-value coded and arranged in a sinogram.

signal should also be de-convoluted, but this step has been omitted here to simplify the representation [5].

Now comparing this with continuously rotating FFL imagers, the number of equivalent projections n_γ acquired in a 180 ° line rotation is defined as

$$n_\gamma = \frac{f_0}{f_\theta}, \tag{3.1}$$

which could appropriately encode one image. Each projection is made of $n_{\text{pp}\gamma}$ points. This number depends on the number of acquired samples n_s per drive-field periods, which is given by

$$n_\text{s} = \frac{f_s}{f_0}. \tag{3.2}$$

If n_s is odd, each sampling point will correspond to a unique sampling position, as seen in Figure 3.4b. This, in turn, leads to different numbers of points per projection and position for any two consecutive projections, even if there is no rotation.

If n_s is even, two cases have to be differentiated. If $n_\text{s}/2$ is even, as in Figure 3.4a, each projection will be made of $n_{\text{pp}\gamma} = n_\text{s}/2+1$ values, with the first and last one being shared with the previous and next projections, respectively. If $n_\text{s}/2$ is odd, as in Figure 3.4c, each

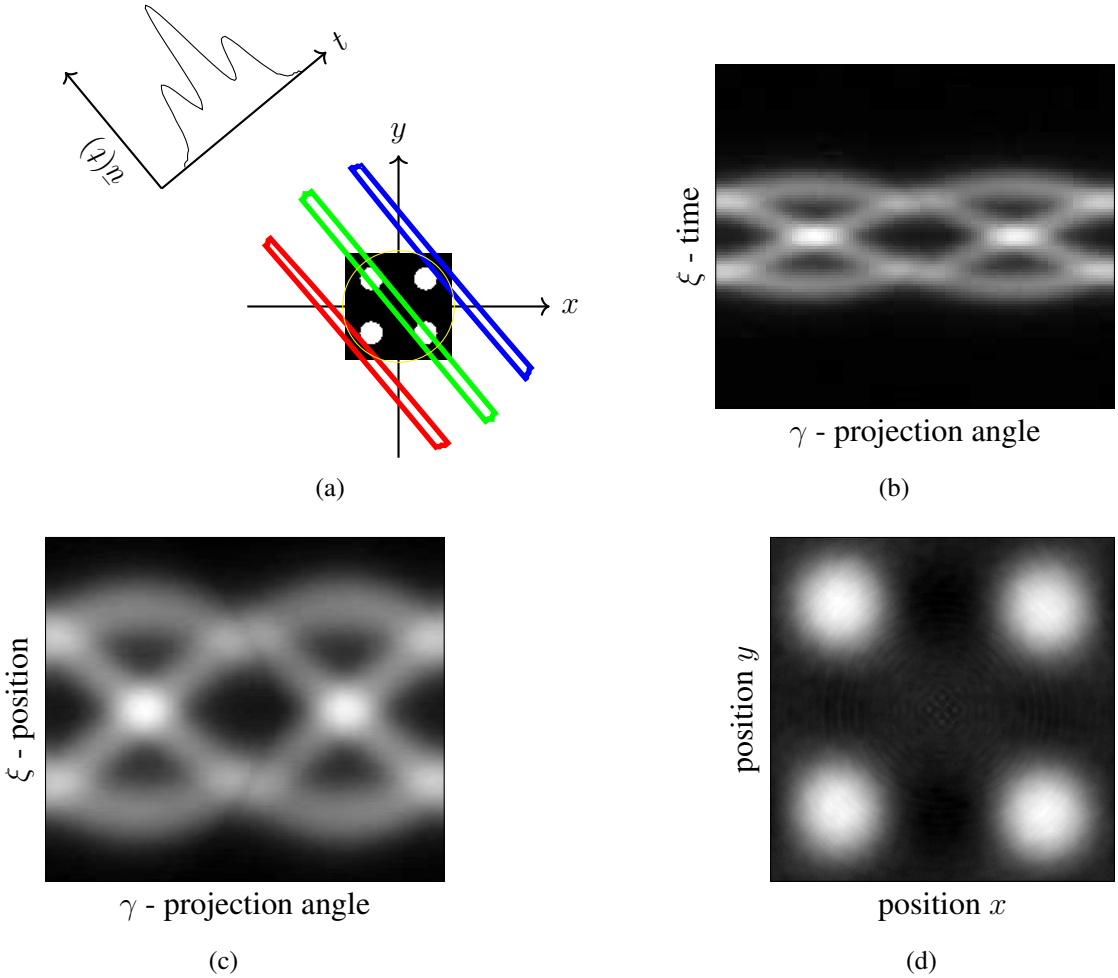

Figure 3.3: Schematic of the projection principles for FFL MPI scanner. (a) starting at t_1, the LFV in red moves to become the green and then the blue LFV. The LFV movement generates the MPI signal and is regrouped in a projection. (b) The projection integral, i.e. the summed-up magnetisation changes along the lines, are then grey-value coded and arranged in a sinogram. But here the integral values are given as a function of the time. The presented sinogram correspond to a 180° line rotation. (c) the integral values are then interpolated to become a function of the position. (d) the tracer concentration map is then obtained via a filtered back-projection (FBP).

projection will be made of $n_{\mathrm{pp}\gamma} = n_{\mathrm{s}}/2$ values, each different between each projection, but all sampled at the same ideal position. The number of sampling points, which could be compared to the number of detector elements, contained in each projection is thus

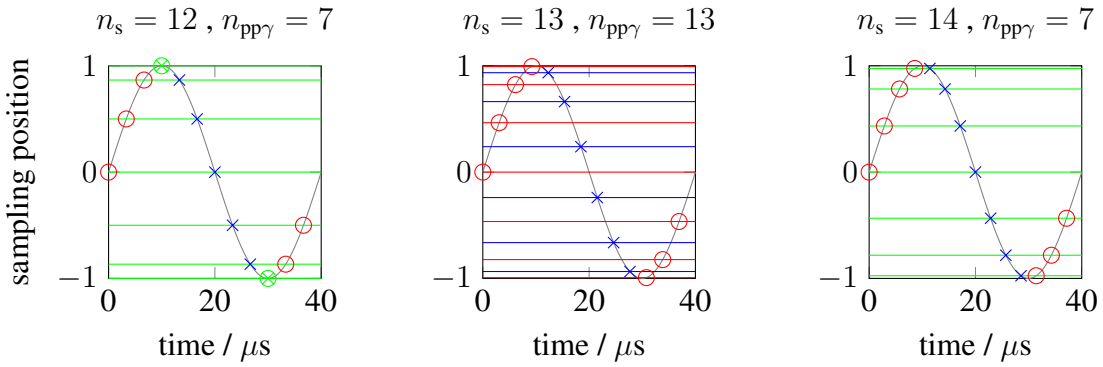

(a) (b) (c)

Figure 3.4: $n_{pp\gamma}$ for three different n_s values sampling a sinusoidally varying position change. The horizontal line represents the sampling position. The red circle indicates that the position is sampled for the first projection, blue cross for the second and green crossed circle for both.

defined as

$$n_{pp\gamma} = \begin{cases} \frac{n_s-1}{2} & n_s \text{ odd and for the } 1^{st} \text{ projection} \\ \frac{n_s+1}{2} & n_s \text{ odd and for the } 2^{nd} \text{ projection} \\ \frac{n_s}{2}+1 & n_s \text{ even and } \frac{n_s}{2} \text{ even} \\ \frac{n_s}{2} & n_s \text{ even and } \frac{n_s}{2} \text{ odd} \end{cases} \tag{3.3}$$

Both n_γ and n_s have to be chosen to be integers to obtain an integer number of projections and a finite sampling frequency. The inverse Radon transform can be then used in order to reconstruct the phantom. In those examples, the FBP implementation of Matlab (7.11.0, Mathworks, USA) is used.

If the line movement perpendicular to the line axis does not cover a larger surface compared to the surface covered by the line elongation, the acquired data are going to be truncated, as represented in Figure 3.5. Different techniques exist to use the FBP reconstruction algorithms [56] on such sinograms. By simply padding zero to the top and the bottom of it, an image clearly showing the region where all the information is present can be reconstructed. This region has different names. We chose to call it the fully-sampled region, but it is also referred to as the measurement field diameter, region-of-interest, interior CT or scanning field of view [96, 97, 98, 99, 100]. This region, delimited by the yellow circle in Figure 3.5a, is where the particle concentration information is available in all directions. To reconstruct this area with minimal error, the relation [96]

$$n_\gamma \approx n_{pp\gamma} \tag{3.4}$$

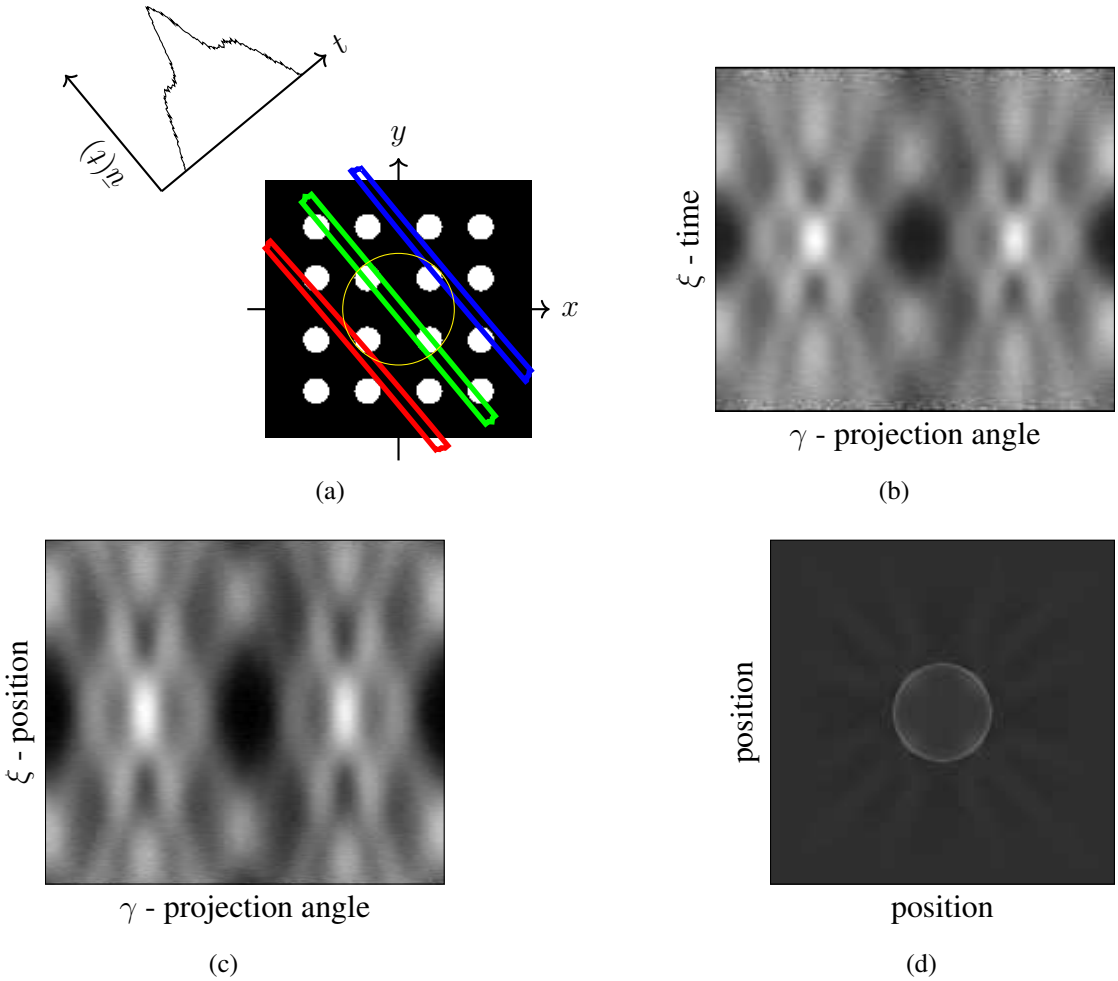

Figure 3.5: Schematic of the origin and impact of truncation artefacts using the projection principles for FFL MPI scanners. (a) The used phantom is larger as compared with 3.3. The point below the red LFV and above the blue one are not covered by the translation of the LFV, but partially contribute to the signal for other angle, as the length of the LFV still cover them. (b) The limited translation leads to a truncated sinogram. The top and bottom parts are missing. The MPI signals are acquired for a 180° rotation.(c) Even after interpolation in space, the truncations are still visible. (d) FBP of the sinogram padded with zeros. A ring artefact includes the fully-sampled region. Outside this area, information is missing in a given direction, creating artefacts.

should be fulfilled.

Outside this region and for the FFL ISIC, information in some or all directions is missing, thus leading to truncation artefacts. Note that in MPI, the term truncation artefact is also used when the SF does not cover the whole area from which we get a signal [O24]. Instead of limiting the scanner FOV to this region or using sophisticated sinogram post-processing techniques, and taking into account the shape of the LFV for a realistic scanner, which is neither straight nor time constant, a SF approach is preferred to reconstruct the images.

In the next Section, the effect of the time-varying LFV shape is investigated for a continuously rotating FFL scanner.

3.2.2 Realistic magnetic fields and reconstruction

As will be further developed in Chapters 4 and 6, it is hardly achievable to build a scanner which generates magnetic fields with a shape similar to those described by an idealised scanner made of idealised coils (ISIC) scanner. One solution might be to limit the imager FOV to the middle of the bore, to minimise the influence of spherical harmonic coefficients (SHCs) of higher order and degrees. The effect of those SHCs can be visually evaluated by looking at Figure 3.6. Figure 3.6a displays the 2D low-field volumes (LFVs) at 1, 2 and 3 mT for an ISIC with a gradient in the plane of 0.8 $T \cdot m^{-1}$ and a drive-field strength of 60 mT/μ_0 in both directions. The different LFVs displayed represent 11 time points for a projection. It can be seen that the line crosses the whole bore and that the LFVs are straight. Thus, the model used by the FBP based on a parallel-beam geometry seems to be appropriate to reconstruct MPI signals coming from an FFL ISIC with a discrete line rotation.

Considering realistic magnetic field shapes, as the one expected for the rabbit-sized scanner presented in Section 6.1, the LFVs are expected to be deformed. One example is given in Figure 3.6. The different LFVs displayed represent 19 time points used to describe a projection. Even if the main SHCs of this scanner and the ISIC presented before are the same, it can be clearly seen that the LFV are different. They are not straight; neither have the same length nor cover the same area. Furthermore, the different LFV are not equidistant to one another, meaning that the gradient of the magnetic field does not linearly vary on the observed slice.

The FBP assumes that the lines are straight and rotated only between two projections. The presented concept of fast FFL scanner rotates the line continuously, even during the acquisition of a projection. Thus the reconstructed images are expected to contain arte-

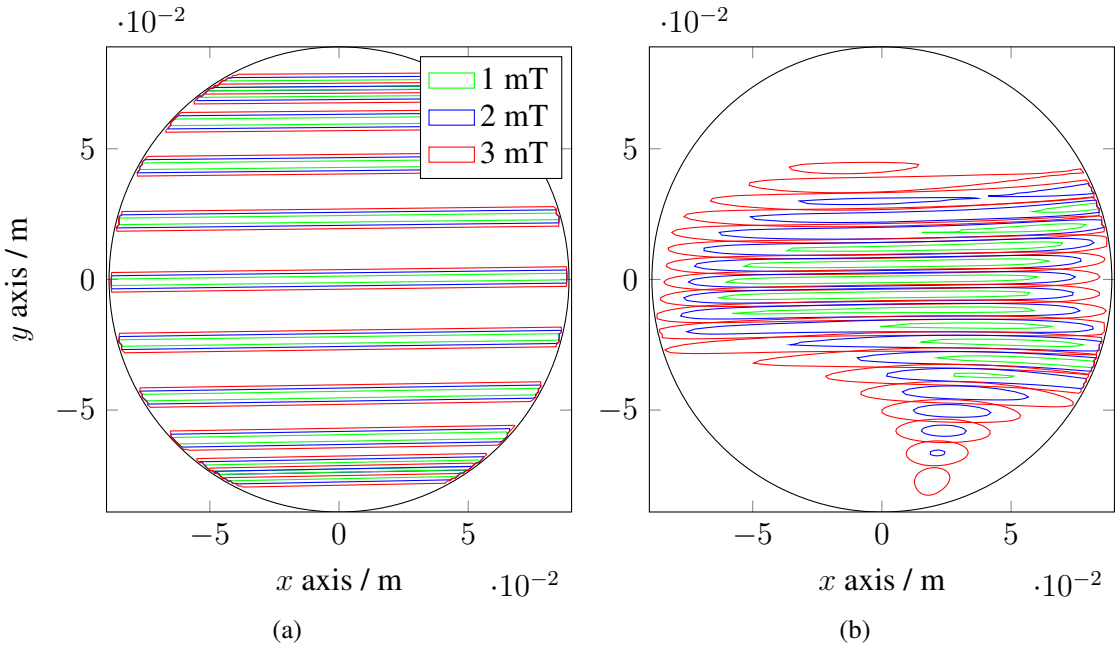

Figure 3.6: Effect of the higher SHCs on the LFV for a main SHC of 60 mT. The isolines represent the LFV with $\|\vec{B}\| = 3$, 2 and 1 mT at different time steps. (a) For an FFL idealised scanner made of idealised coils. (a) For an equivalent realistic scanner, using the same main SHCs. Different time points have been used to represent the LFVs.

facts. Those artefacts are visually evaluated for two different cases in order to assess the influence of the line shape and of the continuous rotation. This is done using two simulations done using the framework described in Chapter 2 and the sinogram assembled using the description given in the previous Section. Both imagers use $f_0 = 25$ kHz, gradients with main SHCs generating 0.8 T·m^{-1}, main SHCs for the drive coils of 45 mT, acquiring $n_{pp\gamma} = 81$ and assume a constant LFV speed on the whole surface equal to the one obtained for the ISIC. A first simulation uses an FFL ISIC scanner with $f_\theta = 1000$ Hz, acquiring thus $n_\gamma = 25$ projections per 180 ° rotation. A second simulation is done using the rabbit-sized imaging device presented in Section 6.1 with $f_\theta = 100$ Hz, acquiring thus $n_\gamma = 250$ projections per 180 ° rotation. Results of the FBP of the MPI signal can be seen in Figure 3.7.

It can be seen in Figures 3.7b and 3.7d that a rotation of the whole phantom seems to be applied to the phantom. Compared both figures, it can be seen that this rotation seems strongly related to f_θ, as the effect is less present when f_θ is smaller. Looking at Figures 3.7c and 3.7e, it can be seen that distortions appear for the points which are further away from the scanner centre. Due to the non-linear relation between the acquisition

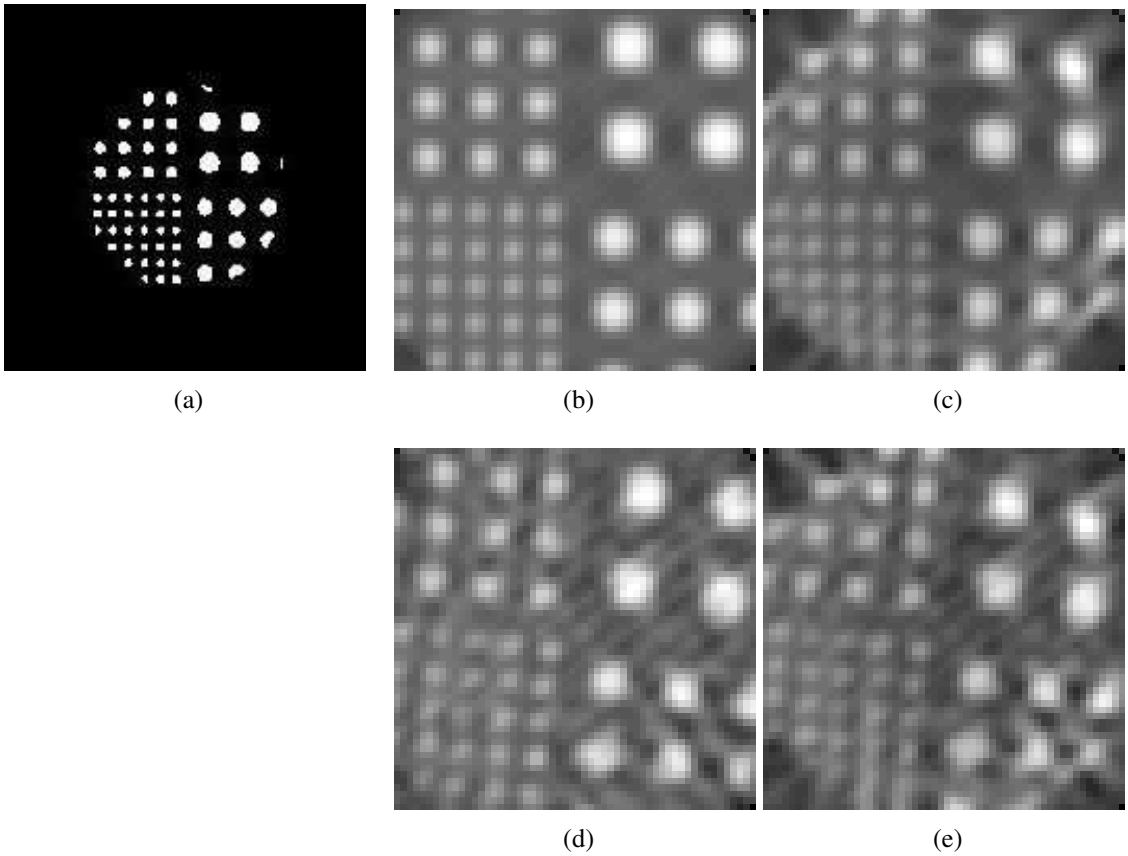

Figure 3.7: FBP results for different imaging devices. (a) used phantoms with circles of 4, 6, 8 and 10 mm diameter limited to a 100 mm diameter circle. (b) and (d) For an FFL ISIC with a line rotation $f_\theta = 100$ Hz and $f_\theta = 1000$ Hz, respectively. (c) and (e) For an FFL scanner using realistic fields with $f_\theta = 100$ Hz and $f_\theta = 1000$ Hz, respectively.

time and the position of the acquired voxel as described in Section 3.2.1, no conclusion could be given on the required amount of points per projection needed to achieve a given resolution. To address those issues, a new Radon transform could be designed to take into account the continuous rotation of the line, the effects of the non-ideal fields and the non-equidistant sampling data. However, such a task is beyond the focus of this work.

Instead, a SF approach is used, which can take into account the actual field shapes, sequence properties and tracer behaviour. Thus, the tools developed here are expected to be directly usable on an actual scanner.

With a line rotation of 100 Hz, 200 images could be acquired per second as only half of a line rotation is needed to obtain all the information for a model based reconstruction [96, 5], leading to an acquisition time of $T_a = 5$ ms per image. A spectrum with a resolution of $\Delta f = 2\, f_\theta = 200$ Hz is obtained via the acquisition of a single image. But the MPI

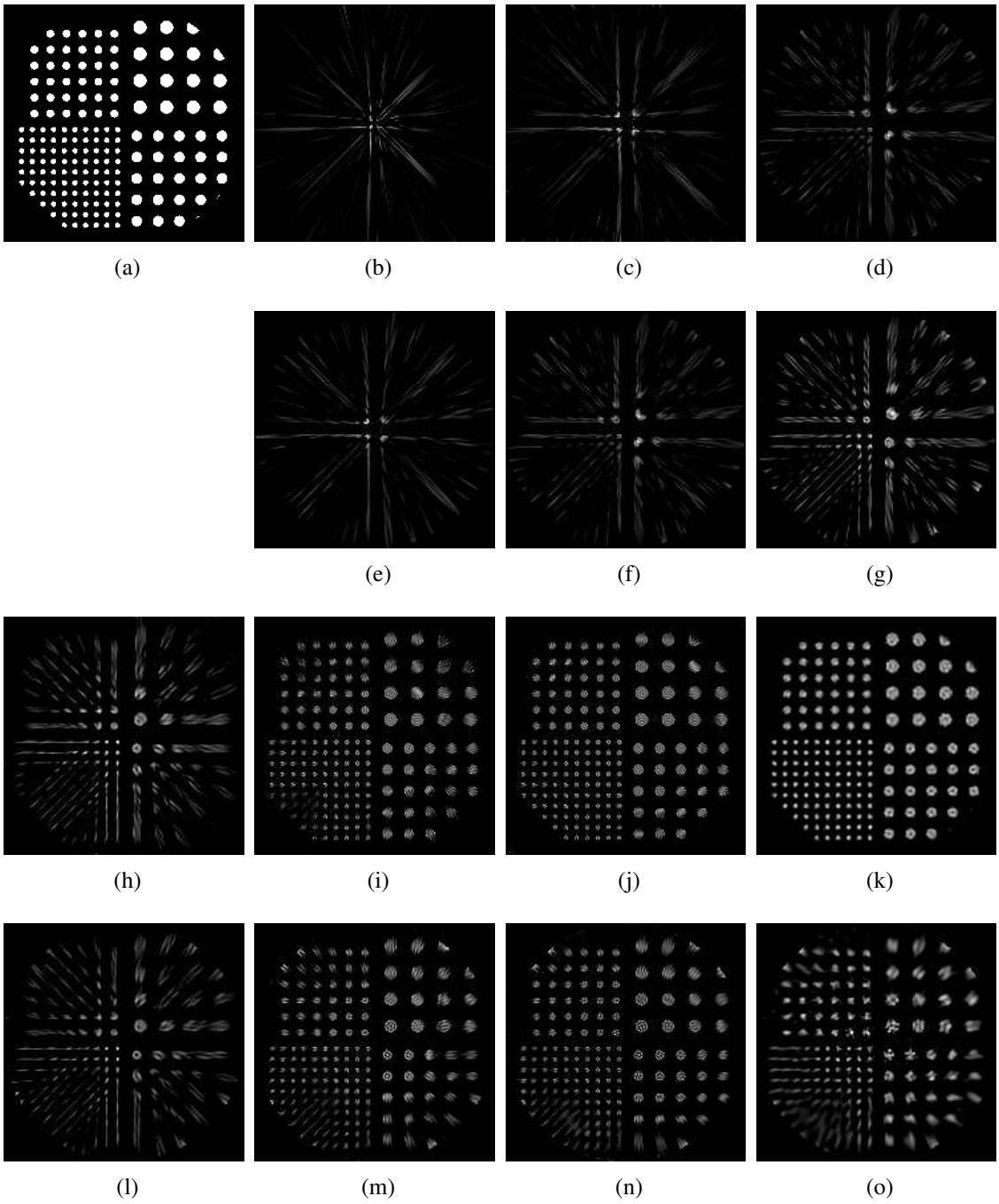

Figure 3.8: Reconstructions for different drive-fields main SHC in a 90×90 mm^2 FOV. (a) used phantom with circles of 4, 6, 8 and 10 mm diameter. (b) to (o) the first and third raw are for the ISIC. The second and fourth are for the realistic scanner. The main SHCs used here are 3.75, 7.5, 11.25, 15, 30, 45 and 75 mT.

signal is generated at frequencies, which are multiples of f_0-f_θ and f_0+f_θ, as described by relations (2.58), (3.36) and (3.37). Thus a spectrum resolution of $\Delta f = f_\theta = 100$ Hz is required for the SF approach. According to relation (2.28), this is only possible by acquiring the signal for a longer period of time, that is during a whole rotation. Once the whole rotation is acquired, only a single image can be reconstructed.

Using the regularised least-square methods described in Section 2.3.9 to reconstruct the image, better results were obtained with $\lambda_{\text{rel}} < 10^{-6}$. Further improvements have been obtained by simply inverting the forward MPI problem described by relation (2.78) using the modified Kaczmarz method. This will be further discussed in Chapter 6. Reconstructions are presented in Figure 3.8. In this Figure, the effect of a given set of realistic SHCs based on the FFL scanner presented in Section 6.1 is further investigated by comparing the results with an equivalent ISIC. Both have been calculated for main SHCs leading to a gradient on the line of 0.8 T·m^{-1}, with varying drive-field strength. The same drive-field strength is used on both channels. The SF has a resolution of $1 \times 1 \times 1$ mm^3 and the phantom is generated with voxels of $0.77 \times 0.77 \times 1$ mm^3. The frequencies are chosen to be $f_0 = 25$ kHz, $f_\theta = 100$ Hz, $f_s = 4$ Mhz for main drive field SHC of 3.75 mT to 15 mT, 6 Mhz for 30 mT, 10 Mhz for 45 mT and 12 Mhz for 75 mT. The increased sampling frequency is required to avoid any aliasing in the spectra. Indeed, the higher drive-field strength generates FCs with an higher amplitude at higher frequencies. For the same reason the FCs with a $\text{SNR}_s^{(4)}$ higher than 6 are kept between 45 kHz and $f_s/2$ for drive-field strengths up to 45 mT and with a $\text{SNR}_s^{(4)}$ higher than 300 for the 75 mT case. The MPI signals are calculated using a tracer with an equivalent iron concentration of 1.5 mol(Fe)·m^{-3} and a mono-disperse core diameter distribution with $d_{\text{np}} = 30$ nm (that is a model for a solution of Resovist diluted 10 times with water) and a noise created with $R_{\text{p}} = 200 \cdot 10^{-6}\ \Omega$ for the SF and $R_{\text{p}} = 185 \cdot 10^{-3}\ \Omega$ for the phantom acquisition. The whole process is done in a FOV of 90×89 mm^2.

Compared to the reconstruction done using the FBP, more information is recovered outside of the fully sampled area. Nevertheless, it is hard to conclude on the quality of those data. By comparing the reconstruction shown in Figure 3.8b to 3.8g with drive main SHC of up to 11.25 mT, the reconstruction area is slightly bigger for a realistic scanner than for an ISIC. Above 30 mT, the periphery of the phantom benefits from small improvements, with the bottom left corner being poorly resolved. At 75 mT, the realistic scanner shows worse reconstruction than the 45 mT reconstruction. This may be due to an inappropriate truncation of the tSF for the reconstruction.

It may be interesting to study the influence of the magnetic field shape on the covered area and the quality of the information acquired. But this could require the design of

coils with finely controlled SHCs, which in turn makes their design more challenging. Another way to achieve the control of the field quality is the use of shimming coils.

To increase the FOV, the FFL sequence could also be improved to acquire more information on the periphery. This could be done by moving the rotating line in the FOV by dynamically changing the rotation centre. This is studied in the next Section.

3.2.3 Moving the FFL rotation centre with focus fields

In [20], the magnetic flux-density $\vec{B}_{\text{global}}(\theta, \vec{r}_{\text{global}})$ in the global coordinate system (CS) at position $\vec{r}_{\text{global}}$ of an FFL rotated by an angle θ in the xy plane in the counter-clockwise direction is defined by

$$\vec{B}_{\text{global}}(\theta, \vec{r}_{\text{global}}) = \underline{\underline{G}}_{\text{global}} \vec{r}_{\text{global}}, \tag{3.5}$$

with $\underline{\underline{G}}_{\text{global}}$ the transformation matrix rotating the FFL. As it is easier to express the transformation in the FFL CS using $\underline{\underline{G}}_{\text{FFL}}$, equation (3.5) is transformed between the two CSs.

It has to be noted that coordinates can be either transformed into new coordinates, both in the same CS, using the relations

$$\vec{r}\,'_{\text{global}} = \underline{\underline{R}}^{\theta} \vec{r}_{\text{global}}, \tag{3.6}$$

$$\vec{r}_{\text{global}} = \underline{\underline{R}}^{-\theta} \vec{r}\,'_{\text{global}}, \tag{3.7}$$

or the CS used to represent them can be changed. In this case we have the relations

$$\vec{r}_{\text{global}} = \underline{\underline{R}}^{\theta} \vec{r}_{\text{FFL}}, \tag{3.8}$$

$$\vec{r}_{\text{FFL}} = \underline{\underline{R}}^{-\theta} \vec{r}_{\text{global}}, \tag{3.9}$$

with $\underline{\underline{R}}^{\theta}$ the matrix rotating coordinates in the counter-clockwise direction with an angle θ, as defined in Figure 3.9a, and $\underline{\underline{R}}^{-\theta}$ its inverse, with

$$\underline{\underline{R}}^{\theta} = \begin{pmatrix} \cos(\theta) & -\sin(\theta) & 0 \\ \sin(\theta) & \cos(\theta) & 0 \\ 0 & 0 & 1 \end{pmatrix}, \tag{3.10}$$

$$\underline{\underline{R}}^{-\theta} = \begin{pmatrix} \cos(\theta) & \sin(\theta) & 0 \\ -\sin(\theta) & \cos(\theta) & 0 \\ 0 & 0 & 1 \end{pmatrix}. \tag{3.11}$$

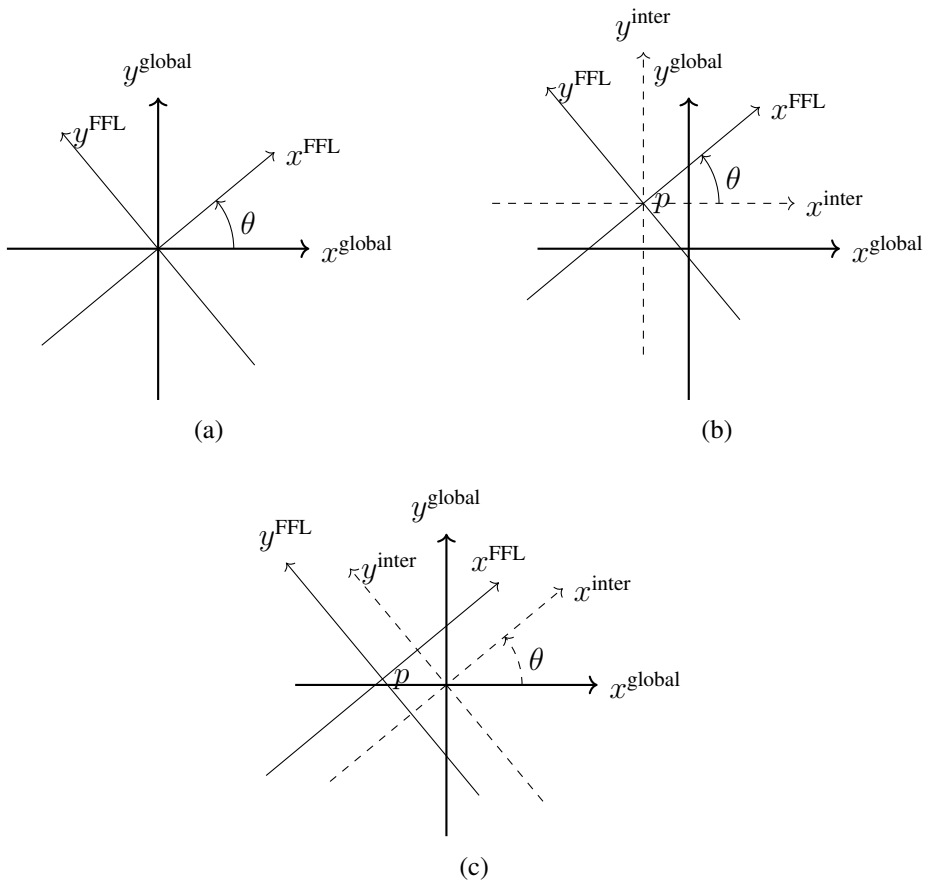

Figure 3.9: Different CSs used to describe the LFV movement. (a) Rotation around the $\vec{z}$ in the counter-clockwise direction. (b) Coordinate system resulting from a translation followed by a rotation, used for the drive fields. (c) Coordinate system resulting from a rotation followed by a translation, used for the focus fields.

Knopp at al. [3, 20] proposed to rewrite equation (3.5) using relations (3.6) and (3.7) as

$$\underline{\underline{G}}_{\text{global}} = \underline{\underline{R}}^{-\theta} \underline{\underline{G}}_{\text{FLL}} \underline{\underline{R}}^{\theta}, \tag{3.12}$$

which in fact describes the rotation of the line in the clockwise direction in the global CS. This is sufficient to decompose the FFL scanner selection coil into three subsets, but the formula has to be corrected to be able to use homogeneous coordinates [101, 102], which includes rotation and translation components in a single 4×4 matrix. Thus, we propose to rewrite (3.5) as

$$\underline{\underline{G}}_{\text{global}} = (\underline{\underline{T}}^{-1})^{\top} \underline{\underline{G}}_{\text{FLL}} \underline{\underline{T}}^{-1}, \tag{3.13}$$

with $\underline{\underline{T}}$ a linear transformation and $\underline{\underline{T}}^{\top}$ its conjugate, both transforming the coordinates. Using $\underline{\underline{T}} = \underline{\underline{R}}^{-\theta}$, that is, a rotation in the clockwise direction, the equation (3.12) is

obtained, validating observations [5, 90].

Let defines the transformation matrix G_{FLL}. It is a matrix which regroups the first-order spatial derivative of $\vec{B}_{\text{FFL}}$. It is the equivalent of the Jacobian matrix $\underline{\underline{J}}_{\text{FLL}}$, defined in the FFL CS by

$$\underline{\underline{J}}_{\text{FLL}} = \begin{bmatrix} \frac{\partial \vec{B}}{\partial x} & \frac{\partial \vec{B}}{\partial y} & \frac{\partial \vec{B}}{\partial z} \end{bmatrix} = \begin{pmatrix} \frac{\partial B_x}{\partial x} & \frac{\partial B_x}{\partial y} & \frac{\partial B_x}{\partial z} \\ \frac{\partial B_y}{\partial x} & \frac{\partial B_y}{\partial y} & \frac{\partial B_y}{\partial z} \\ \frac{\partial B_z}{\partial x} & \frac{\partial B_z}{\partial y} & \frac{\partial B_z}{\partial z} \end{pmatrix}, \tag{3.14}$$

whith the relation

$$\vec{B}_{\text{FFL}}(\vec{r}_{\text{FFL}}) = \underline{\underline{J}}_{\text{FFL}}\, \vec{r}_{\text{FFL}}. \tag{3.15}$$

It is the equivalent of a magnetic fields containing only the SHCs of degree $l = 1$.

To express $\underline{\underline{G}}_{\text{FFL}}$ in the global CS, the directional first-order derivative $\vec{\nabla}_{\vec{u}}\vec{B}$ in direction $\vec{u}$ has to be calculated. It is defined for scalar fields as [103]

$$\begin{aligned} \vec{\nabla}_{\vec{u}} B_x &= \vec{\nabla} B_x \cdot \vec{u} \\ &= \frac{\partial B_x}{\partial x}\frac{u_x}{\|\vec{u}\|} + \frac{\partial B_x}{\partial y}\frac{u_y}{\|\vec{u}\|} + \frac{\partial B_x}{\partial z}\frac{u_z}{\|\vec{u}\|}, \end{aligned} \tag{3.16}$$

which is equivalent to

$$\begin{pmatrix} \frac{u_x}{\|\vec{u}\|} \\ \frac{u_y}{\|\vec{u}\|} \\ \frac{u_z}{\|\vec{u}\|} \end{pmatrix}^{\top} \begin{pmatrix} \frac{\partial B_x}{\partial x} \\ \frac{\partial B_x}{\partial y} \\ \frac{\partial B_x}{\partial z} \end{pmatrix} \tag{3.17}$$

in the matrix notation.

For example, the first basis vector in the global CS is express in the FFL CS by

$$\vec{u} = \underline{\underline{T}}^{-1} \begin{pmatrix} 1 \\ 0 \\ 0 \end{pmatrix}. \tag{3.18}$$

Using the same relation for the other basis vectors, relation (3.17) can be generalised to express the Jacobian in the global CS as

$$\underline{\underline{J}}_{\text{global}} = (\underline{\underline{T}}^{-1})^{\top} \underline{\underline{J}}_{\text{FFL}}. \tag{3.19}$$

Then, expressing the position $\vec{r}_{\text{global}}$ in the FFL CS as

$$\vec{r}_{\text{FFL}} = \underline{\underline{T}}^{-1} \vec{r}_{\text{global}}, \tag{3.20}$$

the relation (3.5) can be expanded as

$$\begin{aligned}\vec{B}_{\text{global}}(\vec{r}_{\text{global}}) &= \underline{\underline{G}}_{\text{global}}\vec{r}_{\text{global}} \\ &= (\underline{\underline{T}}^{-1})^{\top}\,\underline{\underline{J}}_{\text{FFL}}\,\vec{r}_{\text{FFL}} \\ &= (\underline{\underline{T}}^{-1})^{\top}\,\underline{\underline{J}}_{\text{FFL}}\,\underline{\underline{T}}^{-1}\,\vec{r}_{\text{global}} \\ &= \underline{\underline{J}}_{\text{global}}\,\underline{\underline{T}}^{-1}\,\vec{r}_{\text{global}} \\ &= \underline{\underline{G}}_{\text{global}}\vec{r}_{\text{global}}.\end{aligned} \tag{3.21}$$

validating the proposed formulation in (3.13).

In the case relevant for this work, $\underline{\underline{J}}_{\text{FFL}}$ has to describe an FFL, i.e. a magnetic flux-density, which does not have any magnetic flux-density variation in one direction. Thus, to get a line in the x_{FFL} direction the following relation has to be fulfilled in the FFL CS

$$\frac{\partial B_x}{\partial x} = \frac{\partial B_y}{\partial x} = \frac{\partial B_z}{\partial x} = 0. \tag{3.22}$$

Moreover, considering Ampères law as described by equation (2.10), the following condition for an electromagnet follows:

$$\vec{\nabla} \times \vec{B} = \begin{pmatrix} \frac{\partial B_z}{\partial y} - \frac{\partial B_y}{\partial z} \\ \frac{\partial B_x}{\partial z} - \frac{\partial B_z}{\partial x} \\ \frac{\partial B_y}{\partial x} - \frac{\partial B_x}{\partial y} \end{pmatrix} = \begin{pmatrix} 0 \\ 0 \\ 0 \end{pmatrix}, \tag{3.23}$$

which add the relations on some concomitant terms

$$\frac{\partial B_x}{\partial z} = \frac{\partial B_z}{\partial x} = 0, \tag{3.24}$$

$$\frac{\partial B_x}{\partial y} = \frac{\partial B_y}{\partial x} = 0. \tag{3.25}$$

The two missing concomitant terms are set to zero

$$\frac{\partial B_z}{\partial y} = \frac{\partial B_y}{\partial z} = 0. \tag{3.26}$$

Due to Gauss law of magnetism (equation (2.4)), both remaining coefficients have to get the same absolute value, g,

$$\frac{\partial B_y}{\partial y} = -\frac{\partial B_z}{\partial z} = g. \tag{3.27}$$

The simplest way to describe an FFL along the x_{FFL} direction using homogeneous coordinates is

$$\vec{B}_{\text{FFL}}(\vec{r}_{\text{FFL}}) = \underline{\underline{J}}_{\text{FFL}}\,\vec{r}_{\text{FFL}} = \underline{\underline{G}}_{\text{FFL}}\vec{r}_{\text{FFL}} = g \begin{pmatrix} 0 & 0 & 0 & 0 \\ 0 & 1 & 0 & 0 \\ 0 & 0 & -1 & 0 \\ 0 & 0 & 0 & 1 \end{pmatrix} \begin{pmatrix} x \\ y \\ z \\ w \end{pmatrix}. \tag{3.28}$$

Rotating in the counter-clockwise direction, using $\underline{\underline{T}} = \underline{\underline{R}}^{\theta}$, $\underline{\underline{G}}_{\text{global}}$ for a rotating line is expressed in the global CS as

$$\begin{aligned}
\underline{\underline{G}}_{\text{global}} &= (\underline{\underline{R}}^{-\theta})^{\top}\underline{\underline{G}}_{\text{FLL}}\underline{\underline{R}}^{-\theta}\vec{r}_{\text{global}}, \\
&= \begin{pmatrix} \frac{1}{2}g - \frac{1}{2}g\cos(2\theta) & -\frac{1}{2}g\sin(2\theta) & 0 & 0 \\ -\frac{1}{2}g\sin(2\theta) & \frac{1}{2}g + \frac{1}{2}g\cos(2\theta) & 0 & 0 \\ 0 & 0 & -g & 0 \\ 0 & 0 & 0 & 1 \end{pmatrix}, \\
&= \begin{pmatrix} G_{1,1} & G_{1,2} & G_{1,3} & G_{1,4} \\ G_{2,1} & G_{2,2} & G_{2,3} & G_{2,4} \\ G_{3,1} & G_{3,2} & G_{3,3} & G_{3,4} \\ G_{4,1} & G_{4,2} & G_{4,3} & G_{4,4} \end{pmatrix}.
\end{aligned} \tag{3.29}$$

This result can be used to generate an FFL rotating in the xy plane by varying the current in three different coil sets, as presented in [20]. Indeed, the blue, green and black components can each be generated by a given coil, namely a z-gradient coil, also known as Maxwell coil configuration, with the strong gradient in the z direction, and two quadrupoles, rotated by 45 °. In order to continuously rotate the line by an angle

$$\theta(t) = 2\pi f_{\theta} t, \tag{3.30}$$

the magnetic field strength created by the quadrupoles should be varied as

$$B^{\text{Q}_0}(t) = B^{\text{Q}_0}\cos(4\pi f_{\theta} t), \tag{3.31}$$

$$B^{\text{Q}_{45}}(t) = B^{\text{Q}_{45}}\sin(4\pi f_{\theta} t). \tag{3.32}$$

The homogeneous coordinates enable us to fully describe an FFL MPI-sequence, including the modulation applied to the drive fields and the rotation of the line around arbitrary points using focus field.

The drive fields peak strength are chosen in order to translate the line in the FFL CS from a distance $\pm\,\text{A}_{\text{drive}} = b/(2g)$ in the y direction at a frequency of f_0. This can be represented as a translation made with the homogeneous matrix

$$\underline{\underline{D}}_{\text{drive}} = \begin{pmatrix} 1 & 0 & 0 & 0 \\ 0 & 1 & 0 & \frac{b}{2g} \\ 0 & 0 & 1 & 0 \\ 0 & 0 & 0 & 1 \end{pmatrix}, \tag{3.33}$$

leading to the whole transformation

$$\underline{\underline{T}}_{\text{drive}} = \underline{\underline{R}}^{\theta}\underline{\underline{D}}_{\text{drive}}, \tag{3.34}$$

and the expression of $\underline{\underline{G}}_{\text{global}}$ as

$$\begin{pmatrix} G_{1,1} & G_{1,2} & G_{1,3} & \frac{1}{2}b\sin(2\pi f_0 t)\sin(\theta(t)) \\ G_{2,1} & G_{5,2} & G_{5,3} & -\frac{1}{2}b\cos(\theta(t))\sin(2\pi f_0 t) \\ G_{3,1} & G_{3,2} & G_{3,3} & 0 \\ G_{4,1} & G_{4,2} & G_{4,3} & G_{4,4} \end{pmatrix}. \tag{3.35}$$

Here, the expressions in blue and red describe the amplitude variation applied on the x- and y-drive fields, respectively. Along with relation 3.31 and 3.32, this forms the well known FFL sequence, which is illustrated in Figure B.1a. The coefficients $G_{1,1}$ to $G_{3,3}$ are unchanged from equation (3.29) and coefficients $G_{4,1}$ to $G_{4,4}$ have no physical meaning here and are thus ignored. It can be seen that both channels will be modulated by the frequency at which the line will be rotated. This in turn is going to reduce the efficiency of the whole system, as both the power factor correction and the impedance matching are done for a given frequency, and the modulation of the signal actually splits the power between the frequency $f_0 \pm f_\theta$. The MPI sequence of a continuously rotated FFL is thus described as

$$\begin{aligned} B^{x-\text{drive}}(t) &= B^{\text{Drive}_x}\sin(2\pi f_0 t)\sin(2\pi f_\theta t) \\ &= \frac{B^{y\text{drive}}}{2}(\cos(2\pi(f_0 - f_\theta)t) - \cos(2\pi(f_0 + f_\theta)t)), \end{aligned} \tag{3.36}$$

$$\begin{aligned} B^{\text{Drive}_y}(t) &= -B^{\text{Drive}_y}\sin(2\pi f_0 t)\cos(2\pi f_\theta t) \\ &= \frac{-B^{\text{Drive}_y}}{2}(\sin(2\pi(f_0 - f_\theta)t) + \sin(2\pi(f_0 + f_\theta)t)). \end{aligned} \tag{3.37}$$

In order to cover a larger area, the centre of rotation of the line could be moved in the xy plane using focus fields in the x and the y direction. Contrary to the LFV translation with the drive fields, the line is here first rotated and then translated in the x and y direction. The translation is described by the functions $p_{\text{FF}x}$ and $p_{\text{FF}y}$. As those translations are designed to have a low frequency, they are attached to the notion of focus fields. The corresponding transformation matrix describing the translation is

$$\underline{\underline{D}}_{\text{focus}} = \begin{pmatrix} 1 & 0 & 0 & p_{\text{FF}x}(t) \\ 0 & 1 & 0 & p_{\text{FF}y}(t) \\ 0 & 0 & 1 & 0 \\ 0 & 0 & 0 & 1 \end{pmatrix}. \tag{3.38}$$

The whole transformation is therefore expressed as

$$\underline{\underline{T}}_{\text{drive}} = \underline{\underline{D}}_{\text{focus}}\underline{\underline{R}}^{\theta}, \tag{3.39}$$

and $\underline{\underline{G}}_{\text{global}}$ becomes

$$\begin{pmatrix} G_{1,1} & G_{1,2} & G_{1,3} & \frac{1}{2}\sin(2\pi f_\theta t)\left(p_{\text{FF}y}(t)\cos(2\pi f_\theta t) - p_{\text{FF}x}(t)\sin(2\pi f_\theta t)\right) \\ G_{2,1} & G_{2,2} & G_{2,3} & -\frac{1}{2}\cos(2\pi f_\theta t)\left(p_{\text{FF}y}(t)\cos(2\pi f_\theta t) - p_{\text{FF}x}(t)\sin(2\pi f_\theta t)\right) \\ G_{3,1} & G_{3,2} & G_{3,3} & 0 \\ G_{4,1} & G_{4,2} & G_{4,3} & G_{4,3} \end{pmatrix}. \tag{3.40}$$

To cover a greater area, different trajectories can be chosen. As a first result, we propose to use a Lissajous trajectory in the xy plane. Therefore, using equations (2.42) and (2.43) in relation (3.38), components $G_{1,4}$ and $G_{2,4}$ can be simplified as

$$\begin{aligned} G_{1,4} = \frac{1}{4}(\, & \cos(2\pi(f_{\text{FF}y} - 2f_\theta)) \\ & - \cos(2\pi(f_{\text{FF}y} + 2f_\theta)) \\ & - 2\sin(2\pi(f_{\text{FF}x})) \\ & + \sin(2\pi(f_{\text{FF}x} - 2f_\theta)) \\ & + \sin(2\pi(f_{\text{FF}x} + 2f_\theta))) \end{aligned} \tag{3.41}$$

$$\begin{aligned} G_{2,4} = \frac{1}{4}(\, & \cos(2\pi(f_{\text{FF}x} - 2f_\theta)) \\ & - \cos(2\pi(f_{\text{FF}x} + 2f_\theta)) \\ & - 2\sin(2\pi(f_{\text{FF}y})) \\ & - \sin(2\pi(f_{\text{FF}y} - 2f_\theta)) \\ & - \sin(2\pi(f_{\text{FF}y} + 2f_\theta))) \end{aligned} \tag{3.42}$$

In summary, the MPI sequence of an FFLscanner using an arbitrary focus field sequence is described here by relations (3.31) and (3.32) for the quadrupoles; by coefficients $G_{1,4}$ and $G_{2,4}$ from (3.35) for the drive coils; and by coefficients $G_{1,4}$ and $G_{2,4}$ from (3.40) for the focus fields. It can be further defined as relations (3.41) and (3.42) to move the rotation points along a Lissajous curve. An example of such a sequence can be seen in Figure B.2.

3.3 Discussion

This work focuses on the development of continuously rotated FFL.

The analogy to CT has been further developed to integrate the notion of a projection and the number of points per projection. It has been shown that three different sampling

techniques could be used, leading to either sampling the same points for two consecutive projections, or to sampling different positions. Despite the SF, where the sampling strategy aims at resolving all the signal components, this could shift this strategy toward interpolation methods [104].

Looking at the simulation results for the FBP and more specifically the results shown in Figure 3.7, for which $n_{\text{pp}\gamma} = 81$ points per projection are acquired with only $n_\gamma = 25$ projections for a FOV of around 70 mm. Despite the low number of projections, the reconstructed results in the fully sampled area displays artefacts, which seem to be only related to the two main differences between CT and continuously rotated FFL scanner: the continuous rotation and acquisition of the data and the non-ideal field topology.

To take into account all those effects, a generalised Radon transform could be modelled to benefit from the fast reconstruction offered by such approaches. But it is still expected that truncation artefacts appear.

To assess the information quality of the information available outside the fully sampled area and to simplify the implementation of the future measurement based reconstruction, an SF-based approach is chosen. Even if the acquisition rate is two times lower than for a Radon-based approach, the gain of information outside the fully sampled area is seen as more important and should be further studied.

Using a realistic magnetic field topology, the definition of the fully sampled area becomes unclear. Indeed, the spacial extend of each projection becomes strongly dependent on the field topology and the considered time point. Looking at a reconstruction in the whole device bore, the fully sampled area is estimated based on the presence of truncation artefacts. Thus the expected performance of a given scanner has to be evaluated using either simulations based on realistic descriptions of the magnetic field shapes, or its construction.

The effects of realistic magnetic field topologies have been evaluated and presented in Figure 3.8 for a few different drive-fields strength, and only marginal differences have to be expected between an ISIC and a real one up to a FOV covering approximatively half of the drive-coil diameter. Strong artefacts appear closer the the bore. Those differences are considered marginal compared to the other gains, which can be achieved by investing the same resources on other topics, as for example by increasing the SNR of the acquisition process. The optimisation of the magnetic field topology to control the scanner performance should be explored when the technology is more mature. It is not excluded that a whole analytic description of an imaging device may further constrain the magnetic field topology and sequence design. But for short-term perspectives, the increase of the acquisition rate and FOV is more relevant.

In order to increase the FOV, we propose to control the line rotation centre using focus fields. The choice of the curve along which the centre is moved has to be further investigated. This first suggestion, using a Lissajous curve, shows that focus-field signals are constituted of six different frequencies. The implementation of such a system has to be further studied, to find if there is any practicable limitation to its implementation. An example is given in Section 6.2.

All the presented concepts acquired information mainly in a plane, even if the LFV generated by an FFL with realistic fields will slightly move in the third space direction. To acquire information in the third direction, the line or the patient has to be moved along it. This could be done either electrically using magnetic fields or mechanically by moving either the patient or the scanner. The choice between both approaches will be mainly based on the mass of the patient and the safety limits associated with the sequence. The PNS is the main limit seen at the moment, and will be further investigated in Chapter 5. Moving in the third dimension may also increase the amount of redundant information acquired, and the use of interpolation techniques to limit the redundancy should be taken into account when designing such a imaging device [O17, O42].

Finally, to make the reconstruction more robust, a CT could be added to the scanner. Both the MPI tracer concentration and the tissue X-ray attenuation coefficient could be simultaneously acquired and integrated in the reconstruction to obtain more and perhaps more consistent information [O43].

3.4 Conclusion

In this Chapter, all the existing MPI imaging devices have been analysed and sorted in three groups, based on the LFV shapes. It has been shown that all FFL scanners use similar encoding schemes, translating the LFV to acquire information along a projection and later rotating the LFV to acquire another projection.

To further study the effect of realistic shapes of magnetic fields, SF based approach is still the best solution to reconstruct the tracer distribution. Indeed, model based transformation such as the FBP do not take into account the continuous rotation, the actual variation rate of the magnetic field strength, the exact field shape, nor the exact particle behaviour which will lead to artefacts. It has been shown that the ISIC model can be used to predict the general properties of a scanner, but that finer description requires the simulation using realistic magnetic field shape. But, it has also been proven that the maximal reconstruction rate of the FBP compared to the SF approach using a properly resolved spectrum is two times higher. This result should stimulate the development of

more advanced model-based reconstructions.

In order to increase the covered FOV, without increasing the drive-field strength or constraining the magnetic field topology, a general model used to move the rotation point along a given curve has been developed. This may help to increase the fully sampled area without increasing the drive-field strength. The exact limitation will depend on the imaging goal. An example of a human-sized scanner using such a sequence is presented in Chapter 6.

4

Coil Design

Contents

To produce the magnetic fields required by MPI scanners, magnets and coils are used. There are different ways to produce magnetic fields; this work focuses on the design of normal conductive electromagnets, also called coils.

Two ways to guide the magnetic flux are presented: using the air or ferromagnetic materials. This choice greatly influences the whole design process. For air-core coils, the position of each current-carrying wire shapes the magnetic field topology. For ferromagnetic core coils, the form of the interface between the core and the volume of interest shapes the magnetic field topology. Thus, both types require different design techniques, which are explained in Sections 4.1 and 4.2. Additionally, the magnetic field shielding effect of copper surfaces is evaluated by extending the calculation done for the air-core coil design.

4.1 Air-core inductor

Diverse methods exist to design air-core coils, mainly originating from the MRI and particle accelerator communities. Five sources are recommended to gain insight on the variety of approaches [105, 40, 10, 106, 107]. For this work, an inverse boundary element method (BEM) is chosen, as it offers great flexibility in terms of current carrying surface choice and uses optimisation algorithms which are relatively close to the one used for the MPI-signal reconstruction.

In this Section, the method used to optimise the current density and evaluate the induced current on conductive surfaces is detailed. Different constraints are introduced to provide flexible optimisation goals to optimise the current density of cylindrical drive, quadrupole and z-gradient as well as single-sided coils. Part of the results presented here have been published in [O1].

4.1.1 Material and methods

The design technique described here has the purpose of optimising a coil in order to generate a given magnetic flux-density $\vec{B}$ in a volume V_{target} with an electrical permittivity ϵ and a magnetic permeability μ. The magnetic flux-density is generated by a current density $\vec{J}$ flowing in a conducting volume V_{cond} with conductivity ρ.

4.1.1.1 Forward problem

The forward problem can be formulated using Ampère's law (2.2) and the quasi-static approximation (2.5) by reformulating

$$\vec{\nabla} \times \frac{\vec{B}}{\mu} = \vec{J}, \tag{4.1}$$

as [8]

$$\begin{aligned} \vec{B}(\vec{r}_{\text{t}}) &= \frac{\mu}{4\pi} \vec{\nabla} \times \int\limits_{\mathbb{R}^3} \frac{\vec{J}(\vec{r}_{\text{s}})}{\|\vec{r}_{\text{t}} - \vec{r}_{\text{s}}\|^3} \, \mathrm{d}V_{\text{cond}} \\ &= \frac{\mu}{4\pi} \vec{\nabla} \times \vec{A}(\vec{r}_{\text{t}}), \end{aligned} \tag{4.2}$$

with $\vec{r}_{\text{s}} \in V_{\text{cond}}$ and $\vec{r}_{\text{t}} \in V_{\text{target}}$.

Inverting equation (4.2), the current density $\vec{J}$ will be obtained as a function of the required magnetic field $\vec{B}$. To facilitate the expression of $\vec{J}$ in V_{cond}, $\vec{J}$ can be expressed as

a series [10] by

$$\vec{J}(\vec{r}_{\mathrm{s}}) = \sum_{n=1}^{\infty} I_n \widehat{\vec{J}}_n(\vec{r}_{\mathrm{s}}), \tag{4.3}$$

with I_n the current density and $(\widehat{\vec{J}}_n(\vec{r}_{\mathrm{s}}))_{n\in\mathbb{N}}$ being a suitable set of independent basis functions, which guarantees that

$$\vec{\nabla} \cdot \widehat{\vec{J}}_n = 0. \tag{4.4}$$

This means that $\vec{J}$ is source-free, i.e. it represents a physically plausible solution, where no moving charges are created or destroyed.

4.1.1.2 Objective and constraint functions

In order to optimise the current density, objective and constraint functions have to be evaluated. In this work, four quantities are used for this purpose. Two are quadratic functions of $\vec{J}$, namely the dissipated power P_{dis} and the stored energy E_{stored}. The two others are linear functions of $\vec{J}$, namely the Laplacian of the current density, $\mathscr{L}J$, and the magnetic field strength, $\vec{B}$. The latter is already presented in (4.2); the three others are described in detail here.

4.1.1.2.1 Stored energy - mutual inductance One typical coil property is its stored energy, linked to the magnetic field E_{stored}. With a current I, E_{stored} can be calculated as

$$E_{\mathrm{stored}} = \frac{1}{2} L\, I^2. \tag{4.5}$$

with L the coil self-inductance. To calculate it, the mutual inductance M_{mn} between the basis function $\widehat{\vec{J}}_n$ and $\widehat{\vec{J}}_m$ is expressed from the law of conservation of energy as [10]

$$M_{mn} = \int_V \frac{\widehat{\vec{B}}_m(\vec{r}) \cdot \widehat{\vec{B}}_n(\vec{r})}{\mu(\vec{r})} \mathrm{d}V, \tag{4.6}$$

with $\widehat{\vec{B}}_m$ a shorthand for the description of the magnetic field $\vec{B}_m$ using the basis function $\widehat{\vec{J}}_m$ Thus, minimising the stored energy of a coil will also minimise its inductance.

4.1.1.2.2 Dissipated power - mutual resistance Similar to the inductance, the dissipated power P_{dis} is another coil property, which can be evaluated as

$$P_{\mathrm{dis}} = RI^2, \tag{4.7}$$

with R being the resistance of the coil. The mutual resistance R_{mn} between the basis function $\widehat{\vec{J}}_m$ and $\widehat{\vec{J}}_n$ is given by [10]

$$R_{mn} = \int_V \frac{\rho\, \widehat{\vec{J}}_m(\vec{r}) \cdot \widehat{\vec{J}}_n(\vec{r})}{d(\vec{r})} \mathrm{d}V, \tag{4.8}$$

if the two basis functions $\widehat{\vec{J}}_m$ and $\widehat{\vec{J}}_n$ share a common element [106, 10]. Otherwise, the mutual resistance is zero. Thus, minimising the dissipated power will also minimise the resistance of the coil.

4.1.1.2.3 Laplacian Beside the dissipated power and the stored energy, the shape of the current density can be optimised. One way of doing it is to evaluate the Laplacian, a scalar field defined for every point on a surface, which evaluates the smoothness. Minimising the Laplacian will reduce the geometrical variation of the surface current density, hence facilitating the fabrication of the coil. The Laplacian of the current density is expressed as

$$\mathscr{L} J(\vec{r}) = \vec{\nabla}^2 \vec{J}(\vec{r}). \tag{4.9}$$

4.1.1.3 From volume to surface

To simplify the representation of the conducting volume, the thickness d is assumed to be small compared to the other dimensions. Thus, the conducting volume V_{cond} can be represented by the surface S_{cond}. $\vec{J}$ is thus replaced by the surface current density $\vec{j}$ as:

$$\vec{j}(\vec{r}) = d(\vec{r})\vec{J}(\vec{r}), \quad \text{with } \vec{r} \in S. \tag{4.10}$$

4.1.1.4 Stream function

Extracting the conductive path from the $\vec{j}$ is a challenging task, as it may be seen from Figure 4.1. It can be done either to provide a path with constant or varying cross-section and surface current density. The constant surface current density solution is adapted to wire based construction, whereas the varying ones are used for construction based on copper sheets, as presented in Figure 4.3.

In both cases the integral of the surface current density over the cross Section area is constant. Relying on surface or volume integrals to determine either of those paths is intrinsically linked with numerical error. Pissanetzky [108] first proposed to reformulate the problem using the stream function instead of the surface current density. Later,

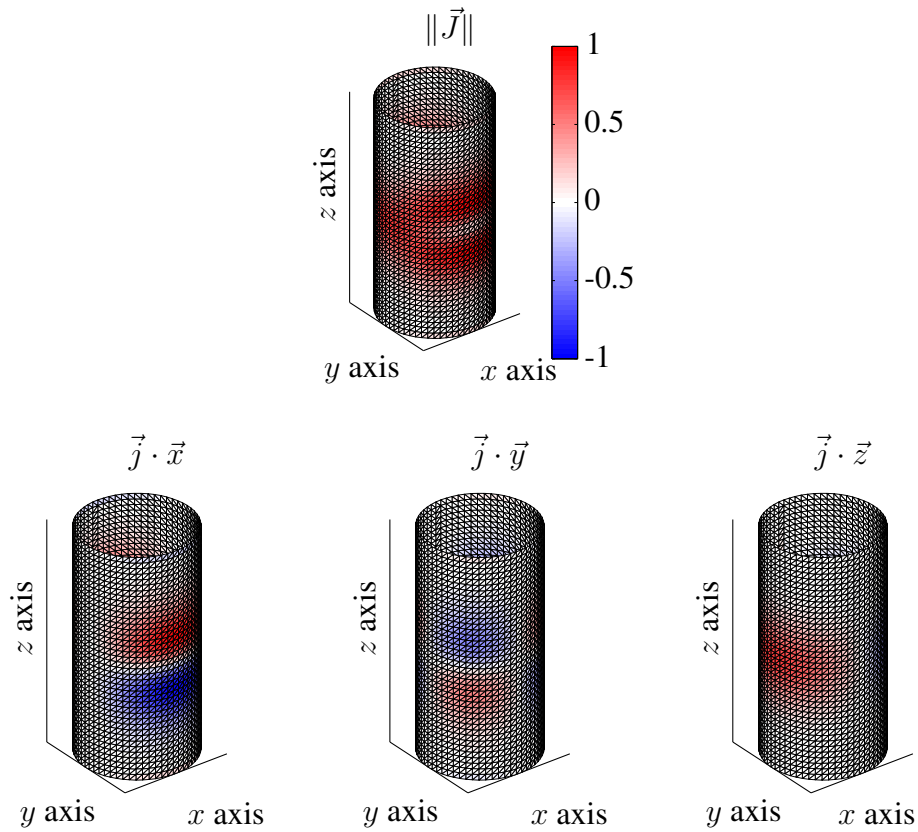

Figure 4.1: Discrete surface current-density associated with a x-drive coil. Looking at the spatial repartition of the surface current density, it can been seen that the extraction of wire path may be challenging.

Peeren [109, 10] fully defined the stream function ψ. The notation used thereafter is inspired from the one used in his work.

As the name indicates, the stream function describes the trajectory of a particle (for a fluid) or a charge (in the case of a current, which is a flow of charges). As the surface current density is source free, those trajectories form closed curves.

The surface current density $\vec{j}$ could thus be modelled here by stream functions as

$$\vec{j}(\vec{r}) = \vec{\nabla} \times (\psi(\vec{r})\, \vec{n}(\vec{r})), \tag{4.11}$$

or as

$$\begin{cases} \vec{j}(\vec{r}) \cdot \vec{x} = \frac{\partial \psi(\vec{r})}{\partial \vec{x}} \\ \vec{j}(\vec{r}) \cdot \vec{y} = \frac{\partial \psi(\vec{r})}{\partial \vec{y}} \end{cases} \tag{4.12}$$

with $\vec{n}(\vec{r})$ being the normal of the surface S at position $\vec{r}$. The normalised stream function values corresponding to the surface current density shown in Figure 4.1 are displayed in

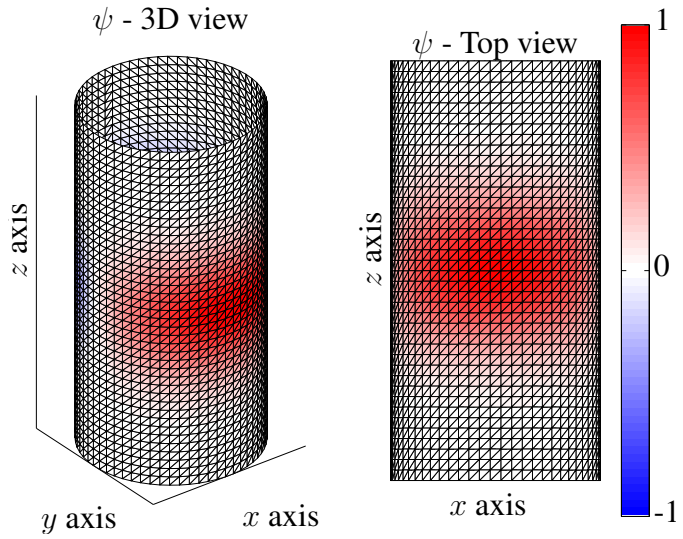

Figure 4.2: Stream-function associated with a x-drive coil. The ideal wire paths could be extracted by taking isocontours of the function.

Figure 4.2.

Instead of integrating $\vec{j}$ in order to discretise it, trajectories with constant ψ can be selected to design the current path. In Figure 4.3, the different curves are obtained by drawing isolines of the function ψ shown in Figure 4.2. The solid and dashed curves present two different approaches to making the current path. The boundaries of each copper track with spatially varying cross Sections are represented by solid curves. Between two curves, where the dashed curve is drawn, surface currents flow with a spatially varying surface current density. The centroid of a constant cross-section and surface current density wire is displayed using dashed curves. It has to be noted that the dashed curve has no apparent reason to be in the middle of the track with solid boundaries.

4.1.1.5 Discretisation

To numerically evaluate the stream function, the continuous functions used in the previous description have to be discretised. Considering a mesh with N nodes, a finite set of basis functions based on the stream function $(\widehat{\psi}_n(\vec{r}))_{n=1}^{N}$ is defined, which are piecewise continuously differentiable on the surface S [10]. Following the decomposition into a new basis as done by equation (4.3), the stream function $\psi(\vec{r})$ can be represented in this

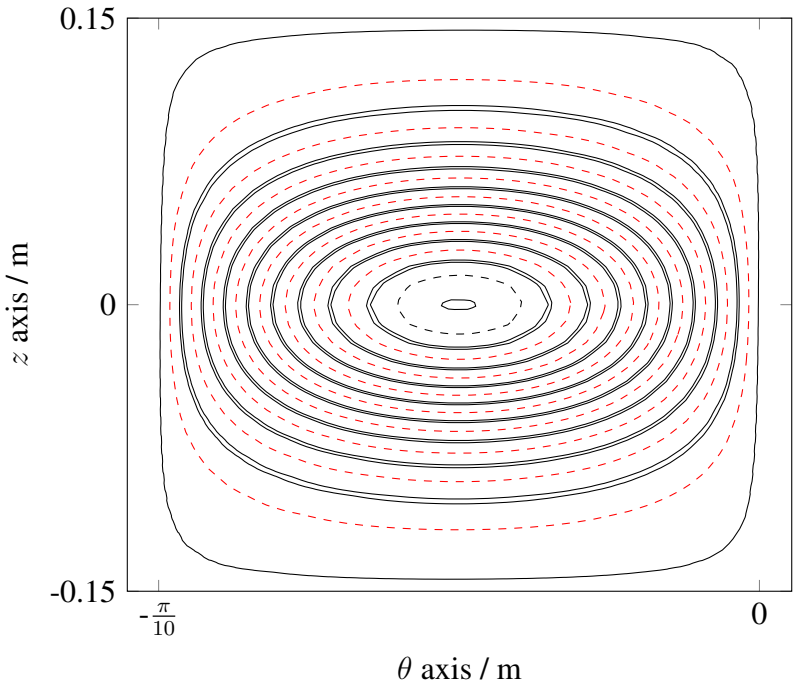

Figure 4.3: Flat projection of two different ways to discretise the surface current density of a drive coil made on a cylinder with a diameter of 0.1 m. The dashed curves represent the position of a wire centroids, whereas the black curves surround the copper track, which may be machined from a copper sheet to form the current path.

basis as the finite series

$$\psi(\vec{r}) \approx \sum_{n=1}^{N} s_n \widehat{\psi}_n(\vec{r}), \tag{4.13}$$

with s_n being the stream-function value at node n. Additionally, all the sub-boundaries ∂S of S have to be closed and the value of ψ has to be constant on each of them. As consequence, any non-self-intersecting surface can be used for S and

$$\vec{s} = [s_1\, s_2\, \cdots\, s_n]^\top, \tag{4.14}$$

is not unique due to the value of ψ on the boundaries [10].

The target volume is discretised into Z points where the target magnetic field is defined, using for example the points required to define a magnetic field using a SHSE.

4.1.1.6 Normalised set of basis function

As ψ is constant on each closed sub-boundary of S, the number of basis functions can be reduced to one single function per closed sub-boundary. Furthermore, by choosing

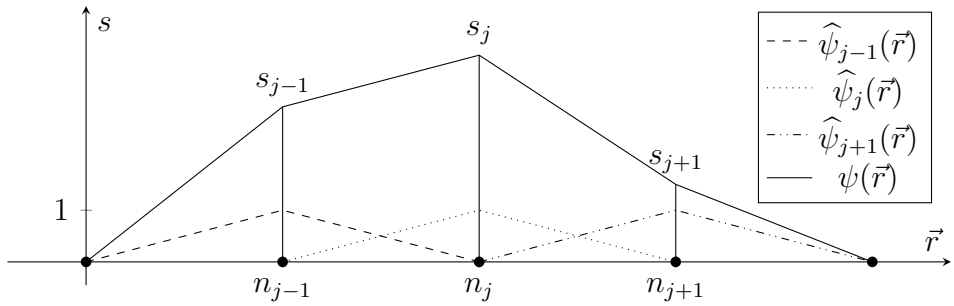

Figure 4.4: 1D example of a function $\psi(\vec{r})$ decomposed on three nodes n_{j-1}, n_j and n_{j+1} as the stream-function value and the respective basis function $\widehat{\psi}_{j-1}(\vec{r})$, $\widehat{\psi}_j(\vec{r})$ and $\widehat{\psi}_{j+1}(\vec{r})$.

the value of the stream function to be zero, the number of degrees of freedom is further reduced by the number of closed sub-boundaries and each vector solution $\vec{s}$ is unique [10, 106].

4.1.1.7 Basis function definition

Similar to BEM approaches [110], the choice of the basis function, named shape function in the BEM literature, is based on a tradeoff between the number of points needed to properly describe the basis function and the number of elements on the surface S. To keep the number of required points on each element low, we are using linear basis function. Considering N nodes with coordinates $\vec{r}_n$, $n = 1, \ldots, N$ on S, the function $\widehat{\psi}_n$ at node n is defined as

$$\widehat{\psi}_n(\vec{r}_j) = \begin{cases} 1 & \text{if } j = n, \\ 0 & \text{if } j \neq n, \end{cases} \qquad j, n = 1, \ldots, N. \tag{4.15}$$

and $\widehat{\psi}_n$ decreases linearly on the edges connected to the node n. This means that the value of the stream function ψ between two nodes of S are interpolated using a linear interpolation function, as shown with a 1D example in Figure 4.4.

In this work, S will be formed by K triangular elements and obtained via the modelisation software Blender (Blender 2.68a, Blender Foundation, Netherlands). Such a mesh can be seen on Figures 4.1 and 4.2. The flat projection of a segment of such a mesh is represented in more details in Figure 4.5a. This can be used to illustrate the reformulation of $\widehat{\vec{J}}_n$ into $\widehat{\psi}_n$.

First, the current density given by equation (4.11) is transformed and expressed on the

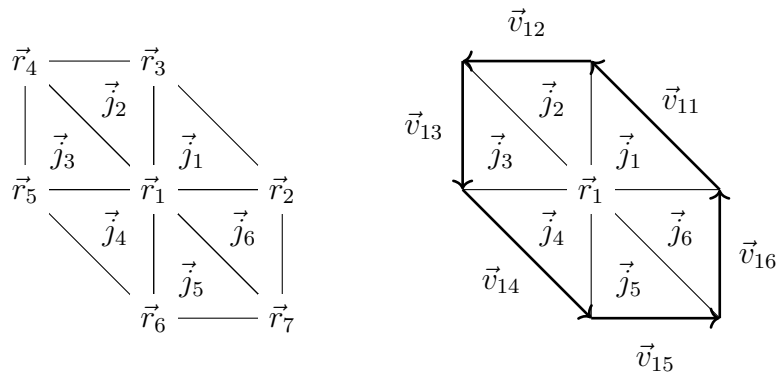

(a) (b)

Figure 4.5: Triangular mesh used as example for the notation. (a) With nodes $\vec{r}_n$ and surface current density $\vec{j}_k$. (b) With the new basis function uses the vector $\vec{v}_n j$ to decompose $\vec{j}$ into $\widehat{\psi}_n$.

unit triangle

$$\{(u,v) \subset \mathbb{R}^2 | u \geq 0, v \geq 0, u + v \leq 1\} \tag{4.16}$$

to simplify later numerical integration, by

$$\vec{j}_k(u,v) \approx \frac{s_1(\vec{r}_3 - \vec{r}_2) + s_2(\vec{r}_1 - \vec{r}_3) + s_3(\vec{r}_2 - \vec{r}_1)}{\|(\vec{r}_2 - \vec{r}_1) \times (\vec{r}_3 - \vec{r}_1)\|}, \tag{4.17}$$

with $\vec{j}_k$ the surface current density on the kth triangle, which is constant on each triangle. It is to be noted that the air of the kth triangle A_{tri} can be expressed by

$$A_{\text{tri}} = \frac{\|(\vec{r}_2 - \vec{r}_1) \times (\vec{r}_3 - \vec{r}_1)\|}{2}. \tag{4.18}$$

To express $\vec{j}_k$ in $\widehat{\psi}$, a reformulation has to be done, which can be better understood by

taking the example shown in Figure 4.5a and expressing $\vec{j}$ by

$$
\begin{aligned}
\vec{j}(\vec{r}(u,v)) &= \sum_{k=1}^{K} \vec{j}_k(\vec{r}(u,v)) \\
&= \vec{j}_1 + \vec{j}_2 + \vec{j}_3 + \vec{j}_4 + \vec{j}_5 + \vec{j}_6 \\
&\approx \begin{array}{l}
\frac{s_1(\vec{r}_3 - \vec{r}_2)}{2\,A_1} + \frac{s_2(\vec{r}_1 - \vec{r}_3)}{2\,A_1} + \frac{s_3(\vec{r}_2 - \vec{r}_1)}{2\,A_1} + \\
\frac{s_1(\vec{r}_4 - \vec{r}_3)}{2\,A_2} + \frac{s_3(\vec{r}_1 - \vec{r}_4)}{2\,A_2} + \frac{s_4(\vec{r}_3 - \vec{r}_1)}{2\,A_2} + \\
\frac{s_1(\vec{r}_5 - \vec{r}_4)}{2\,A_3} + \frac{s_4(\vec{r}_1 - \vec{r}_5)}{2\,A_3} + \frac{s_5(\vec{r}_4 - \vec{r}_1)}{2\,A_3} + \\
\frac{s_1(\vec{r}_6 - \vec{r}_5)}{2\,A_4} + \frac{s_5(\vec{r}_1 - \vec{r}_6)}{2\,A_4} + \frac{s_6(\vec{r}_5 - \vec{r}_1)}{2\,A_4} + \\
\frac{s_1(\vec{r}_7 - \vec{r}_6)}{2\,A_5} + \frac{s_6(\vec{r}_1 - \vec{r}_7)}{2\,A_5} + \frac{s_7(\vec{r}_6 - \vec{r}_1)}{2\,A_5} + \\
\frac{s_1(\vec{r}_2 - \vec{r}_7)}{2\,A_6} + \frac{s_7(\vec{r}_1 - \vec{r}_2)}{2\,A_6} + \frac{s_2(\vec{r}_7 - \vec{r}_1)}{2\,A_6}
\end{array} \\
&\approx \sum_{n=1}^{N} s_n \sum_{j=1}^{W_n} \vec{v}_{nj}.
\end{aligned}
\tag{4.19}
$$

The element highlighted in red forms the new basis function $\sum_{j=1}^{W_n} \vec{v}_{nj}$ associated with the stream function at node $n = 1$, with $W_1 = 6$. A counter-clockwise orientation is chosen as the orientation for this basis, as shown in Figure 4.5b.

4.1.1.8 Magnetic vector potential matrix

The magnetic vector potential matrices $\underline{\underline{A}}_i$ can be calculated from equations (4.2) and (4.19) in the Lorentz gauge by

$$
\begin{aligned}
\vec{A}(\vec{r}_\mathrm{t}) &= \frac{\mu_0}{4\pi} \int_{\mathbb{R}^3} \frac{\vec{J}(\vec{r}_\mathrm{s})}{\|\vec{r}_\mathrm{t} - \vec{r}_\mathrm{s}\|} \,\mathrm{d}V_\mathrm{cond} \\
&\approx \sum_{n=1}^{N} s_n \frac{\mu_0}{4\pi} \int_{S_\mathrm{cond}} \sum_{j=1}^{W_n} \frac{\vec{v}_{nj}}{\|\vec{r}_\mathrm{t} - \vec{r}_\mathrm{s}\|} \,\mathrm{d}S_\mathrm{cond} \\
&\approx \sum_{n=1}^{N} s_n \vec{A}_n(\vec{r}_\mathrm{t}),
\end{aligned}
\tag{4.20}
$$

or in the Coulomb gauge by [22]

$$\begin{aligned}\vec{A}(\vec{r}_\mathrm{t}) &= \frac{\mu_0}{8\pi}\int\limits_{\mathbb{R}^3} \frac{\vec{J}(\vec{r}_\mathrm{s})}{\|\vec{r}_\mathrm{t}-\vec{r}_\mathrm{s}\|} + \frac{(\vec{r}_\mathrm{t}-\vec{r}_\mathrm{s})\left((\vec{r}_\mathrm{t}-\vec{r}_\mathrm{s})\cdot\vec{J}(\vec{r}_\mathrm{s})\right)}{\|\vec{r}_\mathrm{t}-\vec{r}_\mathrm{s}\|^3}\,\mathrm{d}V_\mathrm{cond} \\ &\approx \sum_{n=1}^{N} s_n \frac{\mu_0}{4\pi}\int\limits_{S_\mathrm{cond}} \sum_{j=1}^{W_n} \frac{\vec{v}_{nj}}{\|\vec{r}_\mathrm{t}-\vec{r}_\mathrm{s}\|} + \frac{(\vec{r}_\mathrm{t}-\vec{r}_\mathrm{s})\left((\vec{r}_\mathrm{t}-\vec{r}_\mathrm{s})\cdot\vec{v}_{nj}\right)}{\|\vec{r}_\mathrm{t}-\vec{r}_\mathrm{s}\|^3}\,\mathrm{d}S_\mathrm{cond} \\ &\approx \sum_{n=1}^{N} s_n \vec{A}_n(\vec{r}_\mathrm{t}),\end{aligned} \tag{4.21}$$

with $\vec{A}_n(\vec{r}_\mathrm{t})$ the magnetic vector potential produced at point $\vec{r}_\mathrm{t}$ by the stream function at the mesh node n.

The magnetic vector potential can be approximated on the target volume and expressed as matrices by

$$\vec{A} \approx \begin{pmatrix} \underline{\underline{A}}_x \\ \underline{\underline{A}}_y \\ \underline{\underline{A}}_z \end{pmatrix} \vec{s}, \tag{4.22}$$

with $\underline{\underline{A}}_i \in \mathbb{R}^{Z\times N}$ containing the respective components of $\vec{A}_n(\vec{r}_\mathrm{t})$ for all target points. The target point has to be chosen as not belonging to S_cond, as the expression is singular for such points.

4.1.1.9 Magnetic flux-density matrix

Using equation (4.2) the magnetic flux-density can be approximated by

$$\begin{aligned}\vec{B}(\vec{r}_\mathrm{t}) &= \frac{\mu_0}{4\pi}\int\limits_{\mathbb{R}^3} \vec{\nabla}\times\frac{\vec{J}(\vec{r}_\mathrm{s})}{\|\vec{r}_\mathrm{t}-\vec{r}_\mathrm{s}\|^3}\,\mathrm{d}V_\mathrm{cond} \\ &\approx \sum_{n=1}^{N} s_n \frac{\mu_0}{4\pi}\int\limits_{S_\mathrm{cond}} \vec{\nabla}\times\sum_{j=1}^{W_n}\frac{\vec{v}_{nj}}{\|\vec{r}_\mathrm{t}-\vec{r}_\mathrm{s}\|^3}\,\mathrm{d}S_\mathrm{cond} \\ &\approx \sum_{n=1}^{N} s_n \vec{B}_n(\vec{r}_\mathrm{t}).\end{aligned} \tag{4.23}$$

with $\vec{B}_n(\vec{r}_\mathrm{t})$ the magnetic flux-density produced at point $\vec{r}_\mathrm{t}$ by the stream function at the mesh node n.

The relation (4.23) can be split into its three components, giving one matrix per compo-

nent:

$$B_x(\vec{r}_\mathrm{t}) \approx \sum_{n=1}^{N} s_n \frac{\mu_0}{4\pi} \int\limits_{S_\mathrm{cond}} \sum_{j=1}^{W_n} \frac{(\vec{v}_{nj}\cdot\vec{e}_z)((\vec{r}_\mathrm{t}-\vec{r}_\mathrm{s})\cdot\vec{e}_y) - (\vec{v}_{nj}\cdot\vec{e}_y)((\vec{r}_\mathrm{t}-\vec{r}_\mathrm{s})\cdot\vec{e}_z)}{\|\vec{r}_\mathrm{t}-\vec{r}_\mathrm{s}\|^3}\,\mathrm{d}S_\mathrm{cond}$$

$$\approx \sum_{n=1}^{N} s_n B_{xn}(\vec{r}_\mathrm{t}), \tag{4.24}$$

$$B_y(\vec{r}_\mathrm{t}) \approx \sum_{n=1}^{N} s_n \frac{\mu_0}{4\pi} \int\limits_{S_\mathrm{cond}} \sum_{j=1}^{W_n} \frac{(\vec{v}_{nj}\cdot\vec{e}_x)((\vec{r}_\mathrm{t}-\vec{r}_\mathrm{s})\cdot\vec{e}_z) - (\vec{v}_{nj}\cdot\vec{e}_z)((\vec{r}_\mathrm{t}-\vec{r}_\mathrm{s})\cdot\vec{e}_x)}{\|\vec{r}_\mathrm{t}-\vec{r}_\mathrm{s}\|^3}\,\mathrm{d}S_\mathrm{cond}$$

$$\approx \sum_{n=1}^{N} s_n B_{yn}(\vec{r}_\mathrm{t}), \tag{4.25}$$

$$B_z(\vec{r}_\mathrm{t}) \approx \sum_{n=1}^{N} s_n \frac{\mu_0}{4\pi} \int\limits_{S_\mathrm{cond}} \sum_{j=1}^{W_n} \frac{(\vec{v}_{nj}\cdot\vec{e}_y)((\vec{r}_\mathrm{t}-\vec{r}_\mathrm{s})\cdot\vec{e}_x) - (\vec{v}_{nj}\cdot\vec{e}_x)((\vec{r}_\mathrm{t}-\vec{r}_\mathrm{s})\cdot\vec{e}_y)}{\|\vec{r}_\mathrm{t}-\vec{r}_\mathrm{s}\|^3}\,\mathrm{d}S_\mathrm{cond}$$

$$\approx \sum_{n=1}^{N} s_n B_{zn}(\vec{r}_\mathrm{t}), \tag{4.26}$$

with $B_{in}(\vec{r}_\mathrm{t})$ the magnetic flux-density in the direction i produced at point $\vec{r}_\mathrm{t}$ by the stream function at the mesh node n.

The magnetic flux-density can be approximated on the target volume and expressed as matrices by

$$\vec{B} \approx \begin{pmatrix} \underline{\underline{B}}_x \\ \underline{\underline{B}}_y \\ \underline{\underline{B}}_z \end{pmatrix} \vec{s}, \tag{4.27}$$

with the magnetic flux-density matrices $\underline{\underline{B}}_i \in \mathbb{R}^{Z\times N}$ containing the respective components of $\vec{B}_i(\vec{r}_\mathrm{t})$ for all target points. The target points have to be chosen as not belonging to S_cond, as the expression is singular for such points.

4.1.1.10 Inductance matrix

Using equation (4.6), the mutual inductance between nodes m and n on surfaces S_m and S_n, which can be the same, can be expressed by

$$\begin{aligned} M_{mn} &= \frac{\mu_0}{4\pi} \int_{V_1} \int_{V_2} \frac{\vec{J}_m(\vec{r}_1) \cdot \vec{J}_n(\vec{r}_2)}{\|\vec{r}_1 - \vec{r}_2\|} \mathrm{d}V_2 \mathrm{d}V_1 \\ &\approx s_m s_n \left[\left(\sum_{k=1}^{W_m} \vec{v}_{mk} \right) \cdot \left(\sum_{j=1}^{W_n} \vec{v}_{nj} \right) \right] \frac{\mu_0}{4\pi} \int_{S_m} \int_{S_n} \frac{1}{\|\vec{r}^m - \vec{r}^n\|} \mathrm{d}S_n \mathrm{d}S_m, \end{aligned} \tag{4.28}$$

with surfaces S_m and S_n discretised into N_m and N_n nodes, each connected to W_m and W_n triangle, which are the support for point $\vec{r}^m$ and $\vec{r}^n$ and basis vectors $\vec{v}_{mk}$ and $\vec{v}_{nj}$, respectively.

The stored energy by the system can thus be approximated and expressed as a matrix by

$$E_{\text{stored}} = \frac{1}{2} \vec{s}^\top \underline{\underline{M}} \vec{s}, \tag{4.29}$$

with the mutual inductance matrix $\underline{\underline{M}} \in \mathbb{R}^{N_m \times N_n}$ containing the components M_{mn} for all points of the modelled surfaces. If the surface S_n and S_m are the same, the diagonal elements of $\underline{\underline{M}}$ are the self-inductance of the surface elements. Otherwise, the element of $\underline{\underline{M}}$ are the mutual inductance between the surface elements, with $M_{mn} = M_{nm}$. Moreover, $\underline{\underline{M}}$ is positive definite [10].

4.1.1.11 Resistance matrix

Using equation (4.8), the mutual resistance between nodes m and n exist only when both nodes share a common basis. In this case, it is expressed as

$$\begin{aligned} R_{mn} &= \int_S \frac{\rho\, \widehat{\vec{J}}_m(\vec{r}) \cdot \widehat{\vec{J}}_n(\vec{r})}{d(\vec{r})} \mathrm{d}S \\ &\approx s_m s_n \frac{\rho}{d} \int_S \left(\sum_{k=1}^{W} \vec{v}_{mk} \right) \cdot \left(\sum_{j=1}^{W} \vec{v}_{nj} \right) \mathrm{d}S \end{aligned} \tag{4.30}$$

with surfaces S discretised into N nodes, each connected to W triangles, which are both the support for basis vectors $\vec{v}_{mk}$ and $\vec{v}_{nj}$.

The dissipated energy can thus be approximated and expressed as a matrix by

$$P_{\text{dis}} = \vec{s}^\top \underline{\underline{R}} \vec{s}, \tag{4.31}$$

with the mutual resistance matrix $\underline{\underline{R}} \in \mathbb{R}^{N \times N}$ containing the components R_{mn} for all points of the modelled surfaces. Moreover, $\underline{\underline{R}}$ is positive semi-definite [10].

Figure 4.6: Representation of the transformation from a flat triangle in the general coordinate system to the unit triangle.

4.1.1.12 Laplacian matrix

Taking into account the stream function representation, the Laplacian of the surface current density is replaced by the calculation of the Laplacian of the stream function at the point m by [111]

$$\begin{aligned}\mathscr{L}\psi(\vec{r}_m) &= \frac{1}{4\pi h^2}\sum_{l=1}^{K}\frac{A_{\text{tri}}(l)}{3}\sum_{n=1}^{N} e^{-\frac{\|\vec{r}_n-\vec{r}_m\|}{4h}}(\psi(\vec{r}_n)-\psi(\vec{r}_m)) \\ &\approx \frac{1}{4\pi h^2}\sum_{l=1}^{K}\frac{A_{\text{tri}}(l)}{3}\sum_{n=1}^{N} e^{-\frac{\|\vec{r}_n-\vec{r}_m\|}{4h}}(s_n-s_m),\end{aligned} \tag{4.32}$$

with h being a positive quantity related to the size of the neighbourhood and K the number of triangular elements on a mesh.

The Laplacian of the stream function for each node on the surface S can approximated and expressed by

$$\vec{L}_S \approx \underline{\underline{L}}_S\vec{s}. \tag{4.33}$$

with the Laplacian matrix $\underline{\underline{L}}_S \in \mathbb{R}^{N\times N}$. The resulting Laplacian vector $\vec{L}_S$ can then be used to influence the curvature of the current path.

4.1.1.13 Well-behaved integrals

The magnetic vector potential matrix $\underline{\underline{A}}_i$, the magnetic flux-density matrix $\underline{\underline{B}}_i$ and the mutual inductance matrix $\underline{\underline{M}}$ have to be evaluated on triangular elements. The Gauss-Legendre quadrature is estimated on the unit triangle T_{u}, defined by equation (4.16), as described in [112]. The function is then transformed from the unit triangle to the general

coordinate system, as shown in Figure 4.6. The integral is thus defined by

$$\begin{aligned} I &= \int_S f(\vec{r})\mathrm{d}S \\ &= \det(\underline{\underline{J}}) \int_{T_\mathrm{u}} f(\vec{r}(u,v))\mathrm{d}T_\mathrm{u} \\ &= 2\,A_\mathrm{tri} \int_{T_\mathrm{u}} f(\vec{r}(u,v))\mathrm{d}T_\mathrm{u} \\ &\approx 2\,A_\mathrm{tri} \sum_{k=1}^{n\times n} c_k f(\vec{r}_k(u_k,v_k)) \end{aligned} \tag{4.34}$$

with c_k the weighting factor associated with the point (u_k, v_k) and $\det(\underline{\underline{J}})$ the determinant of the transformation Jacobian. Rathod et al. [112] used a reformulation on a unit square and defined the weighting and the evaluation points by

$$c_k = \frac{1-u_i}{8} w_i\, w_j \tag{4.35}$$

$$u_k = \frac{1+u_i}{2} \tag{4.36}$$

$$v_k = \frac{(1-u_i)(1+u_j)}{4} \tag{4.37}$$

with $(k = 1, 2, \ldots, 2n)$ and $(i, j = 1, 2, \ldots, n)$ and w_i and w_j the weighting associated to the one dimensional Gaussian points u_i and u_j. Note that the Jacobian of the transformation associated with the unit square is already included in the calculation of the weight. The Gaussian points and weight are obtained according to [113].

The transformation from the unit triangle into the flat triangle in the general coordinate system, as pictured in Figure 4.6, is used to evaluate $\vec{r}_k(u_k, v_k)$ by

$$\begin{aligned} r_x &= x_{P_1}\, u + x_{P_2}\, v + x_{P_3}\,(1-u-v) \\ r_y &= y_{P_1}\, u + y_{P_2}\, v + y_{P_3}\,(1-u-v) \\ r_z &= z_{P_1}\, u + z_{P_2}\, v + z_{P_3}\,(1-u-v). \end{aligned} \tag{4.38}$$

To evaluate the integrals, the points (u_k, v_k) are evaluated according to the desired maximal order $n \times n$ along with the weighting c_k. The coordinates of the corresponding points $\vec{r}_k(u_k, v_k)$ are then obtained via equations (4.38) and used to evaluate the function $f(\vec{r}_k(u_k, v_k))$ to be integrated.

4.1.1.14 Weakly-singular double integral for M_{mn}

In order to evaluate the mutual inductance matrices $\underline{\underline{L}}$, integrals with the form

$$I = \int_{S_m}\int_{S_n} \frac{1}{\|\vec{r}^m - \vec{r}^n\|}\mathrm{d}S_n\mathrm{d}S_m, \tag{4.39}$$

have to be evaluated. For the self-inductance, that is for $m = n$, this function is singular since the kernel of the integrand $\|\vec{r}^m - \vec{r}^n\|^{-1}$ reaches infinity. Comparing the integrand $\|\vec{r}^m - \vec{r}^n\|^{-\alpha}$ order α with the dimension of $\vec{r} \in \mathbb{R}^3$, it can be noted that $\alpha = 1 < 3$ making this integral weakly-singular [110]. An analytical solution can be used to evaluate this integral [114, 12] as

$$\begin{aligned}\frac{I}{4\,A_{\text{tri}}} =& \frac{1}{6\sqrt{a}}\log\left(\frac{(a-b+\sqrt{a}\sqrt{a-2b+c})(b+\sqrt{a}\sqrt{c})}{(-b+\sqrt{a}\sqrt{c})(-a+b+\sqrt{a}\sqrt{a}-2b+c)}\right)+\\ &\frac{1}{6\sqrt{c}}\log\left(\frac{(b+\sqrt{a}\sqrt{c})(-b+c+\sqrt{c}\sqrt{a-2b+c})}{(b-c+\sqrt{c}\sqrt{a-2b+c})(-b+\sqrt{a}\sqrt{c})}\right)+\\ &\frac{1}{6\sqrt{a-2b+c}}\log\left(\frac{(a-b+\sqrt{a}\sqrt{a-2b+c})(-b+c+\sqrt{c}\sqrt{a-2b+c})}{(b-c+\sqrt{c}\sqrt{a-2b+c})(-a+b+\sqrt{a}\sqrt{a-2b+c})}\right),\end{aligned} \tag{4.40}$$

with

$$a = (\vec{r}_{P_3} - \vec{r}_{P_1}) \cdot (\vec{r}_{P_3} - \vec{r}_{P_1}) \tag{4.41}$$

$$b = (\vec{r}_{P_3} - \vec{r}_{P_1}) \cdot (\vec{r}_{P_3} - \vec{r}_{P_2}) \tag{4.42}$$

$$c = (\vec{r}_{P_3} - \vec{r}_{P_2}) \cdot (\vec{r}_{P_3} - \vec{r}_{P_2}). \tag{4.43}$$

4.1.1.15 Inverse problem

To obtain the stream function on the surface S_{Cond}, the forward problem defined by equation (4.2) has to be inverted. This problem, which can be expressed via the magnetic flux-density matrix as a linear system of equation, is ill-posed according to definition 1, as the solution is not unique. In this work, two different approaches are used to solve the inverse problem. For the direct minimisation of the field error, the problem is posed as a regularised least-square problem using a Tikhonov regularisation. For minimisation problems involving positive semi-definite and definite matrices, as the resistance or inductance matrices, a quadratic programming problem is formulated.

4.1.1.16 Regularised least-square

Considering relations (4.27), a regularised least-square problem using a Tikhonov regularisation is posed [47] as

$$\min_s\{\|\vec{B} - \vec{B}_{\text{target}}\|^2 + \lambda^2\|\underline{\underline{\Gamma}}\vec{s}\|^2\}, \tag{4.44}$$

with $\underline{\underline{\Gamma}} \in \mathbb{R}^{N\times N}$ the Tikhonov matrix. The Tikhonov matrix gives a preference to solutions based on the norm of the linear relation $\underline{\underline{\Gamma}}\vec{s}$. When using the matrix $\underline{\underline{L}}_S$ as the

Tikhonov matrix, the stream function will look smoother. When using the identity matrix as the Tikhonov matrix, the solution with a small norm will be preferred. The factor λ is called the regularisation parameter and is chosen experimentally. This means that the surface current density to be built is not necessarily the best mathematical solution of the minimisation problem. A specialised Matlab (7.11.0, Mathworks, USA) toolbox [115, 116] has been used to solve the minimisation problem (4.44).

4.1.1.17 Quadratic programming

The optimisation problem can also be posed as a quadratic programming problem with quadratic constrains (QPQC). This will be, for example, the minimisation of the stored energy, while keeping $\vec{B}$ into a 10 % error margin compared to $\vec{B}_{\text{target}}$ and having dissipated power below 1000 W. This can be written as

$$\begin{aligned} \min_s \quad & \frac{1}{2}\vec{s}^{\intercal}\underline{\underline{M}}\vec{s} \\ \text{subject to:} \quad & 0.9\,\vec{B}_{\text{target}} \leq \begin{pmatrix} \underline{\underline{B}}_x \\ \underline{\underline{B}}_y \\ \underline{\underline{B}}_z \end{pmatrix} \vec{s} \leq 1.1\,\vec{B}_{\text{target}} \\ & \vec{s}^{\intercal}\underline{\underline{R}}\vec{s} \leq 1000 \end{aligned} \tag{4.45}$$

and solved using Matlab toolboxes OPTI TOOLBOX [117] or YALMIP [118] and the solver IPOPT [119].

4.1.1.18 Wire approximation

To approximate ψ as the centroid of a single wire, a set of centroids has to be extracted first. According to the number of loops $N_{\text{loops}} \in \mathbb{N}^+$, the corresponding ψ level for each loop is defined by

$$\Delta_s = \frac{\max(\vec{s}) - \min(\vec{s})}{N_{\text{loops}}}. \tag{4.46}$$

The different centroids are then obtained by

$$s_n = \min(\vec{s}) + (n - \frac{1}{2})I_c \qquad n = 1, \ldots, N_{\text{loops}}. \tag{4.47}$$

An example is the dashed red lines in Figure 4.3.

4.1.1.19 Influence of shield

The quasi-static approximation used in the model describing the magnetic field neglects the effect of time-varying magnetic fields. As different elements made of conductive

materials, like high-frequencies shields or other coils, are positioned in the direct vicinity of the coils, the influence of induced current in those elements should be evaluated. The methods presented here have been previously published in [O2] and are similar to the method described by Sanchez et al. [120].

Considering the surface S_{cond} on which the current density represented via $\vec{s}_{\text{cond}}$ is generated, the induced current density represented via $\vec{s}_{\text{ind}}$ on surface S_{ind} has to be determined. The mutual inductance and resistance matrices $\underline{\underline{M}}$ and $\underline{\underline{R}}$ can be partitioned as

$$\underline{\underline{M}} = \begin{bmatrix} \underline{\underline{M}}_{\text{c}} & \underline{\underline{M}}_{\text{ci}} \\ \underline{\underline{M}}_{\text{ic}} & \underline{\underline{M}}_{\text{i}} \end{bmatrix}, \tag{4.48}$$

and

$$\underline{\underline{R}} = \begin{bmatrix} \underline{\underline{R}}_{\text{c}} & 0 \\ 0 & \underline{\underline{R}}_{\text{i}} \end{bmatrix}, \tag{4.49}$$

with $\underline{\underline{M}}_{\text{c}}$ and $\underline{\underline{R}}_{\text{c}}$ the mutual inductance and resistance matrix associated with the surface S_{cond} and $\underline{\underline{M}}_{\text{i}}$ and $\underline{\underline{R}}_{\text{i}}$ the mutual inductance and resistance matrix associated with the surface S_{ind}. $\underline{\underline{M}}_{\text{ci}}$ and $\underline{\underline{M}}_{\text{ic}}$ are the mutual inductance matrices between both surfaces with $\underline{\underline{M}}_{\text{ci}} = \underline{\underline{M}}_{\text{ic}}^{\top}$.

The time dependency of $\vec{s}_{\text{cond}}$ is modelled as a sinusoidal signal by the function

$$\vec{s}_{\text{c}}(t) = \vec{s}_{\text{cond}} \sin(\omega t) \tag{4.50}$$

with the angular frequency $\omega = 2\pi f$.

The time-varying functions $\vec{s}_{\text{i}}(t)$ associated with $\vec{s}_{\text{ind}}$ will depend on $\vec{s}_{\text{c}}(t)$, $\underline{\underline{M}}_{\text{is}}$, $\underline{\underline{M}}_{\text{i}}$ and $\underline{\underline{R}}_{\text{i}}$ according to the law of conservation of energy [10]. The dependency can be written as

$$\underline{\underline{M}}_{\text{is}} \frac{d\vec{s}_{\text{c}}}{dt} + \underline{\underline{M}}_{\text{i}} \frac{d\vec{s}_{\text{i}}}{dt} + \underline{\underline{R}}_{\text{i}} \vec{s}_{\text{i}} = 0. \tag{4.51}$$

This relation describes the voltage across the mutual inductance of the two meshes due to the source current as the sum of the voltage across the inductance of the shield and the voltage across the electrical resistance of the shield.

Equation (4.51) can be rewritten as a standard differential equation

$$\underline{\underline{M}}_{\text{i}} \frac{d\vec{s}_{\text{i}}}{dt} = -\underline{\underline{R}}_{\text{i}} \vec{s}_{\text{i}} - \underline{\underline{M}}_{\text{is}} \frac{d\vec{s}_{\text{c}}}{dt}, \tag{4.52}$$

thus

$$\frac{d\vec{s}_{\text{i}}}{dt} = -\underline{\underline{M}}_{\text{i}}^{-1} \underline{\underline{R}}_{\text{i}} \vec{s}_{\text{i}} - \underline{\underline{M}}_{\text{i}}^{-1} \underline{\underline{M}}_{\text{is}} \frac{d\vec{s}_{\text{c}}}{dt}. \tag{4.53}$$

To solve (4.53), the matrix $\underline{\underline{M}}_{\text{i}}^{-1} \underline{\underline{R}}_{\text{i}}$ is diagonalised as

$$\underline{\underline{M}}_{\text{i}}^{-1} \underline{\underline{R}}_{\text{i}} = \underline{\underline{Q}} \underline{\underline{\Lambda}} \underline{\underline{Q}}^{-1}, \tag{4.54}$$

with $\underline{\underline{Q}}$ the matrix formed by the eigenvectors and $\underline{\underline{\Lambda}}$ the diagonal matrix formed with the eigenvalues λ. Equation (4.54) is then used in equation (4.53) to obtain

$$\frac{d\vec{s}_\mathrm{i}}{dt} = -\underline{\underline{Q}}\underline{\underline{\Lambda}}\underline{\underline{Q}}^{-1}\vec{s}_\mathrm{i} - \underline{\underline{M}}_\mathrm{i}^{-1}\underline{\underline{M}}_\mathrm{is}\frac{d\vec{s}_\mathrm{c}}{dt}, \tag{4.55}$$

$$\underline{\underline{Q}}^{-1}\frac{d\vec{s}_\mathrm{i}}{dt} = -\underline{\underline{\Lambda}}\underline{\underline{Q}}^{-1}\vec{s}_\mathrm{i} - \underline{\underline{Q}}^{-1}\underline{\underline{M}}_\mathrm{i}^{-1}\underline{\underline{M}}_\mathrm{ic}\frac{d\vec{s}_\mathrm{c}}{dt}. \tag{4.56}$$

The variable $\underline{\underline{Q}}^{-1}\vec{s}_\mathrm{i}$ can be substituted by $\vec{y}_\mathrm{i}$, and the product $-\underline{\underline{Q}}^{-1}\underline{\underline{M}}_\mathrm{i}^{-1}\underline{\underline{M}}_\mathrm{ic}$ can be replaced by the matrix $\underline{\underline{P}}$, which leads to

$$\frac{d\vec{y}_\mathrm{i}}{dt} = -\underline{\underline{\Lambda}}\vec{y}_\mathrm{i} + \underline{\underline{P}}\frac{d\vec{s}_\mathrm{c}}{dt}. \tag{4.57}$$

Using the variation of parameters, a solution to (4.57) can be found as

$$\vec{y}_\mathrm{i}(t) = e^{-\underline{\underline{\Lambda}}t}\vec{y}_\mathrm{i}(t_0) + e^{-\underline{\underline{\Lambda}}t}\int_{t_0}^{t} e^{\underline{\underline{\Lambda}}\tau} + \underline{\underline{P}}\frac{d\vec{s}_\mathrm{c}}{d\tau}d\tau, \tag{4.58}$$

with t_0 as the time at which the current starts to flow in the coil. Using the $\vec{s}_\mathrm{i}$ variable, (4.58) can be written as

$$\vec{s}_\mathrm{i}(t) = \underline{\underline{Q}}e^{-\underline{\underline{\Lambda}}t}\underline{\underline{Q}}^{-1}\vec{s}_\mathrm{i}(t_0) + \underline{\underline{Q}}e^{-\underline{\underline{\Lambda}}t}\int_{t_0}^{t} e^{\underline{\underline{\Lambda}}\tau} + \underline{\underline{P}}\frac{d\vec{s}_\mathrm{c}(\tau)}{d\tau}d\tau. \tag{4.59}$$

Assuming that the current density in the shield at $t_0 = 0$ is zero, substituting the relation (4.50) into (4.59) leads to

$$\vec{s}_\mathrm{i}(t) = \underline{\underline{Q}}\int_0^t e^{-\underline{\underline{\Lambda}}(t-\tau)}\frac{d\sin(\omega\,\tau)}{d\tau}d\tau\,\underline{\underline{P}}\vec{s}_\mathrm{cond}. \tag{4.60}$$

This expression can be simplified by defining

$$a_k(t) = \int_0^t e^{-\lambda_k(t-\tau)}\frac{d\sin(\omega\,\tau)}{d\tau}d\tau, \tag{4.61}$$

for $k = 1, \ldots, N_\mathrm{i}, t \geq t_0$, which is equivalent to

$$a_k(t) = \frac{-\omega\lambda_k e^{-\lambda_k t}}{\omega^2 + \lambda_k^2}\ldots \tag{4.62}$$

$$+\frac{\omega\lambda_k\cos(\omega t)}{\omega^2 + \lambda_k^2}\ldots \tag{4.63}$$

$$+\frac{\omega^2\sin(\omega t)}{\omega^2 + \lambda_k^2}. \tag{4.64}$$

Equation (4.60) can thus be rewritten as

$$\vec{s}_\mathrm{i}(t) = \underline{\underline{Q}}\,\mathrm{diag}(a_1(t), \ldots, a_{N_\mathrm{i}}(t))\,\underline{\underline{P}}\vec{s}_\mathrm{cond}. \tag{4.65}$$

It has to be noted that, after a few periods, the term (4.62) can be neglected and thus $\vec{s}_{\mathrm{i}}(t)$ can be expressed as

$$\vec{s}_{\mathrm{i}}(t) = \vec{s}_{\mathrm{iCos}} \cos(\omega t) + \vec{s}_{\mathrm{iSin}} \sin(\omega t), \tag{4.66}$$

with

$$\vec{s}_{\mathrm{iCos}} = \underline{\underline{Q}}\ \mathrm{diag}\left(\frac{\omega\lambda_1}{\omega^2+\lambda_1^2}, \cdots, \frac{\omega\lambda_{N_{\mathrm{i}}}}{\omega^2+\lambda_{N_{\mathrm{i}}}^2}\right) \underline{\underline{P}}\vec{s}_{\mathrm{cond}}, \tag{4.67}$$

$$\vec{s}_{\mathrm{iSin}} = \underline{\underline{Q}}\ \mathrm{diag}\left(\frac{\omega^2}{\omega^2+\lambda_1^2}, \cdots, \frac{\omega^2}{\omega^2+\lambda_{N_{\mathrm{i}}}^2}\right) \underline{\underline{P}}\vec{s}_{\mathrm{cond}}. \tag{4.68}$$

Thus, in the shield will flow a time dependent current density having sine and cosine components. For a given coil stream function $\vec{s}_{\mathrm{cond}}$, the geometry and the frequency play a role in the amplitude of the induced stream function.

4.1.2 Results

In this Subsection, 6 coil designs are realised with different levels of refinement, ranging from a fully designed, built and characterised set of drive coils to a didactic example of a pig-shaped drive coil. The work flow associated with the implementation of this technique is detailed in Appendix F.

4.1.2.1 2D drive coil set for a rabbit system

The 2D drive coil set for a rabbit-sized MPI scanner is designed to have a free cylinder diameter of 173 mm. The design is kept as compact as possible to limit the challenge presented by the design of other coils around it. Different views of the final design can be seen in Figure 6.4. This design is the result of an iterative process, from which only the final iteration results are presented.

The innermost coil is designed on a cylindrical surface with a diameter of 200 mm and a length of 400 mm, as seen on Figure 4.7. The target field B_{target} is defined in a sphere of diameter 50 mm centred on the cylindrical surface. This sphere is discretised into 515 points which are placed on a grid, with a distance of 5 mm between each point on each direction. $\vec{B}_{\mathrm{target}}$ is defined as an ideal field with the single non-zero SHC $c_{x00}^{0.05} = 15$ mT.

The stream-function values are then obtained using a Tikhonov regularisation scheme with the Tikhonov matrix taken as the identity with the regularisation parameter $\lambda = 4.75 \cdot 10^{-6}$. Using this parameter, the stream function is described on the mesh by two areas, as seen in Figure 4.7a, with either positive or negative values. Approximating the stream function with 18 loops, a minimal distance between two loops of 8.9 mm and an extension in the z direction of 250.6 mm are obtained. This design can be seen in

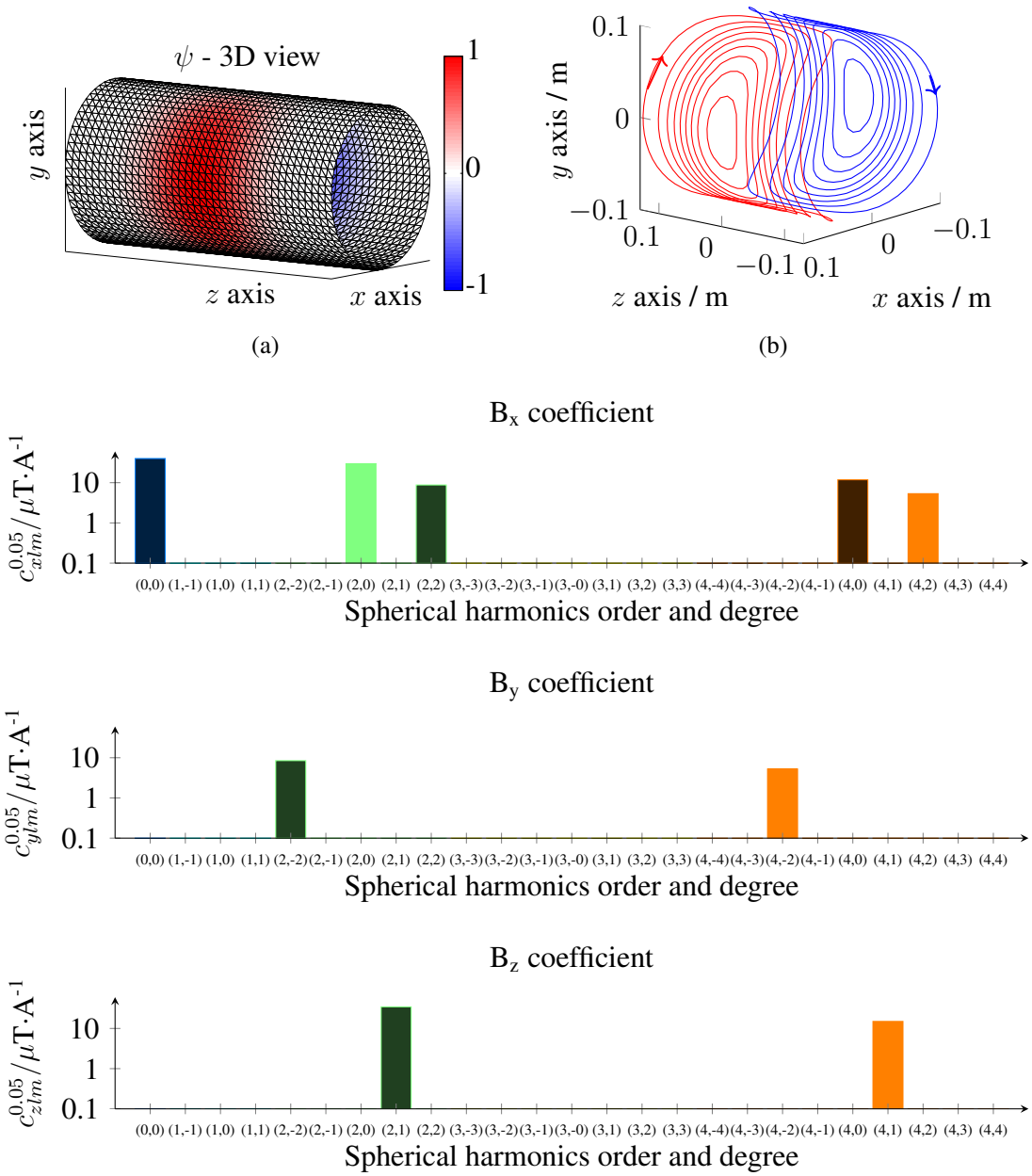

Figure 4.7: x-drive coil design. (a) Chosen normalised stream function on a cylinder with a diameter of 200 mm. (b) Extraction of 18 isolines from the stream function and representation in 3D. The arrows shows the direction in which the current flows. (c) SHSE up to degree $l = 10$ and order $m = 10$ and display up to $m = l = 4$ in a sphere with radius $R = 0.05$ m. Darker filling color indicates a negative coefficient.

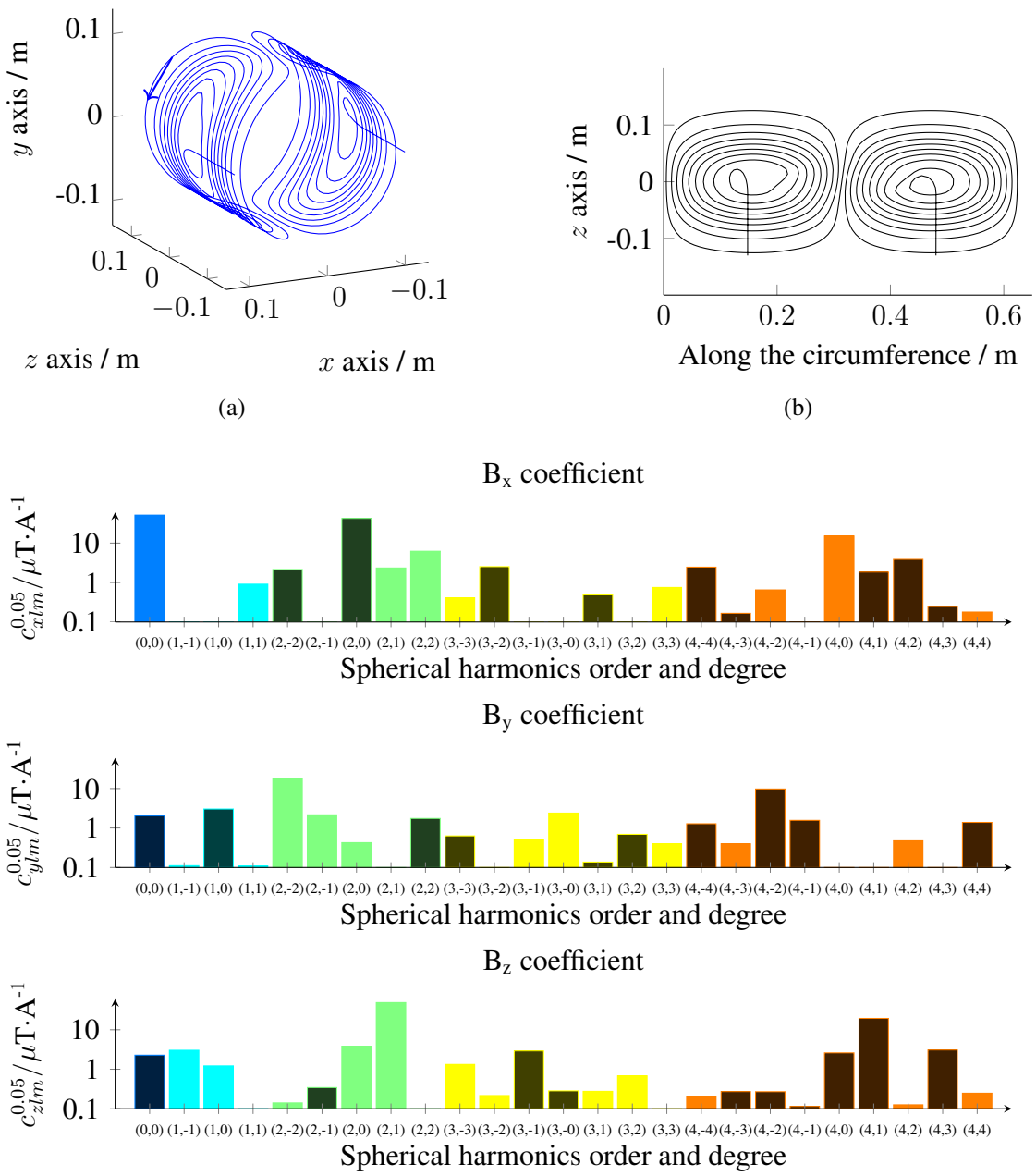

Figure 4.8: Detailed information on the x-drive coil after the connection of each ideal centroid, which forms a single-wire path. (a) 3D view of the wire centroid. The arrow shows the direction in which the current flows. (b) Flat projection of the centroid. (c) SHSE up to degree $l = 10$ and order $m = 10$ and display up to $m = l = 4$ in a sphere with radius $R = 0.05$ m. Darker filling color indicates a negative coefficient.

Figure 4.7b. Using wire loops and the Biot-Savart law (2.17), the main SHC $c_{x00}^{0.05} = 51.2\,\mu\text{T}\cdot\text{A}^{-1}$ is calculated.

Connecting all the loops to obtain a wire path, a single wire with a length of 11.2 m is required to wind this coil, as shown in Figures 4.8a and 4.8b. Using the software FastHenry (FastHenry 3.32, FastFieldSolvers S.R.L, Italy) [121], an inductance of 26.7 μH is calculated. The SHCs of this design can also be evaluated, and the results are presented in Figure 4.8c. The main SHC is slightly reduced to $c_{x00}^{0.05} = 51.1\,\mu\text{T}\cdot\text{A}^{-1}$, and the value of the others SHCs are higher. Especially, SHCs $c_{y00}^{0.05}$ and $c_{z00}^{0.05}$ are increased to 1.4 and 3.0 $\mu\text{T}\cdot\text{A}^{-1}$, respectively. This x-drive coil will thus move any LFV in all three directions of space, not only in one, and will generate a field topology more complex than an idealised coil.

The same procedure is done for the outer coil on a cylinder with a diameter of 238 mm and a length of 400 mm. The target field is defined in the same sphere via the single non-zero SHC $c_{y00}^{0.05} = 15$ mT.

Using a Tikhonov regularisation scheme with the regularisation parameter $\lambda = 1 \cdot 10^{-2}$, 20 loops are obtained from the stream function. The same minimal distance of 8.9 mm between the loops is obtained with a maximal extension in the z-direction of 266.7 mm. This design can be seen in Figure B.3. The main SHC $c_{y00}^{0.05} = 39.9\,\mu\text{T}\cdot\text{A}^{-1}$ is calculated.

Making a single-wire path from the loops, an inductance of 29.3 μH and a wire length of 12.5 m are obtained. The results are shown in Figure B.4. The main SHC is reduced to $c_{y00}^{0.05} = 39.5\,\mu\text{T}\cdot\text{A}^{-1}$, and the value of the others SHCs are higher. Especially, SHCs $c_{y00}^{0.05}$ and $c_{z00}^{0.05}$ are increased to 1.5 and 2.6 $\mu\text{T}\cdot\text{A}^{-1}$, respectively. As for the x-drive coil, the y-drive coil will move the LFV in all three directions of space.

4.1.2.2 Shielding of the 2D drive-coil set for a rabbit system

To protect the measurement volume from external perturbations, a copper plate shielding magnetic fields varying with high frequencies is installed around the set of drive coils. Thus, perturbation from the environment and the other coils are prevented. Due to the time variation of the magnetic fields produced by the coil, a current density will be induced in the shield, which will also reduce the coil efficiency η_{coil}. The y-drive coil being closer to the shield, the reduction of its efficiency and field topology is studied using the method presented in Section 4.1.1.19 and validated with an finite element method (FEM) simulation using COMSOL Multiphysics (COMSOL Inc, USA). Those results have been published in [O2]. For both methods the main SHC c_{y00}^{R} have been calculated, for the DC case and with a frequency of 25 kHz using equation (4.66). For FEM simulation, the

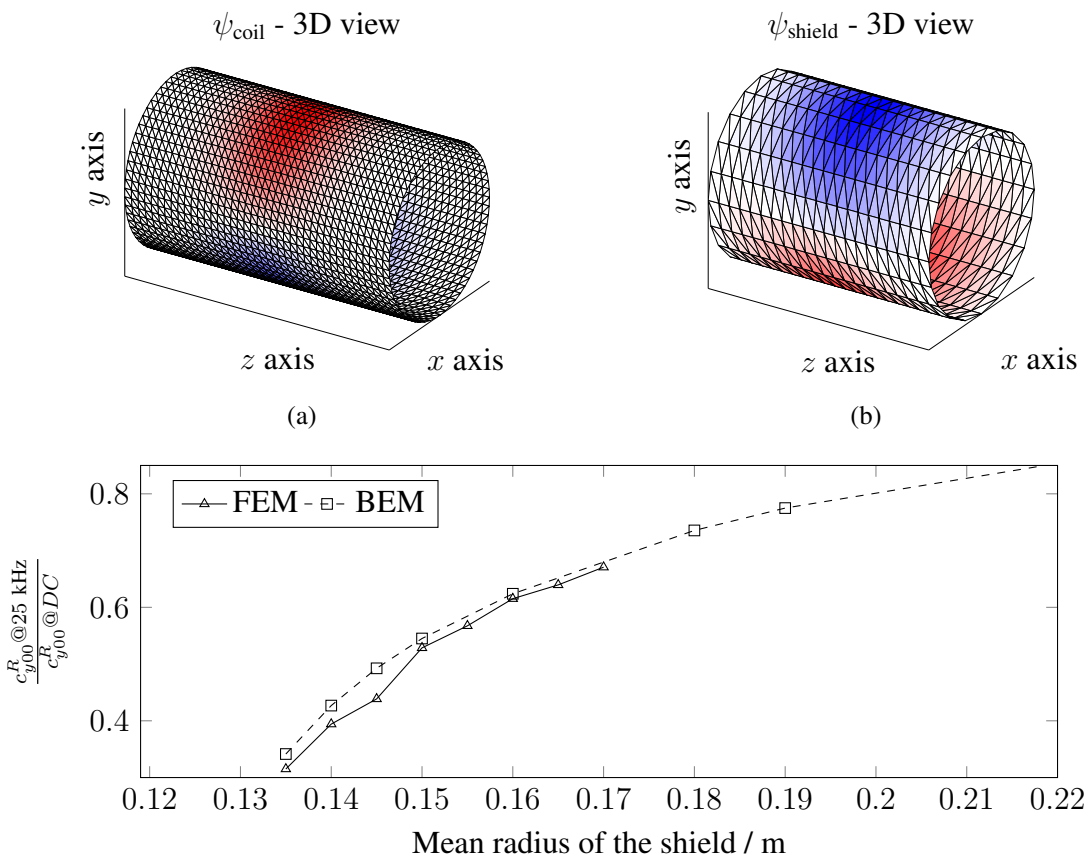

Figure 4.9: Simulation of the shield effect of a copper cylinder placed around a drive coil. (a) Stream function associated with the coil, which is multiplied by a sinusoidal function with a frequency of 25 kHz. (b) Induced stream function on the surface of a shield with a radius of 160 mm. (c) Main SHC c^R_{y00} reduction of a drive coil designed on a cylinder with a radius of 119 mm due to a 2 mm thick copper shield cylinder with a diameter varying from 135 to 220 mm.

shield is modelled as a 2 mm thick copper tube, with a length of 400 mm in z and diameter varying from 135 to 220 mm with mesh elements, which are smaller than the skin depth. For BEM results, the associated resistance is calculated for a cylinder of thickness 4δ, when this value is smaller than the actual shield thickness.

Figure 4.9 presents the stream function of the y-drive coil on a cylinder with a 119 mm radius, which is multiplied by a sine with a frequency of 25 kHz. The induced stream function for a cylinder with a radius of 160 mm shown in Figure 4.9b is then multiplied by a sum formed from a cosine and sine part, as described by equation (4.66). Since the

cosine part has an amplitude 173 times smaller than the sine part, it is further neglected. The top part of stream function associated with the drive coil has a positive amplitude, whereas the induced stream function on the shield has a negative stream function, thus effectively suppressing a part of the field inside the cylinder and the whole field outside of it. This effectively shields the magnetic field outside of the cylinder.

The choice of the shield diameter for the rabbit-sized scanner presented in Section 6.1 is done with the help of the curve presented in Figure 4.9c. It can first be seen that the results from our BEM implementation are in good agreement with the FEM simulation. The value can further be used to find a tradeoff between the shield radius minimisation, which has to be done in order to reduce the constraints put on the design of coil around the shield and the efficiency reduction caused by the shielding effect.

The efficiency reduction can be seen from many aspects. First, to generate a given field strength, more current has to be applied to the coil, thus leading to an increased dissipation in power. Secondly, the current induced in the shield is going to heat it, which will require active cooling. Finally, the dissipated power in the shield will have to be provided by the drive coil power supply, effectively increasing the requirement. We chose to fix the shield diameter at 160 m, thus decreasing c^R_{y00} of 34 %. The dissipated power of both the coil and the shield evaluated using equation (4.31) is increased by 36 %. Thus to generates the same peak field strength as calculated using the quasi-static approximation, it would be expected to have a peak current amplitude 1.34 times higher, thus dissipating $(1.34)^2 \approx 1.8$ more power in the coil housing and increasing the whole power requirement by $1.8 \cdot 1.35 = 2.42$.

Similarly, the shield will also affect the x-drive coil, but at a smaller scale. The expected coil efficiency loss is expected at 15 %, thus increasing the dissipated power in the housing by 32 %. 15 % of the power is expected to be induced in the shield, thus increasing the power supply requirement by $1.32 \cdot 1.15 = 1.52$.

4.1.2.3 Quadrupole sets

The centroids of the two sets of quadrupoles, Q_0 and Q_{45}, are designed as part of the selection fields for a rabbit sized FFL scanner. The power dissipation of the set has to be minimised to allow integration inside our facilities, where 20 kW of cooling power are available for this set. The final design was obtained after many iterations, which mostly included constraints from the cooling requirements and the coil manufacturing process.

Each coil should produce a peak magnetic flux-density of 0.4 T·m^{-1}, which is a main SHC of $c^{0.09}_{x11} = -c^{0.09}_{y1-1} = 0.4 \cdot 0.09$ T $= 0.036$ T. They will be constructed using square hollow

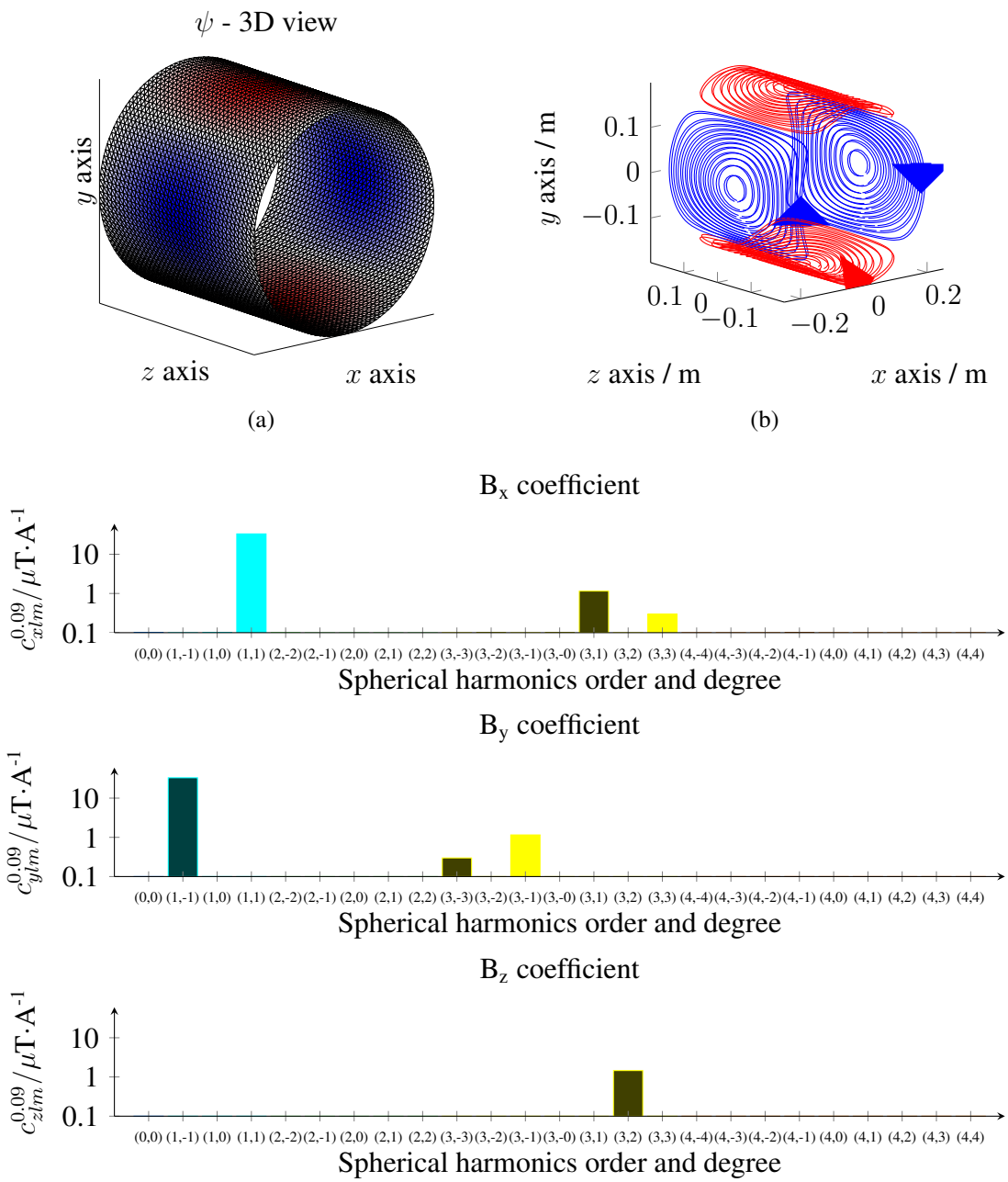

Figure 4.10: Design results for a quadrupole made of 2 layers. (a) Cylindrical support and chosen stream function for the first layer of the first quadrupole. (b) Extracted centroids represented in 3D. The arrows show the direction in which the current flows. (c) SHSE up to degree $l = 10$ and order $m = 10$ and display up to $m = l = 4$ in a sphere with radius $R = 0.09$ m. Darker filling color indicates a negative coefficient.

conductors, with a Section of 6×6 mm^2 and a circular cooling channel with a diameter of 3.5 mm^2. Two layers of conductor are used for each quadrupole, which reduce the dissipated power of the coil while facilitating the connection of cooling and electrical power.

Even if the two coil sets are rotated by an angle of 45 °, each design is made using the same $\vec{B}_{\text{target}}$ points and values, which are defined as an ideal field with the two non-zero SHCs $c_{x11}^{0.09} = -c_{y1-1}^{0.09} = 0.036$ T. The stream function has been optimised using a QPQC method described as

$$\begin{aligned} \min_s \quad & \frac{1}{2}\vec{s}^{\intercal}\underline{\underline{M}}\vec{s} \\ \text{subject to:} \quad & 0.9\,\vec{B}_{\text{target}} \leq \begin{pmatrix} \underline{\underline{B}}_x \\ \underline{\underline{B}}_y \\ \underline{\underline{B}}_z \end{pmatrix} \vec{s} \leq 1.1\,\vec{B}_{\text{target}} \\ & \vec{s}^{\intercal}\underline{\underline{R}}\vec{s} \leq 10000. \end{aligned} \tag{4.69}$$

It has been used for 4 different cylinders, with radius of 191.8 mm and 198.6 mm for the first quadrupole and of 205.6 mm and 212.4 mm for the second. The first quadrupole is made of 2 layers, each made of 4 identical segments. Their properties are given in Tables B.1 and B.2 for a coil temperature of 20 °C and a sinusoidal current with a single frequency. The centroids which are obtained can be seen in Figure B.5 and the details for the first quadrupole is presented in Figure 4.10. Results for the second quadrupole are similar. Due to the increased diameter of the support, the second layer of the second quadrupole segment is made of 13 loops, instead of 12 for all the other segments. This explain the equivalent efficiency between layer 1 and 2 of the second quadrupole.

4.1.2.4 Planar coil

Planar coils are used mainly for open bore or single-sided imagers. Different techniques are used to design coils which generate a magnetic field with main components in a direction parallel to the surface of the coil. That is, if the coil is in the yz plane, the field is generated either in the y or z direction, as shown in Figure 4.11. Such coils are sometimes called D-shaped coil in MPI and could also be designed with a volumetric approach [39] or via a four wire model [O12].

For this example, coisl on two planar surfaces are 314 mm away from each other with radius of 145 mm. To avoid any sharp edges after the discretisation into wire path, the Laplacian of the stream function is used as the Tikhonov matrix to obtain a smooth shape. The target field is defined on a sphere with a radius of 25 mm made of 496 points, centred

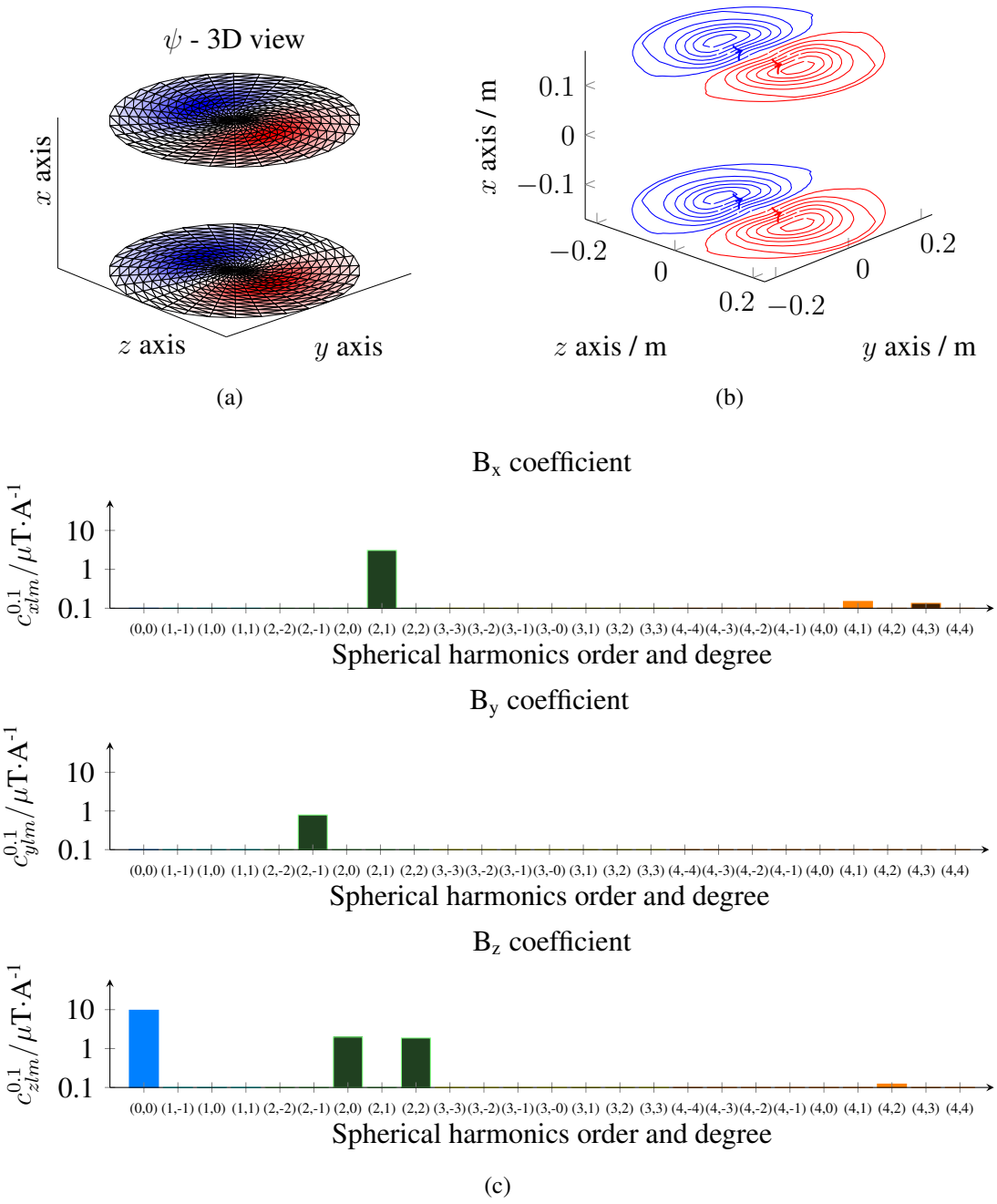

Figure 4.11: Planar coil for an open-bore scanner, which generates a magnetic field mainly in the z direction. The optimisation has been done to obtain smooth wire path on the surface. (a) Stream function on both planar surfaces. (b) Discretisation of the stream function as wire path with a minimal distance of 10 mm. The arrows show the direction in which the current flows. (c) SHSE associate with the wire path, calculated up to degree $l = 10$ and order $m = 10$ and displayed up to $m = l = 4$ in a sphere with radius $R = 0.1$ m. Darker filling color indicates a negative coefficient.

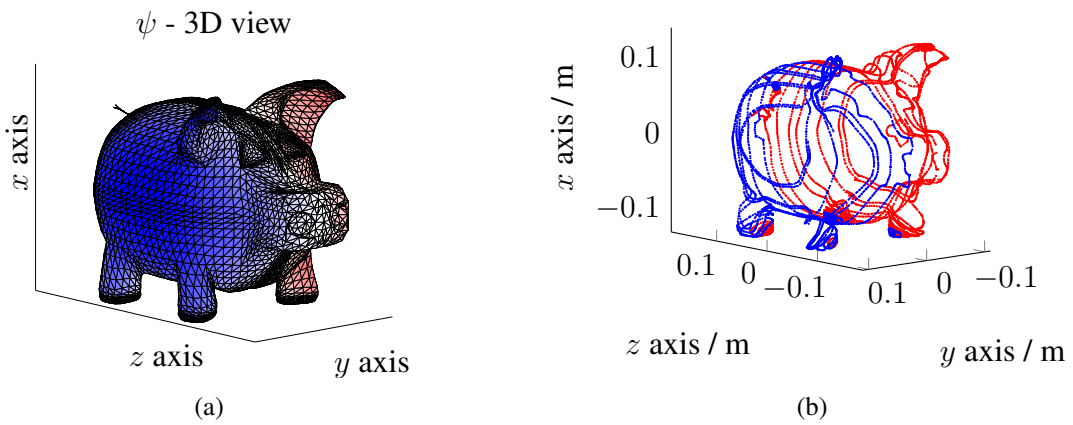

Figure 4.12: Pig-like surface on which a y-drive coil is designed. (a) The chosen stream function. (b) Points belonging to the different stream function level which forms the wire centroids.

between both surfaces and with magnetic flux-density values defined as an ideal field with the single non-zero SHC $c_{z00}^{0.05} = 3$ mT.

Using a Tikhonov regularisation scheme, the regularisation parameter $\lambda = 4 \cdot 10^{-8}$ is chosen experimentally. After the discretisation, a minimal distance between two wires of 8.1 mm is obtained for a total wire length of 21.0 m. A main SHC $c_{z00}^{0.1}$ of 12.3 μT·A^{-1} is calculated.

4.1.2.5 Pig coil

To demonstrate the possibilities in terms of current carrying surface form and to add a more didactic example and show the actual limits of the methods, a design on a pig-like surface is done. Figure 4.12 shows the chosen stream function, which generates a y-drive coil directly on the surface of a subject. A Tikhonov regularisation scheme has been used with the Tikhonov matrix taken as the identity matrix. The regularisation parameter $\lambda = 2.7 \cdot 10^{-8}$ is chosen to obtain two main distinct loop sets.

Figure 4.12b does not represent the wire path but the different points belonging to all the stream function levels. If this coil had to be constructed, the points seen in the feet, at the end of the ears and on the tails which would form small loops of current flowing in different directions may be discarded to simplify the realisation. A better approach would be to add further constraints on the nodes in those regions; for example, to force the stream-function value to be zero.

4.1.3 Discussion

Through those 6 examples, different field topologies are obtained from cylindrical, planar and pig-like current-carrying surfaces. In all cases the method is perfectly suited to obtain a set of ideal wire centroids and could also be used to obtain copper tracks.

The stream function can be optimised based on different sets of constraints and objectives, which are chosen by the designer specifically for each project. Those choices can also deliver counterintuitive results, as for the design of a quadrupole with a minimised dissipated power for a given gradient field strength. Minimising the dissipated power did not prove to deliver the centroids generating the most efficient design. Indeed, after discretisation the stream function into wire only 11 loops are obtained. However, by minimising the stored energy and limiting the dissipated power, designs with 12 and 13 loops are obtained. The increased efficiency leads to a smaller dissipated power for a given target field.

The modification required to go from the ideal centroids to a realistic one, as shown in Figures 4.7 and 4.8, is also independent of the optimisation process. Thus different choices could be made here. For the drive-coil set, it has been preferred to realise the coil with a thick and relatively flexible litz wire to minimise the dissipated power and reduce the coupling factor between the x- and y-drive coils, at the cost of a more complex field topology.

On the contrary, the use of hollow conductors for the quadrupole coils permits the realisation of a smaller bending radius. Added to the two layer design, the connection path from one loop to another could be compensated from one layer to the other. Thus, the obtained SHCs should be closer to the one obtained with the loop centroids.

The efficiency of the cylindrical and planar drive coil can also be compared using scaling law and considering a constant winding density by [122, 123]

$$\eta_{\text{scaled}} = \eta_{\text{original}} \frac{d_{\text{original}}}{d_{\text{scaled}}}, \tag{4.70}$$

with η_{original}, η_{scaled} and d_{original}, d_{scaled} the efficiency and diameter of the original and scaled coils, respectively. The diameter of the y-drive coil presented in Section 4.1.2.1 can be scaled from 238 mm to 314 mm to match the distance at between the two planar surface to have obtain a first efficiency approximation. Taking $\eta_{\text{original}} = 39.5\,\mu\text{T}\cdot\text{A}^{-1}$, η_{scaled} of 29.9 μT·A^{-1} is calculated. Compared to the 12.3 μT·A^{-1} obtained for the planar coil, it can be concluded that 2.4 times more current would be required for a planar drive coil to generate an equivalent main SHC amplitude as a cylindrical coil. As both coils requires almost the same length of wire, the planar design dissipate 6 times more energy. This

illustrates one of the challenges of open bore and single-sided scanner designs.

4.1.4 Conclusion

The stream function from which centroids are discretised is an appropriate method to design coils for MPI scanner. Furthermore, the induced current in conductive surfaces in the close vicinity of the coil can be approximated using the same formulation. The whole implementation is made freely available at `http://www.imt.uni-luebeck.de/` and `https://github.com/gBringout/CoilDesign` to let the community of enthusiastic coil designers take full advantages of this technique.

Some improvements may be integrated in the future. Besides the numerical optimisation of the basis function calculation and the associated derived values, the extraction of the wire centroids from the stream function requires the most attention. On the optimisation side, the integration of the cooling information to limit the hot spots could be beneficial to reduce the overall temperature and, thus, noise generation of the coils [124].

All the coils designed with these methods fulfill three distinctive functions, namely magnetic field generation, heat-dissipation management and magnetic field shaping.

By deporting the function of magnetic field shaping to another element, namely an iron core, coils producing larger main SHC amplitudes for equivalent current amplitudes can be designed. This is discussed in the next Section.

4.2 Ferromagnetic core inductor

MPI requires selection coils generating first order SHCs with very high amplitudes. To produce such fields, iron-core magnets can be used, which are designed in a very different way compared to air-core coils. In this Section, a 2D multi-pole expansion based approach is presented which focuses on a normal conductive, iron-dominated quadrupole magnet.

4.2.1 Material and methods

The required field is designed with a very strong hypothesis. The design is done in 2D, for example in the xy plane, considering a magnet with an infinite length in z, a constant cross-section, infinite extensions in both x and y direction and infinite permeability [125].

Similar to the SHSE, the required 2D field is represented as a multipole series expansion (MSE) with multipole coefficient (MC) C_n for a field of order n. Note that the order n for

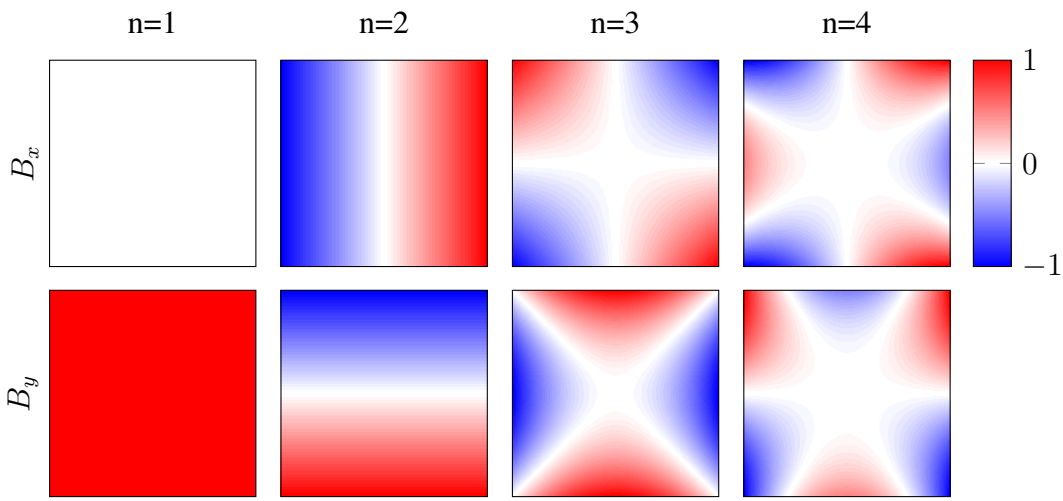

Figure 4.13: Normalised amplitude for 2D pure multipole fields with order $n = 1$ to $n = 4$ with real coefficient. The positive x axis axis is horizontal and to the right and the positive y axis is vertically up.

MSE is not the same as the order m for SHSE. In polar coordinates, with $x = r\cos(\theta)$ and $y = r\sin(\theta)$, the magnetic field can be expressed by [125]

$$B_y + iB_x = \sum_{n=1}^{\infty} C_n r^{n-1} e^{in\theta}. \tag{4.71}$$

Example of pure multipole fields up to order $n = 4$ are shown in Figure 4.13.

Considering the interface between the iron core with an infinite permeability in the region of interest, but with a finite permeability, it has been shown that the magnetic flux-density at the interface is normal to the surface [125]. Moreover, the gradient of a function is normal to the surface on which it is defined [103]. For the quasi-static case, equation (2.20) defines the gradient of the magnetic vector potential $\vec{A}$ as equal to the magnetic flux-density $\vec{B}$. Thus defining the interface between the iron core and the region of interest as a surface with a constant $\vec{A}$ will shape the magnetic flux-density accordingly.

Wolski [125] showed that the shape of the iron core required to generate a pure multipole field of order n is given in polar coordinate system by

$$r(\theta) = \sqrt[n]{\frac{r_0^n}{sin(n\,\theta)}}, \tag{4.72}$$

with r_0 the radius of the innermost free circle at the centre of the magnet. The radius describing the shape becomes singular when $n\,\theta$ tends to an integer multiple of π. Figure 4.14 present four different designs, for pure multipoles of order $n = 1$ to 4, with

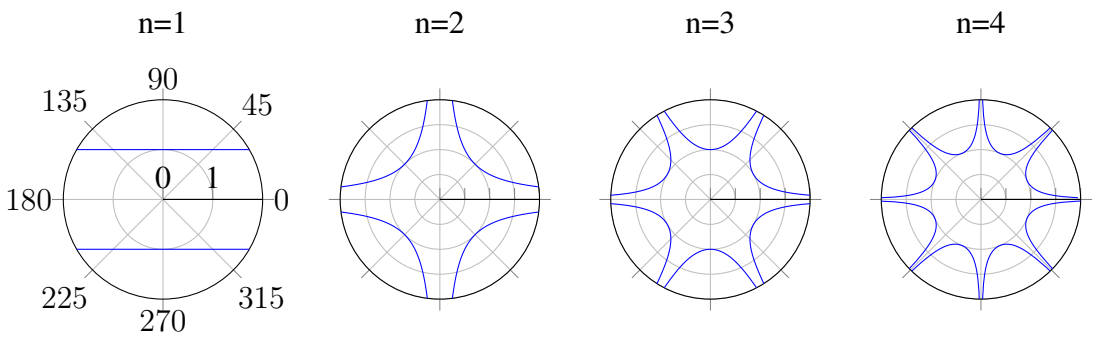

Figure 4.14: Line of constant magnetic vector potential around a circle with a radius of 1 m for order $n = 1$ to $n = 4$. The positive x axis is horizontal and to the right and the positive y axis is vertically up.

$R_0 = 1$ m. Each area situated between the singularity points is a core or pole shoe. An iron-core magnet generating a pure multipole field of order n has $2n$ poles. To achieve the adequate magnetic fields, adjacent poles guide magnetic flux going in the opposite direction.

The current carrying wires are then only used as a source for magnetic flux. To invert the flowing direction of the magnetic flux, currents flowing in opposite directions between each pole shoe are used. The MC can thus be directly linked to the number of turns N and the current amplitude I which flows in them by

$$\|C_n\| = \mu_0 N I \frac{n}{r_0^n}. \tag{4.73}$$

Using relation (4.73) in (4.71), the field gradient generated by a quadrupole ($n = 2$) can be expressed by

$$\frac{\partial B_x}{\partial y} = \frac{2\mu_0 N I}{r_0^2}. \tag{4.74}$$

An iron-dominated magnet is thus required to have the right pole shape to generate the matching field shape. Then coils around each pole shoe having an adequate number of turns and current amplitude generate the required magneto-motive which is directly linked to the magnetic field strength.

4.2.2 Results

A set of iron-dominated quadrupoles is designed as part of a human sized 2D FFL scanner. An inner radius of $r_0 = 0.5$ m is taken, and both quadrupoles are integrated to form an octupole-like assembly, as shown in Figure 4.15. The red shoes are forming the

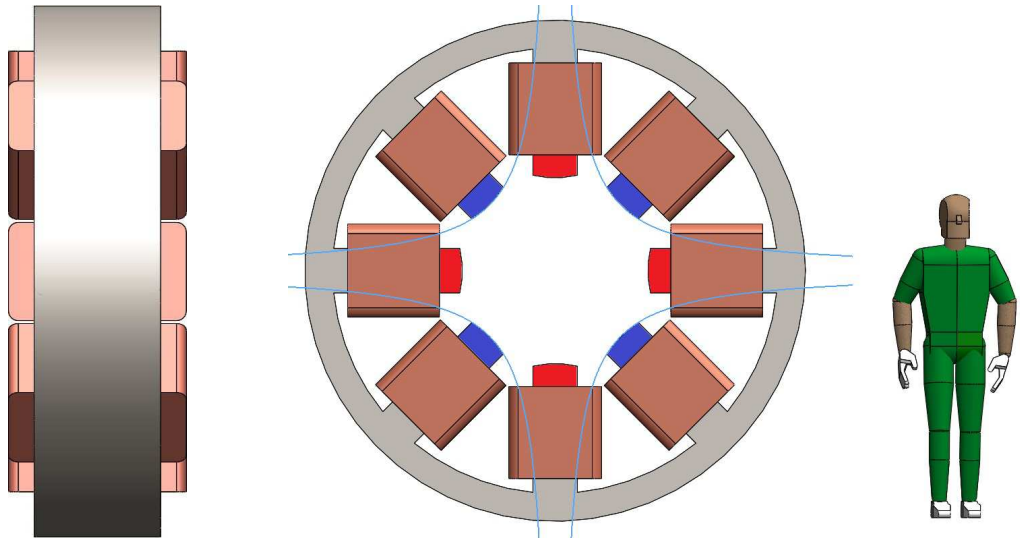

Figure 4.15: Model of a dual quadrupole iron-dominated magnet with a free bore of 1 m. The line with a constant magnetic vector potential used to design the shoe is superimposed on the model. Even if the magnet may look like an octupole ($n = 4$), the shape of each shoe is the one of an quadrupole ($n = 2$). Around each shoe are the coils generating the magnetic flux. A human model is presented to give an idea of the magnet size.

first quadrupole, whereas the blue ones are forming the second one. According to equation (4.74) which neglects any saturation effect on the iron, the coil requires a magneto-motive force of 50 kA·T (kilo Ampere Turn) in order to generate a gradient of 0.5 T·m^{-1}. To keep the design compact, the length of the magnet is chosen to be 640 mm. Around each pole, a resistive coil is modelled with a cross Section of 135×495 mm^2. The magnetisation curve used to characterise the iron used for the poles is typically used for magnet poles (Armco Special CR magnet Steel, AK Steel Holding corporation, USA) [126, 127], for which a linear approximation may be valid up to $\|\vec{H}\| = 100$ A·m^{-1}. The magnetisation curve is shown in Figure 4.16. The magnetic fields generated by each quadrupole is calculated using FEM with COMSOL Multiphysics (COMSOL Inc, USA). The fields are simulated on the points required to obtain the SHCs up to degree and order 10. An efficiency of $\eta_{Q0} = 7.4$ mT·m^{-1}·A^{-1}, which represents a magneto-motive force of 76 kA·T to generate a gradient of 0.5 T·m^{-1}, is obtained, taking into account the main SHC. The first SHCs are given in Figure B.12 for the 0 ° quadrupole. The SHCs for the quadrupole at 45 ° are similar.

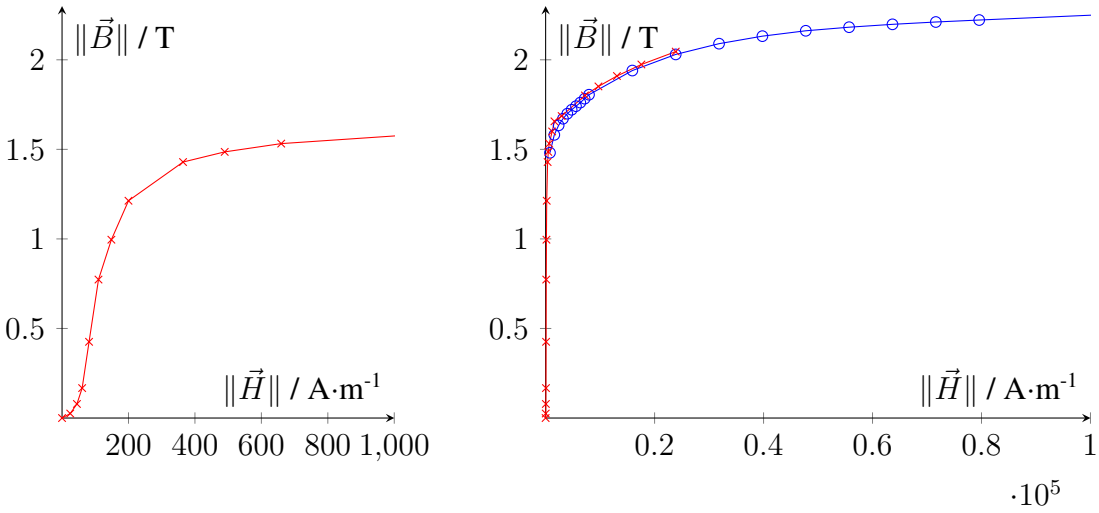

Figure 4.16: BH curves for a steel typically used in laminated iron cores. The red curves with crosses is obtained from [127] and the blue curve with circles from [126].

4.2.3 Discussion

To shape the magnetic fields with iron-core magnets, each pole shoe has to be correctly formed. Even if the final magnets largely violate the hypothesis used to design them, SHCs of first degree included in the fields, all have an amplitude smaller than 1 % of the main SHC. Significant SHCs appears for the third degree, which will distort the field mainly on the periphery of the volume of interest. Compared to the air coils designed in this Chapter, the influence of the connection wire scheme is not expected to have any significant influence on the SHCs. The main sources of discrepancy are expected to come from the mechanical misalignment of the pole [128, 129, 130].

Regarding the magneto-motive force required to obtain the required field strength, it can be noted that the value obtained via FEM simulation are 52 % higher than expected. This strong difference is associated with the short extension in the z direction of the magnet and the saturation of the pole, which are both neglected by relation (4.74). Extending the magnet in the z direction should at the same time reduce the amplitude of the unwanted SHCs and improve the magnet efficiency by reducing the iron saturation. The influence of the iron saturation on the SHCs should be in the order of a few percent [131, 132], which is so far seen as negligible for our application.

Using a hollow conductor of 16×16 mm^2 that has a copper surface of 252 mm^2, 250 loops would be wound for the coils. Using these coils, a current density of 3 A·mm$^{-2}_{\text{copper}}$ is required to generate 0.5 T·m^{-1}. Such a low current density does not present any major challenge to maintaining a reasonable constant temperature.

As the magnet will be used with an AC current and the design was done using a quasi-static approach, further effects will have to be considered for the actual realisation of the magnet, such as the eddy-currents arising in the pole.

4.2.4 Conclusion

An iron dominated normal conductive magnet offers a better performance in terms of magnetic field strength per ampere than air-core coils. For the magnetic field strength required in MPI applications, it is likely that a human sized FFL scanner will use poles which are at least partially saturated. This will in turn mainly influence the performance of the magnet, as the magnetic field strength will not linearly depend on the current amplitude applied to it. The design will be also influenced, as placing the current carrying wire closer to the target volume will increase the efficiency of the magnet. The exact function between the required field of each pole and the current will then depend on the the pole geometry and the saturation level of each pole. To reduce those effects, the iron part of the magnet may be redesigned in order to increase the Section available for the magnetic flux.

4.3 Conclusion

Both techniques are aimed at the design of specific coils. Air coils produce field shapes which vary linearly in strength with the used current amplitude, whereas iron-core magnets designed for human-sized scanners will present non-linearities due to the saturation of the used ferromagnetic material. Each type of magnet uses different design technique.

Air-coil magnet designs rely heavily on numerical optimisation to find the best repartition of the current density on a surface which satisfy given constraints. Despite the relative simplicity of the concepts, the actual implementation of such optimisation has not been available. For the first time, this work focused on a clear and coherent explanation of some state-of-the-art techniques. Moreover, a working implementation of those optimisation technique is publicly released in a toolbox. This regroups different approaches, which have been used to design all the coils of the first rabbit-sized FFL scanner. This may help to quickly optimise most of the magnets required to generate the magnetic field used in MPI scanners to encode the MPI signal. This step is also crucial for scaling-up imaging devices, where the minimisation of the dissipated power and peak voltage are crucial for the development of safe prototypes.

Iron-core magnets are in comparison simple to design. But for human-sized scanners, the

saturation effect of the core has to be taken into account as the efficiency of the magnet will quickly decrease with increasing currents.

Both, rabbit and human-sized FFL scanners made from the presented magnets are detailed in Chapter 6.

5

Peripheral nerves stimulation

Contents

To create and encode the MPI signal, a variety of magnetic field shapes, amplitudes and time variations are used. From the literature, and more specifically the one associated with MRI, there are two main safety risks associated with the time variation of magnetic fields. The first one is the specific absorption rate (SAR), which defines the ratio of absorbed power by a biological tissue per mass of tissue. The second is the PNS due to the time variation of the magnetic fields, which induces an electrical field in the human body.

The most accepted standard which defines SAR limits is in the second part of Chapter 33 of the Standard 60601, published by the International Electrotechnical Commission [133]. To limit adverse effects from the power deposition in human subject, the temperature in any tissue should not rise by more than 1 °C during a sequence. To comply with this limit, the mean whole body SAR should be limited to 4 $W \cdot kg^{-1}$ and the

mean local SAR to 20 W·kg^{-1} for an exposition of 6 minutes. Those limits can be doubled for an exposition of 10 seconds. The local SAR is defined in a tissue mass of 10 g. Indirect measurements carried out on five healthy human volunteers found that scanners suitable for human imaging could fall within the mean whole body range [134]. The local SAR could only be determined by simulation. Unfortunately, the few available models in this frequency range do not provide convergent results with the measurements, and could therefore not be used to determine the limits [135, 136]. They are nevertheless great steps towards the numerical determination of local SAR value.

The same standard defines the PNS limits as a threshold imposed on the rate of change of the magnetic field $\frac{\partial \|\vec{B}\|}{\partial t}$. Unfortunately, it defines limits for pulsed magnetic fields, whereas MPI actually mostly uses magnetic fields sinusoidally varying over a longer period of time. Other standards [137] and guidelines [138] exist, which considerer the effect of a sinusoidally varying magnetic field with a single frequency taken in a range from 0 to 100 kHz. The values in those guides are taken with an safety margin, to offer a safe use for a wide variety of devices. But the environment in which MRI are used and in which MPI may be used can be more precisely controlled. In such an environment and with the proper warning given to the operators, scanners can be used in a mode called the first level controlled operating mode. In this mode, the PNS limits used in MRI are set to avoid PNS in half of the people used to validate the threshold, thus allowing the occurrence of PNS in the other half. All the standards and guidelines are based on or take into account the model first introduced by Reilly [139, 140] to determine the thresholds at which the stimulation happens. In 2013 [134], an experimental evaluation estimated the stimulation threshold in five healthy volunteers, and found out that the thresholds estimated by Reilly are also too conservative. At 150 kHz, the experimental magnetic field amplitude limit for drive coils was found to be approximately 4 times larger than expected from Reilly's model.

To further evaluate the risk associated with new imaging concepts, informations related to the PNS for each magnetic field shape have to be obtained. For each single frequency excitation, the PNS risk could be evaluated through the evaluation of the maximal amplitude of the induced electrical field [139, 140]. Calculating the induced electrical field in a human body from different magnetic field shapes is a valid way to obtain a first evaluation of the PNS risk associated with this magnetic field shape and frequency [141]. But since the exact mechanism behind PNS is unknown, the prediction of the stimulation is not reliable enough to replace experiments. Thus, those first estimations should only be used to validate new imaging concepts, and further experimental validation has to be carried out to precisely asses the risk of PNS.

Previous works [21, 142] have successfully formulated the induced electrical fields on a human body model from a surface current density used for MRI gradient coils. Here, the same method is here applied using the notation introduced in Chapter 4. The induced electrical fields on a human surface is evaluated for different magnetic field shapes used in MPI imaging devices. From there, the field shape, amplitude and frequency, as well as the specific patient geometry, are taken into account in the comparison of the estimated maximal induced electrical field amplitude (MIEFA) and given thresholds. Those thresholds will be then obtained using Reilly's model corrected with the measurements from [134].

5.1 Material and methods

The calculation of the induced electrical field amplitude is done numerically using a BEM approach. The analytical model is derivated from the magneto-static case, for which the divergence of the magnetic field is null. The equations are then discretised using linear shape functions and are applied to triangular elements. Finally, the notion of highest maximal induced electrical field amplitude (HMIEFA) is introduced, which permits the formulation of the induced electrical field as a linear relation between the field topology, frequency and amplitude applied on a human subject.

5.1.1 Formulation

Modelling the induced current using the magneto-static approximation, equation (2.8) states that

$$\vec{\nabla} \cdot \vec{J} = 0 \tag{5.1}$$

moreover, the current density $\vec{J}$ flowing in a material with resistivity ρ_e is related to the electrical field via the relation

$$\vec{J} = \frac{\vec{E}}{\rho_e}. \tag{5.2}$$

Assuming that the resistivity is non-null and homogeneous, equation (2.8) can be rewritten as

$$\vec{\nabla} \cdot \vec{J} = \vec{\nabla} \cdot \frac{\vec{E}}{\rho_e} = \frac{1}{\rho_e} \vec{\nabla} \cdot \vec{E} = \vec{\nabla} \cdot \vec{E} = 0. \tag{5.3}$$

Using relation (2.21), this can be further extended as

$$\vec{\nabla} \cdot \left(-\vec{\nabla}\phi_e - \frac{\partial \vec{A}^t}{\partial t} \right) = 0, \tag{5.4}$$

expanding the divergence operator, the relation becomes

$$-\vec{\nabla}\cdot\vec{\nabla}\phi_e - \vec{\nabla}\cdot\frac{\partial\vec{A}^t}{\partial t} = 0. \tag{5.5}$$

Consider that the time-varying magnetic vector potentials $\vec{A}^t$ defined by

$$\vec{A}^t = f\,\vec{A}, \tag{5.6}$$

with f a time-varying function, (5.5) can be further expanded as

$$\vec{\nabla}\cdot\left(\vec{\nabla}\phi_e\right) + \frac{\partial f}{\partial t}\,\vec{\nabla}\cdot\vec{A} = 0, \tag{5.7}$$

and simplified using the Coulomb gauge (2.22) as

$$\vec{\nabla}\cdot\left(\vec{\nabla}\phi_e\right) = \vec{\nabla}^2(\phi_e) = 0, \tag{5.8}$$

which is the Laplace equation. Solving the Laplace equation will give us a solution for the electrical scalar potential, which will then be used along with the magnetic vector potential and the equation (2.21) to obtain the electrical field $\vec{E}$.

Solving the Laplace equation for a scalar function is referenced as the potential problem in the BEM literature [143, 110]. For 3D problems, it is solved by introducing the fundamental solution of the Laplace equation as

$$\vec{\lambda}(\vec{r}_\mathrm{t},\vec{r}_\mathrm{s}) = \frac{1}{4\pi\|\vec{r}_\mathrm{t}-\vec{r}_\mathrm{s}\|}, \tag{5.9}$$

which describes the effect of a potential at $\vec{r}_\mathrm{s}$ on a point situated at $\vec{r}_\mathrm{t}$. Considering a closed surface, the second Green identity formulate a transformation between the volume and surface integral of the functions $\vec{\lambda}(\vec{r}_\mathrm{t},\vec{r}_\mathrm{s})$ and $\phi_e(\vec{r}_\mathrm{t})$ as

$$\int_V \phi_e(\vec{r}_\mathrm{t})\vec{\nabla}^2\vec{\lambda}(\vec{r}_\mathrm{t},\vec{r}_\mathrm{s}) - \vec{\lambda}(\vec{r}_\mathrm{t},\vec{r}_\mathrm{s})\vec{\nabla}^2\phi_e(\vec{r}_\mathrm{t})\mathrm{d}V = \int_S \phi_e(\vec{r}_\mathrm{t})\frac{\partial\vec{\lambda}(\vec{r}_\mathrm{t},\vec{r}_\mathrm{s})}{\partial\vec{n}} - \vec{\lambda}(\vec{r}_\mathrm{t},\vec{r}_\mathrm{s})\frac{\partial\phi_e(\vec{r}_\mathrm{t})}{\partial\vec{n}}\mathrm{d}S. \tag{5.10}$$

$\vec{n}$ is the unit normal vector on the considered closed surface, the normal being directed outwards. It is demonstrated in [143] that equation (5.10) can be simplified using a Cauchy principal value approach as

$$\frac{1}{2}\phi_e(\vec{r}_\mathrm{s}) = \int_S \vec{\lambda}(\vec{r}_\mathrm{t},\vec{r}_\mathrm{s})\,\frac{\partial\phi_e(\vec{r}_\mathrm{t})}{\partial\vec{n}}\mathrm{d}S - \int_S \phi_e(\vec{r}_\mathrm{t})\,\frac{\partial\vec{\lambda}(\vec{r}_\mathrm{t},\vec{r}_\mathrm{s})}{\partial\vec{n}}\mathrm{d}S, \tag{5.11}$$

with $\vec{r}_\mathrm{s}$ a point on the surface S. Furthermore, the gradient of relation (5.11) is calculated as [21]

$$\frac{1}{2}\frac{\partial\phi_e(\vec{r}_\mathrm{s})}{\partial r_{\mathrm{t}i}} = \int_S \frac{\partial\vec{\lambda}(\vec{r}_\mathrm{t},\vec{r}_\mathrm{s})}{\partial r_{\mathrm{t}i}}\frac{\partial\phi_e(\vec{r}_\mathrm{t})}{\partial\vec{n}}\mathrm{d}S - \int_S \frac{\partial\left(\frac{\partial\vec{\lambda}(\vec{r}_\mathrm{t},\vec{r}_\mathrm{s})}{\partial\vec{n}}\right)}{\partial x_i}\phi_e(\vec{r}_\mathrm{t})\mathrm{d}S. \tag{5.12}$$

Thus an expression for the gradient of the potential on the surface S is obtained, which is a first step for the calculation of the electrical field according to equation (2.21). To be able to evaluate $\vec{E}$, an expression for the derivative of the potential in the normal direction has to be determined. This can be done using the boundary conditions.

The conservation of the current density in the whole domain leads to the discontinuity of the normal components of the electrical fields on the surface, that is:

$$\vec{E}(\vec{r}_{\mathrm{t}}) \cdot \vec{n} = 0, \tag{5.13}$$

as the surface is surrounded by air, which is modelled with a conductivity of zero. Using relation (2.21) and the discontinuuity of the electrical field, the following relation is obtained

$$\left(-\vec{\nabla}\phi_e(\vec{r}_{\mathrm{t}}) - \frac{\partial \vec{A}^t(\vec{r}_{\mathrm{t}}, t)}{\partial t}\right) \cdot \vec{n} = 0 \tag{5.14}$$

which can be then expended as

$$\vec{\nabla}\phi_e(\vec{r}_{\mathrm{t}}) \cdot \vec{n} = -\frac{\partial \vec{A}^t(\vec{r}_{\mathrm{t}}, t)}{\partial t} \cdot \vec{n}. \tag{5.15}$$

It is then reformulated as a directional derivative in the direction $\vec{n}$ by

$$\frac{\partial \phi_e(\vec{r}_{\mathrm{t}})}{\partial \vec{n}} = -\frac{\partial \vec{A}^t(\vec{r}_{\mathrm{t}}, t)}{\partial t} \cdot \vec{n}, \tag{5.16}$$

which defines a Neumann boundary condition. This is only valid for a single interface, which is surrounded by a non-conductive material. As the magnetic vector potential $\vec{A}^t$ originates only from the current flowing on the coil surface, the problem is now completely defined.

Relation (5.11) and (5.12) can be rewritten using relation (5.16) as

$$\frac{1}{2}\phi_e(\vec{r}_{\mathrm{s}}) = -\int_S \vec{\lambda}(\vec{r}_{\mathrm{t}}, \vec{r}_{\mathrm{s}}) \left(\frac{\partial \vec{A}^t(\vec{r}_{\mathrm{t}}, t)}{\partial t} \cdot \vec{n}\right) \mathrm{d}S - \int_S \phi_e(\vec{r}_{\mathrm{t}}) \frac{\partial \vec{\lambda}(\vec{r}_{\mathrm{t}}, \vec{r}_{\mathrm{s}})}{\partial \vec{n}} \mathrm{d}S, \tag{5.17}$$

$$\frac{1}{2}\frac{\partial \phi_e(\vec{r}_{\mathrm{s}})}{\partial r_{\mathrm{s}i}} = -\int_S \frac{\partial \vec{\lambda}(\vec{r}_{\mathrm{t}}, \vec{r}_{\mathrm{s}})}{\partial r_{\mathrm{s}i}} \left(\frac{\partial \vec{A}^t(\vec{r}_{\mathrm{t}}, t)}{\partial t} \cdot \vec{n}\right) \mathrm{d}S - \int_S \frac{\partial \left(\frac{\partial \vec{\lambda}(\vec{r}_{\mathrm{t}}, \vec{r}_{\mathrm{s}})}{\partial \vec{n}}\right)}{\partial r_{\mathrm{s}i}} \phi_e(\vec{r}_{\mathrm{t}}) \mathrm{d}S, \tag{5.18}$$

and the i component of the electrical field is expressed as

$$E_i(\vec{r}_{\mathrm{s}}) = \frac{\partial A_i(\vec{r}_{\mathrm{s}})}{\partial t} + 2\int_S \frac{\partial \vec{\lambda}(\vec{r}_{\mathrm{t}}, \vec{r}_{\mathrm{s}})}{\partial r_{\mathrm{s}i}} \left(\frac{\partial \vec{A}^t(\vec{r}_{\mathrm{t}}, t)}{\partial t} \cdot \vec{n}\right) \mathrm{d}S + 2\int_S \frac{\partial \left(\frac{\partial \vec{\lambda}(\vec{r}_{\mathrm{t}}, \vec{r}_{\mathrm{s}})}{\partial \vec{n}}\right)}{\partial r_{\mathrm{s}i}} \phi_e(\vec{r}_{\mathrm{t}}) \mathrm{d}S. \tag{5.19}$$

5.1.2 Discretisation

As for Section 4.1, the surface S on which the induced electrical fields has to be evaluated is discretised in N nodes and K triangles. The shape function are also kept linear, leading to a constant current density on each element, as described by equation (4.17). The magnetic vector and electrical scalar potential are also taken as constant on the whole element. The derivative of the electrical scalar potential will be evaluated at the barycentre of the triangular element, the center of mass, and displayed as constant over the element, even if it is not.

Therefore, equation (5.17) and (5.18) can be approximated on element l by

$$\frac{1}{2}\phi_e^l = -\sum_{k=1}^{K} \frac{\partial \vec{A}^t(\vec{r}_k,t)}{\partial t} \cdot \vec{n}_k \int_{S_k} \vec{\lambda}(\vec{r}_k,\vec{r}_l)\,\mathrm{d}S_k - \sum_{k=1}^{K} \phi_e^k \int_{S_k} \frac{\partial \vec{\lambda}(\vec{r}_k,\vec{r}_l)}{\partial \vec{n}_k}\,\mathrm{d}S_k, \tag{5.20}$$

$$\frac{1}{2}\frac{\partial \phi_e^l}{\partial r_{li}} = -\sum_{k=1}^{K} \frac{\partial \vec{A}^t(\vec{r}_k,t)}{\partial t} \cdot \vec{n}_k \int_{S_k} \frac{\partial \vec{\lambda}(\vec{r}_k,\vec{r}_l)}{\partial r_{li}}\,\mathrm{d}S_k - \sum_{k=1}^{K} \phi_e^k \int_{S_k} \frac{\partial \left(\frac{\partial \vec{\lambda}(\vec{r}_k,\vec{r}_l)}{\partial \vec{n}_k}\right)}{\partial r_{li}}\,\mathrm{d}S_k. \tag{5.21}$$

Let introduce the matrix element U_{lk} and V_{lk} defined as

$$U_{lk} = \int_{S_k} \vec{\lambda}(\vec{r}_k,\vec{r}_l)\,\mathrm{d}S_k, \tag{5.22}$$

$$V_{lk} = \frac{1}{2}\delta_{lk} + \int_{S_k} \frac{\partial \vec{\lambda}(\vec{r}_k,\vec{r}_l)}{\partial \vec{n}_k}\,\mathrm{d}S_k, \tag{5.23}$$

with δ_{lk} Kronecker's delta function defined as

$$\delta_{lk} = \begin{cases} 1 & l = k \\ 0 & l \neq k \end{cases} \tag{5.24}$$

with U_{lk} the elements of the single layer matrix $\underline{\underline{U}} \in \mathbb{R}^{K\times K}$ and V_{lk} the element of the double layer matrix $\underline{\underline{V}} \in \mathbb{R}^{K\times K}$. Relation (5.20) can be reformulated in matrix form as

$$\underline{\underline{V}}\vec{\phi}_e = \underline{\underline{U}}\vec{A}^n, \tag{5.25}$$

which leads to the expression of the electrical scalar potential on the mesh as

$$\vec{\phi}_e = \underline{\underline{V}}^{-1}\underline{\underline{U}}\vec{A}^n. \tag{5.26}$$

The vectors $\vec{\phi}_e$ and $\vec{A}^n$ are both defined in $\mathbb{R}^K$, with $\vec{A}^n$ made of elements

$$A_k^n = \frac{\partial f}{\partial t}\vec{A}(\vec{r}_k) \cdot \vec{n}_k. \tag{5.27}$$

Similarly, the matrix elements X_{lki} and Y_{lki} defined by

$$X_{lki} = \int_{S_k} \frac{\partial \vec{\lambda}(\vec{r}_k, \vec{r}_l)}{\partial r_{li}} \, \mathrm{d}S_k, \tag{5.28}$$

$$Y_{lki} = \int_{S_k} \frac{\partial \left(\frac{\partial \vec{\lambda}(\vec{r}_k, \vec{r}_l)}{\partial \vec{n}_k} \right)}{\partial r_{li}} \, \mathrm{d}S_k, \tag{5.29}$$

with X_{lki} the elements of the matrix $\underline{\underline{X}} \in \mathbb{R}^{K \times K}$ and Y_{lki} the element of the matrix $\underline{\underline{Y}} \in \mathbb{R}^{K \times K}$. Relation (5.21) can be reformulated in matrix form as

$$\frac{1}{2} \frac{\partial \phi_e^l}{\partial r_{li}} = -\underline{\underline{X}} \vec{A}^n - \underline{\underline{Y}} \vec{\phi}_e. \tag{5.30}$$

Using expression (5.26) in (5.30), the gradient of the potential is formulated as

$$\begin{aligned} \frac{\partial \phi_e^l}{\partial r_{li}} &= -2\underline{\underline{X}} \vec{A}^n - 2\underline{\underline{Y}}\,\underline{\underline{V}}^{-1}\underline{\underline{U}} \vec{A}^n \\ &= (-2\underline{\underline{X}} - 2\underline{\underline{Y}}\,\underline{\underline{V}}^{-1}\underline{\underline{U}}) \vec{A}^n \\ &= \underline{\underline{Z}} \vec{A}^n. \end{aligned} \tag{5.31}$$

Using back expression (2.21), the component in the direction i of the electrical field on the mesh is expressed as

$$\vec{E}_i = -\underline{\underline{Z}} \vec{A}^n - \frac{\partial \vec{A}_i^t}{\partial t} \tag{5.32}$$

with $\vec{A}_i^t \in \mathbb{R}^K$ the vector containing the time dependent magnetic vector potential in the direction i, A_i^t, for each element defined by

$$A_i^t(\vec{r}_\mathrm{t}, t) = f(t) \left(\vec{A}(\vec{r}_\mathrm{t}) \cdot \vec{e}_i \right). \tag{5.33}$$

$\vec{A}$ is evaluated from the stream-function values on the coil mesh $\vec{s}$ using relation (4.21). The amplitude of the electrical fields can then be evaluated at each element barycentre by

$$\|\vec{E}\| = \sqrt{\left(\vec{E}_x\right)^2 + \left(\vec{E}_y\right)^2 + \left(\vec{E}_z\right)^2} \tag{5.34}$$

To evaluate the matrix $\underline{\underline{Z}}$ composed of the matrices $\underline{\underline{U}}$, $\underline{\underline{V}}$, $\underline{\underline{X}}$ and $\underline{\underline{Y}}$, integrals of the function $\vec{\lambda}$ over the mesh elements have to be approximated. Most of the coefficients of those integrals can be evaluated using the Gauss-Legendre quadrature described in (4.34). But the diagonal elements, for which the source and target terms are the same, are always singular. For each matrix, the singular integrals are evaluated using different approaches, which are described in the following Subsections.

5.1.3 Singular integrals

The formulation of the induced electrical field uses four different singular integrals. Each of them is treated differently, as described in the following Sections.

5.1.3.1 Weakly-singular integral for U_{ll}

As the element of $\underline{\underline{U}}$ are evaluated at the barycentre of the triangle, the singular point is always situated there. To be able to evaluate the integrals, sub-triangles are created using the barycentre as a new vertex, placing the singular point at a vertex [107, 144]. In this way, the weakly-singular integral can be reformulated on each sub-triangle as a regular integral and can be evaluated using Gauss-Legendre quadrature.

5.1.3.2 Singular integral for V_{ll}

The elements V_{lk} are evaluated using equation (5.23), which integral parts can be reformulated as:

$$\begin{aligned}\int_{S_k} \frac{\partial \vec{\lambda}(\vec{r}_k, \vec{r}_l)}{\partial \vec{n}_k} \, \mathrm{d}S_k &= \int_{S_k} \vec{\nabla} \vec{\lambda}(\vec{r}_k, \vec{r}_l) \cdot \vec{n}_k \, \mathrm{d}S_k \\ &= \int_{S_k} \frac{\vec{r}_\mathrm{k} - \vec{r}_\mathrm{l}}{4\pi \|\vec{r}_\mathrm{k} - \vec{r}_\mathrm{l}\|^3} \cdot \vec{n}_k \, \mathrm{d}S_k\end{aligned} \tag{5.35}$$

For the singular elements where $l = k$, $\vec{r}_\mathrm{k}$ and $\vec{r}_\mathrm{l}$ belongs to the same triangle. Thus $\vec{r}_\mathrm{k} - \vec{r}_\mathrm{l}$ and $\vec{n}_k$ are perpendicular and $(\vec{r}_\mathrm{k} - \vec{r}_\mathrm{l}) \cdot \vec{n}_k = 0$. Therefore, the diagonal element of $\underline{\underline{V}}$ are

$$V_{ll} = \frac{1}{2}. \tag{5.36}$$

5.1.3.3 Strongly-singular integral for X_{lli}

Despite matrix $\underline{\underline{V}}$, the singular element of matrix X has to be numerically evaluated. Similar to the matrix $\underline{\underline{U}}$, each triangle is divided into three subtriangle, all of which have a singular point on a vertex. Thus the strong singularity can be reformulated and evaluated using a Gauss-Legendre quadrature [107, 145].

5.1.3.4 Singular integral for Y_{lli}

Sanchez [107] used a rigid body motion argument, which originates from elastic theory as described in [110] to evaluate the diagonal elements of X_{lki}. Applying a constant

potential ϕ_e, equation (5.21) can be simplified as

$$\sum_{k=1}^{K} Y_{lki} = 0, \tag{5.37}$$

for any source point $\vec{r}_l \in S$. The diagonal element Y_{lli} can therefore be obtained by

$$Y_{lli} = -\sum_{\substack{k \neq l \\ k=1}}^{K} Y_{lki}. \tag{5.38}$$

5.1.4 Highest maximal induced electrical field amplitude

Using relation (5.34), the electrical field amplitude induced on the volume of a human model can be calculated at the barycentre of each triangular element. It corresponds to the expected induced electrical field in the skin layer of a human model.

As the MIEFA strongly depends on the relative position of the source of the time-varying magnetic field and the human model, the HMIEFA, $\|\vec{E}_{\text{max}}\|$, is defined for the position at which the highest maximum is calculated. The HMIEFA is thus different for each field shape, as obtained from x-drive, y-drive or quadrupoles coils. Referring to equation (5.32), it can be seen that $\|\vec{E}_{\text{max}}\|$ depends linearly on the frequency f and the magnetic field amplitude generated by the coil.

Thus the HMIEFA and the MIEFA can be easily normalised with the frequency and the amplitude of the magnetic field to give the normalised highest maximal induced electrical field amplitude (nHMIEFA) and the normalised maximal induced electrical field amplitude (nMIEFA). Once the nHMIEFA is obtained for a given magnetic field shape, the HMIEFA can be calculated using the linear relation

$$\|\vec{E}_{\text{max}}\| = \text{nHMIEFA} \cdot f \cdot \text{current} \cdot \eta_{coil}, \tag{5.39}$$

with the magnetic field amplitude defined as the applied current multiplied by the efficiency of the used coil.

In this work, the HMIEFA is obtained from the translation of a human model relative to the coil model in a single direction, mimicking the movement of a table into a scanner, as shown in Figure 5.1.

As the nerves are stimulated when an electrical field with a high enough amplitude is applied at a nerve ending [139], the nHMIEFA simplifies the estimation of the HMIEFA. The HMIEFA can then be compared to threshold values determined experimentally, to easily estimate the risk of stimulation for any field shape having a defined nHMIEFA used at any amplitude or frequency.

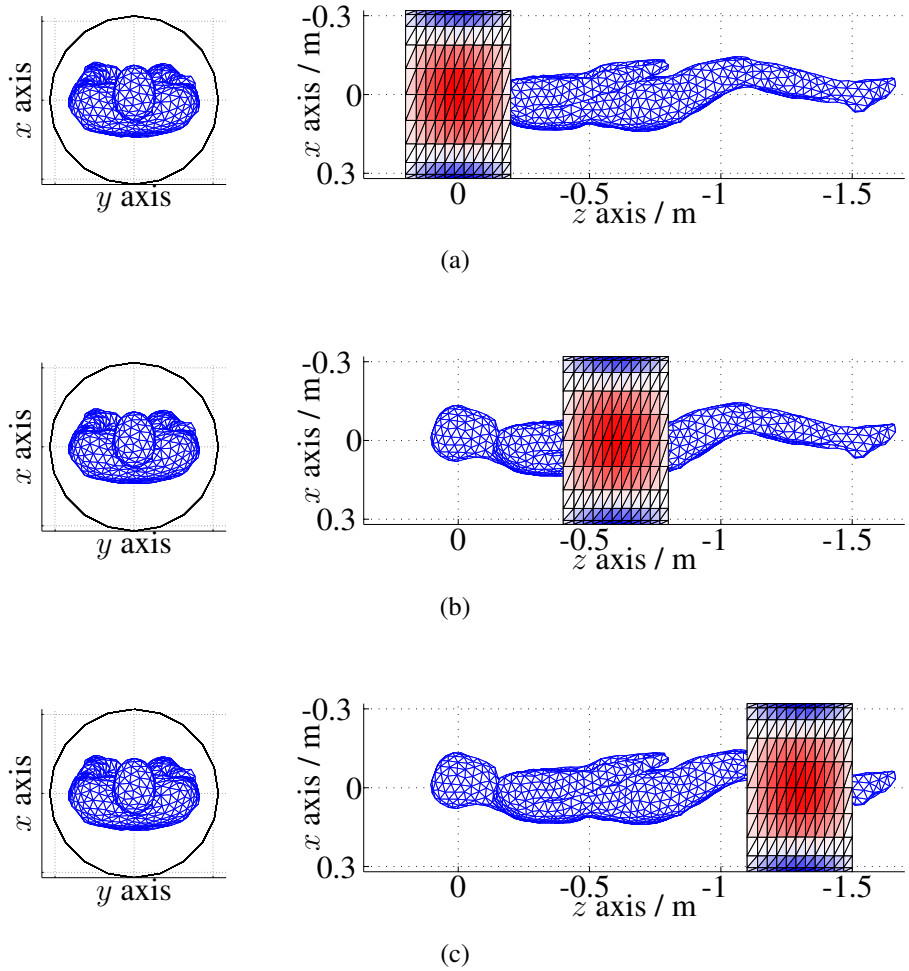

Figure 5.1: The HMIEFA is determined for coil translation along the human model, in a single direction. (a), (b) and (c) show three different positions for a stream function suitable for the creation of a quadrupole.

Conversely, the nHMIEFA can also be used to estimate the thresholds of the electrical field amplitudes for experiments such as the one conducted in 2013 [134], where only the coil types, field amplitudes and frequencies are provided. To further increase the precision of this method, the model of each subject should be used in the estimation of $\|\vec{E}_{\max}\|$.

5.2 Results

The implementation of the calculation of the induced electrical field is done in Matlab (7.11.0, Mathworks, USA) using the same framework as defined in Chapter 4. The main difference is linked to the discretisation, which is done considering the triangular elements, as explained in Section 5.1.2, instead of the triangle nodes for the design of coils.

5.2.1 Validation of the implementation

The validation of the numerical calculation is done in two steps. First, each singular integral calculation is compared with analytical results from the literature as well as from symbolic and numerical calculation done with Mathematica (v10, The Wolfram Centre, UK). Then, the shape and amplitude of the induced electrical field amplitude is visually compared to the results of two analytical solutions from the literature [146].

The models are constitued by a 80 mm radius sphere, which is placed inside a MRI z-gradient coil. The main SHC $c_{z10}^{0.08}$ is chosen to obtain a flux-density of 30 mT·m^{-1} in the middle of the coil. Its strength is then varied sinusoidally at a frequency of 1 kHz. For the first model, the sphere is perfectly centred with the coil. For the second model, the sphere is translated by 130 mm in the x-direction. All electrical field calculations presented in this work use a Gauss-Legendre quadrature of order 5. The amplitude and shape of the induced electrical field are then compared.

As can be seen in Figure 5.2, the numerical calculations are in good agreement with the analytical calculation, both for the shape and the amplitude of the solution. This validates the implementation presented here.

5.2.2 Human models

To assess the influence of the human geometry on the induced electrical field amplitude, meshed models have to be used. In this work, two meshed models have been created which represent a human subject.

The first one is based on photographs of a 28 years old male subject, measuring 174 cm and with a weight of 73 kg (see Figure 5.3a). It is modelled using Blender (Blender 2.69.0, Blender foundation, the Netherlands) to approximate the subject volume with a maximal extension in the y direction of 500 mm. The mesh is then processed using Meshmixer (v10.7.84, Autodesk Inc, USA) to obtain triangles as close as possible to equilateral triangles. The final mesh is made out of $N = 3211$ nodes and $K = 6418$

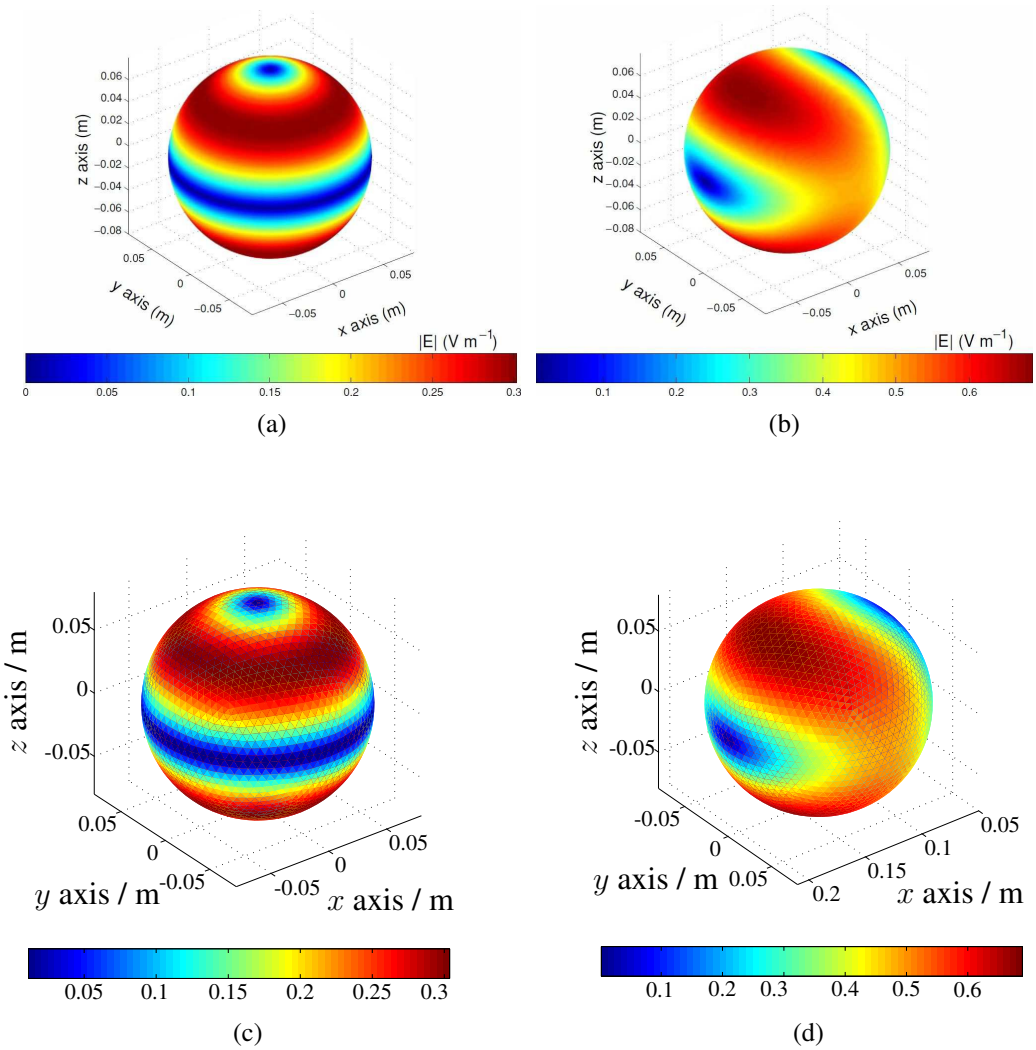

Figure 5.2: Three-dimensional plot of the electrical field amplitude $\|\vec{E}\|$ in V·m^{-1}. Top row: Analytical solution from [146] for: (a) centred sphere, (b) translated sphere. Bottom row: Numerical solution for: (c) centred sphere, (d) translated sphere. Figures (a) and (b) are reproduced by permission of IOP Publishing. All rights reserved. © Institute of Physics and Engineering in Medicine.

triangles. The result is presented in Figures 5.3b and 5.3c.

The second model is based on a whole body MRI acquisition of the same subject. T2 weighted images were acquired using Turbo spin echo sequences and parallel imaging. The whole body dataset has been measured in 6 consecutive acquisitions on a 3 T MRI scanner (Ingenia 3.0T, Philips Medical Systems, The Netherlands) and assembled in a single 3D dataset. 65 slices where acquired in the x-direction, with a slice thickness of

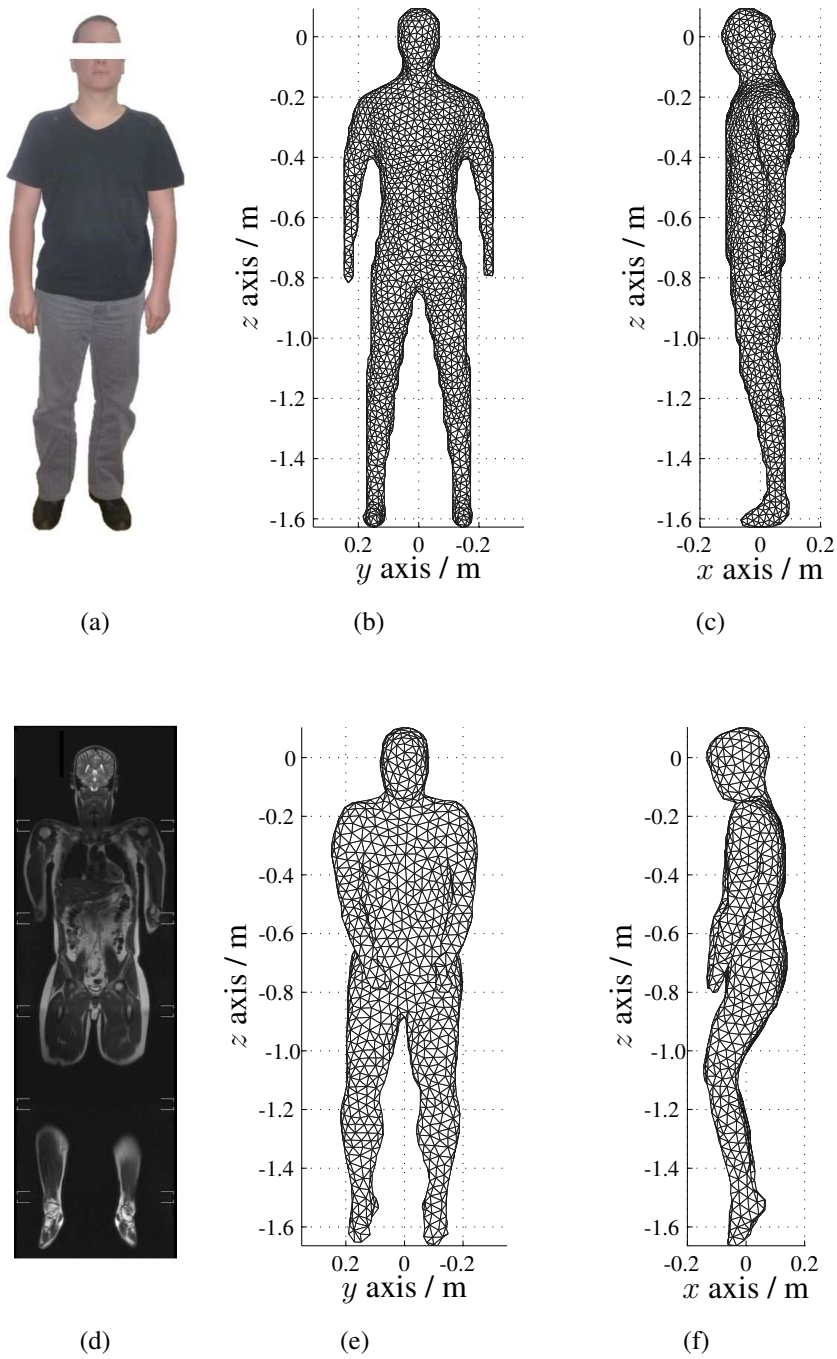

Figure 5.3: Two 3D models are used to model the volume a human body. The top line shows a model based on a photograph (a) and the corresponding front (b) and side (c) views. The bottom line shows a model based on a whole-body MRI acquisition (d) and the corresponding front (e) and side (f).

5.0 mm and distance between slices of 5.5 mm. In the yz plane, each slice is acquired with a voxel resolution of 0.8 mm. The patient was positioned to limit the extension in the y direction to about 500 mm, to make the measurement process possible. The measurement of the whole dataset took about 1 hour. One slice extracted from this dataset can be seen in Figure 5.3d. The patient volume was then segmented using the EM segmentation algorithm without Atlas [147] implemented in 3DSlicer [148, 149]. The results were then exported and post-processed using Meshmixer (v10.7.84, Autodesk Inc, USA) to obtain the final mesh. The final mesh is made of $N = 1582$ nodes and $K = 3160$ triangles and can be seen in Figure 5.3e and 5.3f.

Due to the low element size of the mesh, the variation of the element normal direction are not smooth in areas like the axilla, the groin and the feet ending. Those regions are thus filtered out from both models by setting the respective value of electrical fields to zero.

5.2.3 Induced electrical field for given coil topologies

Different coils are obtained via the minimisation of the dissipated power of the current density on the cylindrical surface shown in Figure 5.1 as defined in paragraph 4.1.1.2.2. The used current carrying surface has a radius of 320 mm, a 400 mm extension in the z direction and is made from $N = 240$ nodes and $K = 440$ triangles. Five coils often used in MPI are obtained, via their respective SHCs as defined in Tables 2.1 and 2.2. Additionally, three common gradient coils used by closed bore MRI are obtained, each defined by a single SHC. A z-gradient coil is defined by the SHC c^R_{z10}, whereas the x- and y-gradient coils are defined via SHC c^R_{z11} and c^R_{z1-1}, respectively.

For each coil, the surface carrying the current density is moved along the human model. The position of the whole surface is represented by the position of its centre. It is moved from a position slightly above the head to a position slightly below the feet, as shown in Figure 5.1. Note that the position in Figure 5.1 corresponds to the one in Figure 5.6a.

For each coil and position, the nMIEFAs are extracted from both human models and represented on graphs as shown in Figure 5.6 for the MPI coils and in Figure D.1 for the MRI coils. The influence of the body size and shape can be seen by comparing Figure 5.4 and 5.5, where the nHMIEFA is situated in the shoulder region for the thinner, photo based model, whereas for the model with a bigger volume, the nHMIEFA is situated in the abdomen region.

Then the nHMIEFA are calculated for each coil and indexed in Table 5.1. It can be clearly seen that the simulated nHMIEFAs are higher for the bigger model. A similar effect is seen in Appendix C for the y-drive coil but not for the z-drive coil nor the quadrupoles.

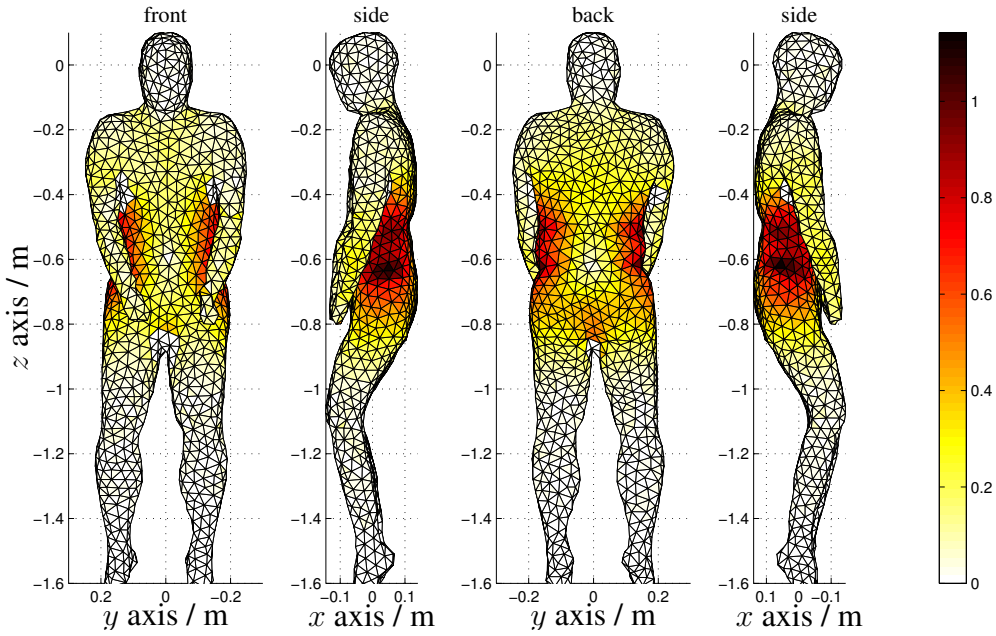

Figure 5.4: nMIEFA of the x-drive coil on an MRI-based model. The represented relative position is the one leading to the nHMIEFA.

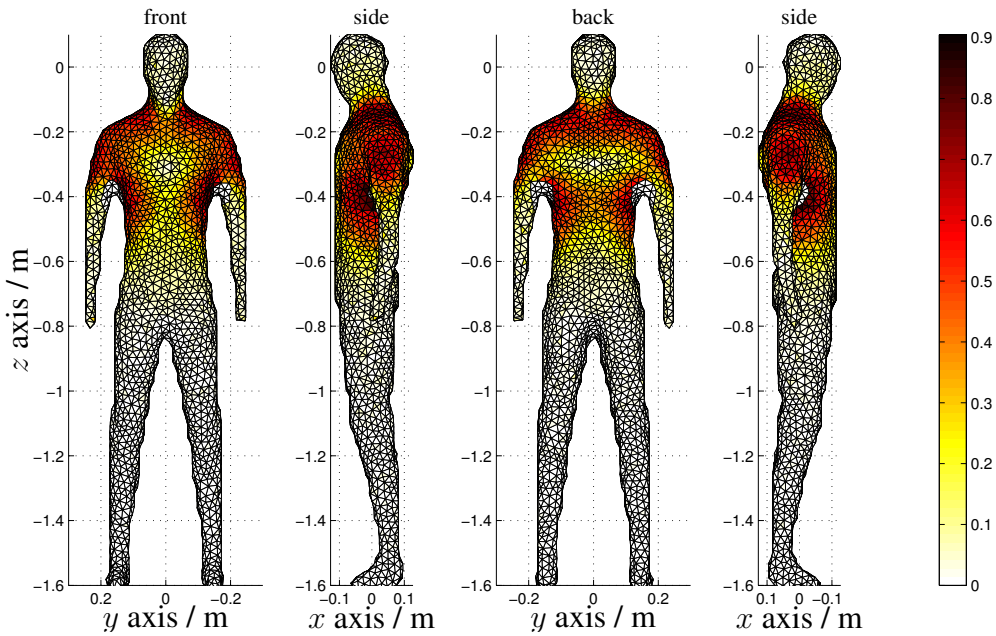

Figure 5.5: nMIEFA of the x-drive coil on an photo-based model. The represented relative position is the one leading to the nHMIEFA.

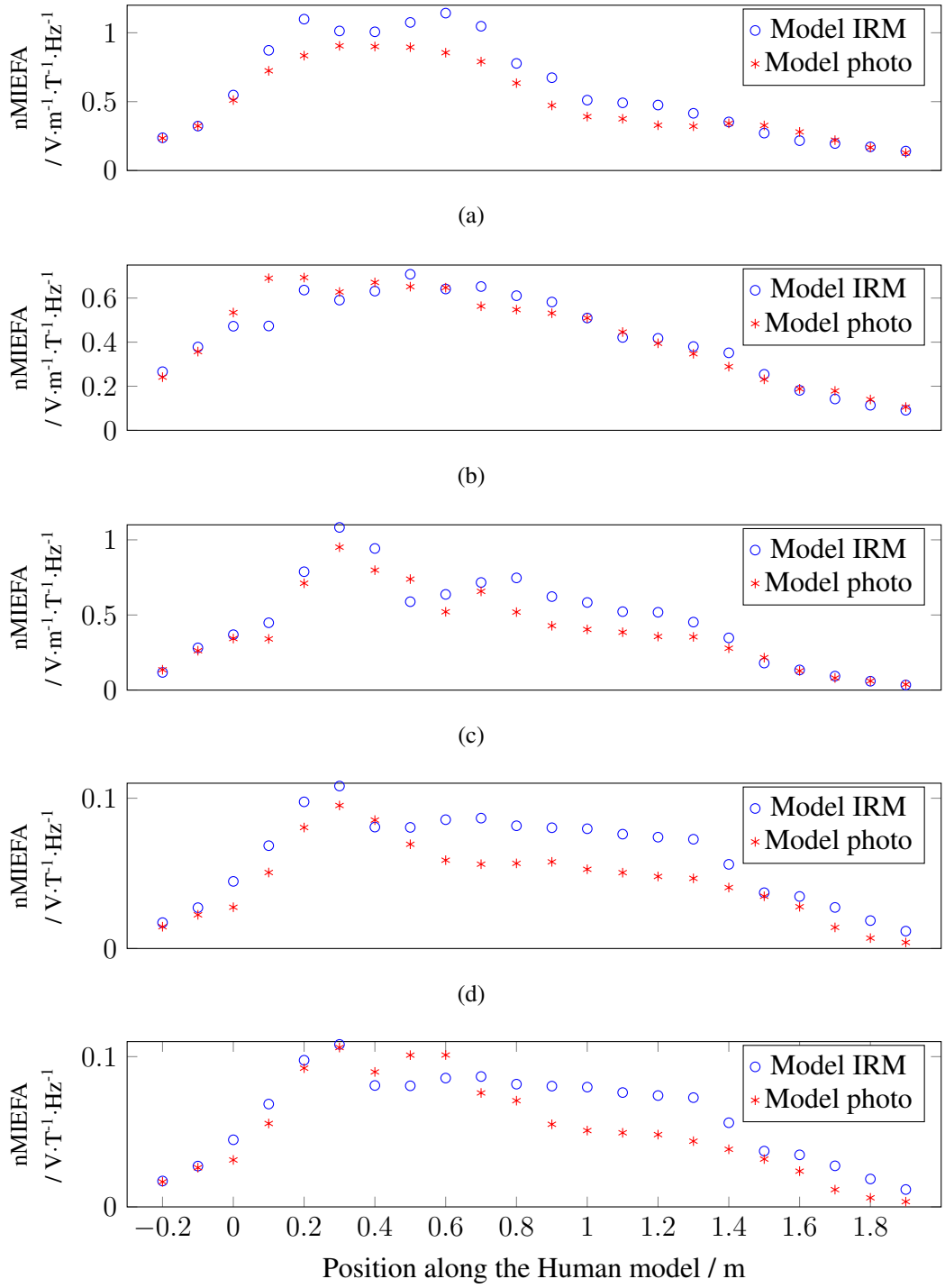

Figure 5.6: nMIEFA for different field topologies. (a) x-drive coil. (b) y-drive coil. (c) z-drive coil. (d) Q_0 coil. (e) Q_{45} coil.

Table 5.1: nHMIEFA for 8 coils, taken separately.

Coil name	nHMIEFA Photo model	nHMIEFA IRM model	Unit
x-drive coil	0.90	1.14	$V \cdot m^{-1} \cdot T^{-1} \cdot Hz^{-1}$
y-drive coil	0.69	0.70	$V \cdot m^{-1} \cdot T^{-1} \cdot Hz^{-1}$
z-drive coil	0.95	1.08	$V \cdot m^{-1} \cdot T^{-1} \cdot Hz^{-1}$
Q_0 coil	0.10	0.11	$V \cdot T^{-1} \cdot Hz^{-1}$
Q_{45} coil	0.11	0.11	$V \cdot T^{-1} \cdot Hz^{-1}$
x-gradient coil	0.09	0.11	$V \cdot T^{-1} \cdot Hz^{-1}$
y-gradient coil	0.11	0.16	$V \cdot T^{-1} \cdot Hz^{-1}$
z-gradient coil	0.09	0.10	$V \cdot T^{-1} \cdot Hz^{-1}$

5.2.4 Analyse of published stimulation thresholds

To date, two experimental studies [134, 150] have been published which try to determine the stimulation thresholds for x and z-drive coils using excitation frequencies relevant for MPI. But none of them choose the induced electrical fields amplitude as outcome parameters, as suggested by the literature [140, 133][O8]. Instead, the main SHC resulting from the averaged results on the patient is used as a threshold, as it is commonly done in the MRI literature [151].

The excitation thresholds are either given as function of the applied peak magnetic flux-density [134] or corrected with a cylindrical approximation of the body part under test (arm or leg) and fitted to a pulse-based model [150]. The first study covers a frequency range from 24 to 162 kHz whereas the second one covers a range from 0.46 to 50 kHz. To avoid the error introduced by the pulse-based model, only the information of the first study will be further used.

Using both human models, the mean threshold values of 2.9/2.8/3.8/3.8 mT peak by 24/46/106/147 kHz for a x-drive coil and 4.4/5.3/7.2/7.6 mT peak by 26/45/100/162 kHz for a z-drive coil can be converted into an equivalent induced electrical field amplitude. Using the MIEFA at the the position $z = -0.6$ m given in Figure 5.6, a comparison with the model of Reilly [140] is done in Figure 5.7.

As the numbers used are average numbers from 3 to 5 different subjects, the calculated electrical field amplitude should not be considered exact and should not be used to deduce further model parameter. But it can be observed that the stimulation thresholds obtained are higher than the ones predicted by Reilly's model. At 150 kHz, thresholds of 580 $V \cdot m^{-1}$, 4 times higher than Reilly's 145 $V \cdot m^{-1}$, could be assumed.

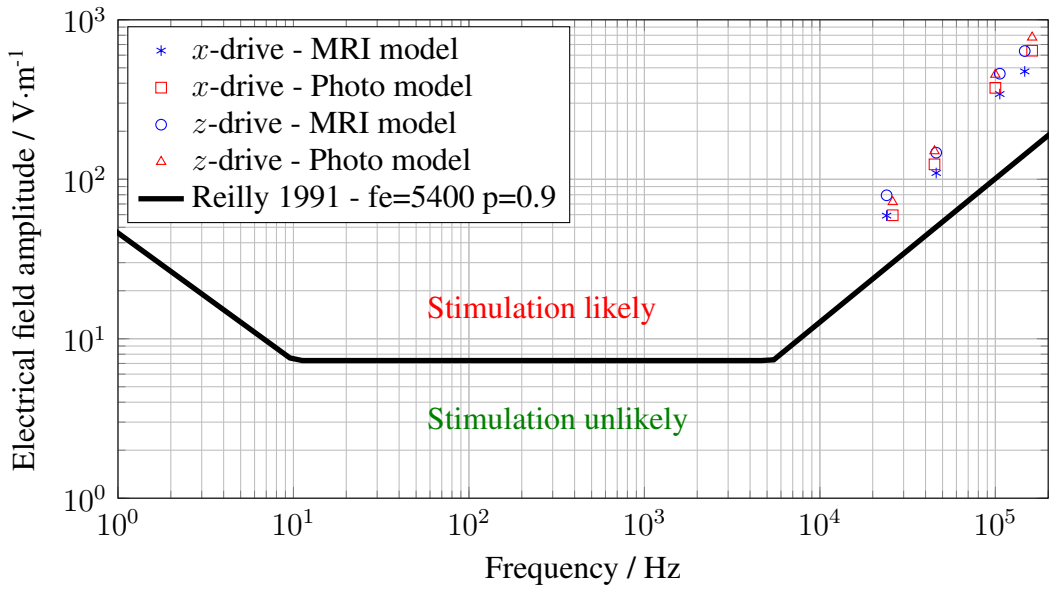

Figure 5.7: PNS thresholds from Reilly's model with added points from Schmale et al. averaged thresholds converted using the human model developed here.

5.2.5 HMIEFA for a human 2D FFL scanner

An FFL scanner relies heavily on rotating magnetic fields for both the drive fields and the selection fields. Using the present model and thresholds, it can be investigated, which SHCs could be used for a human-sized imaging device. In order to model the effect of the FFL rotation at different angles, a set of simulations using a constant angle θ, as described in Section 3.2.3, are done. Frequencies of 150 kHz and 20 Hz are used for the drive and line rotation frequencies. The MIEFA is then calculated for different discrete angles and the coil surface centre position. The results are displayed as surfaces, as seen in Figure 5.8. As a reference, the modulation applied to the drive-coil current, described in equation (3.35), is represented on top of Figure 5.8. As the electrical currents in the quadrupoles varies at a frequency two times higher than the line rotation, the MIEFA are repeated two times.

The two first surfaces of Figure 5.8 are made with the x- and y-drive coils. On the first surface, both coils are set to generate a magnetic field with a main SHC of 3.6 mT. This leads to a HMIEFA of 580 V·m^{-1}, which is at the limits of the PNS thresholds for this frequency according to the previous Section.

The second surface shows that by increasing the SHC associated with the y-coil by 33 % to 4.8 mT, the HMIEFA is not changed. This shows that MPI sequences could be op-

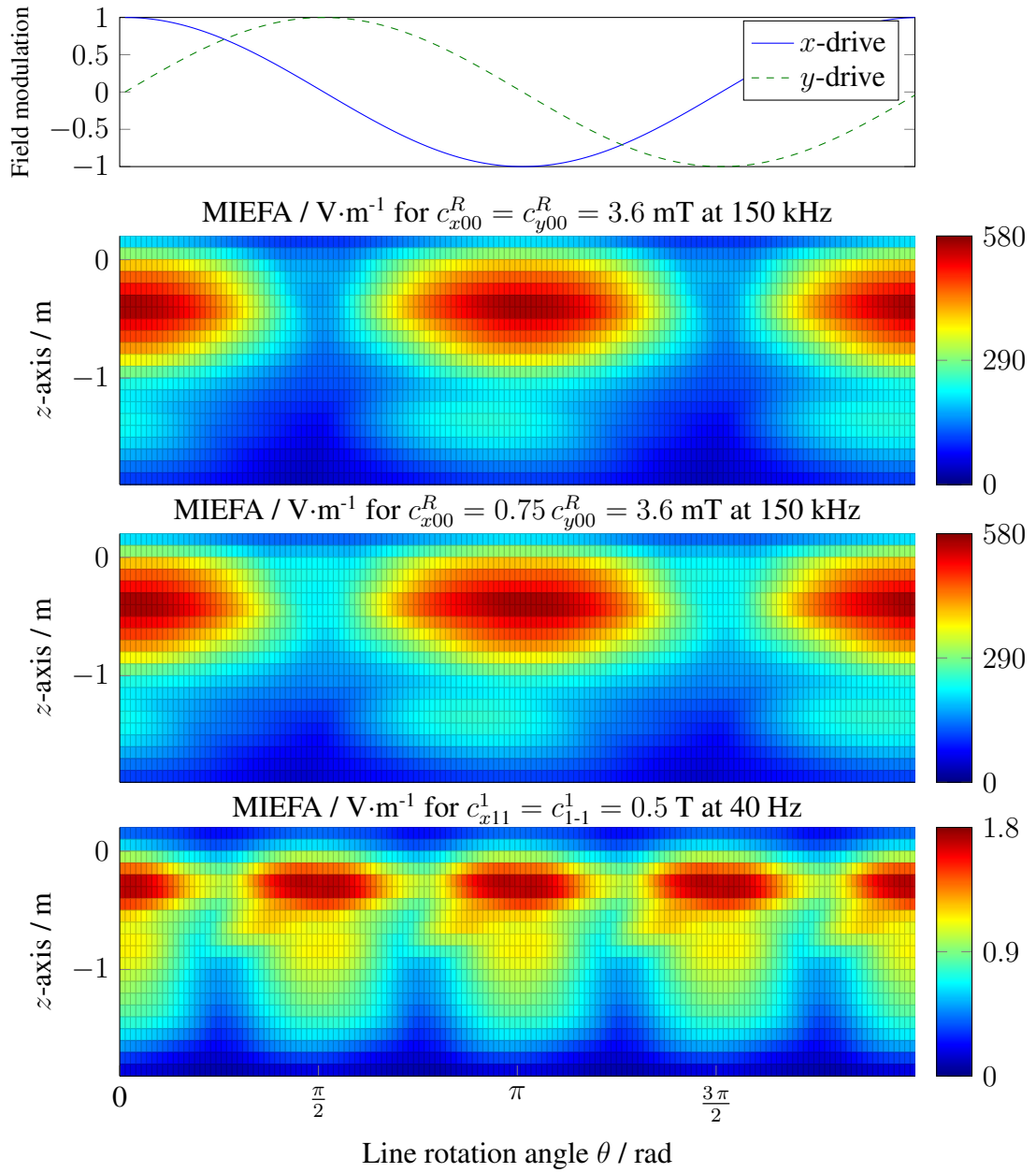

Figure 5.8: MIEFA for a rotated fields from drive coils and quadrupoles.

timised in order to maximise the drive-field strength without substantially changing the HMIEFA in a subject.

The third surface represents the MIEFA produced by the quadrupole. The gradient strength on the line is 1 T·m^{-1}, half of it coming form the quadrupole. In those conditions, an HMIEFA of 1.8 V·m^{-1} is to be expected. According to Figure 5.7, this is below the stimulation thresholds. Thus, it could be envisaged to safely place a human

patient inside a set a quadrupoles generating a rotating line.

5.3 Discussion

The presented method calculates the induced electrical field amplitudes on a surface, based on an external time-varying magnetic vector potential generated by a current carrying surface. It is assumed that the calculated electrical field is equivalent to the one induced in the skin layer. The MIEFA on the model is then used as outcome parameters for the evaluation of the PNS risk. Furthermore, the HMIEFA is evaluated for the translation in z direction of a patient. Both amplitudes are also normalised in order to provide a quick way to scale the results for different magnetic field strength and frequencies. This concept have been presented for the first time at a conference [O9].

This model does not take into account the electrical potential which appears at the interface between different tissue types such as skin, fat and muscle, even if such formulations are already available [107]. Our effort has been focused on the skin, as it has been shown that the HMIEFA is situated there or in the fat layer beneath [152, 141]. Furthermore, the body size and shape have been shown to play a dominating role in the location and amplitude of the induced electrical field, even in models taking the tissue heterogeneity into account [153, 154].

To be able to fully use the relation (5.39) to optimise coming MPI-scanners and MPI-sequences as presented in Section 5.2.5, the method presented in Section 5.2.4 used to determined the stimulation thresholds should be refined using the body size and shape of each patient. Acquiring the patient geometry using a hand-held 3D laser scanner could decrease the time required for the data acquisition and post-processing. But a whole body MRI scan offers the possibility to segment other tissue layers, if the single layer approach is not proved sufficient to reach a good correlation between PNS origin and simulated MIEFA position.

Despite the relative inaccuracy of the actual frequency dependent PNS threshold and the lake of a statistically relevant human body model, the nHMIEFA values introduced for two human model give us insight in a first relation between the main SHC component of a field, the spatial repartition of the induced electrical field amplitude and an MPI-sequence. This can be used to limit the used frequencies and magnetic field amplitude to reasonable values. The parallel from similar systems which are already approved, as for hyperthermia treatments, could also be done [155, 156]. To be able to further compared the nHMIEFA with the literature, values for the more common MRI gradient coils have been provided. This could help to speed up the adaptation of current safety standards.

But the effect of the superposition of different time-varying magnetic field, essential for any MPI sequence, has still to be investigated. The first approximation proposed in Section 5.2.5 should be experimentally validated. Furthermore, the superposition of drive and focus fields, which induces the same MIEFA into the patient body but at different frequencies and are thus linked to different PNS thresholds, should also be investigated.

5.4 Conclusion

In this Chapter, two different quantities have been introduced to evaluate the likelihood of PNS in human models. The first one, the nMIEFA, gives the relation between the patient volume, field topology, the field frequency and maximal induced electrical field amplitude for a given position of the patient in the coil. This could be used to design MPI scanner for specific target areas or optimise sequences to minimise the PNS likelihood. The second one, the nHMIEFA, provides the same optimisation possibilities but for any position of the patient inside the imaging device.

The nHMIEFA have been calculated for two different human models to provide a first evaluation of the PNS risk for the main magnetic field topologies used in today closed bore MPI scanner. y-drive coils offers the lowest nHMIEFA at 0.70 $V \cdot m^{-1} \cdot Hz^{-1} \cdot T^{-1}$. x- and z-drive coil have nHMIEFA, which are between 30 % to 63 % higher, due to the magnetic field direction and patient volume. Quadrupoles offers similar nHMIEFA for both orientations, with nHMIEFA of 0.10 to 0.11 $V \cdot Hz^{-1} \cdot T^{-1}$.

As an example, an FFL MPI-sequence has been optimised to maximise the FOV. A 33 % increase of the drive-field strength generated by the y-drive coil has been obtained, without increasing the HMIEFA.

Finally, a first example of how this method could be used to adjust the MPI sequence in order to influence the outcome parameter of coming PNS studies has been demonstrated. It has been estimated that current PNS thresholds overestimate by a factor of approximately 4 the magnetic field strength required to excite nerves at frequencies around 150 kHz. Further experimental validation, which take into account patient volume variation, should be carried out in order get a better estimation of the thresholds.

6
Scanner design

Contents

Up to 2015, all available scanners have been designed to accommodate either rats, mice or smaller animals and samples. In 2013, Philips presented their concept of a human-sized FFP scanner [157]. To further develop the technology, the University of Lübeck chose to develop a mini-pig-sized open FFP imaging device [O5]. This development has been stopped as the concept came closer to the human sized scanner designed by Philips. Thus the development of a rabbit-sized FFL scanner was started, which should offer fast 2D imaging for an adult New Zealand rabbit. The design study of this imaging device, the development of the first coil of the scanner, and the expected performance of the coming imaging device are presented here. The performance is presented using a SF approach, to make the comparison between existing FFP scanners easier.

The up-scaling of magnetic systems is challenging [122, 123], and the creation of human MPI scanners being particularly complex. Therefore, a first concept of a human sized, whole body FFL scanner is presented in Section 6.2. This study was designed to identify

the limiting factor of such imaging devices. The most interesting questions arising from such a study is whether or not a large FOV could be covered and at what rate images could be acquired. Using the results of all the previous chapters, those two points are addressed through the creation of the concept and the analysis of the expected MPI performance.

6.1 Pre-clinical FFL scanner

The design of a rabbit-sized drive-coil set and the construction of the corresponding selection-coil sets are detailed in this Section.

Here, the determination of the required magnetic field topology, dissipated power, heat-extraction system, electrical insulation and safety of the system are of first interest. All those aspects have to be evaluated, keeping the imaging objectives as well as the construction feasibility of the filters and power transmission in mind.

In the following Sections, the concept of the scanner is presented, followed by the definition of the imaging goals, the coil realisations and the expected MPI properties.

6.1.1 Concept

The pre-clinical FFL scanner has been designed to accommodate a sedated adult New Zealand rabbit with appropriate life support and monitoring accessories. Measurements of a living specimen of 3.5 kg lead to the choice of a 173 mm inner diameter cylinder as a bore diameter.

The whole imaging device should allow for a continuous acquisition mode to acquire an SF, which can take several hours.

A field of view of around 30×30 mm^2 is desired, to be able to image structures from the liver or the heart in a single acquisition. This corresponds, in the case of similar drive-field strengths in both directions, to a circle with a diameter of 42 mm. The FOV is centred in the middle of the bore. A volume can then be acquired in the third spatial direction by moving the subject along the bore axis. To obtain a resolution high enough to differentiate some blood vessel bifurcations in the chosen anatomy, a gradient strength of 0.8 T·m^{-1} is chosen. Drive-field strength of 15 mT have to be generated in order to cover the FOV.

6.1.2 Choices of frequencies

The choice of the drive frequency f_0 before the construction of the scanner is of high importance, as all the filters, impedance matching and resonance circuits associated with the imaging device are optimised for a single frequency. As equations (3.36) and (3.37) show, the power is actually transmitted at two frequencies, linked to f_0 and the line rotation frequency f_θ. Finding the best tradeoff between the frequencies for which the filters, impedance matching and resonance circuits are designed and the two frequencies at which the power is transmitted is beyond the the scope of this work. For this scanner, $f_0 = 25$ kHz has been chosen mainly to stay close to the presently used frequencies of other MPI scanners and spectrometers. This frequency is above the hearing range of humans but is in the hearing range of rabbits and other common laboratories animals [158]. Regarding the PNS likelihood, no stimulation is expected in the rabbit thanks to its small size and the relatively low drive-field strength used [O8].

To facilitate the implementation of the signal chains a 10 Hz line rotation frequency f_θ has been chosen. Moreover, the PNS likelihood in an operator staying around the scanner has been evaluated. The nHMIEFA in the human model shown in Figure 5.3b staying at a distance of 50 mm of the outermost coil reached a maximum of 0.03 V·Hz^{-1}·T^{-1}. This corresponds to a HMIEFA of 0.1 V·m^{-1}, for a main SHC given by current·$\eta_{Q_0} = 0.4$ T·m^{-1} at 20 Hz, which is well below the 7.3 V·m^{-1} limit presented in Figure 5.7. Thus, a line rotation around 10 Hz does not present PNS risk for persons staying next to the scanner.

Using the SF approach, sampling at $f_s = 1$ MHz to obtain information below $f_{Ny} = 500$ kHz is expected to be enough to reconstruct an image with the required resolution. 10 images per seconds could be reconstructed, with an MPI sequence using a 360 ° line rotation.

6.1.3 Realisation

The realisation of the magnetic field generators can be divided into two main units, which are divided based on the frequency range in which they are going to be used.

The drive coils, used at frequencies around 25 kHz, are realised using a litzwire to limit the increase of the coil resistance due to the skin and proximity effect. The high frequency and high current amplitudes, in association with the inductance of the coils, leads to the application of high voltages on the coils. Therefore the cooling of the set is done with an electrically insulating oil.

The selection coils, used at a frequency of 20 Hz, are realised using hollow conductors to

facilitate the cooling.

Both sets are separated by a 2 mm thick copper plate, which shield the measurement volume from high frequency perturbation arising from the selection coils. It also avoids any coupling from the high frequency signals of the drive coils in the high inductance selection coils.

6.1.3.1 Drive-coil set

Based on the simulation presented in Section 4.1.2.1 and the reduction of the coil efficiency linked to the presence of a 160 mm radius shield, the current and voltage amplitude applied to the coil can be evaluated.

The currents required by the drive coils are expected to be

$$I_{\text{peak}}^{x\text{-drive}} = \frac{c_{x00}^{R}}{\eta_{x\text{-drive}}} = \frac{0.015\,\text{T}}{(1-0.15)\cdot 51.1\cdot 10^{-6}\,\text{T}\cdot\text{A}^{-1}} = 346\,\text{A}_{\text{peak}}, \tag{6.1}$$

$$I_{\text{peak}}^{y\text{-drive}} = \frac{c_{x00}^{R}}{\eta_{x\text{-drive}}} = \frac{0.015\,\text{T}}{(1-0.34)\cdot 39.5\cdot 10^{-6}\,\text{T}\cdot\text{A}^{-1}} = 575\,\text{A}_{\text{peak}}. \tag{6.2}$$

Neglecting the small voltage arising from the resistance and the inductance, reduction expected from the shielding [159], it is expected to have maximal peak voltages of

$$\begin{aligned} V_{\text{peak}}^{x\text{-drive}} &= I_{\text{peak}}^{x\text{-drive}}\, 2\pi\, f_0\, L^{x\text{-drive}} \\ &= 346\,\text{A}\cdot 2\pi\cdot 25000\,\text{Hz}\cdot 26.7\cdot 10^{-6}\,\text{H} \\ &= 1460\,\text{V}, \end{aligned} \tag{6.3}$$

$$\begin{aligned} V_{\text{peak}}^{y\text{-drive}} &= I_{\text{peak}}^{y\text{-drive}}\, 2\pi\, f_0\, L^{y\text{-drive}} \\ &= 575\,\text{A}\cdot 2\pi\cdot 25000\,\text{Hz}\cdot 29.3\cdot 10^{-6}\,\text{H} \\ &= 2648\,\text{V}. \end{aligned} \tag{6.4}$$

Those four values show that the reduction of the dissipated power, the extraction of the generated heat and the coil electrical insulation have to be considered before the construction of the coil. Keys results are presented in the following paragraphs.

6.1.3.1.1 Litz wire In order to evaluate the dissipated power and the buildability of the coil, more information about the wire has to be obtained. The coils are wound with a litz wire. It is a type of cable woven from several single strands and used to minimise the resistance increase which happens with an increasing signal frequency due to the skin effect and the proximity effect [11]. No standard, off-the-shelf, high-frequency litz wire

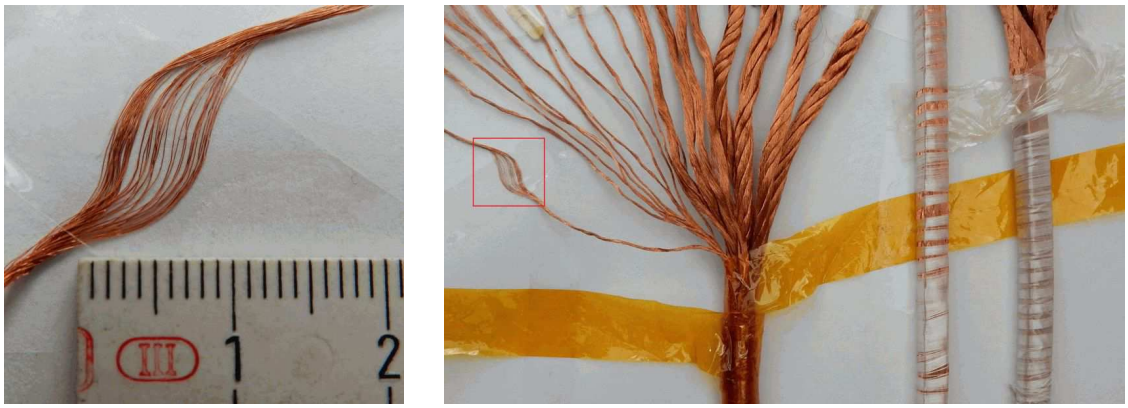

(a) (b)

Figure 6.1: Detailed view of the litz wire developed for the drive coil. (a) Closed view of a bundle of 40 63 μm strands. (b) Left: View of the 10, 5 and 5 bundles from the litz prototype. Middle and right: second wire production, without and with insulation film. Both are covered with a natural silk layer.

exists on the market. Thus, a custom product has to be designed and produced specifically for our application. The wire is constructed as a wreath, defined by the assembly of different bunch made from the single strands with given twisting and stranding, lay length and direction. The smaller strand gauge is ideally chosen as a function of f_0. But the availability of small strands, the woven feasibility, the bending radius and the cost associated with the fabrication are the factors which have limited the design.

Three litz wires have been developed in the course of this work, all using 63 μm copper strands covered with a solder-able polyurethane enamel insulation, which can withstand a voltage of 100 V. They are woven in bunches of 40, 10, 5 and 5 units, as can been seen in Figure 6.1. The litz wire is thus formed from 10000 single strands and offer a copper cross Section of 31 mm^2. It is then profiled into a square cross Section of 7.5$\pm$0.4 mm$\times$7.5$\pm$0.4 mm.

The first prototype, which can bee seen on the left part of Figure 6.1b) is then insulated with 2 polyimide film (Apical AV, Kaneka, USA) with a thickness of 100 μm and an overlapping of 50 %, leading to a 400 μm thickness of polyimide and a theoretical breakdown voltage of 128 kV. It should be noted that to validate the actual breakdown voltage of such a wire, the creepage distance should be taken into account.

In our case, this first litz prototype has been used to validate the wire stiffness, evaluate the wire temperature as a function of the applied current density with a oil cooling and validate the first design of the drive coil presented in Section 4.1.2.1. A second proto-

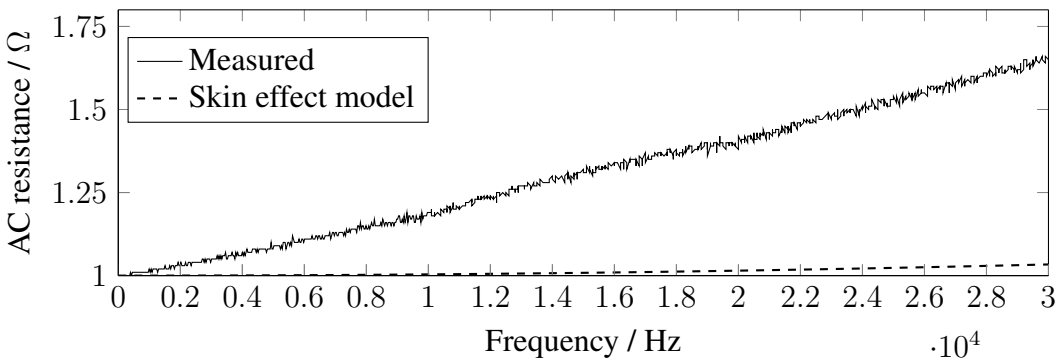

Figure 6.2: Measurement up to 30 kHz of the resistance from a 20 m Section of the second litz wire prototype. The resistance increased relative to the DC resistance is displayed.

type has been developed in two versions, with and without insulation film, as seen in Figure 6.1b. A 20 m section of the second litz-wire prototype has been used to determine its AC resistance. It has been measured from DC to 30 kHz using a precision LCR meter (E4980A, Agilent Technologies, USA). As can be seen in Figure 6.2, at 25 kHz this wire has a resistance equal to 1.5 times the DC resistance, which does not match the skin-effect model [11]. The proximity effect is thus dominant for this wire [11]. As the proximity effect is strongly dependent on the coil winding geometry, the wire resistance in function of the frequency will change for the winded coil. Unfortunatly, the high inductance associated with a coil makes the resistance measurement challenging. Thus, this measurement could not be carried out.

6.1.3.1.2 Cooling concept A cooling test has been done using 4 parallel wires with a thin (<0.5 mm) layer of epoxy glue on top, as seen in Figure 6.3. A laminar oil flow is produced in two 1.5×89 mm^2 channels below and above the wire samples. A transformer oil (Diala D, Shell Oil Company, USA) is chosen as cooling fluid to guarantee electrical insulation. A mean flow speed of 1.3 m·s^{-1} is applied. This value is chosen as a technically reasonable maximum for the coil implementation. The channel height is calculated to maximise the heat exchange rate between the surface and the fluid [160]. According to relation (6.2) and (3.36), a RMS current density of 9.3 A·mm$^{-2}_{\text{copper}}$ is required. But with our current equipment, a current density of only 6.4 A·mm$^{-2}_{\text{copper}}$ can be applied to the sample. With this current density, a stable temperature of 66 °C is measured with a thermocouple in the middle of the sample with an input oil temperature of 19 °C. Notice that a good practice is to maintain the wire temperature around 15 to 30 °C above the input cooling fluid temperature [125]. Thus, the design has been improved.

(a) (b)

Figure 6.3: (a) Cooling model used to estimate the cooling efficiency.(b) Coil prototype used to validate the wire stiffness and the coil design.

A second litz-wire prototype has been developed without any insulation besides the polyurethane layer on each strand. It contributed to the wire stiffness reduction, which reduced the diameter of the inner loops, as seen by comparing Figure 6.3b and 6.4e. The epoxy layer, used to maintain the litz wire in position, has been replaced by a mechanical design which holds the wire in a tight fit. The whole assembly can be seen in Figure 6.4. The whole set design also maximises the pressure, which could be applied by the cooling fluid in order to increase the flow speed.

6.1.3.1.3 Housing The housing has been made of $t = 4$ mm thick glass fibre reinforced plastic cylinders, which offer a good tradeoff between MPI compatibility, high Young module, low Poisson ratio, low thermal conductivity, low electrical conductance, good temperature stability, good machinability. Krülit 700 (Krüger und Sohn, Germany) has been chosen for its good characteristic. It is a parallel wound S-glass fibre composite with a high fibre to resin ratio. It is expected to have a transverse modulus of E_{GRP} of 8.9 GPa, a major Poisson ratio $\nu = 0.27$ and a transverse tensile strength $\sigma_2 = 49$ MPa [161]. The housing is closed by two polyoxymethylene (POM) rings fixed with 48 screws each. The screws are made of high tensile strength polyether ether ketone (PEEK) with a tensile strength $\sigma_{\text{PEEK}} = 91$ MPa for M5 screws with a core surface of $S_{\text{screw}} = 12.7$ mm^2. The surface between both rings $S_{\text{ring}} = 23 \cdot 10^{-3}$ m^2 on which is applied a pressure q_1 transfers the whole force on the screws. The screws can hold a maximal pressure difference before deformation of

$$q_1 = 0.5 \frac{48\, \sigma_{\text{PEEK}}\, S_{\text{screw}}}{S_{\text{ring}}} = 12.0\,\text{bar}, \tag{6.5}$$

with the 0.5 factor being chosen to model the resistance reduction from a shear stress, compared to traction forces linked to the tensile strength of the screws.

The maximal outer pressure which can be applied on the short inner cylinder of length $l = 0.4$ m with a radius $R = 88.5 \cdot 10^{-3}$ m before deformation is [162]

$$q_2 = 0.807 \frac{E_{\text{GRP}}\, t^2}{l\, R} \sqrt[4]{\left(\frac{1}{1-\nu^2}\right)^3 \frac{t^2}{R^2}} = 7.2\,\text{bar}. \tag{6.6}$$

The inner pressure which can be applied to a cylinder with a diameter of 250 mm before deformation of this part is given by [162]

$$q_3 = \frac{\sigma_2\, t}{R} = 15.5\,\text{bar} \tag{6.7}$$

To comply with the IEC standards on medical equipment [163] which impose a minimum safety factor of 3, the maximum permissible working pressure of the housing is limited by the inner cylinder at a relative pressure of 2.4 bar. This can be guaranteed by measuring the absolute pressure of the cooling fluid, which should not go above 3.4 bar.

Both coils are kept at a minimal distance of 1.5 mm using a POM spacer. Between the spacers flows the transformer oil, which provides both the heat exchange and electrical insulation functions. The channel can be visualised in Figure 6.4d. The 1.5 mm oil layer provides a minimal breakdown voltage of 15 kV [164].

6.1.3.1.4 Validation The coil set designed in Section 4.1.2.1 is implemented using the second litz-wire prototype and an housing supporting a maximal cooling-fluid absolute pressure of 3.4 bar for a laminar forced convection oil-cooling with an unknown efficacy. To assess the efficiency, a variable DC current has to be used. To compare with the usage of the set, the expected power dissipation of the set has been evaluated. The cooling fluid pressure is measured with Bourdon pressure gauges. The input pressure of 1.4 bar and a pressure difference of 1 bar are applied using a pump (Neptun NGP 100i, Bauhaus, Germany). The oil flow is measured at a rate of 40 l·min^{-1} (EZ-View flow meter, Badger Meter, USA). A mean flow speed of 0·16 m.s^{-1} is thus expected in the cooling channel. The input temperature is maintained at a constant 19 °C via the building cooling circuit. Currents of 500 and 600 A are applied on the first and second drive coils, which result in a dissipated power in the coils of 2.3 and 4.1 kW. The coil temperature is measured on one point for each coil via a PT2000 sensor (32 208 541, Heraus, Germany), and is held at 42 and 40 °C with variation of ± 2 °C for 45 minutes, respectively. This temperature variation is associated with the variation of the input temperature.

At 25 kHz, coil resistances of 21 mΩ and 27 mΩ have been evaluated, which is 64 % and 87 % higher than the resistance measured from the wire alone. This resistance increase

(a) (b) (c)

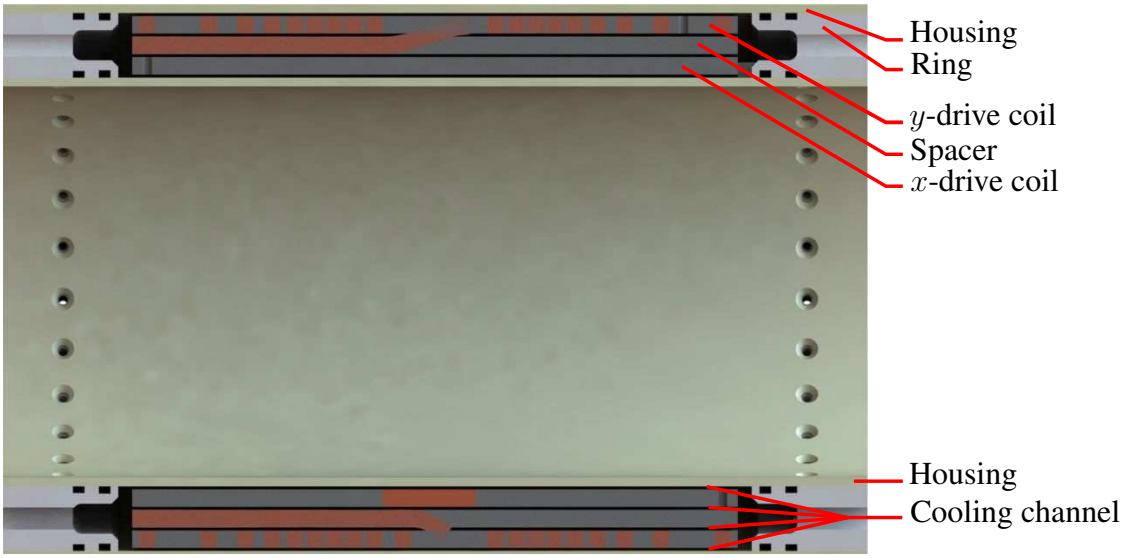

(d)

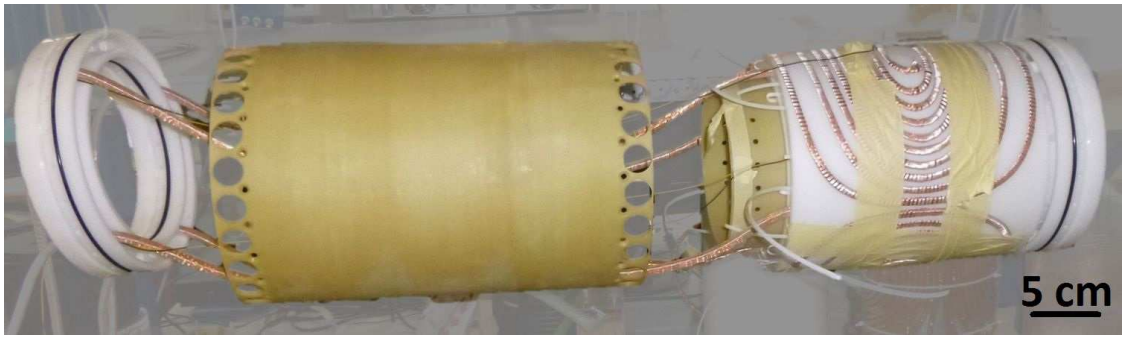

(e)

Figure 6.4: Computer model of the drive coil components. (a) x-drive coil inside its form. (b) y-drive coil inside its form. (c) Housing assembled with the two rings. (d) Cross Section in the yz plan of the whole coil set. (e) Elements before final assembly.

is associated with the eddy-current losses in the magnetic field shield and the additional proximity effects added by the winded pattern of the coils [165]. Thus, it is expected that the coils will dissipate 2.3 and 4.1 kW with RMS currents of 319 and 384 A or peak current of 639 and 767 A. This in turn could produce a magnetic field strength of up to 28 and 22 mT_{peak}, respectively.

The coil efficiency could not be measured at 25 kHz, but the DC SHCs up to order and degree $m = l = 5$ have been measured using a Hall probe, a Gaussmeter (MMZ-2508-UH and Model 460, Lake shore, USA) and a robot (3D set of linear axis, isel Germany AG, Germany). It is challenging to asses the precision of the SHC measurements, as it implies to measure at positions for which the magnetic fields strength is zero. To asses the uncertainties, the magnetic field at the points required to make the SHSE has been measured for all five coils of the rabbit-sized FFL imager. Summing 324 measurements on 18 points, a magnetic flux-density mean standard deviation of 24.5 μT and a mean relative standard deviation of 1.1 % have been obtained. Those deviations are probably associated with many effects, including but not limited to the current fluctuation during the 18 minutes required for the measurement of a SHC set, the measurement set-up vibration due to the robot movement, the positioning error of the robot and the measurement error of the sensor. In Figures B.7 and B.8 the obtained SHSEs can be compared with the simulated one given in Figures 4.8c and B.4. The transformation between the coordinates has been taken into account by comparing the root square values of the SHC for all three magnetic field components. The main SHCs are measured, using each time a current of 100 A, for the x-drive coils at 51.7 $\mu T \cdot A^{-1}$ and 39.7 $\mu T \cdot A^{-1}$ for the y-drive coil. This deviate from the simulated values by +1.1 % and +0.4 % for the x- and y-drive coil, respectively. Up to the expected RMS currents and considering the relative measurement error, the magnetic fields strength depends linearly on the current amplitude.

6.1.3.2 Selection-coil set validation

The selection-coil set, presented in Figure 6.5 with the drive-coil set inserted, is constituted, as indicated in Table 2.2, of a solenoid and two quadrupoles. All three coils are wound on top of a 320 mm diameter, 2 mm thick copper shield in a glass fibre matrix. The coil concept and centroid design has been done by the author, whereas the exact conductor path and the coils realisation has been carried out under the author's advice by the company Futura Composites, the Netherlands.

The quadrupoles are used at a frequency of $2f_\theta = 20$ Hz, for which the quasi-static approximation is still reasonable. Thus, hollow copper conductors are selected to wind those coils and the DC resistance is used to estimate the dissipated power. A 6×6 mm^2

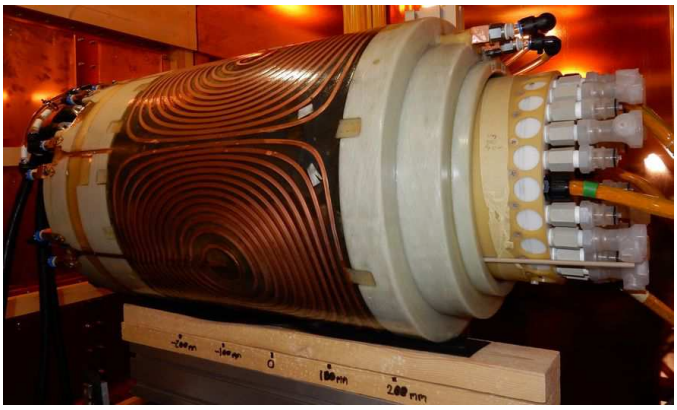

Figure 6.5: Selection-coil set on its support, with the last layer of the quadrupoles visible. On the right, the end of the drive-coil set is visible.

conductor, with a circular hollow Section of diameter 3.5 mm, is chosen to wind both quadrupoles. It offers a compact design, which can be water-cooled using a turbulent forced heat convection mechanism [166]. With the design presented in Figure B.5, Tables B.1 and B.2, one segment of each layer is cooled in series with one segment of the second layer. With a pressure drop of 8 bar, a flow rate of around 50 $l \cdot min^{-1}$ and an input-temperature of 19 °C, the water output temperature is expected to stay below 45 °C when generating our target magnetic field.

The actual Q_0 and Q_{45} quadrupoles dissipate 9.3 and 12.9 kW with RMS currents of 428 and 480 A, respectively, requiring 16 % and 18 % more power than expected. This is due to the connection wire and the conductor length which was not modelled. Using the same measurement protocol as for the drive-coil sets, the SHSE of the quadrupoles is presented in Figures B.9 and B.10, which can be compared with the simulated ones displayed in Figure 4.9 and B.6. The main SHCs are measured for the Q_0 and Q_{45} quadrupole at 644.1 $\mu T \cdot m^{-1} \cdot A^{-1}$ and 578.6 $\mu T \cdot m^{-1} \cdot A^{-1}$, respectively. Both measures have been done with a current of 400 A in the coils. This deviates from the simulated values by -2.5 % and -2.0 % for the Q_0 and Q_{45} quadrupoles, respectively.

Moreover, as the quadrupoles have to be used with a low frequency, their efficiencies have been evaluated with a sinusoidally varying current amplitude. The magnetic field strength as a function of the frequency has been measured with a Hall probe and a Gaussmeter (MMZ-2508-UH and Model 460, Lake shore, USA) between 20 and 100 Hz. The result is shown in Figure 6.6. According to simulations done with the model presented in Section 4.1.1.19, the strong decrease of the efficiency with increasing frequency could not be explained by the shielding effect of the 2 mm thick copper shield. It is possible

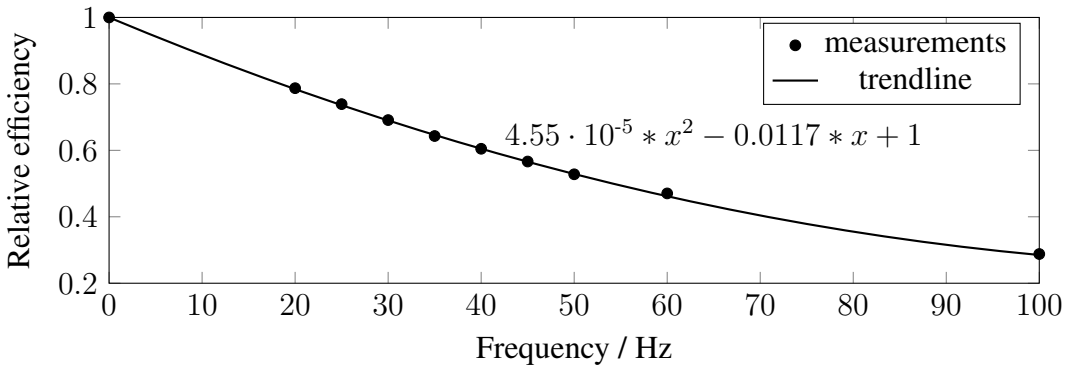

Figure 6.6: Relative efficiency of the quarupole Q_{45} in function of the frequency.

that the solenoid actually shields the field. Nevertheless, a reduction of the efficiency of 21% is expected when using the quadrupole at a frequency of 20 Hz.

The solenoid is used with a DC current and is also wound with a hollow conductor. Using a 8×13 mm^2 conductor with a 9×4 mm^2 opening, a dual-layer solenoid with mean diameter of 335 and 363 mm can generate the required field with a dissipated power of 12.1 kW. This requires 40 loops per layer and a DC current of 750 A. Each layer is cooled separately, using a water flow rate of 250 l·min^{-1} leading to a pressure drop of 8 bar. A water input-temperature of 19 °C leads to a water output temperature of 33 and 35 °C for the first and second layers, respectively.

The actual solenoids dissipate 13.6 kW with an RMS current of 750 A, dissipating 12 % more power than expected. This is also associated with the connector length and the higher conductor length between the design and realisation. Using the same material for the solenoids as for the drive-coil set, the main SHSE has been measured at 600 A and is displayed in Figure B.11. A main SHC of 1036 μT·m^{-1}·A^{-1} is calculated, which is 2.8 % smaller than simulated.

The whole selection-coil set can use the same cooling circuit, requiring a flow rate of $2 \cdot 250 + 8 \cdot 50 = 900$ l·min^{-1} with a pressure loss of 8 bar for each circuits. This is provided by a single pump (MH1405-2, Wilo, Germany) which is frequency-regulated to adapt the pressure to the power requirements using a variable frequency drive (ST 9100, Sourcetronic, Germany).

6.1.4 Expected MPI-properties

To assess the expected quality of our signal acquisition, further MPI-data optimisation possibilities and to point out the differences between FFP and FFL imaging devices, it is

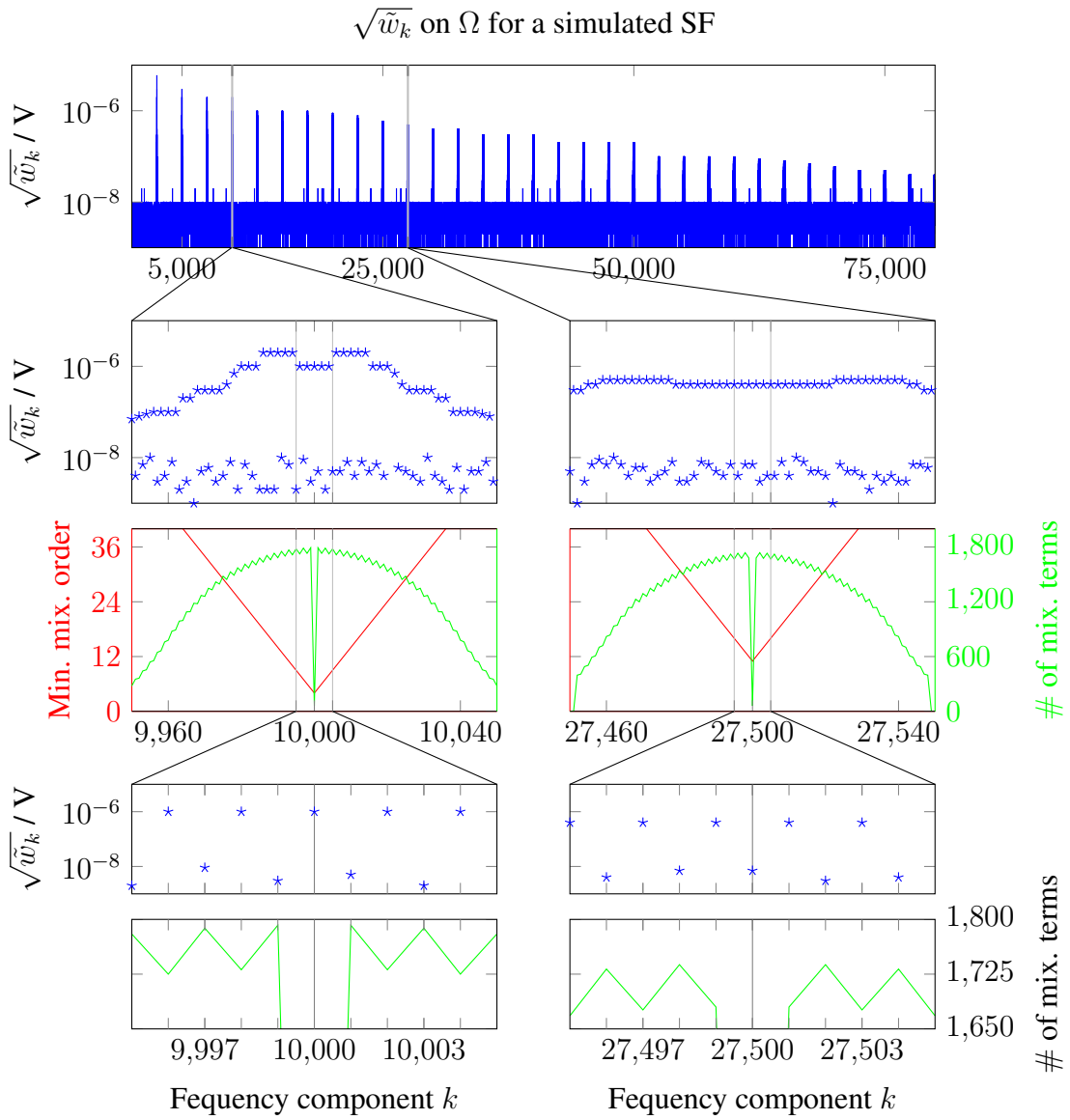

Figure 6.7: Energy repartition of a simulated SF for the x channel of the rabbit-sized FFL scanner. Two closer view are done around the 4th and the 11th harmonics. The minimal mixing order and the number of mixing terms forming each frequency is given in the lower part of the Figure.

useful to analyse at the expected MPI-properties of this FFL scanner. The simulated data presented here are realised with the simulation framework presented in Appendix E.

The energy repartition of an SF $\tilde{w}_k$ as defined by equation (2.56) as a function of the frequency is given in Figure 6.7. This has been simulated with $f_{\text{drive}} = 25$ kHz, $f_\theta = 10$ Hz, $T_\text{a} = 100$ ms, $f_\text{s} = 2$ MHz with a gradient on the line of 0.8 T·m^{-1} and both

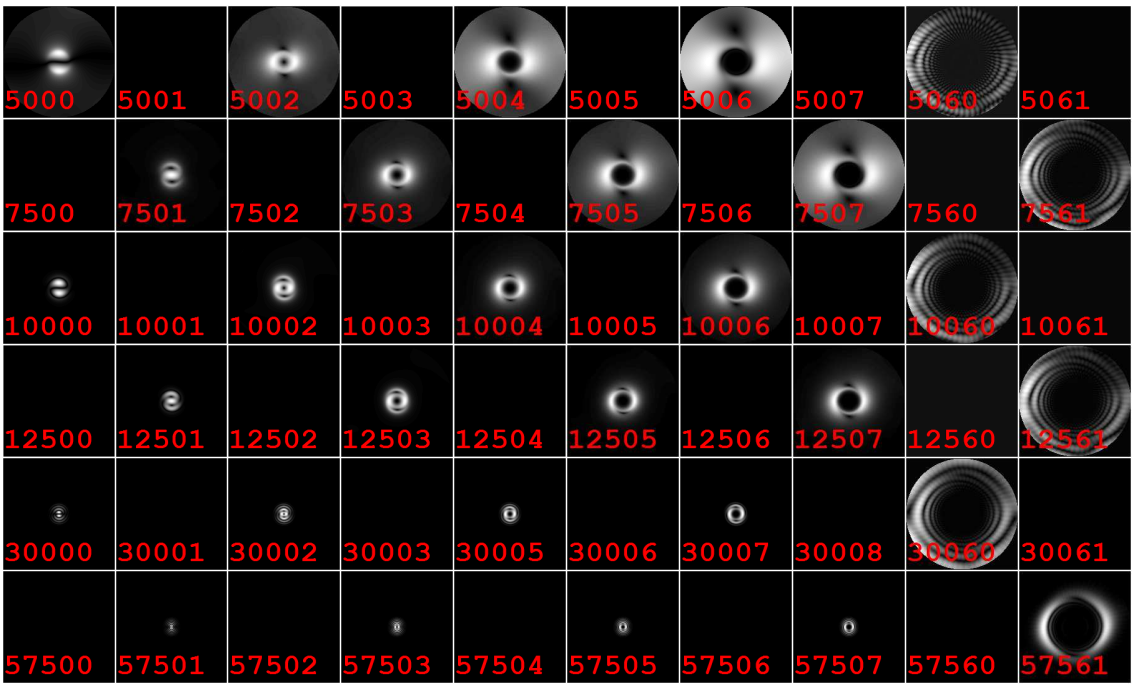

Figure 6.8: $\|\hat{s}_k^{(3)}\|$ in the x channel simulated with $\Delta f = 10$ Hz and $f_{\text{drive}} = 25$ kHz. The FC used for each image is written in the bottom left corner. Every pair (5000 and 5001, 7502 and 7503) is using the same scaling, which is different for all pairs.

drive coils generating a main SHC of 15 mT. The SF is calculated using a cubic tracer probe of $1\times1\times1$ mm^3 filled with a tracer having an equivalent iron concentration of 1.5 mol(Fe).m^{-3} and a mono-disperse core-diameter distribution of $d_{\text{np}} = 30$ nm (that is a model for a solution of Resovist diluted 10 times with water) and a noise created with $R_{\text{p}} = 822 \cdot 10^{-6}\ \Omega$. This gives a $\Delta f = 10$ Hz and a second harmonics at 50 kHz by the FC $k = 5000$. The whole process is done in a FOV of 180×178 mm^2. The mix-products have been calculated for mixing power smaller than 60 and maximal mixing order of 40. Those results can be compared with the equivalent information for a 3D FFP scanner as presented in Figures 2.17, 2.18 and 2.19.

It can be seen that most of the energy is situated in small frequency bands with a bandwidth of only 4 kHz at the 34th harmonics. Note that the measurable bandwidth highly depends on the noise level of the scanner.

The structure of each energy peak is also different from the Lissajous based FFP imaging device. The energy around each pure harmonics has an amplitude shaped as an 'M'. As presented on the middle of Figure 6.7, this can neither be explained by looking at the minimal mixing order nor by taking the number of mixing terms into account. The

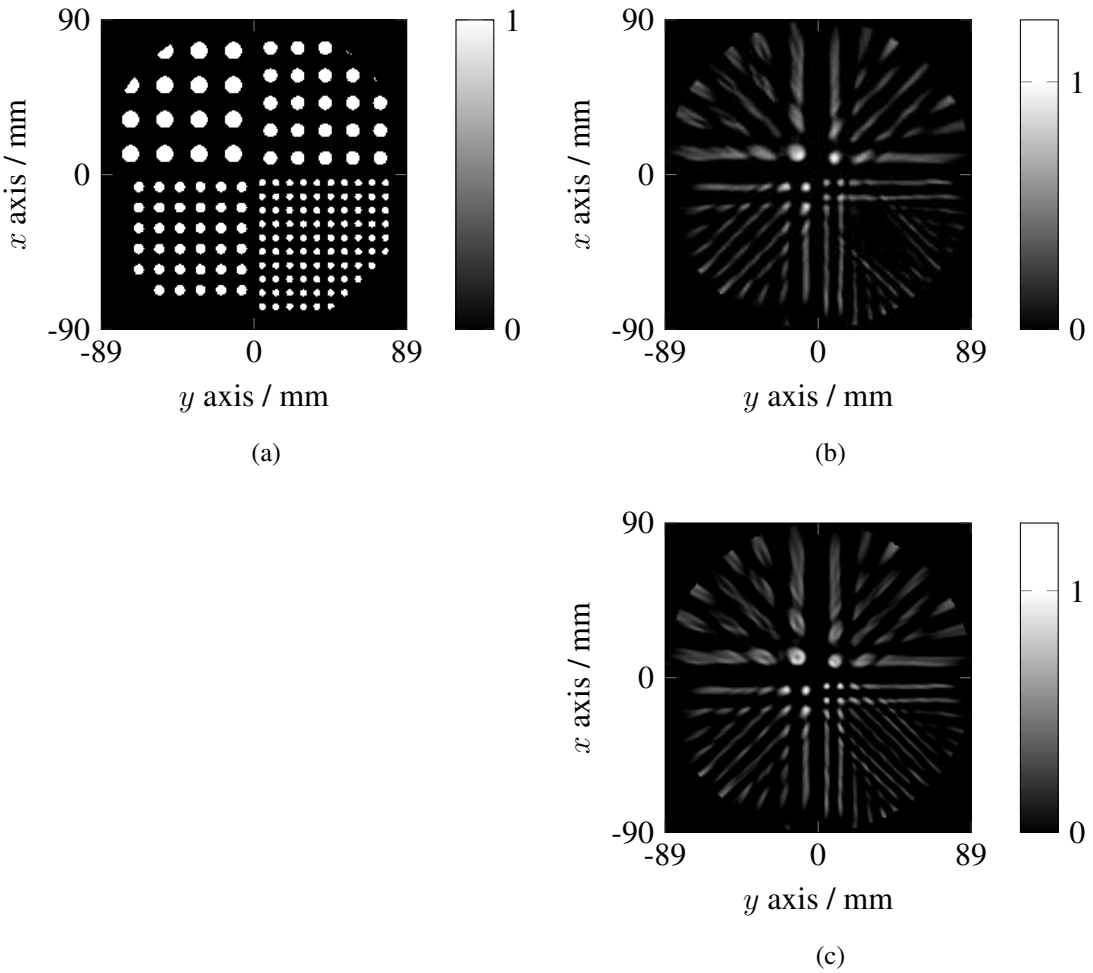

Figure 6.9: Expected reconstruction with the presented FFL scanner. (a) Phantom made of 4, 6, 8 and 10 mm diameters circles. (b) Reconstruction with a 300 kHz bandwidth. (c) Reconstruction with a 450 kHz bandwidth.

relatively small amount of mixing terms for pure harmonics is explained by the limitation of the mixing power and order. Indeed, to let the 10 Hz components influence the number of mixing terms by the fourth harmonics, mixing power and order of above 2500 are required, but are here limited to 60 and 40. Moreover, the sawtooth seen in the number of mixing terms is inversely correlated with the high energy peaks.

Another difference can bee seen by comparing the bottom plots of Figures 6.7 and 6.8. Only the even pure harmonics contain energy. This means that the minimum mixing order curve alone cannot be related to the energy structure in the MPI signal for the presented FFL scanner. This represent a huge difference with the signal-energy repartition of the 3D Lissajous FFP imaging device, where this information could be used to filter the MPI

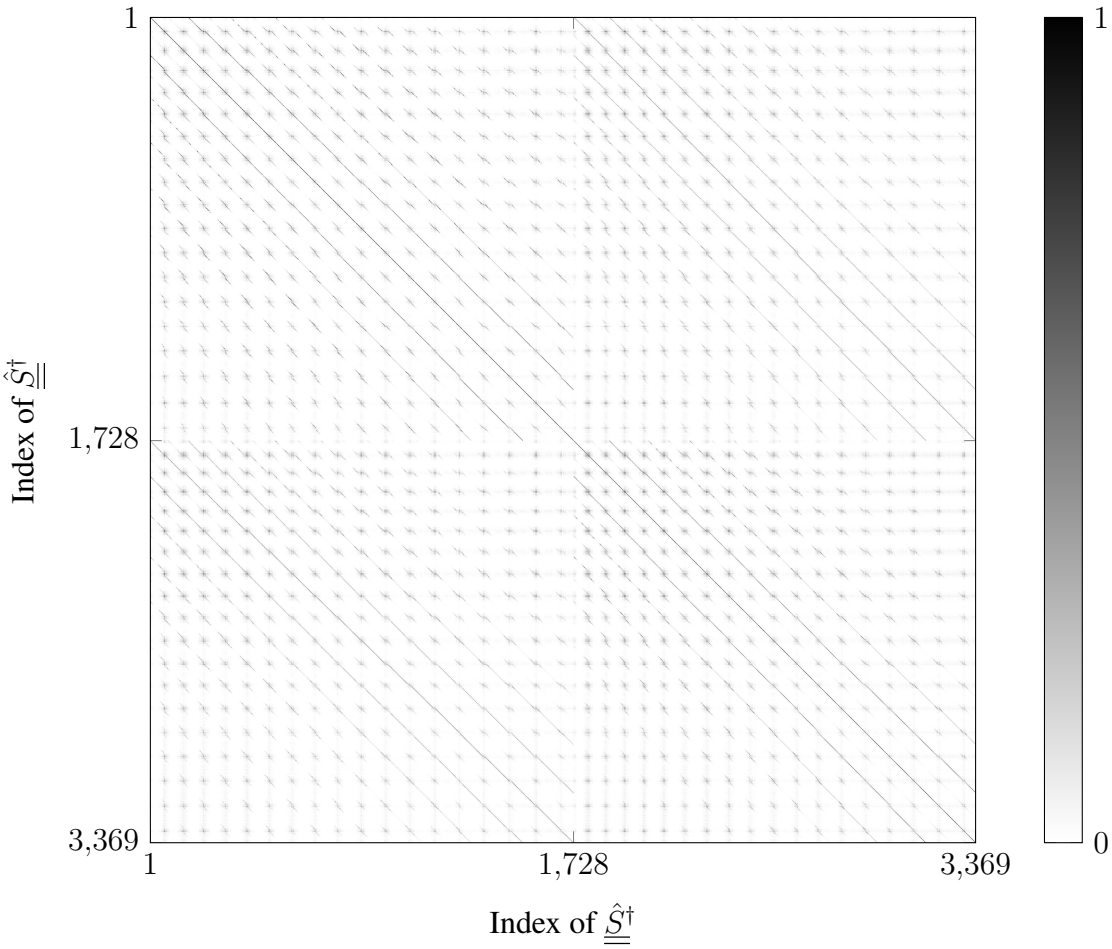

Figure 6.10: Orthogonality plot between the FCs of a tSF regrouping both receive channels. A black point means that both FCs are similar, whereas a white point means that there is no similarities between two FC. One regroups 1728 FCs and the other 1641.

signal [60, 32].

Despite the presence of high mixing order and what may be interpreted by high spatial variation in the SF components, as can been seen on the component 5060 in Figure 6.8, a large bandwidth is required to obtain satisfying reconstructed images. Figure 6.9 presents the simulated reconstruction for the phantom made of 4, 6, 8 and 10 mm diameters circles using a bandwidth of 300 and 450 kHz, corresponding to 12 and 18 harmonics. Both signals have been generated from a phantom having a resolution of $0.77\times0.77\times1$ mm^3 and the same tracer properties and concentration as for the SF simulation. The noise added on the simulated particle signal is generated with a high resistance of $R_\mathrm{p} = 185 \cdot 10^{-3}\ \Omega$. The SNR is calculated using the AS according to $\mathrm{SNR}_\mathrm{S}^{(4)}$ and used as a threshold.

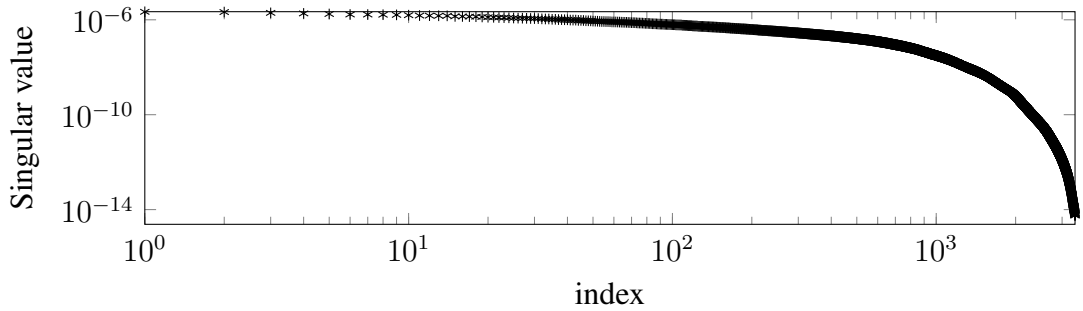

Figure 6.11: Singular values obtained from a tSF of a continuously rotated 2D FFL scanner.

Frequency components leading to frequencies higher than 49990 Hz, lower than 350 or 500 kHz and having an SNR higher than 20 are kept for the reconstruction. For both reconstructions, the iterative algorithm is stopped at the fourth iteration. The results are shown in figure 6.9. By visually inspecting the reconstruction, the fully sampled area is evaluated to have a diameter of 37 mm, which is 12 % smaller than expected from the ISIC model.

Looking at the orthogonality of the tSF used for the reconstruction shown in Figure 6.10, structures similar to the one observed in Figure 2.20 are present. This also includes the coupling between tSF FCs from both channels. Looking at the singular values obtained for the used tSF shown in Figure 6.11, it can be seen that the problem is still severely ill-posed. But compared with the 2D FFP imaging device; a smaller condition number of $8.8 \cdot 10^8$ is calculated for a tSF containing almost two time more FCs. This smaller condition number of the tSF is a first explanation of why the introduction of a Tikhonov regularisation is not required to obtain a first satisfying reconstruction. But other additional regularisation could still be used to further reduce artefacts.

6.1.5 Discussion

The field generators designed and constructed for the rabbit-sized FFL scanner are able to produce the expected field shape for a period of time long enough to record a SF. The acquisition of a SF with a resolution of 1×1 mm^2 as displayed in Figure 6.8 is expected to take around 100 minutes. But before acquiring MPI signals with this imaging device, the filters, impedance matching and power factor correction have to be installed.

The presented drive-coil set can also be later used in an improved scanner. The cooling used for the drive coils can already support the generation of fields with main SHCs 46

and 86 % higher. Further increasing the current amplitude used on the drive-coil set and the selection-coil set will require upgrades to the power supplies, filters and impedance matching circuits. Additionally, the thermal stability of the setup should be further tested. Nevertheless, this could be used to increase the fully sampled FOV and/or to generate higher gradients.

f_θ could also be increased until the voltage across the coil reaches 1 kV. For a 0.8 T·m^{-1} gradient, this limit will be exceeded for a f_θ around 250 Hz. Increasing f_θ will directly increase the image acquisition rate of the scanner. From the SF perspective, the energy repartition and the structure of the SF will be changed. To assess the effect of those changes, a study should be carried out for each frequency, as no analytical formulas exist to describe them.

Using the Radon approach and relations (3.1) and (3.3), an optimal f_θ can be estimated for a constant number of measurements per projection $n_{\mathrm{pp}\gamma} \approx 40$. To fulfill relation (3.4) $f_\theta = 1250$ Hz with $f_\mathrm{s} \approx 2$ MHz has to be used, with the exact value depending on the sampling scheme chosen (see relation (3.3)). Further development of the models have to be carried out in order to calculate the expected resolution of this approach, taking into account the non-ideal magnetic field topology and the different sampling scheme.

Thus, to evaluate the maximal f_θ, the electrical insulation of the quadrupole has to be revised to go beyond 250 Hz. Moreover, the filters and impedance matching circuits have to be redesigned to further support the power transmitted (which is transmitted at both frequencies $f_0 \pm f_\theta$). Finally, a new selection-coil set design, removing the strong dependency of the quadrupole efficiency on the frequency, should be investigated.

Considering the nHMIEFA of 0.03 V·Hz^{-1}·T^{-1} for a human staying at a distance of 50 mm and a gradient of 0.8 T·m^{-1}, 30 V·m^{-1} could be induced in the person for $f_\theta = 1250$ Hz. This is more than 4 times the PNS thresholds proposed in [140]. Thus, to safely use such a scanner, the personal access to the magnet should probably be limited or the gradient strength reduced.

The field shapes used in this scanner produce a LFV shaped as a line. The LFV where the magnetic flux-density is smaller than 3 mT, from where a large part of the signal comes from [1], crosses the whole scanner bore for any θ when no drive fields are applied. The application of the drive will translate the LFV closer to the bore, increasing the influence of the SHCs of higher degree and order, thus deforming the LFV, making it look like a banana or even split it in many parts. Furthermore, the line will not reach the bore with a reasonable drive-field strength, thus limiting the actual FOV of the scanner. As shown in Figure 3.8, the maximal diameter of the fully sampled area should be covered using drive coils with a field strength three times higher or 45 mT$_{\mathrm{peak}}$.

Visually inspecting the FFL SF, only one symmetry axis can be seen, which is one less than the FFP SF presented in this work and studied by Weber and Knopp [167]. In their study, the authors uses the symmetry axis to reduce the time required for a SF acquisition. This is done by sampling only 25 % of the FOV and adding overlapping region. For an FFL, it can be expected that 50 % of the points instead of 25 % will have to be acquired. The amount of overlapping has to be determined experimentally. The influence of the realistic field topology and the actual symmetry are still being investigated to confirm this assumption. Furthermore, information from the fully sampled area seems to be coded in the first mix-product, whereas the one coding the outer seems to be coded by mix-products with higher frequencies.

The structure of the tSF has an higher condition number, which allows reconstruction of the images without having to add other knowledge besides the MPI-signal SNR, scanner properties and the number of iterations. This could be very useful to obtain a first reliable reconstruction, which does not require the selection of an arbitrary regularisation parameter.

Despite all the effort done in this work, a minimal acquisition bandwidth of 450 kHz is still required to reconstruct satisfying images. This does not mean that the acquisition bandwidth could not be further reduced, or split in some separate frequency ranges, but the sophistication level of the frequency selection should be probably increased to achieve such a result. It is interesting to try to reduce the acquisition bandwidth further, as this will further increase the MPI-signal SNR. Indeed, future imaging devices are expected to be limited by the patient noise, which can be modelled by a Johnson noise as shown by relation (2.72) and reduced by reducing the acquisition bandwidth.

To further increase the SNR of the MPI signal, it may be required to either increase the sampling frequency or the acquisition time in order to average the signal. The first approach will increase the digitalisation process complexity, whereas the second one will reduce the image acquisition rate.

Finally, to confirm the presented results and the small bandwidth required to reconstruct images, a measured SF should be acquired and analysed. Indeed, the actual scanners are not limited by the patient noise, but by a wide range of noise sources which have to be identified and reduced, either mechanically - by removing the source or improving the shielding of the system - or digitally, by carefully selecting the clean frequency and filtering the spurious signals. As those sources are not modelled in our simulation, and are strongly dependent on the actual implementation of an imager concept, their effects on the reconstruction are not predictable.

The presented design offers also the possibility to test other sequences such as the radial

trajectory [43]. This can be tested by turning the quadrupole-power supplies off.

6.1.6 Conclusion

The coils which generate the magnetic fields required to create and encode the MPI signal have been designed and constructed. Using state-of-the-art optimisation techniques, the obtained design is a tradeoff among the heat dissipation, the maximum current amplitude and the peak voltage.

Moreover, the magnetic field topology has been carefully characterised to refine the model base reconstructions.

Custom litz wires cooled by a laminar oil flow have been used to construct the drive coil, which can generate up to 186 % and 146 % of the initially designed main SHC of 15 mT. The selection coils have been made of hollow copper wire and can dissipate around 15 % more power than originally required without heating the cooling fluid over 50 °C. For the presented scanner concept, the maximum selection field strength is limited by the available power supply.

Associated with the correct filters, impedance matching, power factor correction and power supply, the whole scanner can achieve an image rate of 10 images per second, using a SF-based reconstruction in a circular fully sampled area having a diameter of approximately 37 mm.

In future designs, both the FOV and the acquisition rate could be increased.

6.2 Human-sized FFL scanner

To apply MPI in the clinic, a large FOV and fast acquisition are to be preferred [168]. Using an FFL scanner, it has been shown that data could be acquired in the whole bore diameter of the scanner, but the exactitude of the reconstructed image should be improved, especially in the region outside the fully sampled diameter. In this Section, an original approach to extend the FOV of a human-sized FFL imaging device using focus fields is presented. A part of those results have been presented here [O10].

6.2.1 Concept

Increasing the drive-field strength in order to increase the fully sampled region is an approach, which is limited at least by the PNS, as described in Chapter 5. To cover a circle with a radius of 150 mm with a magnetic flux-density gradient strength of 1 $T \cdot m^{-1}$, a

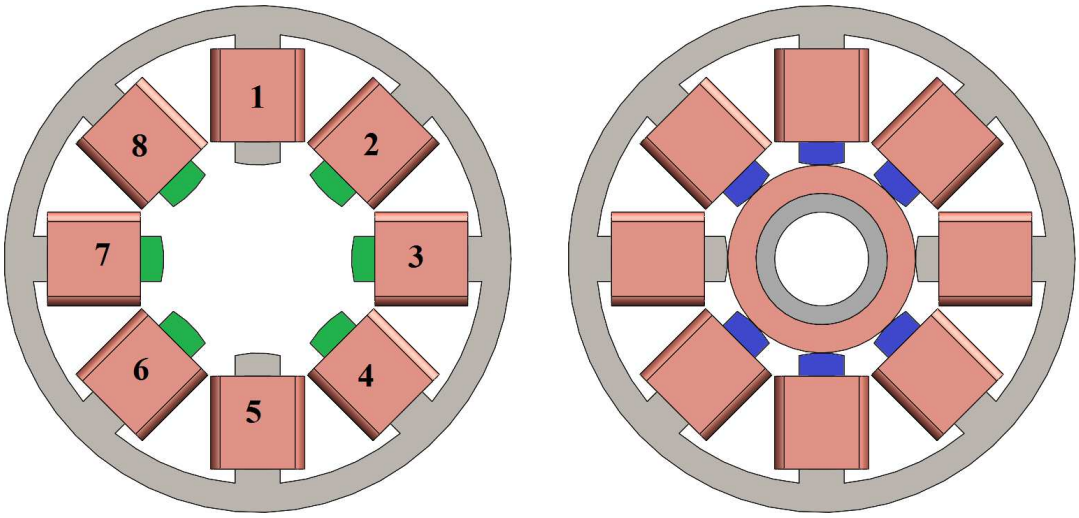

(a) (b)

Figure 6.12: Front view of the human FFL scanner concept. (a) The poles used to generate the y-focus field are highlighted in green. (b) The poles used to generates the x-focus field are highlighted in blue. Inside the quadrupole is a solenoid and x- and y-drive coils.

magnetic flux-density of 300 mT peak to peak should be applied. This could be achieved by either substantially decreasing or increasing the excitation frequency compared to the 150 kHz for which experimental data exist. As it is preferred to keep the encoding speed high, increasing the frequency in the MHz range is a solution which could be studied. From a safety point-of-view, this could replace the PNS limitation by an SAR one, as seen in the Chapter 5. Instead, a tradeoff using an excitation frequency at 150 kHz with a low frequency focus field is considered.

The magnet design done in Section 4.2 is used as the generator of the selection and the focus fields. The later is generated using the three upper and lower poles for one direction and the three on the left and on the right for the other direction as presented in Figure 6.12. Ignoring the magnetisation saturation of the pole, those focus-field generators have an efficiency of $\eta_{x\mathrm{FF}} = 0.5$ mT·A^{-1} when they are made of 250 loops.

The magnets used for this concept have been designed for the acquisition of a SF of a conventional FFL imaging device with a continuously rotating line. This is the most demanding mode of operation of the scanner, as the stability has to be guaranteed for the whole time during which the SF is acquired. Thus, the current density has been kept low to avoid any high temperature gradient inside the system which is the main source of instabilities [125]. The numbers presented here are the results of the first steps of an iterative design. Modifications could be done to all the aspects, which are not directly

linked to the current density. For example, the number of turns in the winding around each pole could be adapted to facilitate the impedance matching of the magnets. The solenoid should be wound with a conductor thin enough to limit the efficiency reduction due to the eddy-currents. The drive coils are designed to be far from the solenoid and the shield associated with it to maximise the coil efficiency. As those coils are used as drive and receive coils, this will also lead to a higher amplitude of the induced particle signal. The litz wire foreseen to wind this coil has a square cross Section of 15×15 mm^2. To be able to wind a coil despite the wire stiffness, a design with only 3 loops is planned. Taking into account the shield, an efficiency of $\eta_{x\text{-drive}} = 5.4 \cdot 10^{-6}$ T·A^{-1} is expected. Further details are given in Appendix B in Table B.3. The whole scanner has a bore diameter of 500 mm, which can accommodate a human subject.

The SHCs of the drive, quadrupole and focus-field magnets are similar to the one shown in Figures 4.7 and 4.10c and are therefore not included here.

The next design iteration step should include the results presented here; i.e. the expected magnetic field flux-density and the required frequencies for each poles of a focus-field based MPI sequences.

6.2.2 Choices of frequencies

Following the results of Chapter 5, an excitation frequency of 150 kHz is chosen for the x- and y-drive fields, which generates a magnetic flux-density with a main SHC of 3.6 and 4.8 mT. These amplitudes are chosen to be at the PNS limit.

The focus-field frequency is chosen so that the imaging device delivers at least 10 images per second. The case for which the signal is processed after each single image acquisition is considered. This results in an acquisition time $T_\text{a} = T_\text{Rs} = 0.1$ s and a spectrum resolution of $\Delta f = 10$ Hz. As $f_0 = 150$ kHz is also an integer multiple of Δf, the whole MPI-signal spectrum will be properly resolved.

The FOV is extended by moving the LFV rotation centre in space. The time dependent position of the rotation point is described by the function $p_{\text{FF}x}$ and $p_{\text{FF}y}$ used in relation (3.38). As an example, the rotation point is moved along a Lissajous curve. The Lissajous figure is chosen over other simple trajectories like a circle or an oval, as it is expected to better cover the centre of the surface. The two frequencies used to describe the Lissajous figure, $f_{\text{FF}x}$ and $f_{\text{FF}y}$, create 4 additional frequencies in the signal, as described by relations (3.41) and (3.42). To properly resolve all those frequencies and their mix-products, they have to be integer multiples of Δf. Describing those frequencies as a product of a natural number with Δf, 4 relations are used to ensure that the whole signal

component can be properly resolved. First, the frequencies used to describe the Lissajous figure are defined as

$$f_{\mathrm{FF}x} = n_{\mathrm{FF}x}\,\Delta f, \tag{6.8}$$

$$f_{\mathrm{FF}y} = \frac{N_{\mathrm{D}}}{N_{\mathrm{D}}+1}\,n_{\mathrm{FF}x}\,\Delta f, \tag{6.9}$$

with $n_{\mathrm{FF}x} \in \mathbb{N}$ according to relation (2.45). Moreover, the 4 additional frequencies introduced by the focus fields should also be properly resolved, which leads to the relations

$$\frac{2\,f_\theta \pm f_{\mathrm{FF}x}}{\Delta f} = 2\,n_\theta \pm n_{\mathrm{FF}x} \in \mathbb{Z}, \tag{6.10}$$

$$\frac{2\,f_\theta \pm f_{\mathrm{FF}y}}{\Delta f} = 2\,n_\theta \pm \frac{N_{\mathrm{D}}}{N_{\mathrm{D}}+1}\,n_{\mathrm{FF}x} \in \mathbb{Z}, \tag{6.11}$$

with $f_\theta = n_\theta\,\Delta f$, $n_\theta \in \mathbb{N}$. Relation (6.11) is fulfilled only for $N_{\mathrm{D}} + 1 = n \cdot n_{\mathrm{FF}x}$, with $n \in \mathbb{N}$. It can be noted that the rotation centre will be moved n_{Lis} times along the Lissajous curve, with

$$n_{\mathrm{Lis}} = \frac{T_{\mathrm{Rs}}}{T_{\mathrm{Rl}}} = \frac{N_{\mathrm{D}}+1}{n_{\mathrm{FF}x}}. \tag{6.12}$$

Considering $N_{\mathrm{D}} = 2$, $f_{\mathrm{FF}x}$ could be equal to $30, 60, 90, \ldots$ Hz and f_θ to $10, 20, 30, \ldots$ Hz. For this scanner, $T_{\mathrm{Rs}} = 0.1$ s, $N_{\mathrm{D}} = 2$, $n_{\mathrm{FF}x} = 9$ and $n_\theta = 2$ has been used. Thus, in one repetition, the line is rotated $n_\theta = 2$ times and the rotation points will go $n_{\mathrm{Lis}} = 3$ times over the Lissajous curve. Those coefficients have been minimised, to reduce the MIEFA, while reconstructing a phantom equivalent to the one seen in Figure 6.13, free of any area from which no information at all could be reconstructed.

6.2.3 Expected MPI properties

A simulation study has been carried out to determine, which focus-field strengths are required to cover a FOV of 400×405 mm^2, which represent the biggest part of the 500 mm diameter inner bore. It has been done using a SF resolution of 1×1 mm^2, a phantom resolution of 0.5×0.5 mm^2, a resistance of 33 and 185 mΩ for the generation of the noise on the SF and the measurements. The tracer is simulated as a mono-disperse solution of SPION with $d_{\mathrm{np}} = 30$ nm, with a concentration of 15 mol(Fe).m^{-3} (that is a model equivalent to a solution of Resovist undiluted). The signals have been simulated with $f_{\mathrm{s}} = 4$ Mhz and the reconstructed images have been obtained with frequencies from 50 to 500 kHz having a $\mathrm{SNR}_{\mathrm{S}}^{(4)}$ higher than 6. A single period of the sequence has been simulated, leading to a spectral resolution of $\Delta f = 10$ Hz. The reconstruction has been stopped after 50 iterations. The field of view has been divided into 25 sub-areas,

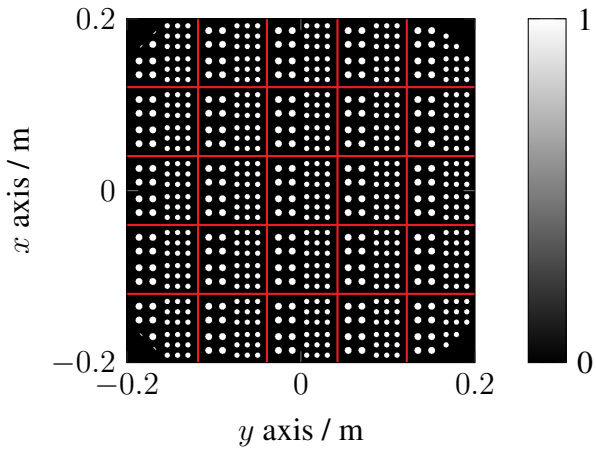

(a)

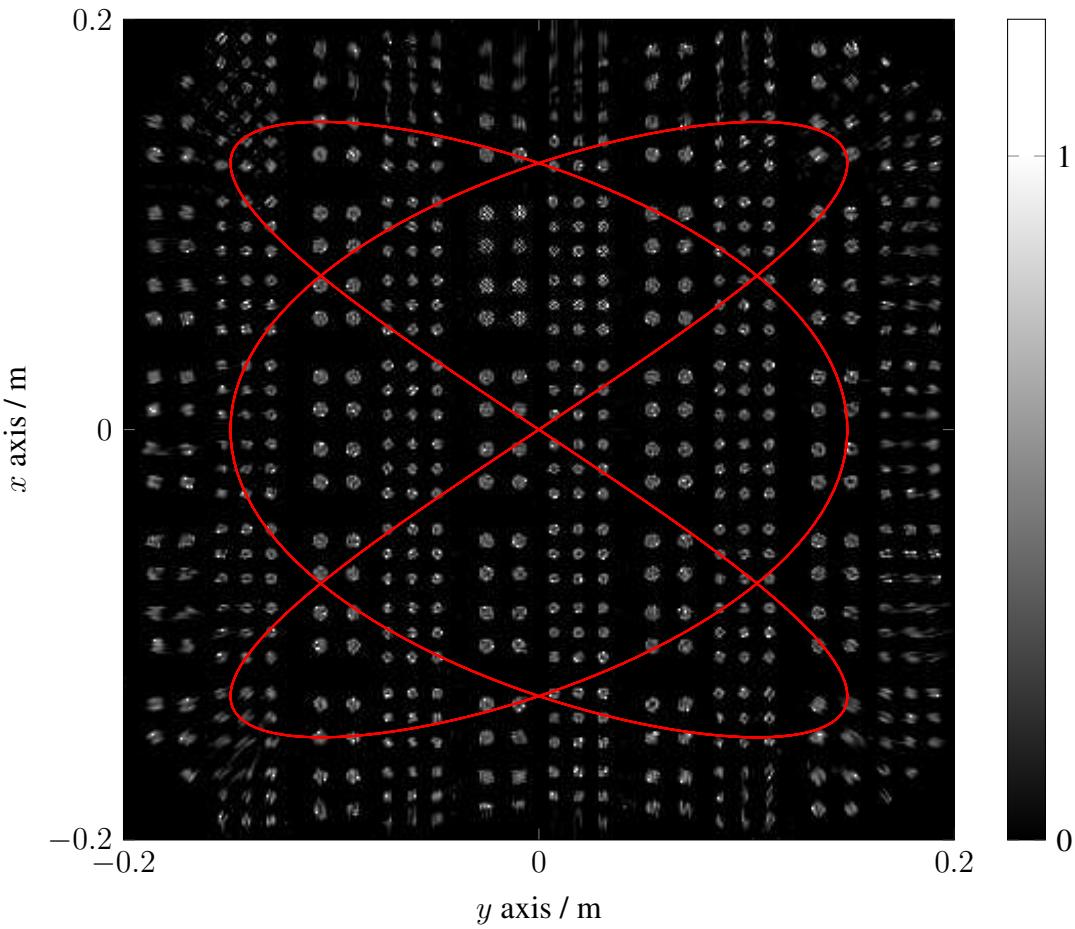

(b)

Figure 6.13: Assembly of the expected reconstruction and phantoms. (a) Phantoms made of 6 and 8 mm diameters circles. (b) Reconstruction with a 450 kHz bandwidth. The Lissajous along which the line rotation point is moved is superimposed in red.

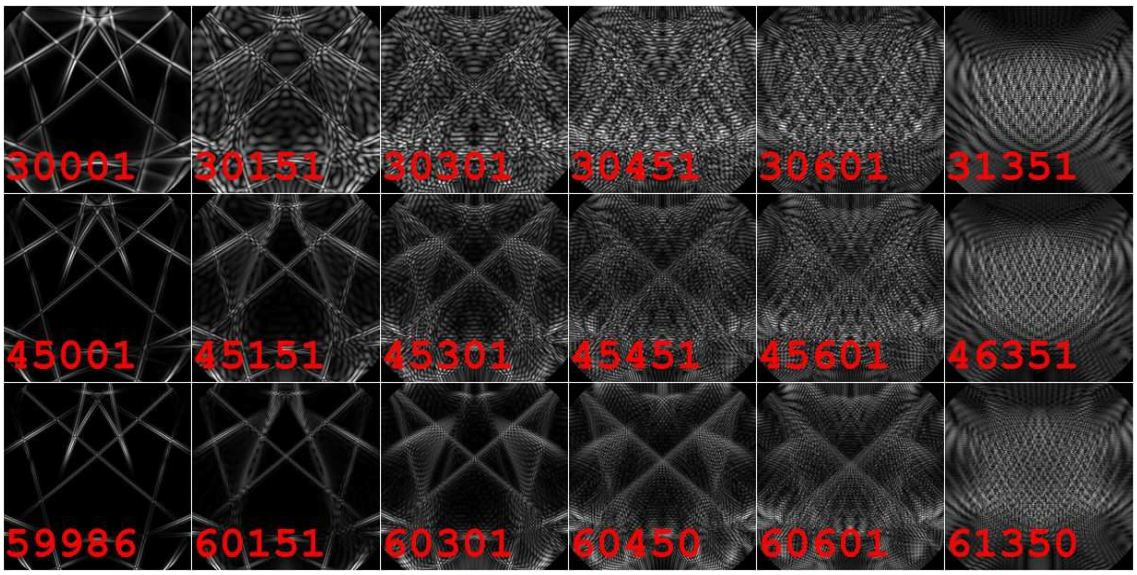

Figure 6.14: Assembly of some FCs with frequencies close to the second, third and fourth harmonics. A spectrum resolution of $\Delta f = 10$ Hz is used. Note that the scaling is different for each image.

which are represented in Figure 6.13a between vertical and horizontal lines. Each sub-area is simulated separately on a single-core of an Intel E5-4657L processor with 1 TB of RAM. The quantity of RAM used to calculate the SF and other relevant parameters was the limiting factor, which forced the division of the simulation. Each sub-area took approximately 8 hours and 30 minutes to simulate. The assembled reconstructions are shown in Figure 6.13b. This demonstrates that the sequence is able to acquire information which is of good quality on the biggest part of the FOV. This is particularly visible when comparing Figures 6.9 and 6.13. In order to cover a field of view of 400×405 mm^2, both focus fields have to produce fields with main SHCs of 320 mT.

Looking at the assembly of the SF components, shown in Figure 6.14, gives another idea of the information available at the different position. Comparing them with the one of an FFL (figure 6.8) and FFP scanner (figure 2.14 and 2.15), it can been seen that the more complex pattern, which contains high spatial variation, are present in a bandwidth of only 14 kHz. The energy repartition $\|\hat{s}_k^{(3)}\|$ is similar to the one of the FFL SF, with the exception of the alternating energy at odd and even FCs for odd and even harmonics.

By filtering the FCs, keeping the one above the second harmonic in a bandwidth of 13 kHz and having an $\mathrm{SNR}_{\mathrm{S}}^{(4)}$ in this bandwidth of at least 8 % of the maximal $\mathrm{SNR}_{s}^{(4)}$ in the bandwidth, only 1499 components are kept for the MPI signal simulated for the phantom presented in Figure 6.15a. Those components are used along with the assembled tSF

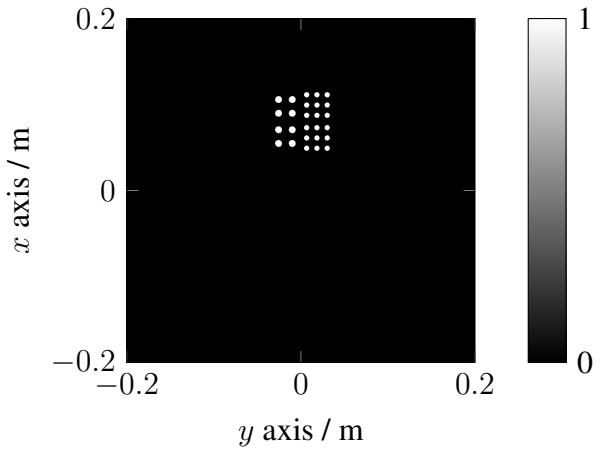

(a)

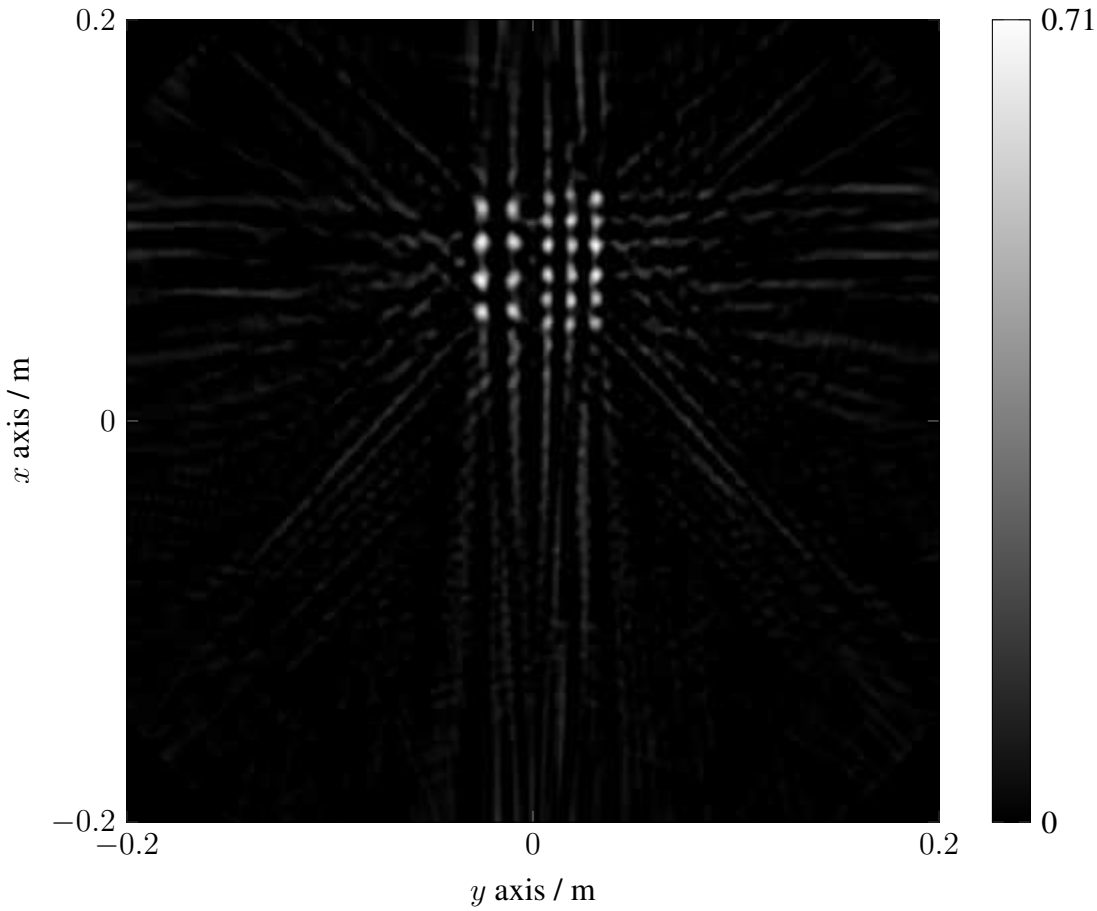

(b)

Figure 6.15: Reconstruction of a phantom (a) using the assembled tSF (b). Only 1499 FCs are used, which are in a 13 kHz bandwidth above the second harmonic. The ratio between the highest and the lowest SNR used is 12.5.

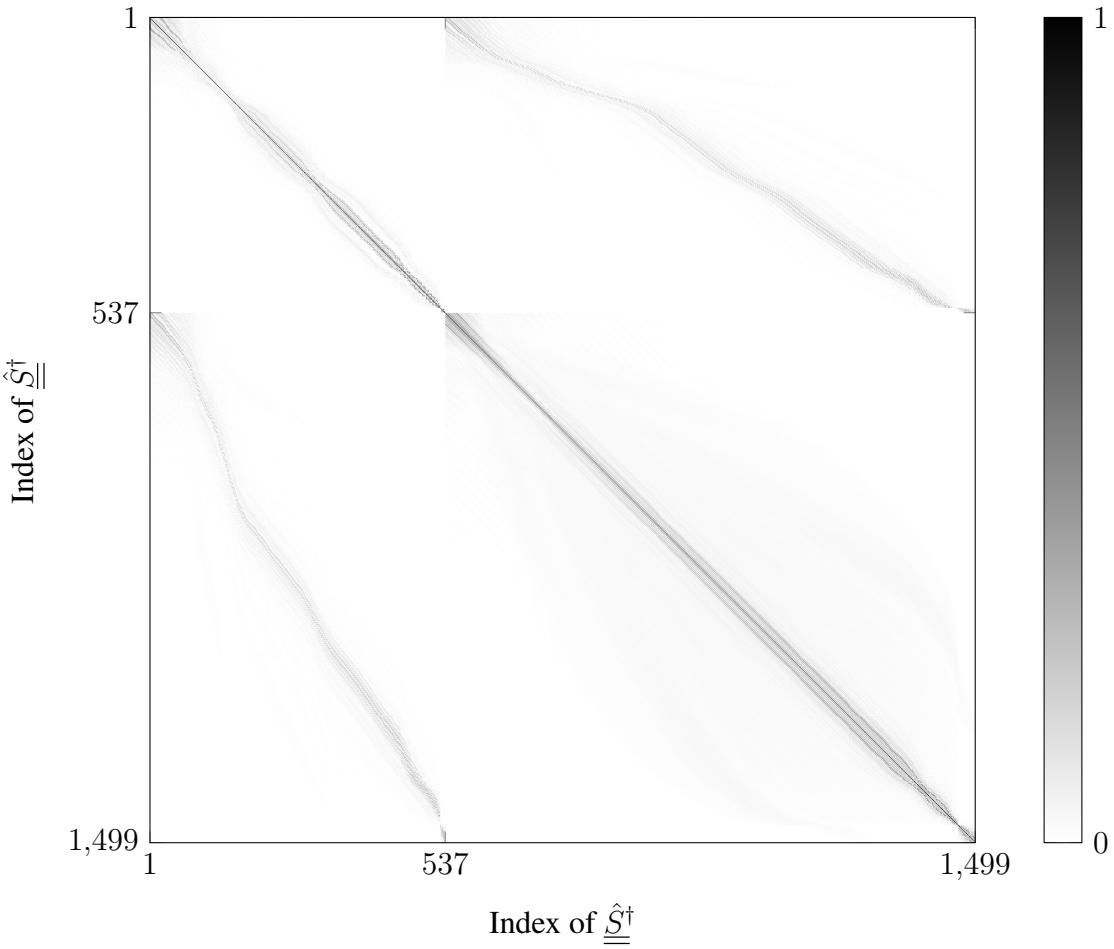

Figure 6.16: Orthogonality plot between the FCs of a tSF regrouping both receive channels. A black point means that both FCs are similar, whereas a white point means that there is no similarities between two FC. One regroups 537 FCs and the other 962.

to reconstruct the particle concentration visible in Figure 6.15b by inverting problems (2.78) using the Kaczmarz method. The reconstruction is stopped at the 10th iteration and the results is shown in Figure 6.15. The visible artefacts are not related to the low bandwidth and small number of used FCs, as they are also present in reconstructions done using the same FCs as used to reconstruct sub-areas presented in 6.13. They are directly linked to the structure of the SF and the associated MPI sequence and magnetic field shapes. This shows that the structure of the SF, the MPI sequence, the MPI scanner and the chosen reconstruction technique are suited to encode the MPI signal, but can be further improved.

Looking at the orthogonality of the tSF used for the reconstruction and displayed in Fig-

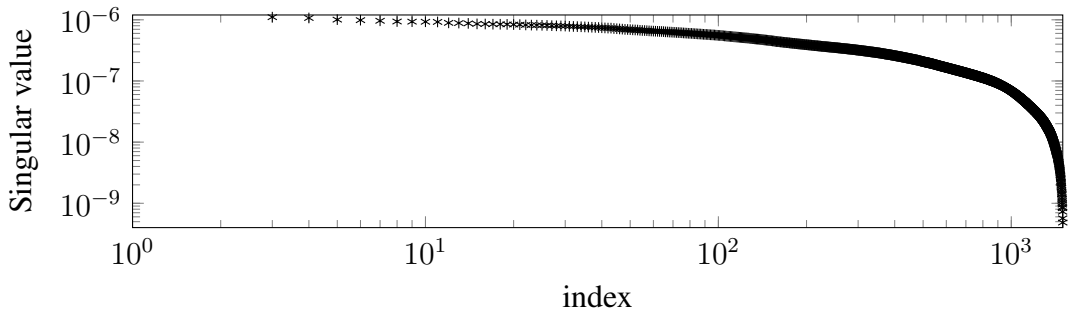

Figure 6.17: Singular values obtained from a tSF of a continuously rotated 2D FFL scanner using focus fields.

ure 6.16, structures different from the ones observed in Figures 2.20 and 6.10 are present. The coupling between the tSF FCs seems smaller, especially the one between both receive channels. Looking at the singular values shown in Figure 6.17, it can be seen that the problem is still severely ill-posed. But compared with the 2D FFP and FFL imaging devices, it has a smaller condition number of $2.6 \cdot 10^3$. As for the previous FFL scanner, this smaller condition number of the tSF is a first explanation of why it is not necessary to use an additional Tikhonov regularisation to obtain a satisfying reconstruction. Additional regularisations could still be used to further reduce artefacts.

To refine the concept, it is of interest to estimate the induced electrical field amplitude in a patient for such a scanner and sequence. As the superposition of time-varying magnetic fields with different shapes and frequencies, the MIEFA induced by the drive, selection and focus fields are evaluated separately.

As presented in Section 5.2.5, the HMIEFA obtained for x- and y-drive fields having a main SHCs of 3.6 and 4.8 mT varying at 150 kHz are at the limits of the PNS.

The HMIEFA from the quadrupoles generates up to 0.5 T·m^{-1} at $2n_\theta\Delta_f = 40$ Hz induced around 2 V·m^{-1}, which is three time smaller than the 7 V·m^{-1} thresholds proposed by Reilly and represented in Figure 5.7.

The focus fields, generating up to 320 mT at frequencies of around $2n_{\text{Lis}}\Delta_f = 90$ Hz, will induce up to 33 V·m^{-1}, around 5 times more than the thresholds proposed by Reilly.

In order to generate the required magnetic fields for this sequence, some pole shoes have to produce up to 2.9 times more field strength than they would have with an FFL sequence, as presented in Figure B.2a. Taking into account the saturation of the material, a peak current of 3000 A has to be produced; that is more than 10 times the peak current for which the design has been laid-out. The whole current requirement is visible in Figure B.2b. Due to the complexity of the sequence and the saturation of the pole shoes, the

peak value has no simple relation to the RMS current. Using a numerical approach, the dissipated power in the different pole shoes, as defined in Figure 6.12a, has been evaluated. Pole shoe 1, 3 and 5 will dissipate 18 kW; 2 and 4 44 kW; 6 and 8 49 kW and 7 19 kW. The main difference from pole shoes 1, 3, 5 and 7 comes from the fact they are almost not used for the focus fields, where the other ones are used for the focus-field in both directions.

6.2.4 Discusion

The presented sequence and reconstruction technique covers a FOV of 400×405 mm^2, with partial information successfully recovered over the whole area. No large areas are missing. But the quality of the encoded signal has to be further investigated, to analyse if phantoms, including smaller structures, can also be reconstructed. Furthermore, this concept does not deliver quantitative information. As seen in Figure 6.15, a difference of 29 % exists between the phantom and the reconstructed image.

The reconstructed images have been obtained from a signal having a bandwidth of only 13 kHz, showing that a large amount of spatial information is included in the mix product. The small MPI-signal bandwidth can be used in order to decrease the acquisition noise, and thus increase the SNR and the minimal amount of tracer which can be detected. Nevertheless, it may be possible that a larger bandwidth increases the reconstruction robustness for this sequence.

Looking at the SF structure, a single symmetry axis is present, this time in the vertical direction. In contrast, two are present for a Lissajous based FFP scanner and a single horizontal for the FFP sequence. As for the FFL scanner, the actual influence of the realistic field topology has to be further investigated to confirm any practicable applications.

The focus-field strength required to cover a 400×405 mm^2 FOV generates a MIEFA 5 times higher than the expected thresholds for a sinusoidal field excitation at 90 Hz. As presented in Figure B.1b, the real waveforms applied to those magnet is more complex than a simple sinusoidal signal, and the actual PNS thresholds for such an exposition should be experimentally validated. Moreover, the induced electrical field is not only coming from the focus field, but also from the drive fields and the quadrupoles fields. Even if the two other fields taken separately are expected to avoid PNS in half of the patient, the question of superposition arises. Looking at the spatial repartition of the nMIEFA shown in Appendix C, the quadrupole induce an electrical field with a maximum situated at the periphery of the patient. But, as the drive and focus fields use the same magnetic field topology, both will produce their respective MIEFA at the same position in

the patient. Looking at the representation of the sequence in Figure B.1b, the MIEFA for both contributions could happen at the same time. But as both sources use fundamentally different frequencies, 150 kHz for the drive fields and around 90 Hz for the focus field, their interactions have to be investigated and experimentally validated. If the stimulation thresholds are still exceeded, the FOV could be reduced, aiming, for example, at imaging the heart with a FOV of 120×80 mm^2 [169].

The human-sized scanner presented here was designed to generate a simple FFL sequence and adapted to generates focus fields. The resulting required current in each magnet poles is thus largely influenced by the saturation of the cores. Peak currents of more than 3000 A are required. Taking into account the required power, current densities and associated power-electronic requirements to generate such currents for the magnetic fields, a redesign of the iron core magnet should be done. Maximising the available Section of ferromagnetic materials as well as increasing the length of the whole magnet are two possibilities available to reduce the saturation level and the current density of the magnet. The results presented here show that the magnet has to be designed for a maximum efficiency, and that the field quality has little influence for SF-based approaches.

Translating the concept of focus fields for smaller scanners, it could be also of interest to further study the influence of the drive frequency on the signal structure. Reducing the bandwidth between harmonics below the useful bandwidth of the signal could fundamentally change the energy repartition of the MPI signal and allow further optimisation. Keeping Figure 6.7 in mind and using a 25 kHz drive-field frequency with the FFL sequence using focus fields, which have a useful bandwidth of 13 kHz, the M-shaped energy-bands will merge for all consecutive harmonics. This could help to acquire higher spatial information modulated with the second harmonics at FCs dominated either by noise or by information modulated with the third harmonics.

6.2.5 Summary

A human sized, whole body FFL imageing device, which could acquire information in a FOV of 400×405 mm^2 has been presented. This design has been created to study the limiting factor of fast, high FOV FFL imaging. It has been found that an image rate of 10 images per second could be obtained with a sequence covering 400×405 mm^2. Nevertheless, to validate this performance, further PNS studies have to be done to estimate the effect of magnetic field superposition of fields with equivalent topology but different frequencies. Then, the concept could be validated and the magnet further optimised.

6.3 Conclusion

Two FFL concepts have been presented, one rabbit-sized and one human-sized scanner. The rabbit-sized imaging device is currently under construction. Both scanners are characterized by tSF with a condition number low enough to avoid the use of the additional Tikhonov regularisation. This is particularly of interest, as this regularisation requires several tries to be set and requires knowledge about the imaged structure. Those tSF permit a reliable first approximation of the solution, which can then be refined using further regularisation techniques. This result has yet to be experimentally validated.

In this work, the design and implementation of the coils near the patient are presented, and the performance obtained validate the design study. Imaging at a rate of at least 20 images per second could be done with a model-based approach, which is halved for a SF approach. A circular, fully sampled area with a diameter of 37 mm is expected. In the future, this could be almost doubled without further modification of the drive-coil set. The line rotation frequency could also be increased by two order of magnitude, further increasing the acquisition rate. For any of those modification, the PNS likelihood should be again evaluated.

At a human scale, the patient PNS limits the rotation frequencies as well as the fully sampled FOV. In order to cover larger FOV, a focus-field based sequence has been presented. To validate the sequence, the PNS thresholds for the superposition of magnetic fields with the same topology and different rates of variation should be investigated. Moreover, further studies have to be done on the superposition of different field topologies. Considering those results, the magnet and the associated power system have to be further improved, to take into account the requirement of the focus fields.

7 Summary

The presented thesis constitutes a further step towards the clinical application of fast FFL imagers, following the work of Erbe [5] and others in the FFL MPI community. This work focused on the extension of the FFL technology to rabbit and human-sized scanners. To support the community, the developed MPI simulation and coil design toolboxes have been made freely available at http://www.imt.uni-luebeck.de/ and https://github.com/gBringout/CoilDesign.

The relation between the parallel-beam model used in CT and FFL has been defined, which gives an insight to the flexibility offered by MPI, especially in terms of sampling position. Indeed, by simply varying the sampling frequency, different acquisition schemes can be used.

Two main artefacts associated with the use of the FBP as model-based reconstruction on data coming from a continuously rotated FFL have been described. One is associated with the continuous rotation, which rotates the reconstructed image by an angle proportional to the rotation frequency of the line. The other one is linked to the magnetic field topology, which will deform the reconstructed image.

Furthermore, using an iterative reconstruction the effect of the magnetic field topology has been investigated on simulated data. It has been shown that for fully sampled FOV smaller than half the bore diameter of the scanner, only a few artefacts are to be expected.

But, increasing the fully sampled FOV will lead to severe artefacts, mainly emerging from regions not fully covered by the line.

Also, the FBP is able to reconstruct two times more images per second, as it does not require an MPI signal which resolved all the tracer harmonics in Fourier space. This strong requirement, which is applied at the moment to SF-based reconstruction, should encourage further developments of model-based reconstruction techniques.

In order to increase the FOV without increasing the drive-field strength, either to avoid the artefacts previously detailed or to limit the risk of PNS, the sequence rotating the line around a time dependent position has been analytically derived. Furthermore, one application using a Lissajous curve as the time dependent position of the rotation centre is detailed and used to sketch a human-sized imaging device.

To be able to optimise the required coils, a BEM coil-optimisation method has been implemented. Starting from an ideal field topology representation and an arbitrary support structure, this method is used to optimise the wire centroid using different constraints. Those constraints range from norm minimisation of the solution, to power dissipation, stored energy or curvature minimisation. This technique has been here implemented and validated using a robust representation of magnetic fields through the three main steps of the design of a coil. Those are the calculations of the wire centroids, the design of a realistic wire path and finally the measurement of the actual magnetic field topology produced by the coil.

The evaluation of the induced eddy current in an arbitrary surface has been added to the method. Thus, the positioning of the magnetic field shielding surfaces can be studied. This, in turn, enable the study of the tradeoffs between the size of the shielded volume and the coil efficiency.

The design of iron-core magnets has also been studied, showing that their design is easier to use than those of air-core coils. The presented technique has been used to propose a first concept of a dual-quadrupole iron-core magnet to be used in a human-sized FFL scanner.

To assess the PNS risk associated with the development of fast rotating FFL scanners, the evaluation of the induced electrical field amplitude in a human model have been conducted. Using a BEM implementation, the electrical field induced in a subject by a current carrying surface is evaluated. This has been done for two human models and 8 coils, 5 commonly used by the MPI community and 3 by the MRI community. Indeed, besides the electrical field amplitudes, the thresholds at which the nerves are stimulated have to be known. Unfortunately, it exists too few reliable data to be able to calculate these thresholds, so that many experiments have to validated the sequences used in MPI.

Those 8 coils have thus been chosen to facilitate the transfer of the threshold knowledge from the MRI community to the MPI one. Furthermore, a linear relation between the fields strength, coil topology, frequency of a sinusoidally signal and the normalised highest maximal induced electrical field amplitude (nHMIEFA) has been introduced. This aims to facilitate the interpolation of the scarce experimental thresholds to new scanner concepts. Those tools have been used in this work to demonstrate that it is possible to optimise an MPI sequence, by increasing the drive-field strength, without automatically increasing the highest maximal induced electrical field amplitude (HMIEFA). This has been achieved using the particular spatial repartition of the induced electrical field of each drive coils. A 33 % strength increase for one direction has been obtained, without increasing the electrical field amplitude in the model. Those predictions have to be experimentally validated.

The designs of two FFL scanners have been performed. The first one, aiming at preclinical applications with a bore diameter of 173 mm, has been designed to acquire 10 images per seconds in a 2D FOV with a diameter of 37 mm. The selection and drive-field coils have been designed, implemented, characterised and validated. All coil sets are actively cooled. With the coming filters, power matching circuits and acquisition systems, this will become the world biggest FFL scanner. Only Philips, who is currently building the first clinical MPI scanner, develops a larger scanner.

It has also been shown that the tSF of an FFL imaging device benefits from a better condition number, but is still severely ill-posed. Nevertheless, the better condition number should allow to automatically reconstruct a first approximation of the tracer distribution, as only knowledge about the fixed scanner parameters and the actual acquired signal are required to truncate the SF. This represents a major difference with actual SF-based reconstruction process. Indeed, it still requires additional information for the Tikhonov regularisation, which has to be provided by the user and for which no robust automation techniques have been presented.

Finally, the concept of a human-sized FFL using focus fields is introduced and studied. In order to cover a large FOV of 400×405 mm^2 with the estimated PNS limitations on the drive-field strength and despite the optimisation done in Chapter 5, a focus-field flux density of 320 mT is required. This field strength will put a huge thermal stress on the dual-quadrupole magnet, which should be redesigned. This should be done to reduce the current density and the saturation level of the core, to limit the current peak amplitudes required to drive the magnet. Even if the field varies below 100 Hz, the first calculation done using the nHMIEFA shows that this sequence could lead to nerve stimulation in the patient. But the used thresholds, which lead to this conclusion have

not been experimentally validated for the field topology and frequency range used here. It has been proven in the past that these thresholds are too low in the frequency range between 20 and 160 kHz. Further experimental test has to be carried out in this lower frequency band before validating this concept.

8

Discussion and outlook

In this work, the design and the first steps of the implementation of a rabbit-sized FFL scanner using a continuous line rotation have been carried out. The validation of the presented expected performances still has to be done, especially in regard to the noise figures of the actual scanner.

The proposed division between fast and slow MPI sequences appears to be strongly patient-size dependent. Indeed, for mouse scanners, the acquisition rate seems to be solely limited by the imaging device sensitivity, without limits on the magnetic field strength or frequency. In contrast, the human-sized system appears to be clearly limited by the safety aspect, and more particularly for the results presented in this work, by the PNS. To alleviate the dependency of the patient-size, the voxel encoding rate could be used to account for the acquisition rate, as proposed by Gleich in 2013. But the differences between fully sampled and non-fully sampled FOV is still unclear and should be clearly determined before using a voxel based acquisition rate.

Nevertheless, the characterisation of both sequences presented here demonstrates that the tSF, which is the basis function in which the signal is coded, have a non-negligible influence on the image reconstruction process. It would be of interest to design an MPI sequence not from simple, even elegant, concepts or well known encoding schemes, but from a pure optimisation point of view. Maximising the tSF orthogonality for a given FOV by constraining the sequence parameters and the magnetic field topology could be

a starting point.

For preclinical scanners, the acquisition rate could be massively increased, but the careful design of such a scanner will have to take all the shielding aspects into account. The development of a better model-based reconstruction may play a decisive role in the design of future FFL, which could either use higher drive-fields strength or focus fields strength to enlarge the covered area. The model-based reconstruction offers a reconstruction rate 2 times higher than the actual SF-based reconstruction. The increased acquisition rate could push the development of new sequences acquiring data in 3D without moving the patient.

Due to safety limits, the increased drive-field strength for clinical application is not realistic for drive frequency close to 100 kHz. The author tried, with the help of Johan Löfberg, to optimise the stream function of a drive-coil set to reduce the highest maximal induced electrical field amplitude (HMIEFA) without significant success. Indeed, a reduction of up to 5 % was observed, but was strongly dependent on the patient anatomy. Nevertheless, this indicates that the main SHC plays a significant role regarding PNS, and strengthens the idea of field shape based linear factors between the patient geometry and the HMIEFA.

The rotating nature of FFL scanners also force the use of time-varying magnetic fields to move the line rotation centre in space. Even if the rotation point is kept constant at a position different from the bore centre point, time-varying magnetic fields have to be applied, which will contribute to the PNS. Significant efforts have to be invested to characterise the PNS thresholds at low frequencies for signal containing single and multiples frequencies. The last point could be proven difficult, as it could actually describe any waveform.

Finally. reducing the constrains applied to the sequence design, as the covered FOV, could also significantly reduce the required focus-field strengths required to cover the whole FOV.

This works may give you a better insight on the complexity of the comparison of MPI scanners and on the advantages and disadvantages of FFL imaging devices. It has to be kept in mind that most of the technology required to develop better MPI scanners are not commercially available, which makes their development particularly challenging.

Publication list

[O1] G. Bringout and T. M. Buzug, "Coil design for magnetic particle imaging: Application for a preclinical scanner," *IEEE Transactions on Magnetics*, vol. 51, no. 2, Feb 2015. DOI:10.1109/TMAG.2014.2344917

[O2] G. Bringout, K. Graefe, and T. M. Buzug, "Performance of shielded electromagnet-evaluation under low-frequency excitation," *IEEE Transactions on Magnetics*, vol. 51, no. 2, Feb 2015. DOI:10.1109/TMAG.2014.2329396

[O3] G. Bringout and T. M. Buzug, "A robust and compact representation for magnetic fields in magnetic particle imaging," *Biomedical Engineering / Biomedizinische Technik*, vol. 59, no. s1, pp. 675–678, 2014.

[O4] G. Bringout, J. Stelzner, M. Ahlborg, A. Behrends, K. Bente, C. Debbeler, A. von Gladiss, K. Graefe, M. Graeser, C. Kaethner, S. Kaufmann, K. Lüdtke-Buzug, H. Medimagh, W. Tenner, M. Weber, and T. M. Buzug, "Concept of a rabbit-sized FFL-scanner," in *2015 5th International Workshop on Magnetic Particle Imaging (IWMPI)*, March 2015. DOI:10.1109/IWMPI.2015.7107032

[O5] G. Bringout, H. Wojtczyk, W. Tenner, M. Graeser, M. Gruttner, J. Haegele, R. Duschka, N. Panagiotopoulos, F. M. Vogt, J. Barkhausen, and T. M. Buzug, "A high power driving and selection field coil for an open MPI scanner," in *2013 International Workshop on Magnetic Particle Imaging (IWMPI)*, 2013. DOI:10.1109/IWMPI.2013.6528332

[O6] G. Bringout, M. Ahlborg, M. Graeser, C. Kaethner, J. Stelzner, W. Tenner, H. Wojtczyk, and T. M. Buzug, "Shielded drive coils for a rabbit sized FFL scanner," in *International Workshop on Magnetic Particle Imaging 2014*, 2014, p. 98.

[O7] G. Bringout and T. M. Buzug, "Design optimisation of a field free point magnetic particle imaging scanner," in *COMSOL Conference 2013*, 2013.

[O8] G. Bringout, H. Wojtczyk, M. Grüttner, M. Graeser, W. Tenner, J. Hägele, F. M. Vogt, J. Barkhausen, and T. M. Buzug, "Safety aspects for a pre-clinical magnetic particle imaging scanner," in *Magnetic Particle Imaging*, ser. Springer Proceedings in Physics, T. M. Buzug and J. Borgert, Eds. Berlin: Springer-Verlag, 2012, vol. 140, pp. 355–359.

[O9] G. Bringout and T. M. Buzug, "Induced electrical fields on a human body by various magnetic field topologies in the light of peripheral nerve stimulation thresholds," in *2015 5th International Workshop on Magnetic Particle Imaging (IWMPI)*, March 2015. DOI:10.1109/IWMPI.2015.7107077

[O10] G. Bringout, K. Graefe, and T. M. Buzug, "Performance and safety evaluation of a human sized FFL imager concept," in *2015 5th International Workshop on Magnetic Particle Imaging (IWMPI)*, March 2015. DOI:10.1109/IWMPI.2015.7107022

[O11] T. M. Buzug, G. Bringout, M. Erbe, K. Gräfe, M. Graeser, M. Grüttner, A. Halkola, T. F. Sattel, W. Tenner, H. Wojtczyk, J. Hägele, F. M. Vogt, J. Barkhausen, and K. Lüdtke-Buzug, "Magnetic particle imaging: Introduction to imaging and hardware realization," *Zeitschrift für Medizinische Physik*, vol. 22, no. 4, pp. 323–334, December 2012.

[O12] H. Wojtczyk, G. Bringout, W. Tenner, M. Graeser, M. Gruttner, T. Sattel, K. Graefe, and T. M. Buzug, "Toward the optimization of D-shaped coils for the use in an open magnetic particle imaging scanner," *IEEE Transactions on Magnetics*, vol. 50, no. 7, July 2014. DOI:10.1109/TMAG.2014.2303113

[O13] R. L. Duschka, H. Wojtczyk, N. Panagiotopoulos, J. Haegele, G. Bringout, T. M. Buzug, J. Barkhausen, and F. M. Vogt, "Safety measurements for heating of instruments for cardiovascular interventions in magnetic particle imaging (MPI) - first experiences," *Journal of Healthcare Engineering*, vol. 5, no. 1, pp. 79–93, 2014.

[O14] K. Gräfe, G. Bringout, M. Graeser, T. F. Sattel, and T. M. Buzug, "Single-sided magnetic particle imaging scanner: System matrix measurement," *Biomedizinische Technik / Biomedical Engineering*, vol. 59, Suppl. 1, pp. 638–642, 2014.

[O15] K. Graefe, G. Bringout, M. Graeser, T. Sattel, and T. M. Buzug, "System matrix recording and phantom measurements with a single-sided magnetic particle imaging device," *IEEE Transactions on Magnetics*, vol. 51, no. 2, Feb 2015. DOI:10.1109/TMAG.2014.2330371

[O16] C. Kaethner, M. Ahlborg, K. Graefe, G. Bringout, T. Sattel, and T. M. Buzug, "Asymmetric scanner design for interventional scenarios in magnetic particle imaging," *IEEE Transactions on Magnetics*, vol. 51, no. 2, Feb 2015. DOI:10.1109/TMAG.2014.2337931

[O17] C. Kaethner, M. Ahlborg, G. Bringout, M. Weber, and T. M. Buzug, "Axially elongated field-free point data acquisition in magnetic particle imaging," *IEEE Transactions on Medical Imaging*, vol. 34, no. 2, pp. 381–387, 2015.

[O18] N. Panagiotopoulos, R. Duschka, M. Ahlborg, G. Bringout, C. Debbeler, M. Graeser, C. Kaethner, K. Lüdtke-Buzug, H. Medimagh, J. Stelzner, T. M. Buzug, J. Barkhausen, F. M. Vogt, and J. Haegele, "Magnetic particle imaging – current developments and future directions," *International Journal of Nanomedicine*, vol. 10, pp. 3097–3114, 2015.

[O19] K. Gräfe, A. von Gladiß, G. Bringout, M. Ahlborg, and T. M. Buzug, "2d images recorded with a single-sided magnetic particle imaging scanner," *IEEE Transactions on Medical Imaging*, vol. 35, no. 4, pp. 1056–1065, April 2016.

[O20] M. Grüttner, T. F. Sattel, M. Graeser, H. Wojtczyk, G. Bringout, W. Tenner, and T. M. Buzug, "Enlarging the field of view in magnetic particle imaging - a comparison," in *Magnetic Particle Imaging*, ser. Springer Proceedings in Physics, T. M. Buzug and J. Borgert, Eds., vol. 140. Berlin: Springer-Verlag, 2012, pp. 249–253.

[O21] H. Wojtczyk, J. Haegele, M. Grüttner, W. Tenner, G. Bringout, M. Graeser, F. M. Vogt, J. Barkhausen, and T. M. Buzug, "Visualization of instruments in interventional magnetic particle imaging (impi): A simulation study on spio labelings," in *Magnetic Particle Imaging*, ser. Springer Proceedings in Physics, T. M. Buzug and J. Borgert, Eds., vol. 140. Berlin: Springer-Verlag, 2012, pp. 167–172.

[O22] M. Graeser, T. F. Sattel, M. Grüttner, H. Wojtczyk, G. Bringout, W. Tenner, and T. M. Buzug, "Determination of system functions in magnetic particle imaging," in *Magnetic Particle Imaging*, ser. Springer Proceedings in Physics, T. M. Buzug and J. Borgert, Eds., vol. 140. Berlin: Springer-Verlag, 2012, pp. 59–64.

[O23] R. L. Duschka, H. Wojtczyk, N. Panagiotopoulos, J. Hägele, G. Bringout, J. Rahmer, C. Bontus, T. M. Buzug, J. Borgert, J. Barkhausen, and F. M. Vogt,

"Magnetic particle imaging (MPI) meets Katheter und co. - Temperaturmessungen interventioneller Materialen im Wechselmagnetfeld," in *RöFo: Fortschritte auf dem Gebiet der Röntgenstrahlen und bildgebenden Verfahren*, vol. 184, 2012, p. A25, symposium Experimentelle Radiologie 2012 Kiel.

[O24] M. Grüttner, T. F. Sattel, G. Bringout, M. Graeser, W. Tenner, H. Wojtczyk, and T. M. Buzug, "Truncation artifacts in magnetic particle imaging," in *2013 International Workshop on Magnetic Particle Imaging (IWMPI)*, 2013. DOI:10.1109/IWMPI.2013.6528335

[O25] M. Graeser, T. Knopp, M. Grüttner, T. F. Sattel, G. Bringout, W. Tenner, H. Wojtczyk, and T. M. Buzug, "Cancellation techniques for MPI," in *2013 International Workshop on Magnetic Particle Imaging (IWMPI)*, 2013. DOI:10.1109/IWMPI.2013.6528331

[O26] A. Timmermeyer, H. Wojtczyk, W. Tenner, G. Bringout, M. Grüttner, M. Graeser, T. Sattel, A. Halkola, and T. M. Buzug, "Super resolution approaches for resolution enhancement in magnetic particle imaging," in *2013 International Workshop on Magnetic Particle Imaging (IWMPI)*, 2013.

[O27] W. Tenner, H. Wojtczyk, G. Bringout, M. Graeser, M. Grüttner, J. Haegele, R. L. Duschka, N. Panagiotopoulos, F. M. Vogt, J. Barkhausen, and T. M. Buzug, "Receive coil optimization for an open magnetic particle imaging scanner," in *2013 International Workshop on Magnetic Particle Imaging (IWMPI)*, 2013. DOI:10.1109/IWMPI.2013.6528336

[O28] H. Wojtczyk, A. Timmermeyer, W. Tenner, T. F. Sattel, G. Bringout, M. Grüttner, M. Graeser, and T. M. Buzug, "Measure of trajectory quality in magnetic particle imaging," in *2013 International Workshop on Magnetic Particle Imaging (IWMPI)*, 2013. DOI:10.1109/IWMPI.2013.6528351

[O29] R. L. Duschka, H. Wojtczyk, N. Panagiotopoulos, J. Hägele, G. Bringout, J. Rahmer, C. Bontus, T. M. Buzug, J. Borgert, J. Barkhausen, and F. M. Vogt, "Heating of interventional instruments in magnetic particle imaging - first experiences of safety measurements," in *2013 International Workshop on Magnetic Particle Imaging (IWMPI)*, 2013. DOI:10.1109/IWMPI.2013.6528370

[O30] ——, "Magnetic Particle Imaging (MPI): Sicherheitsmessungen gängiger, interventionell verwendeter Materialien mit gezieltem Focus auf die Materialerwärmung," in *Deutscher Röntgenkongress*, 2013. DOI:10.1055/s-0033-1346219

[O31] A. Timmermeyer, H. Wojtczyk, W. Tenner, G. Bringout, M. Grüttner, M. Gräser, T. F. Sattel, A. Halkola, and T. M. Buzug, "Super-resolution approach in magnetic particle imaging - evaluation of effectiveness at various noise levels," in *Proceedings der 44. Jahrestagung der Deutschen Gesellschaft für Medizinische Physik*, H. Treuer, Ed., 2013.

[O32] A. Timmermeyer, H. Wojtczyk, W. Tenner, G. Bringout, M. Gruttner, M. Graeser, T. Sattel, A. Halkola, and T. M. Buzug, "Super-resolution approaches for resolution enhancement in magnetic particle imaging," in *2013 International Workshop on Magnetic Particle Imaging (IWMPI)*, March 2013. DOI:10.1109/IWMPI.2013.6528360

[O33] H. Wojtczyk, G. Bringout, W. Tenner, M. Graeser, M. Grüttner, T. F. Sattel, K. Gräfe, J. Haegele, R. L. Duschka, N. Panagiotopoulos, F. M. Vogt, J. Barkhausen, and T. M. Buzug, "Comparison of open scanner designs for interventional magnetic particle imaging," *Biomedizinische Technik / Biomedical Engineering*, vol. 58, no. s1, 2013. DOI:10.1515/bmt-2013-4279

[O34] K. Bente, G. Bringout, C. Debbeler, K. Gräfe, M. Gräser, M. Grüttner, C. Kaethner, W. Tenner, M. Weber, H. Wojtczyk, T. Buzug, and K. Lüdtke-Buzug, "Magnetic particle imaging - eine Einführung in die Instrumentierung und Bildrekonstruktion," in *Proceedings der 44. Jahrestagung der Deutschen Gesellschaft für Medizinische Physik*, H. Treuer, Ed., 2013, pp. 95–100.

[O35] C. Kaethner, M. Ahlborg, K. Gräfe, G. Bringout, T. F. Sattel, and T. M. Buzug, "On the way to a patient table integrated scanner system in magnetic particle imaging," in *Proceedings of SPIE Medical Imaging 2014: Biomedical Applications in Molecular, Structural, and Functional Imaging*, vol. 9038, 2014, pp. 903 816–1–903 816–6.

[O36] C. Kaethner, K. Gräfe, M. Ahlborg, G. Bringout, T. F. Sattel, and T. M. Buzug, "Asymmetric scanner design for unlimited patient access in magnetic particle imaging," in *International Workshop on Magnetic Particle Imaging 2014*, 2014.

[O37] M. Graeser, M. Ahlborg, A. Behrends, K. Bente, G. Bringout, C. Debbeler, A. von Gladiss, K. Graefe, C. Kaethner, S. Kaufmann, K. Lüdtke-Buzug, H. Medimagh, J. Stelzner, M. Weber, and T. M. Buzug, "A device for measuring the trajectory dependent magnetic particle performance for MPI," in *2015 International Workshop on Magnetic Particle Imaging (IWMPI)*, March 2015. DOI:10.1109/IWMPI.2015.7107078

[O38] K. Graefe, A. von Gladiss, G. Bringout, M. Ahlborg, and T. M. Buzug, "2d imaging with a single-sided MPI device," in *2015 5th International Workshop on Magnetic Particle Imaging (IWMPI)*, March 2015. DOI:10.1109/IWMPI.2015.7107024

[O39] J. Stelzner, G. Bringout, M. Graeser, and T. M. Buzug, "Toroidal variometer for a magnetic particle imaging device," in *2015 5th International Workshop on Magnetic Particle Imaging (IWMPI)*, March 2015. DOI:10.1109/IWMPI.2015.7107074

[O40] H. Medimagh, P. Weissert, G. Bringout, K. Bente, M. Weber, K. Graefe, A. Cordes, and T. M. Buzug, "Artifacts in field free line magnetic particle imaging," in *2015 5th International Workshop on Magnetic Particle Imaging (IWMPI)*, March 2015. DOI:10.1109/IWMPI.2015.7107043

[O41] H. Medimagh, P. Weissert, G. Bringout, K. Bente, M. Weber, K. Gräfe, A. Cordes, and T. M. Buzug, "Artifacts in field free line magnetic particle imaging in the presence of inhomogeneous and nonlinear magnetic fields," in *Biomedical Engineering / Biomedizinische Technik*, vol. 60, no. Suppl. 1, 2015, pp. 245–248.

[O42] T. M. Buzug, C. Kaethner, M. Grüttner, G. Bringout, and M. Weber, "Method for magnetic particle imaging with an unrestricted axial field of view," German Patent Apllication PCT/EP2013/075 148, 11 29, 2013.

[O43] T. M. Buzug, C. Kaethner, and G. Bringout, "Röntgen-CT-Verfahren mit simultanem Magnetic Particle Imaging," German Patent Apllication PCT/EP2015/062 757, 6 16, 2014.

Bibliography

[1] B. Gleich and J. Weizenecker, "Tomographic imaging using the nonlinear response of magnetic particles," *Nature*, vol. 435, pp. 1214–1217, 2005.

[2] J. Weizenecker, B. Gleich, and J. Borgert, "Magnetic particle imaging using a field free line," *Journal of Physics D: Applied Physics*, vol. 41, no. 10, p. 105009, 2008.

[3] T. Knopp, T. F. Sattel, S. Biederer, and T. M. Buzug, "Field-free line formation in a magnetic field," *Journal of Physics A: Mathematical and Theoretical*, vol. 43, no. 1, p. 012002, 2010.

[4] T. Knopp, M. Erbe, S. Biederer, T. F. Sattel, and T. M. Buzug, "Efficient generation of a magnetic field-free line," *Medical Physics*, vol. 37, no. 7, pp. 3538–3540, 2010.

[5] M. Erbe, "Field free line magnetic particle imaging," Ph.D. dissertation, Universität zu Lübeck, 2013.

[6] M. Weber, "Power loss optimized field free line generation for magnetic particle imaging," Master's thesis, Institute of Medical Engineering, Universität zu Lüebeck, Lübeck, 2012.

[7] K. Bente, M. Weber, M. Graeeser, T. F. Sattel, M. Erbe, and T. M. Buzug, "Electronic field free line rotation and relaxation deconvolution in magnetic particle imaging," *IEEE Transactions on Medical Imaging*, vol. 34, no. 2, pp. 644–651, 2014.

[8] J. D. Jackson, *Classical Electrodynamics*, 3rd ed. New Jersey: John Wiley & Sons, Inc., 1998.

[9] D. J. Griffiths and R. College, *Introduction to electrodynamics*, 3rd ed. Prentice hall, Inc., 1999.

[10] G. N. Peeren, "Stream function approach for determining optimal surface currents," Ph.D. dissertation, Technische Universiteit Eindhoven, 2003.

[11] H. Kaden, *Wirbelströme und Schirmung in der Nachrichtentechnik*, 2nd ed., ser. Klassiker der Technik. Berlin: Springer-Verlag, 1999.

[12] M. Poole, "Improved equipment and techniques for dynamic shimming in high field MRI," Ph.D. dissertation, University of Nottingham, 2007.

[13] G. B. Arfken and H. J. Weber, *Mathematical Methods For Physicists*, 4th ed. Waltham: Academic Press, 1995.

[14] D. Winch, D. Ivers, J. Turner, and R. Stening, "Geomagnetism and schmidt quasi-normalization," *Geophysical Journal International*, vol. 160, no. 2, pp. 487–504, 2005.

[15] S. Chapman and J. Bartels, "Geomagnetism, vol. 2," *Oxford, Clarendon Press, 1940*, p. 833, 1940.

[16] D. R. Schmitz, J. Meyer, and J. C. Cain, "Modelling the earth's geomagnetic field to high degree and order," *Geophysical Journal International*, vol. 97, no. 3, pp. 421–430, 1989.

[17] M. Hermann, *Numerische Mathematik*, 3rd ed. München: Oldenbourg Wissenschaftsverlag, 2006.

[18] A. Weber, "Magnetfeldmessung," private communication, 2013.

[19] M. J. Mohlenkamp, "A user's guide to spherical harmonics," 2011.

[20] T. Knopp and T. M. Buzug, *Magnetic Particle Imaging: An Introduction to Imaging Principles and Scanner Instrumentation*. Berlin: Springer-Verlag, 2012.

[21] C. C. Sánchez, "Forward and inverse analysis of electromagnetic fields for MRI using computational techniques," Ph.D. dissertation, University of Nottingham, 2008.

[22] J. D. Jackson, "From lorenz to coulomb and other explicit gauge transformations," *American Journal of Physics*, vol. 70, no. 9, pp. 917–928, 2002.

[23] J. D. Jackson and L. B. Okun, "Historical roots of gauge invariance," *Reviews of Modern Physics*, vol. 73, no. 3, p. 663, 2001.

[24] A. Mertins, *Signaltheorie*, 3rd ed. Wiesbaden: Springer Vieweg, 2012.

[25] G. Heinzel, R. A., and S. R., "Spectrum and spectral density estimation by the discrete fourier transform (dft), including a comprehensive list of window functions and some new at-top windows." 2002.

[26] M. Frigo and S. G. Johnson, "FFTW subroutine package," http://www.fftw.org/, [Online; accessed 31-Oct-2012].

[27] M. Grüttner, T. Knopp, J. Franke, M. Heidenreich, J. Rahmer, A. Halkola, C. Kaethner, J. Borgert, and T. M. Buzug, "On the formulation of the image reconstruction problem in magnetic particle imaging," *Biomedizinische Technik / Biomedical Engineering*, vol. 58, no. 6, pp. 583–591, 2013.

[28] R. Lawaczeck, H. Bauer, T. Frenzel, M. Hasegawa, Y. Ito, K. Kito, N. Miwa, H. Tsutsui, H. Vogler, and H.-J. Weinmann, "Magnetic iron oxide particles coated with carboxydextran for parenteral administration and liver contrasting: preclinical profile of sh u555a," *Acta Radiologica*, vol. 38, no. 4, pp. 584–597, 1997.

[29] S. Biederer, "Magnet-Partikel-Spektrometer: Entwicklung eines Spektrometers zur Analyse superparamagnetischer Eisenoxid-Nanopartikel für magnetic-particle-imaging," Ph.D. dissertation, Universität zu Lübeck, 2011.

[30] B. D. Cullity and C. D. Graham, *Introduction to magnetic materials*, 2nd ed. New Jersey: John Wiley & Sons, 2009.

[31] J. Weizenecker, J. Borgert, and B. Gleich, "A simulation study on the resolution and sensitivity of magnetic particle imaging," *Physics in Medicine and Biology*, vol. 52, no. 21, p. 6363, 2007.

[32] J. Rahmer, J. Weizenecker, B. Gleich, and J. Borgert, "Analysis of a 3-d system function measured for magnetic particle imaging," *IEEE Transactions on Medical Imaging*, vol. 31, no. 6, pp. 1289–1299, 2012.

[33] J. Gehrcke, M. Rückert, T. Kampf, W. Kullmann, P. Jakob, and V. Behr, "Investigation of the magnetic particle imaging signal's dependency on ferrofluid concentration," in *Magnetic nanoparticles: Particle science, imaging technology, and clinical application.* Singapore: World Scientific Publishing Co Pte Ltd, 2010, pp. 73–78.

[34] D. Eberbeck, F. Wiekhorst, S. Wagner, and L. Trahms, "How the size distribution of magnetic nanoparticles determines their magnetic particle imaging performance," *Applied Physics Letters*, vol. 98, no. 18, p. 182502, 2011.

[35] M. Graeser, K. Bente, and T. M. Buzug, "Dynamic single-domain particle model for magnetite particles with combined crystalline and shape anisotropy," *Journal of Physics D: Applied Physics*, vol. 48, no. 27, p. 275001, 2015.

[36] L. M. Bauer, S. F. Situ, M. A. Griswold, and A. C. S. Samia, "Magnetic particle imaging tracers: State-of-the-art and future directions," *Journal of Physical Chemistry Letters*, vol. 6, pp. 2509–2517, 2015.

[37] B. Gleich, J. Weizenecker, and J. Borgert, "Experimental results on fast 2d-encoded magnetic particle imaging," *Physics in Medicine and Biology*, vol. 53, no. 6, pp. N81–N84, 2008.

[38] J. Weizenecker, B. Gleich, J. Rahmer, H. Dahnke, and J. Borgert, "Three-dimensional real-time in vivo magnetic particle imaging," *Physics in Medicine and Biology*, vol. 54, no. 5, pp. L1–L10, 2009.

[39] T. F. Sattel, T. Knopp, S. Biederer, and T. M. Buzug, "Open coil arrangement for interventional magnetic particle imaging," in *Proceedings of the International Society for Magnetic Resonance in Medicine*, vol. 18, 2010, p. 945.

[40] J. Jin, *Electromagnetic analysis and design in magnetic resonance imaging*. Boca Raton: CRC Press, 1998, vol. 1.

[41] H. E. Knoepfel, *Magnetic fields: a comprehensive theoretical treatise for practical use*. New Jersey: John Wiley & Sons, 2008.

[42] P. W. Goodwill, G. C. Scott, P. P. Stang, and S. M. Conolly, "Narrowband magnetic particle imaging," *IEEE Transactions on Medical Imaging*, vol. 28, no. 8, pp. 1231–1237, 2009.

[43] T. Knopp, S. Biederer, T. Sattel, J. Weizenecker, B. Gleich, J. Borgert, and T. M. Buzug, "Trajectory analysis for magnetic particle imaging," *Physics in Medicine and Biology*, vol. 54, no. 2, pp. 385–397, 2009.

[44] S. Wolfram, *A New Kind of Science*. Champaign, IL: Wolfram Media, 2002. [Online]. Available: http://www.wolframscience.com

[45] J. Rahmer, J. Weizenecker, B. Gleich, and J. Borgert, "Signal encoding in magnetic particle imaging: properties of the system function," *BMC Medical Imaging*, vol. 9, no. 1, 2009. DOI:10.1186/1471-2342-9-4

[46] T. Knopp, S. Biederer, T. F. Sattel, J. Rahmer, J. Weizenecker, B. Gleich, J. Borgert, and T. M. Buzug, "2d model-based reconstruction for magnetic particle imaging," *Medical Physics*, vol. 37, no. 2, pp. 485–491, 2010.

[47] P. C. Hansen, *Rank-deficient and discrete ill-posed problems: numerical aspects of linear inversion*. Philadelphia: Siam, 1998.

[48] D. Self, *Audio Power Amplifier Design*. Abingdon: Taylor & Francis, 2013.

[49] J. Stelzner, M. Gräser, and T. M. Buzug, "Design and construction of a toroidal filter coil for a magnetic particle imaging device," *Biomedical Engineering / Biomedizinische Technik*, vol. 59, pp. 679–682, 2014.

[50] A. Behrends, M. Gräser, J. Stelzner, and T. M. Buzug, "Signal chain optmimization in magnetic particle imaging," *Biomedical Engineering / Biomedizinische Technik*, vol. 59, pp. 526–529, 2014.

[51] I. Schmale, J. Borgert, B. Gleich, and J. Weizenecker, "Noise within magnetic particle imaging," in *Magnetic nanoparticles: Particle science, imaging technology, and clinical application.* Singapore: World Scientific Publishing Co Pte Ltd, 2010, pp. 154–160.

[52] J. Johnson, "Thermal agitation of electricity in conductors," *Physical Review*, vol. 32, pp. 97–109, 1928.

[53] A. Weber, J. Weizenecker, U. Heinen, M. Heidenreich, and T. M. Buzug, "Reconstruction enhancement by denoising the magnetic particle imaging system matrix using frequency domain filter," *IEEE Transactions on Magnetics*, vol. 51, no. 2, Feb 2015. DOI:10.1109/TMAG.2014.2332612

[54] J. Lampe, C. Bassoy, J. Rahmer, J. Weizenecker, H. Voss, B. Gleich, and J. Borgert, "Fast reconstruction in magnetic particle imaging," *Physics in Medicine and Biology*, vol. 57, no. 4, 2012. DOI:10.1088/0031-9155/57/4/1113

[55] T. Knopp, J. Rahmer, T. F. Sattel, S. Biederer, J. Weizenecker, B. Gleich, J. Borgert, and T. M. Buzug, "Weighted iterative reconstruction for magnetic particle imaging," *Physics in Medicine and Biology*, vol. 55, no. 6, 2010. DOI:10.1088/0031-9155/55/6/003

[56] G. T. Herman, *Fundamentals of computerized tomography: image reconstruction from projections*. Berlin: Springer-Verlag, 2009.

[57] P. C. Hansen, "Regularization tools: A matlab package for analysis and solution of discrete ill-posed problems," *Numerical Algorithms*, vol. 6, no. 1, pp. 1–35, 1994.

[58] T. Knopp, T. F. Sattel, S. Biederer, J. Rahmer, J. Weizenecker, B. Gleich, J. Borgert, and T. M. Buzug, "Model-based reconstruction for magnetic particle imaging," *IEEE Transactions on Medical Imaging*, vol. 29, no. 1, pp. 12–18, 2010.

[59] D. Eberbeck and L. Trahms, "Experimental investigation of dipolar interaction in suspensions of magnetic nanoparticles," *Journal of Magnetism and Magnetic Materials*, vol. 323, no. 10, pp. 1228–1232, 2011.

[60] P. Szwargulski, J. Rahmer, M. Ahlborg, C. Kaethner, and T. M. Buzug, "Experimental evaluation of different weighting schemes in magnetic particle imaging reconstruction," *Student Conference on Medical Engineering Science*, vol. 4, 2015.

[61] H. Bagheri, C. Kierans, K. Nelson, B. Andrade, C. Wong, A. Frederick, and M. Hayden, "A novel scanner architecture for MPI," in *2015 5th International Workshop on Magnetic Particle Imaging (IWMPI)*, March 2015. DOI:10.1109/IWMPI.2015.7107089

[62] P. Vogel, M. Ruckert, P. M. Jakob, V. C. Behr *et al.*, "μmpi—initial experiments with an ultrahigh resolution MPI," *IEEE Transactions on Magnetics*, vol. 51, no. 2, 2015. DOI:10.1109/TMAG.2014.2329135

[63] P. Vogel, M. Ruckert, P. Klauer, W. Kullmann, P. Jakob, and V. Behr, "Traveling wave magnetic particle imaging," *IEEE Transactions on Medical Imaging*, 2014. DOI:10.1109/TMI.2013.2285472

[64] P. Vogel, M. Ruckert, W. Kullmann, P. Jakob, and V. Behr, "Slice scanning mode for traveling wave MPI," in *2013 International Workshop on Magnetic Particle Imaging (IWMPI)*, March 2013. DOI:10.1109/IWMPI.2013.6528369

[65] P. Vogel, M. Ruckert, P. Klauer, W. Kullmann, P. Jakob, and V. Behr, "Rotating slice scanning mode for traveling wave MPI," *IEEE Transactions on Magnetics*, vol. 51, no. 2, Feb 2015. DOI:10.1109/TMAG.2014.2335255

[66] J. Rahmer, B. Gleich, J. Weizenecker, and J. Borgert, "3d real-time magnetic particle imaging of cerebral blood flow in living mice," in *International Society for Magnetic Resonance in Medicine*, vol. 18, 2010, p. 714.

[67] I. Schmale, J. Rahmer, B. Gleich, J. Kanzenbach, J. Schmidt, C. Bontus, O. Woywode, and J. Borgert, "First phantom and in vivo MPI images with an extended field of view," in *SPIE Medical Imaging*. International Society for Optics and Photonics, 2011, pp. 796 510–796 510.

[68] B. Gleich, J. Weizenecker, H. Timminger, C. Bontus, I. Schmale, J. Rahmer, J. Schmidt, J. Kanzenbach, and J. Borgert, "Fast MPI demonstrator with enlarged field of view," in *Proceedings of the International Society for Magnetic Resonance in Medicine*, vol. 18, 2010, p. 218.

[69] T. Wawrzik, F. Ludwig, and M. Schilling, "Assembly for one-dimensional magnetic particle imaging," in *World Congress on Medical Physics and Biomedical Engineering, September 7-12, 2009, Munich, Germany*. Berlin: Springer-Verlag, 2009, pp. 898–900.

[70] T.-A. Le, T. D. Do, Y. Noh, A. Mahmood, M. O. Kim, and J. Yoon, "Hardware implementation of a 1d MPI hybrid system for targeted drug delivery," in *2015 5th International Workshop on Magnetic Particle Imaging (IWMPI)*, 2015. DOI:10.1109/IWMPI.2015.7107010

[71] T. Wawrzik, F. Ludwig, and M. Schilling, "Two-dimensional magnetic particle imaging," in *Magnetic Nanoparticles: Particle Science, Imaging Technology, and Clinical Applications*, vol. 1. Singapore: World Scientific Publishing Co Pte Ltd, 2010, pp. 100–105.

[72] P. W. Goodwill and S. M. Conolly, "Multidimensional x-space magnetic particle imaging," *IEEE Transactions on Medical Imaging*, vol. 30, no. 9, pp. 1581–1590, 2011.

[73] T. Wawrzik, C. Kuhlmann, F. Ludwig, and M. Schilling, "Scanner setup and reconstruction for three-dimensional magnetic particle imaging," in *SPIE Medical Imaging*. International Society for Optics and Photonics, 2013, pp. 86 721B–86 721B.

[74] P. Goodwill, L. Croft, J. Konkle, K. Lu, E. Saritas, B. Zheng, and S. Conolly, "A 7 t/m 3d x-space MPI mouse and rat scanner," in *2013 International Workshop on Magnetic Particle Imaging (IWMPI)*, 2013. DOI:10.1109/IWMPI.2013.6528387

[75] H. Hong, J. Lim, C.-J. Choi, S.-W. Shin, and H.-J. Krause, "Magnetic particle imaging with a planar frequency mixing magnetic detection scanner," *Review of Scientific Instruments*, vol. 85, no. 1, 2014. DOI:10.1063/1.4861916

[76] Y. Ishihara, T. Honma, S. Nohara, and Y. Ito, "Evaluation of magnetic nanoparticle samples made from biocompatible ferucarbotran by time-correlation magnetic particle imaging reconstruction method," *BMC Medical Imaging*, vol. 13, no. 1, 2013. DOI:10.1186/1471-2342-13-15

[77] J. Rahmer, B. Gleich, B. David, C. Bontus, I. Schmale, J. Schmidt, J. Weizenecker, O. Mende, O. Woywode, C. Vollertsen *et al.*, "3d line imaging on a clinical magnetic particle imaging demonstrator," in *2015 5th International Workshop on Magnetic Particle Imaging (IWMPI)*, 2015. DOI:10.1109/IWMPI.2015.7107029

[78] H. Tsuchiya, S. Shimizu, T. Hatsuda, T. Takagi, T. Noguchi, and Y. Ishihara, "Two-dimensional magnetic imaging system for evaluating iterative reconstruction method based on time-correlation information," in *2015 5th International Workshop on Magnetic Particle Imaging (IWMPI)*, 2015. DOI:10.1109/IWMPI.2015.7107053

[79] N. D. Nothnagel and J. Sanchez-Gonzalez, "Measurement of system functions with extended field-of-view," *IEEE Transactions on Magnetics*, vol. 51, no. 2, 2015. DOI:10.1109/TMAG.2014.2326253

[80] K. Murase, S. Hiratsuka, R. Song, and Y. Takeuchi, "Development of a system for magnetic particle imaging using neodymium magnets and gradiometer," *Japanese Journal of Applied Physics*, vol. 53, no. 6, 2014. DOI:10.7567/JJAP.53.067001

[81] P. W. Goodwill, K. Lu, B. Zheng, and S. M. Conolly, "An x-space magnetic particle imaging scanner," *Review of Scientific Instruments*, vol. 83, no. 3, 2012. DOI:10.1063/1.3694534

[82] J. Rahmer, B. Gleich, J. Weizenecker, A. Halkola, C. Bontus, J. Schmidt, I. Schmale, O. Woywode, T. M. Buzug, and J. Borgert, "Fast continuous motion of the field of view in magnetic particle imaging," in *2013 International Workshop on Magnetic Particle Imaging (IWMPI)*, 2013. DOI:10.1109/IWMPI.2013.6528353

[83] J. Rahmer, B. Gleich, J. Schmidt, C. Bontus, I. Schmale, J. Kanzenbach, J. Borgert, O. Woywode, A. Halkola, and J. Weizenecker, "Continuous focus field variation for extending the imaging range in 3d MPI," in *Magnetic Particle Imaging*,

ser. Springer Proceedings in Physics, T. M. Buzug and J. Borgert, Eds. Berlin: Springer-Verlag, 2012, vol. 140, pp. 255–259.

[84] P. Vogel, S. Lother, M. Ruckert, W. H. Kullmann, P. M. Jakob, F. Fidler, and V. C. Behr, "MRI meets MPI: a bimodal MPI-MRI tomograph," *IEEE Transactions on Medical Imaging*, 2014. DOI:10.1109/TMI.2014.2327515

[85] J. Franke, U. Heinen, H. Lehr, A. Weber, F. Jaspard, W. Ruhm, M. Heidenreich, and V. Schulz, "First 3d dual modality phantom measurements of a hybrid MPI-MRI system using a resistive 12 channel MPI-MRI magnet design," in *2015 5th International Workshop on Magnetic Particle Imaging (IWMPI)*, March 2015. DOI:10.1109/IWMPI.2015.7106990

[86] S. Waanders, M. Visscher, T. Oderkerk, H. Krooshoop, and B. Haken, "Method and apparatus for measuring an amount of superparamagnetic material in an object," Netherlands Patent Apllication EP20,120,194,029, 5 28, 2014.

[87] T. F. Sattel, T. Knopp, S. Biederer, B. Gleich, J. Weizenecker, J. Borgert, and T. M. Buzug, "Single-sided device for magnetic particle imaging," *Journal of Physics D: Applied Physics*, vol. 42, no. 2, 2009. DOI:10.1088/0022-3727/42/2/022001

[88] J. B. Weaver, A. M. Rauwerdink, B. S. Trembly, and C. R. Sullivan, "Imaging magnetic nanoparticles using the signal's frequency spectrum," in *Proceedings SPIE*, vol. 6916. International Society for Optics and Photonics, 2008, pp. Y0–8.

[89] K. Murase, R. Song, and S. Hiratsuka, "Magnetic particle imaging of blood coagulation," *Applied Physics Letters*, vol. 104, no. 25, 2014. DOI:10.1063/1.4885146

[90] J. J. Konkle, P. W. Goodwill, O. M. Carrasco-Zevallos, and S. M. Conolly, "Projection reconstruction magnetic particle imaging," *IEEE Transactions on Medical Imaging*, vol. 32, no. 2, pp. 338–347, 2013.

[91] J. J. Konkle, P. W. Goodwill, E. U. Saritas, B. Zheng, K. Lu, and S. M. Conolly, "Twenty-fold acceleration of 3d projection reconstruction MPI," *Biomedizinische Technik / Biomedical Engineering*, vol. 58, no. 6, pp. 565–576, 2013.

[92] M. Weber, K. Bente, A. von Gladiss, and T. M. Buzug, "MPI with a mechanically rotated FFL," in *2015 5th International Workshop on Magnetic Particle Imaging (IWMPI)*, March 2015. DOI:10.1109/IWMPI.2015.7107026

[93] M. Weber, personal communication, Universität zu Lübeck, march 2015.

[94] M. Straub, S. Hubertus, F. Kiessling, and V. Schulz, "MPI field generator design for an FFL based image acquisition," in *2015 5th International Workshop on Magnetic Particle Imaging (IWMPI)*, March 2015. DOI:10.1109/IWMPI.2015.7107056

[95] X. Lv, Z. Wang, S. Wei, H. Wang, and W. Yang, "A simulation study for a novel generation method of electro-drive rotating field free line," in *2015 5th International Workshop on Magnetic Particle Imaging (IWMPI)*, March 2015. DOI:10.1109/IWMPI.2015.71070567107075

[96] T. M. Buzug, *Computed tomography: from photon statistics to modern cone-beam CT*. Berlin: Springer-Verlag, 2008.

[97] S. Cho, J. Bian, C. A. Pelizzari, C.-T. Chen, T.-C. He, and X. Pan, "Region-of-interest image reconstruction in circular cone-beam microct," *Medical Physics*, vol. 34, no. 12, pp. 4923–4933, 2007.

[98] K. Ogawa, M. Nakajima, and S. Yuta, "A reconstruction algorithm from truncated projections," *IEEE Transactions on Medical Imaging*, vol. 3, no. 1, pp. 34–40, 1984.

[99] G. T. Herman and R. M. Lewitt, "Evaluation of a preprocessing algorithm for truncated ct projections." *Journal of Computer Assisted Tomography*, vol. 5, no. 1, pp. 127–135, 1981.

[100] H. Yu, Y. Ye, S. Zhao, and G. Wang, "Local roi reconstruction via generalized fbp and bpf algorithms along more flexible curves," *International Journal of Biomedical Imaging*, 2006. DOI:10.1155/IJBI/2006/14989

[101] A. A. Shabana, *Dynamics of multibody systems*. Cambridge: Cambridge University Press, 2013.

[102] F. Dunn and I. Parberry, *3D math primer for graphics and game development*. Boca Raton: CRC Press, 2011.

[103] W. Kaplan, *Advanced calculus*, 5th ed. Reading, MA: Addison-Wesley, 1952.

[104] W. Erb, C. Kaethner, M. Ahlborg, and T. M. Buzug, "Bivariate lagrange interpolation at the node points of non-degenerate lissajous curves," *arXiv preprint arXiv:1411.7589*, 2014.

[105] R. Turner, "Gradient coil design: a review of methods," *Magnetic Resonance Imaging*, vol. 11, no. 7, pp. 903–920, 1993.

[106] M. S. Poole, "Improved equipment and techniques for dynamic shimming in high field MRI." Ph.D. dissertation, University of Nottingham, 2007.

[107] C. Cobos Sanchez, "Forward and inverse analysis of electromagnetic fields for MRI using computational techniques," Ph.D. dissertation, University of Nottingham, 2008.

[108] S. Pissanetzky, "Minimum energy MRI gradient coils of general geometry," *Measurement Science and Technology*, vol. 3, no. 7, p. 667, 1992.

[109] G. N. Peeren, "Stream function approach for determining optimal surface currents," *Journal of Computational Physics*, vol. 191, no. 1, pp. 305–321, 2003.

[110] F. París and J. Cañas, *Boundary element method: fundamentals and applications*. Oxford: Oxford University Press, 1997.

[111] M. Belkin, J. Sun, and Y. Wang, "Discrete laplace operator on meshed surfaces," in *Proceedings of the twenty-fourth annual symposium on Computational geometry*. ACM, 2008, pp. 278–287.

[112] H. Rathod, K. Nagaraja, B. Venkatesudu, and N. Ramesh, "Gauss legendre quadrature over a triangle," *Journal of the Indian Institute of Science*, vol. 84, no. 5, pp. 183–188, 2013.

[113] W. H. Press, S. A. Teukolsky, W. T. Vetterling, and B. P. Flannery, *Numerical recipes in Fortran 77 and Fortran 90*. Cambridge: Cambridge University Press, 1996.

[114] T. F. Eibert and V. Hansen, "On the calculation of potential integrals for linear source distributions on triangular domains," *IEEE Transactions on Antennas and Propagation*, vol. 43, no. 12, pp. 1499–1502, 1995.

[115] P. C. Hansen, "Regularization tools: A matlab package for analysis and solution of discrete ill-posed problems," *Numerical Algorithms*, vol. 6, no. 1, pp. 1–35, 1994.

[116] ——, "Regularization tools version 4.0 for matlab 7.3," *Numerical Algorithms*, vol. 46, no. 2, pp. 189–194, 2007.

[117] J. Currie and D. I. Wilson, "Opti: Lowering the barrier between open source optimizers and the industrial matlab user," in *Foundations of Computer-Aided Process Operations*, N. Sahinidis and J. Pinto, Eds., Savannah, Georgia, USA, 8–11 January 2012.

[118] J. Löfberg, "Yalmip : A toolbox for modeling and optimization in MATLAB," in *Computer Aided Control Systems Design, 2004 IEEE International Symposium on*, 2004, pp. 284–289.

[119] A. Wächter and L. T. Biegler, "On the implementation of an interior-point filter line-search algorithm for large-scale nonlinear programming," *Mathematical Programming*, vol. 106, no. 1, pp. 25–57, 2006.

[120] H. Sanchez Lopez, F. Freschi, A. Trakic, E. Smith, J. Herbert, M. Fuentes, S. Wilson, L. Liu, M. Repetto, and S. Crozier, "Multilayer integral method for simulation of eddy currents in thin volumes of arbitrary geometry produced by MRI gradient coils," *Magnetic Resonance in Medicine*, vol. 71, no. 5, pp. 1912–1922, 2014.

[121] M. Kamon, M. J. Tsuk, and J. K. White, "Fasthenry: A multipole-accelerated 3-d inductance extraction program," *IEEE Transactions on Microwave Theory and Techniques*, vol. 42, no. 9, pp. 1750–1758, 1994.

[122] R. Bowtell and P. Robyr, "Multilayer gradient coil design," *Journal of Magnetic Resonance*, vol. 131, no. 2, pp. 286–294, 1998.

[123] B. Chronik, A. Alejski, and B. K. Rutt, "Design and fabriacation of a three-axis multilayer gradient coil for magnetic resonance microscopy of mice," *Magnetic Resonance Materials in Physics, Biology and Medicine*, vol. 10, no. 2, pp. 131–146, 2000.

[124] M. S. Poole, P. T. While, H. S. Lopez, and S. Crozier, "Minimax current density gradient coils: analysis of coil performance and heating," *Magnetic Resonance in Medicine*, vol. 68, no. 2, pp. 639–648, 2012.

[125] L. Walckiers, "Cern accelerator school: specialized course on magnets," CERN, Tech. Rep. CERN-2010-004, 2009.

[126] M. Tannenbaum, A. Ghosh, K. Robins, and W. Sampson, "Magnetic properties of the iron laminations for cba magnets," *IEEE Transactions on Nuclear Science*, vol. 30, no. 4, pp. 3472–3474, 1983.

[127] "A simulation with mafia for the hermes transverse target magnet," Desy, Tech. Rep. Hermes report 2001, 2001.

[128] G. Ramesh, "Field quality aspects of the different magnet designs," Berkeley lab, Tech. Rep. FERMILAB-VLHCPUB-109, 1998.

[129] J. Tanabe, "Iron dominated electromagnets design, fabrication, assembly and measurement," Stanford Linear Accelerator Center, Tech. Rep. slac-r-754, 2005.

[130] W. Scandale, R. Bartolini, P. Ferracin, E. Todesco, and P. Fessia, "Field-shape imperfections of the CERN-LHC dipole arising from mechanical deformations and component tolerances," CERN, Tech. Rep. LHC-project-report-225, 1998.

[131] G. V. Velev, R. Bossert, S. Caspi, G. Chlachidze, J. DiMarco, P. Ferracin, V. V. Kashikhin, M. Lamm, G. L. Sabbi, P. Schlabach, T. M, J. Tampkins, and A. V. Zlobin, "Field quality measurements and analysis of the larp technology quadrupole models," *IEEE Transactions on Applied Superconductivity*, vol. 18, no. 2, pp. 184–187, 2008.

[132] P. Thompson, R. Gupta, S. Kahn, H. Hahn, G. Morgan, P. Wanderer, and E. Willen, "Iron saturation control in RHIC dipole magnets," Brookhaven National Laboratory, Tech. Rep. PAC1991 2242, 1991.

[133] *Medical electrical equipment—Part 2-33: particular requirements for the safety of magnetic resonance equipment for medical diagnosis*, International Organization for Standardization Std. IEC 60 601-2-33:2008, 2008.

[134] I. Schmale, B. Gleich, J. Schmidt, J. Rahmer, C. Bontus, R. Eckart, B. David, M. Heinrich, O. Mende, and O. Woywode, "Human PNS and SAR study in the frequency range from 24 to 162 khz," in *2013 International Workshop on Magnetic Particle Imaging (IWMPI)*, 2013. DOI:10.1109/IWMPI.2013.6528346

[135] J. Bohnert, "Effects of time-varying magnetic fields in the frequency range 1 khz to 100 khz upon the human body: Numerical studies and stimulation experiment," Ph.D. dissertation, Karlsruhe Institute of Technology, 2011.

[136] I. Schmale, B. Gleich, J. Rahmer, C. Bontus, J. Schmidt, and J. Borgert, "MPI safety in the view of MRI safety standards," *IEEE Transactions on Magnetics*, 2015. DOI:10.1109/TMAG.2014.2322940

[137] I. S. C. C. . on Non-Ionizing Radiation Hazards, *C95.6 IEEE Standard for Safety Levels with Respect to Human Exposure to Radio Frequency Electromagnetic*

Fields, 3kHz to 300 GHz, Institute of Electrical and Electronics Engineers, Incorporated Std., 1992.

[138] *Guidelines for limiting exposure to time-varying electric and magnetic fields (1 Hz to 100 kHz)*, International Commission on Non-Ionizing Radiation Protection Std., 1998.

[139] J. Reilly, "Peripheral nerve stimulation by induced electric currents: exposure to time-varying magnetic fields," *Medical and Biological Engineering and Computing*, vol. 27, no. 2, pp. 101–110, 1989.

[140] ——, "Magnetic field excitation of peripheral nerves and the heart: a comparison of thresholds," *Medical and Biological Engineering and Computing*, vol. 29, no. 6, pp. 571–579, 1991.

[141] M. Bencsik, R. Bowtell, and R. Bowley, "Electric fields induced in the human body by time-varying magnetic field gradients in MRI: numerical calculations and correlation analysis," *Physics in Medicine and Biology*, vol. 52, no. 9, 2007. DOI:10.1088/0031-9155/52/9/001

[142] C. C. Sanchez, S. G. Garcia, and H. Power, "E-coil: an inverse boundary element method for a quasi-static problem," *Physics in Medicine and Biology*, vol. 55, no. 11, pp. 10.1088/0031–9155/55/11/007, 2010.

[143] A. A. Becker, *The boundary element method in engineering: a complete course*. London: McGraw-Hill, 1992.

[144] C. Pozrikidis, *A practical guide to boundary element methods with the software library BEMLIB*. Boca Raton: CRC Press, 2002.

[145] M. Guiggiani and A. Gigante, "A general algorithm for multidimensional cauchy principal value integrals in the boundary element method," *Journal of Applied Mechanics*, vol. 57, no. 4, pp. 906–915, 1990.

[146] M. Bencsik, R. Bowtell, and R. Bowley, "Electric fields induced in a spherical volume conductor by temporally varying magnetic field gradients," *Physics in Medicine and Biology*, vol. 47, no. 4, p. 557, 2002.

[147] K. M. Pohl, S. Bouix, M. Nakamura, T. Rohlfing, R. W. McCarley, R. Kikinis, W. E. L. Grimson, M. E. Shenton, and W. M. Wells, "A hierarchical algorithm for mr brain image parcellation," *IEEE Transactions on Medical Imaging*, vol. 26, no. 9, pp. 1201–1212, 2007.

[148] P. Doe, "Slicer v4.4.0 r23774," Jun. 2014. [Online]. Available: http://www.slicer.org

[149] A. Fedorov, R. Beichel, J. Kalpathy-Cramer, J. Finet, J.-C. Fillion-Robin, S. Pujol, C. Bauer, D. Jennings, F. Fennessy, M. Sonka *et al.*, "3d slicer as an image computing platform for the quantitative imaging network," *Magnetic Resonance Imaging*, vol. 30, no. 9, pp. 1323–1341, 2012.

[150] E. U. Saritas, P. W. Goodwill, G. Z. Zhang, and S. M. Conolly, "Magnetostimulation limits in magnetic particle imaging," *IEEE Transactions on Medical Imaging*, vol. 32, no. 9, pp. 1600–1610, 2013.

[151] D. J. Schaefer, J. D. Bourland, and J. A. Nyenhuis, "Review of patient safety in time-varying gradient fields," *Journal of Magnetic Resonance Imaging*, vol. 12, no. 1, pp. 20–29, 2000.

[152] K. Caputa, P. Dimbylow, T. Dawson, and M. Stuchly, "Modelling fields induced in humans by 50/60 hz magnetic fields: reliability of the results and effects of model variations," *Physics in Medicine and Biology*, vol. 47, no. 8, 2002. DOI:10.1088/0031-9155/47/8/311

[153] M. Brand and O. Heid, "Induction of electric fields due to gradient switching: a numerical approach," *Magnetic Resonance in Medicine*, vol. 48, no. 4, pp. 731–734, 2002.

[154] P. P. So, M. A. Stuchly, and J. A. Nyenhuis, "Peripheral nerve stimulation by gradient switching fields in magnetic resonance imaging," *IEEE Transactions on Biomedical Engineering*, vol. 51, no. 11, pp. 1907–1914, 2004.

[155] U. Gneveckow, A. Jordan, R. Scholz, V. Brüss, N. Waldoefner, J. Ricke, A. Feussner, B. Hildebrandt, B. Rau, and P. Wust, "Description and characterization of the novel hyperthermia-and thermoablation-system MFH® 300f for clinical magnetic fluid hyperthermia," *Medical Physics*, vol. 31, no. 6, pp. 1444–1451, 2004.

[156] J. Gao, "A novel concept for hyperthermia induced local chemotherapy," Ph.D. dissertation, Freie Universität Berlin, 2011.

[157] J. Borgert, J. D. Schmidt, I. Schmale, C. Bontus, B. Gleich, B. David, J. Weizenecker, J. Jockram, C. Lauruschkat, O. Mende *et al.*, "Perspectives on clinical magnetic particle imaging," *Biomedizinische Technik / Biomedical Engineering*, vol. 58, no. 6, pp. 551–556, 2013.

[158] H. E. Heffner and R. S. Heffner, "Hearing ranges of laboratory animals," *Journal of the American Association for Laboratory Animal Science*, vol. 46, no. 1, pp. 20–22, 2007.

[159] F. E. Terman, *Radio engineer's handbook*. London: McGraw-Hill, 1943.

[160] A. Bejan and E. Sciubba, "The optimal spacing of parallel plates cooled by forced convection," *International Journal of Heat and Mass Transfer*, vol. 35, no. 12, pp. 3259–3264, 1992.

[161] I. M. Daniel, O. Ishai, I. M. Daniel, and I. Daniel, *Engineering mechanics of composite materials*, 3rd ed. Oxford: Oxford University Press, 1994.

[162] W. C. Young and R. G. Budynas, *Roark's formulas for stress and strain*, 7th ed. New York: McGraw-Hill, 2002.

[163] *Medical electrical equipment*, International Organization for Standardization Std. IEC 60 601-1, 2005.

[164] A. M. Nagel, "Erzeugung hochfrequenter Hochspannung zur Untersuchung des dielektrischen Verhaltens von Isolierstoffen," Ph.D. dissertation, Karlsruher Institut für Technologie, 2008.

[165] I. Schmale, B. Gleich, O. Mende, and J. Borgert, "On the design of human-size MPI drive-field generators using RF litz wires," in *2015 5th International Workshop on Magnetic Particle Imaging (IWMPI)*, March 2015. DOI:10.1109/IWMPI.2015.7107071

[166] W. M. Rohsenow, J. P. Hartnett, Y. I. Cho *et al.*, *Handbook of heat transfer*. New York: McGraw-Hill, 1998, vol. 3.

[167] A. Weber and T. Knopp, "Symmetries of the 2d magnetic particle imaging system matrix," *Physics in Medicine and Biology*, vol. 60, no. 10, 2015. DOI:10.1088/0031-9155/60/10/4033

[168] B. Gleich, "Principles and applications of magnetic particle imaging," Ph.D. dissertation, Universität zu Lübeck, 2013.

[169] J. G. Betts, P. DeSaix, E. Johnson, and J. E. Johnson, *Anatomy and Physiology*. Houston: OpenStax College, 2013.

A

Circuit diagram of the rabbit-sized system

In this Appendix, the basic circuits required to build an MPI scanner are summarized. The power-factor correction and impedance matching seen in Figure A.1 are used to transfer the maximal energy from the power source to the coils. Two strategies used to acquire the MPI signal are shown in Figure A.2. In the rabbit-sized scanner presented in this work, the second solution is preferred to avoid the installation of additional coils in the scanner bore.

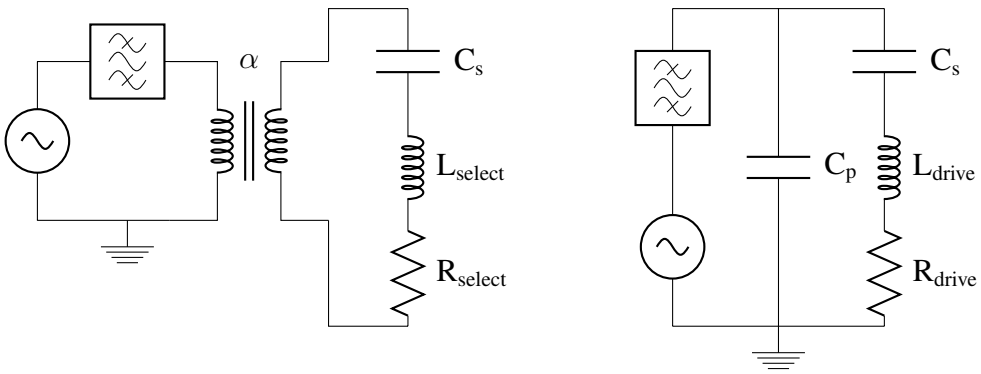

Figure A.1: Left: Power-factor correction done with a capacity in series and impedance matching realised with a transformer. Right: Power-factor correction and impedance matching achieved with two capacities. Both circuits include a band-pass filter (BPF)

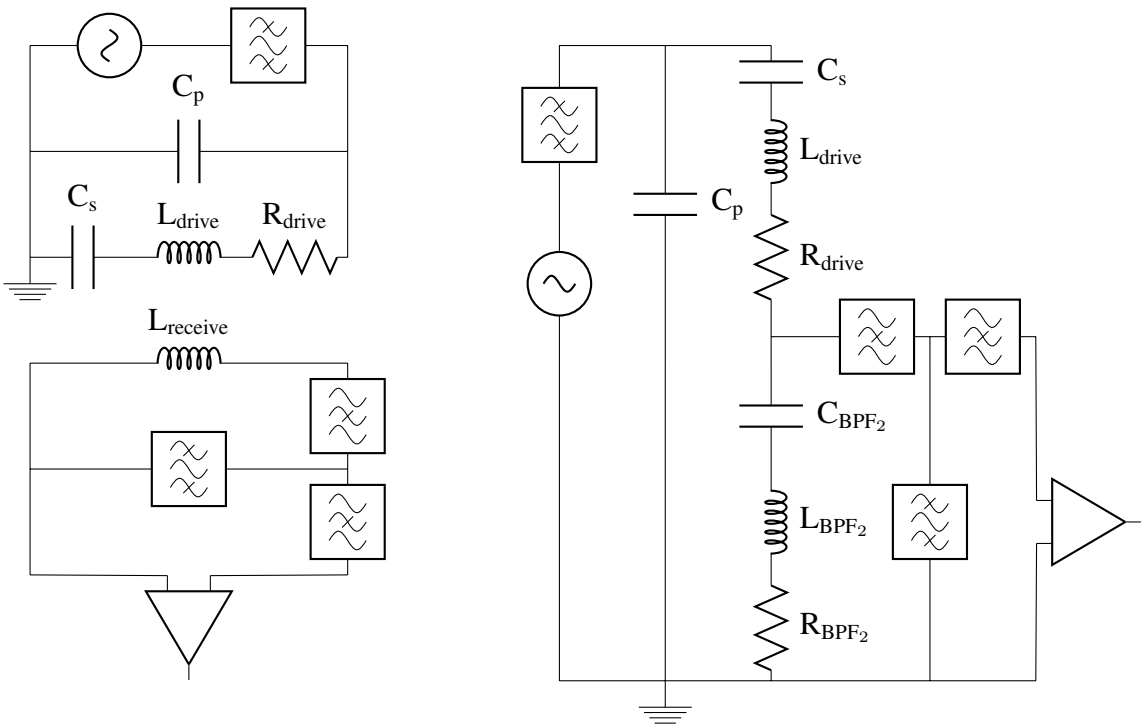

Figure A.2: Left: The receive coil is coupled with one or many drive coils. To filter the high voltage, a band-stop filter increasing the impedance at the excitation frequency is put in series with the receive coil. Right: The drive coil is also used as receive coil. A band-pass filter in series is used to carry the high voltage to the ground, while the MPI signal is brought to the LNA.

B

Details of the imaging devices

Further details of the imaging devices are given in this appendix. An example of the FFL sequences presented here are displayed in Figures B.1 and B.2.

The characterisation of the centroids, wire paths and actual coils for the rabbit-sized scanner are given in Figures 4.7, 4.8 and B.7 for the x-drive coil and in B.3, B.4 and B.8 for the y-drive coil.

The expected properties of the quadrupoles are given in Tables B.1 and B.2. The flat centroids used for the quadrupoles construction are presented in Figure B.5. The expected and measured field topologies are displayed in Figures 4.10 and B.9 for Q_0 and in B.6 and B.10 for Q_{45}. The measured field topology of the z-gradient is presented in Figure B.11.

The main coil properties of the rabbit-sized and human-sized scanners are outlined in Tables B.3 and B.4.

Finally, the simulated field topologies produced by the iron-core dual-quadrupole is presented in Figures B.13 and B.12.

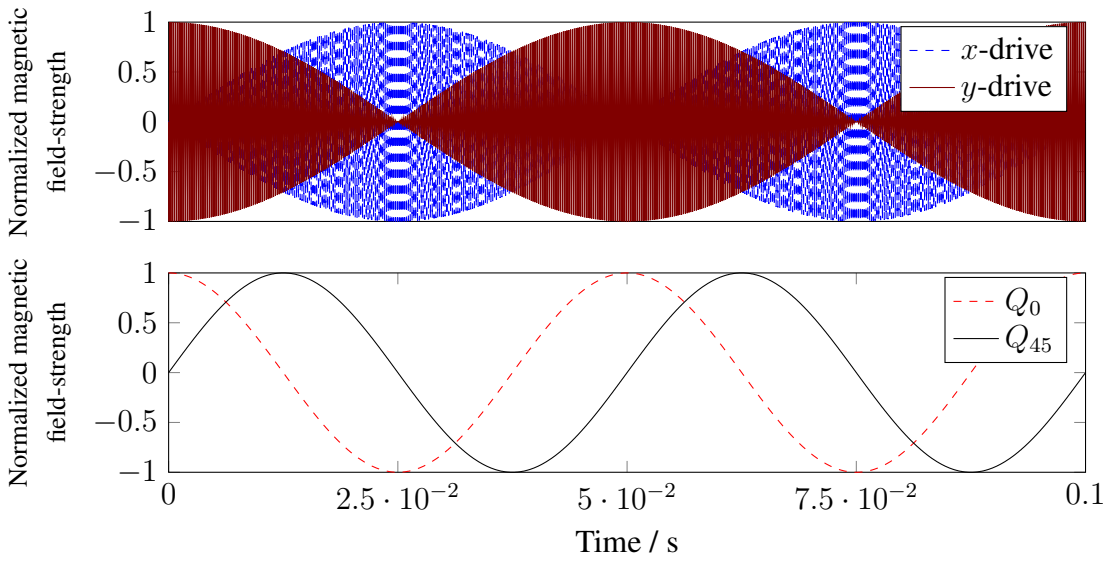

(a)

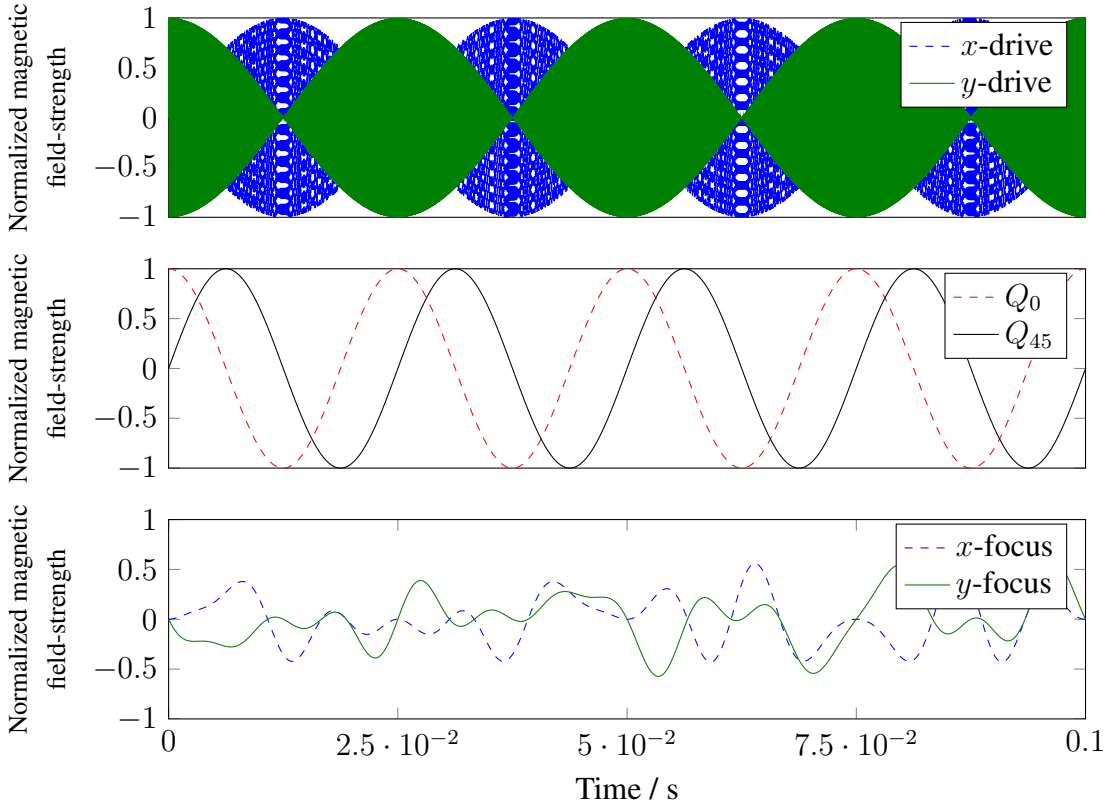

(b)

Figure B.1: FFL sequences, (a) for a rabbit-sized scanner, and (b) for the presented human-sized scanner using focus fields.

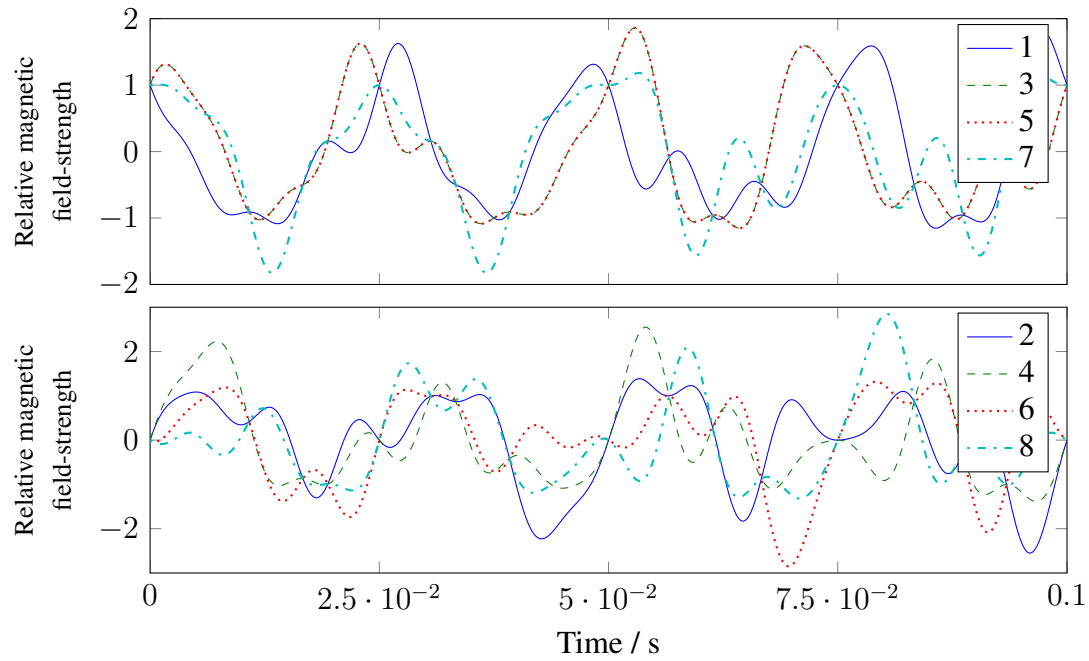

(a)

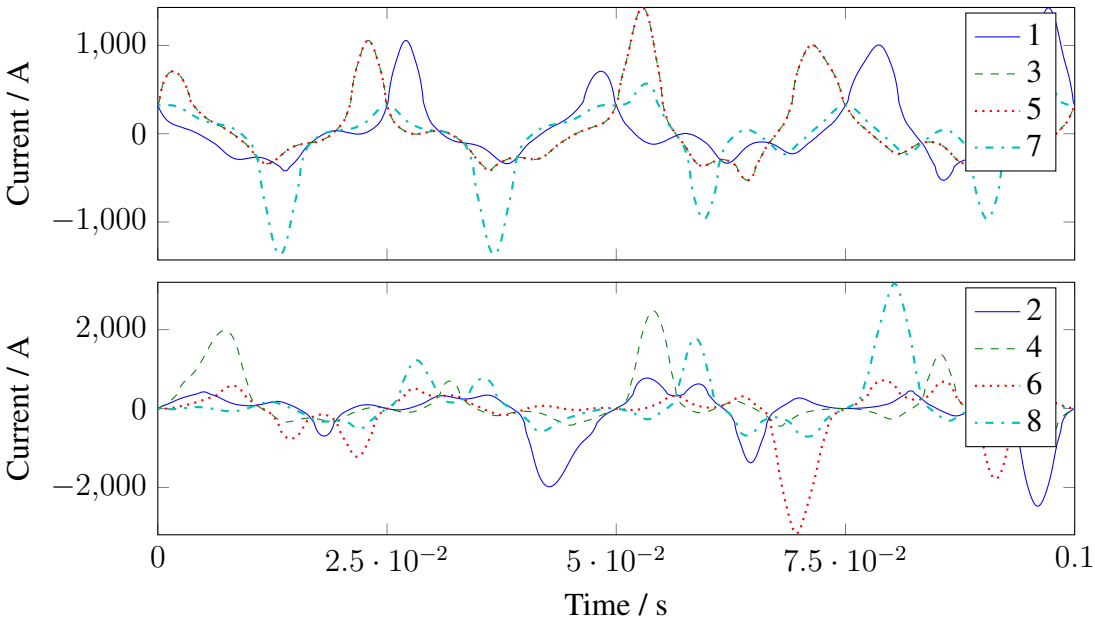

(b)

Figure B.2: Analysis of the requirements for a dual-quadrupole magnet used for an FFL sequence using focus fields to cover a large FOV. (a) Relative magnetic field strength required for each pole shoe compared to the amplitude required by a FFL sequence without focus fields. (b) Current required by each pole shoe taking into account the non-linear magnetisation curve of the Armco steel used to produce iron-core magnet.

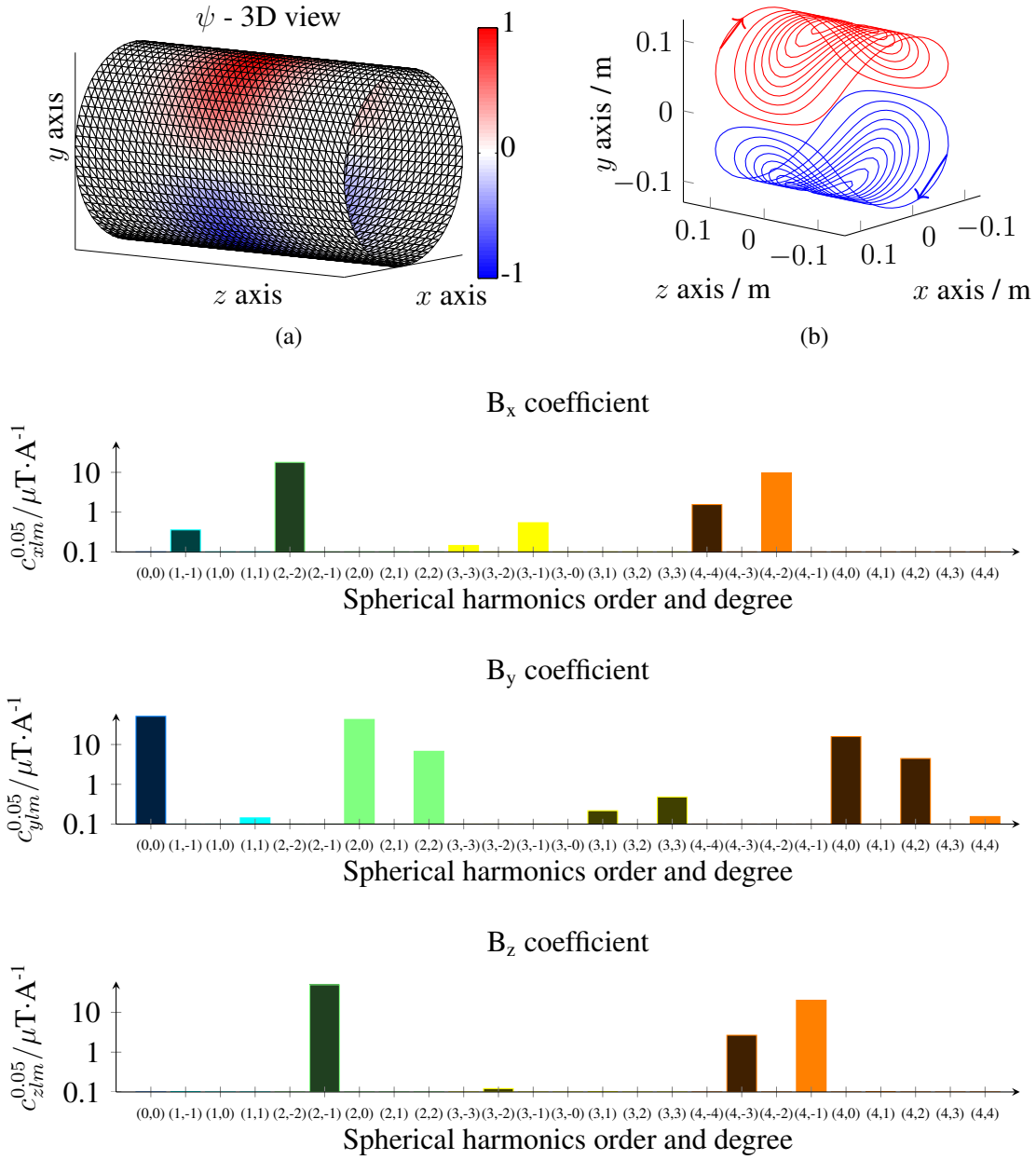

Figure B.3: y-drive coil design. (a) Normalised stream function on a cylinder with a diameter of 238 mm. (b) Extraction of 20 isolines from the stream function and representation in 3D. The arrows show the direction in which the current flows. (c) SHSE up to degree $l = 10$ and order $m = 10$ and display up to $m = l = 4$ in a sphere with radius $R = 0.05$ m. Darker filling color indicates a negative coefficient.

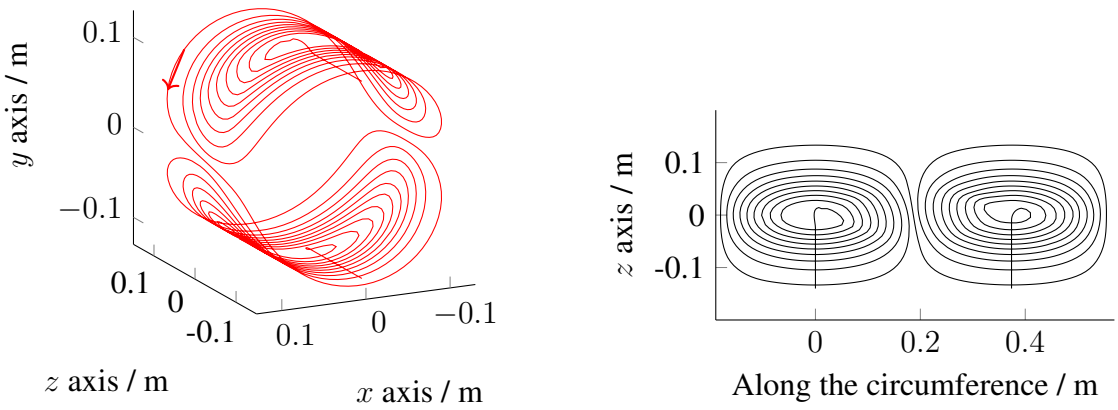

(a)

(b)

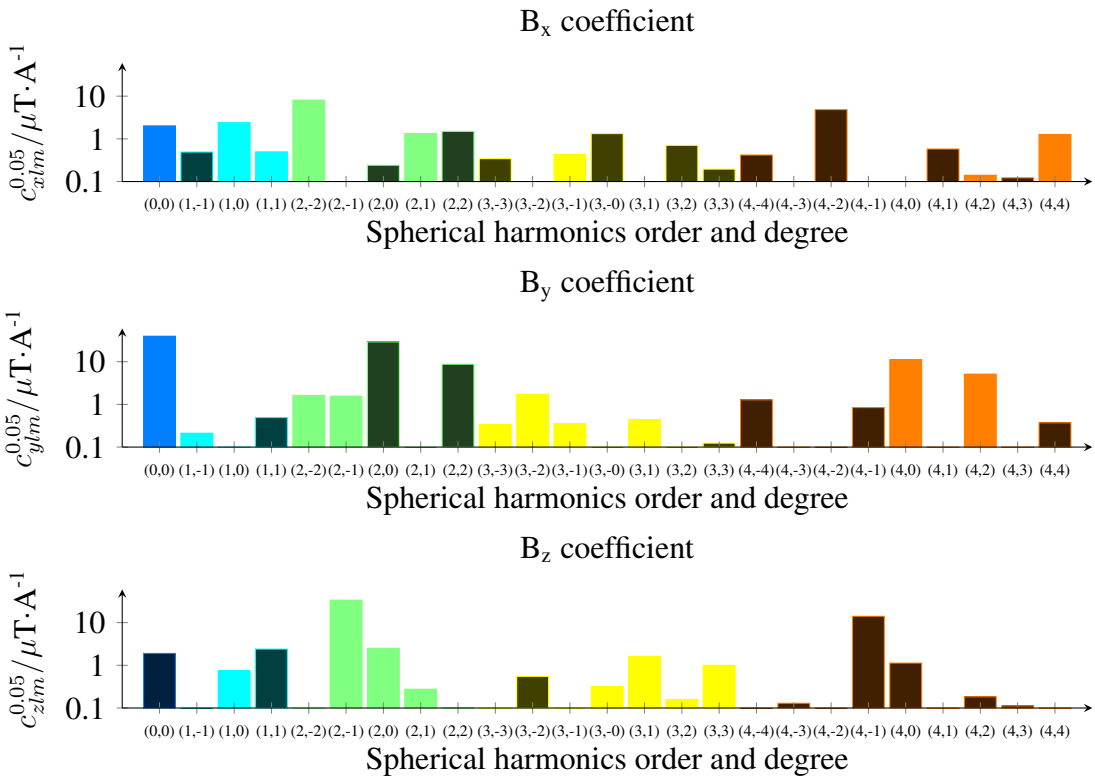

(c)

Figure B.4: Detailed information on the y-drive coil after the connection of each ideal centroid, which forms a single-wire path. (a) 3D view of the wire centroid. The arrows show the direction in which the current flows. (b) Flat projection of the centroid. (c) SHSE up to degree $l = 10$ and order $m = 10$ and display up to $m = l = 4$ in a sphere with radius $R = 0.05$ m. Darker filling color indicates a negative coefficient.

Table B.1: Properties of the centroids for the first quadrupole.

	1st layer	2nd layer	1st quadrupole
Diameter / mm	191.1	198.6	
Target $c_{x11}^{0.09}$ / T	0.018	0.018	0.036
Target diameter / T	0.09	0.09	0.09
Number loops	12	12	24
Efficiency / μT·m^{-1}·A^{-1}	343	318	661
Length of wire / m	34	35	69
Resistance / mΩ	21	22	43
Self-inductance / μH			474
Nominal peak current / A			606
RMS dissipated power / W	3856	4039	7895

Table B.2: Properties of the centroids for the second quadrupole.

	1st layer	2nd layer	2nd quadrupole
Diameter / mm	205.6	212.4	
Target $c_{x11}^{0.09}$ / T	0.018	0.018	0.036
Target diameter / m	0.09	0.09	0.09
Number loops	12	13	25
Efficiency / μT·m^{-1}·A^{-1}	294	296	590
Length of wire / m	35	39	74
Resistance / mΩ	22	25	47
Self-inductance / μH			539
Nominal peak current / A			678
RMS dissipated power / W	5057	5746	10803

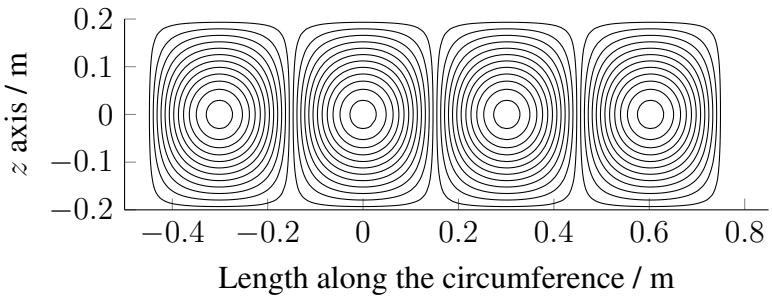

(a)

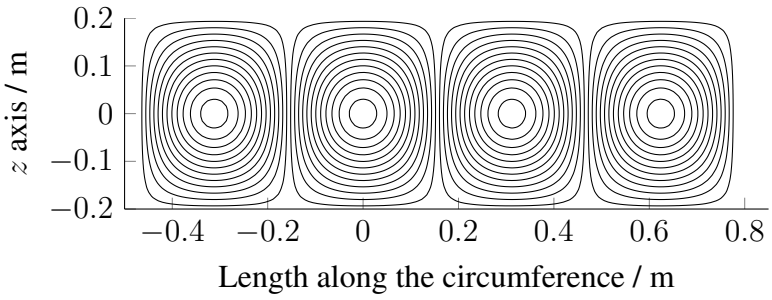

(b)

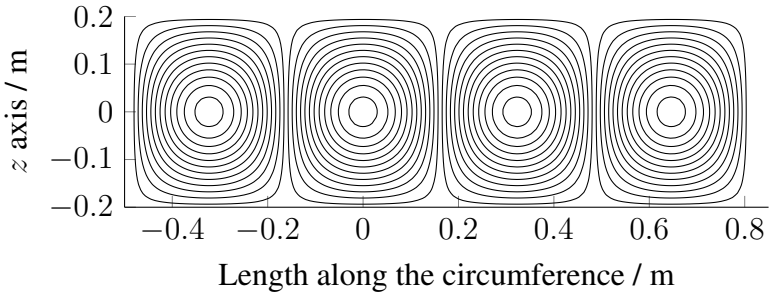

(c)

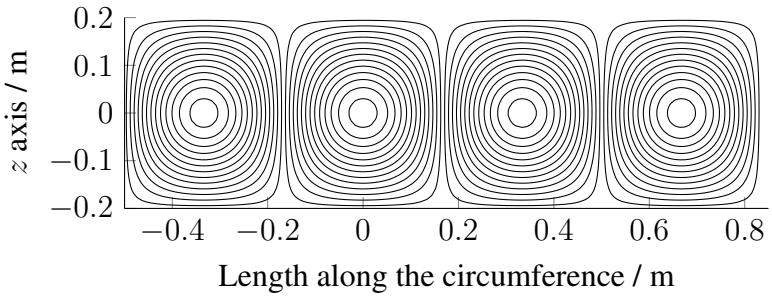

(d)

Figure B.5: Centroids as obtained via the design methods for four quadrupoles build on cylinders with different diameters. (a)-(b) First and second layers of the first quadrupole. (c)-(d) First and second layers of the second quadrupole.

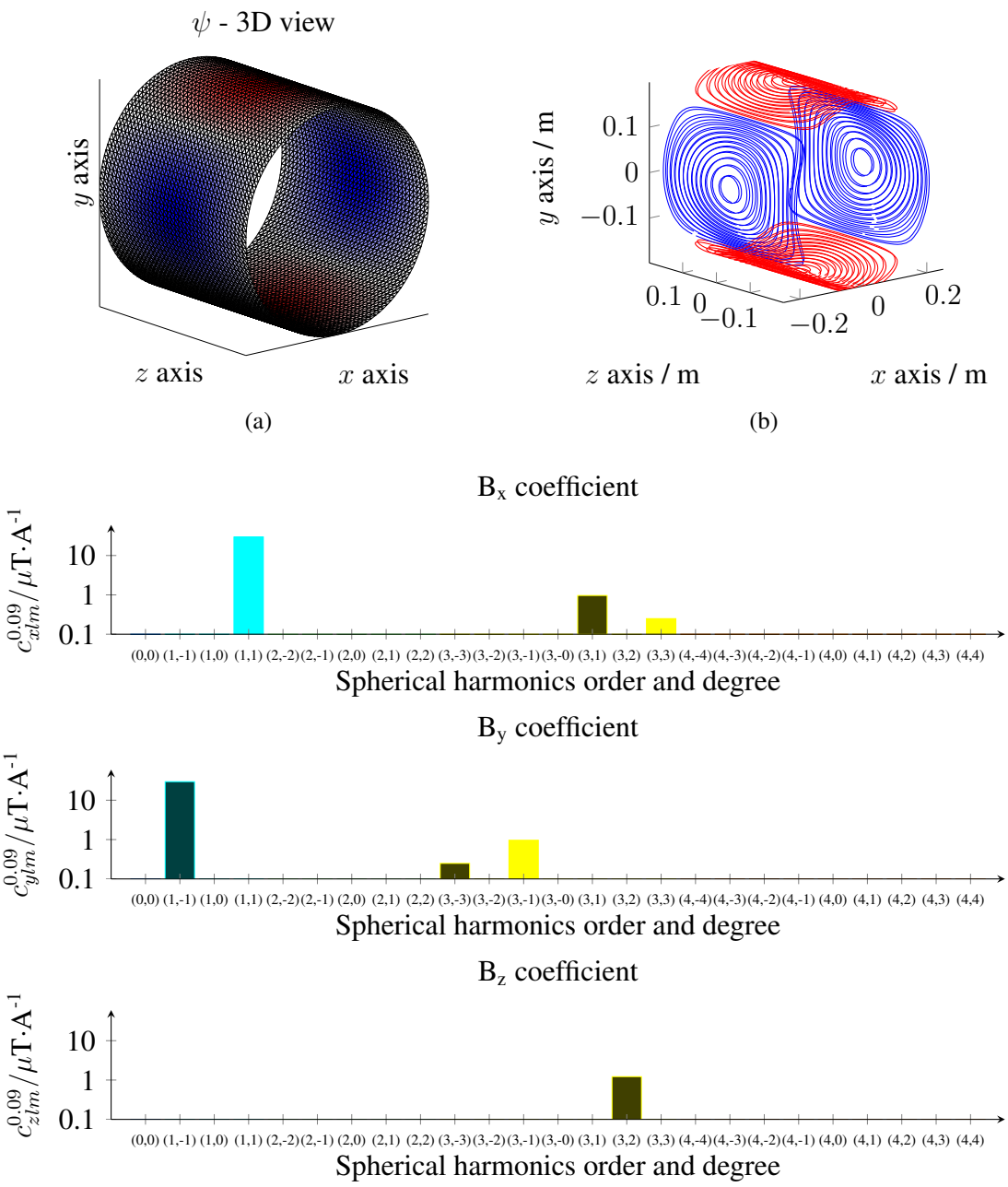

Figure B.6: Design results for a quadrupole made of 2 layers. (a) Cylindrical support and obtained stream function for the first layer of the first quadrupole. (b) Extracted centroids represented in 3D. (c) SHSE up to degree $l = 10$ and order $m = 10$ and display up to $m = l = 4$ in a sphere with radius $R = 0.09$ m. Darker filling color indicates a negative coefficient.

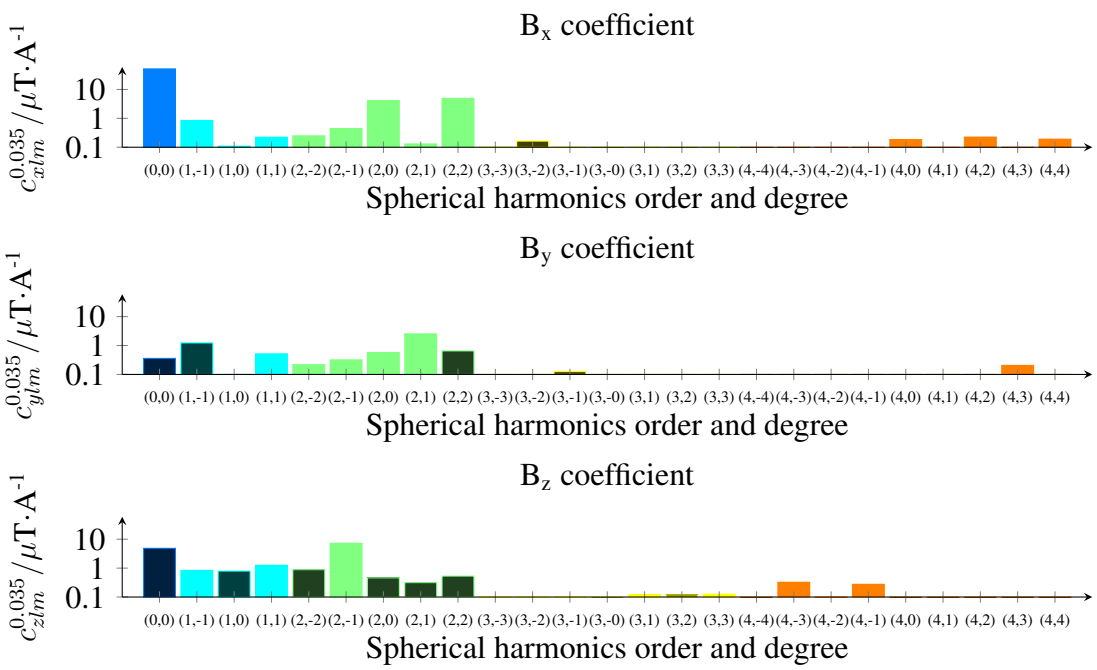

Figure B.7: Measured SHSE for the rabbit-sized x-drive coil up to degree $l = 5$ and order $m = 5$. Darker filling color indicates a negative coefficient.

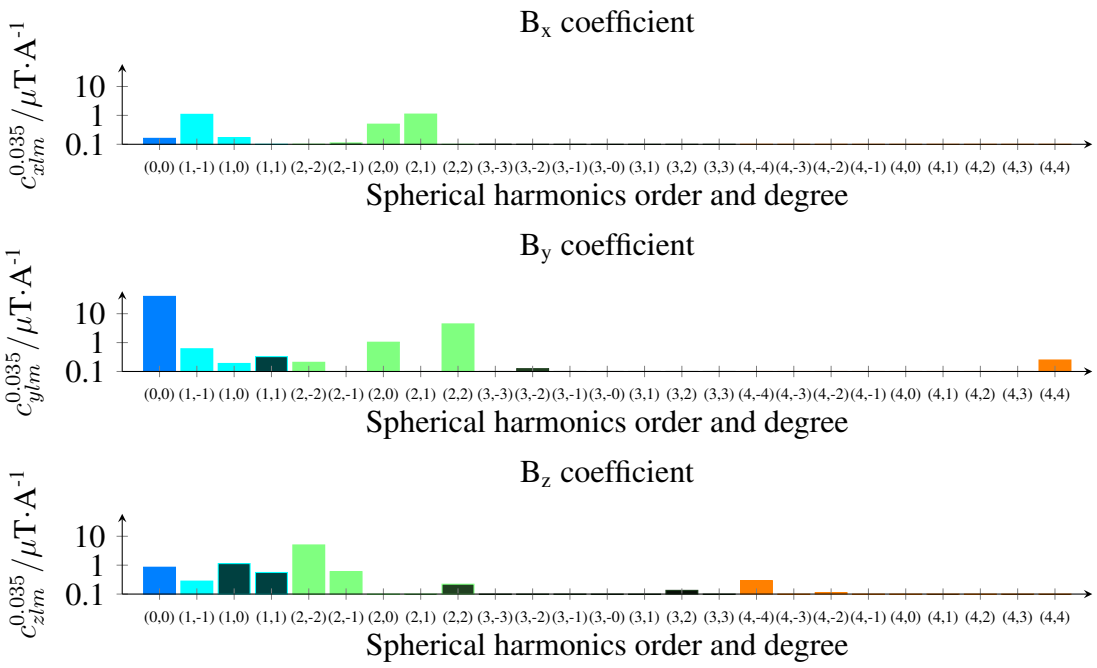

Figure B.8: Measured SHSE for the rabbit-sized y-drive coil up to degree $l = 5$ and order $m = 5$. Darker filling color indicates a negative coefficient.

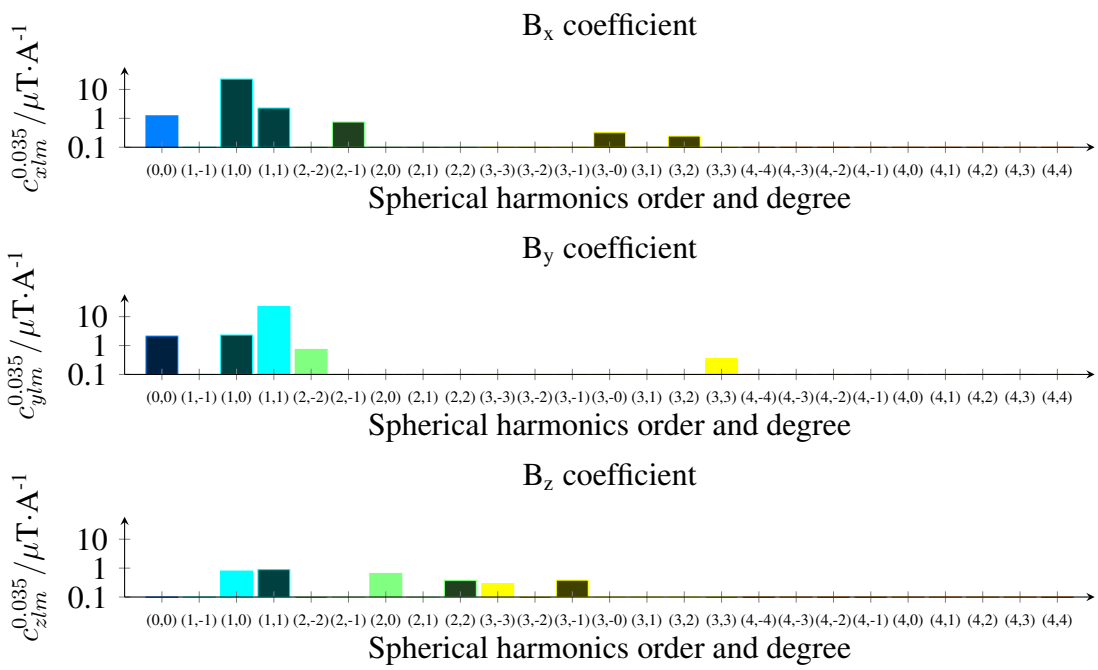

Figure B.9: Measured SHSE for the rabbit-sized quadrupole at 0° up to degree $l = 5$ and order $m = 5$. Darker filling color indicates a negative coefficient.

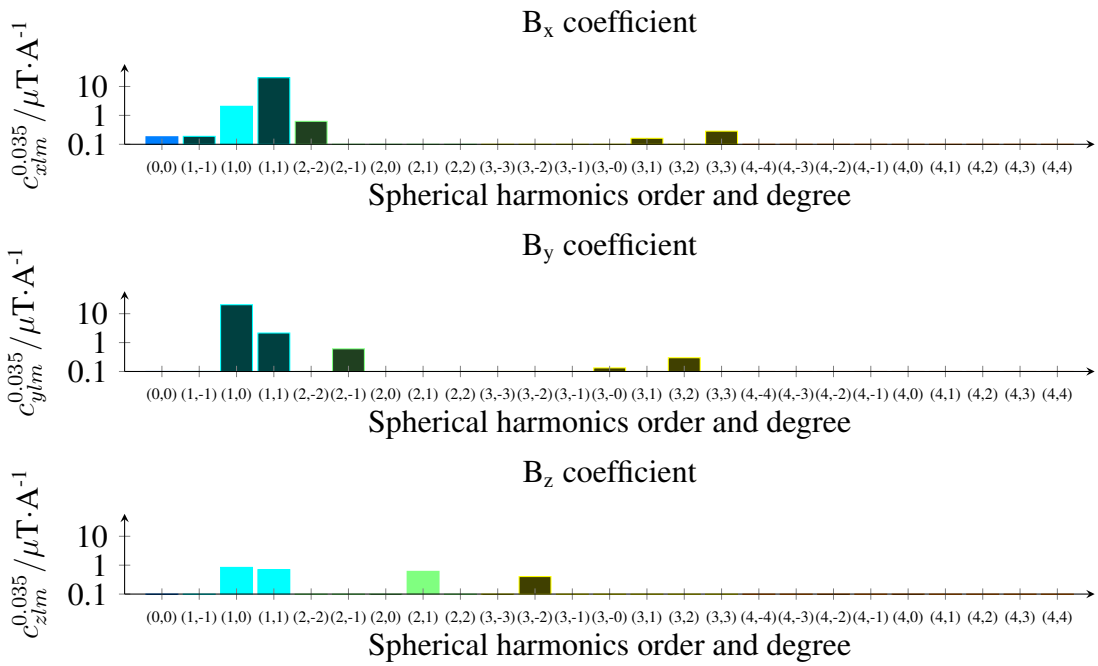

Figure B.10: Measured SHSE for the rabbit-sized quadrupole at 45° up to degree $l = 5$ and order $m = 5$. Darker filling color indicates a negative coefficient.

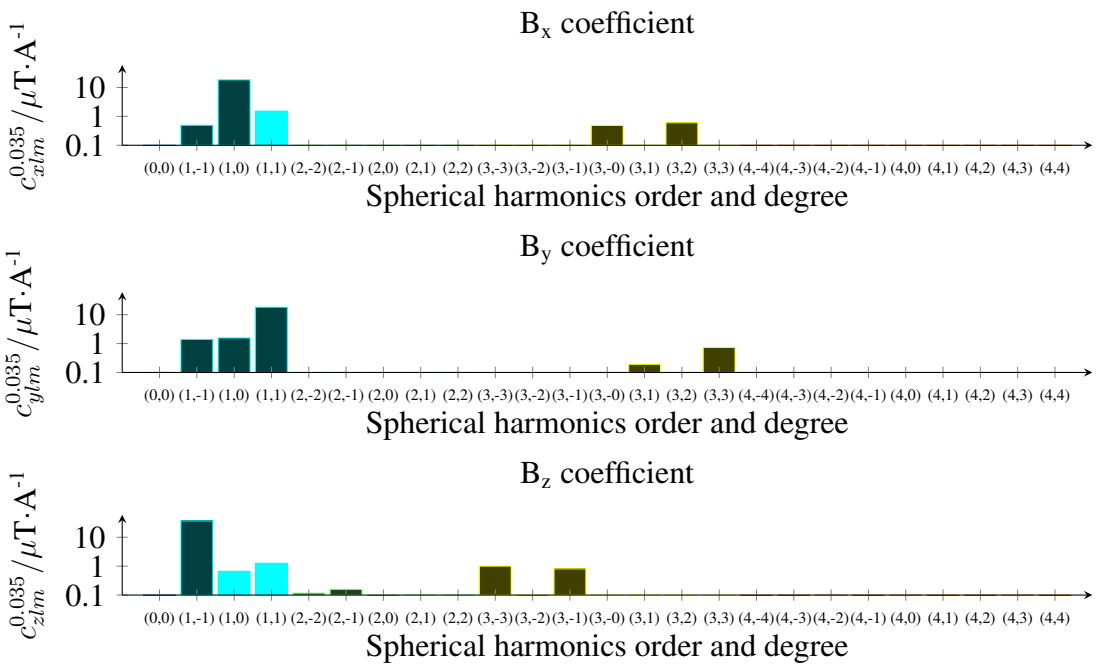

Figure B.11: Measured SHSE for the rabbit-sized z-gradient coil set up to degree $l = 5$ and order $m = 5$. Darker filling color indicates a negative coefficient.

Table B.3: Details on the simulated rabbit-sized FFL imaging device concept.

	Mean radius / m	η_{coil}	R / Ω at 20 °C	L / H (self)	f / kHz	Target amplitude	I_{peak} / A	$\lVert \vec{J}_{\text{RMS}} \rVert$ / A·mm$^{-2}_{\text{copper}}$	V_{peak} / V	P_{diss} / kW
x-drive	0.100	$43.8 \cdot 10^{-6}$	$13 \cdot 10^{-3}$	$27 \cdot 10^{-6}$	$25 * 0.01$	$15 \cdot 10^{-3}$	342	7.9	1460	0.4
y-drive	0.119	$30.0 \cdot 10^{-6}$	$14 \cdot 10^{-3}$	$29 \cdot 10^{-6}$	$25 * 0.01$	$15 \cdot 10^{-3}$	575	13.1	2648	1.3
z-gradient	0.174	$1.07 \cdot 10^{-3}$	$22 \cdot 10^{-3}$		0	0.8		11.0		12.1
Q_0	0.195	$661 \cdot 10^{-6}$	$43 \cdot 10^{-3}$	$474 \cdot 10^{-6}$	0.005	0.4	606	16.2	44	8.0
Q_{45}	0.209	$590 \cdot 10^{-6}$	$47 \cdot 10^{-3}$	$539 \cdot 10^{-6}$	0.005	0.4	678	18.2	55	10.9

Table B.4: Details on the simulated human-sized FFL imaging device concept.

	Mean radius / m	η_{coil}	R / Ω at 20 °C	L / H (self)	f / kHz	Target amplitude	I_{peak} / A	$\lVert \vec{J}_{\text{RMS}} \rVert$ / A·mm$^{-2}_{\text{copper}}$	V_{peak} / V	P_{diss} / kW
x-drive	0.263	$5.4 \cdot 10^{-6}$	$8.9 \cdot 10^{-3}$	$11 \cdot 10^{-6}$	$150 * 0.02$	$4.8 \cdot 10^{-3}$	889	4.9	9413	1.8
y-drive	0.296	$4.2 \cdot 10^{-6}$	$9.9 \cdot 10^{-3}$	$13 \cdot 10^{-6}$	$150 * 0.02$	$3.7 \cdot 10^{-3}$	870	4.8	10465	1.9
z-gradient	0.425	$3.9 \cdot 10^{-3}$	8.0		0	1		5.6		130
Q_0 - 1 pole		$1.6 \cdot 10^{-3}$	0.1	$180 \cdot 10^{-3}$	0.04	0.5	324	2.3	14675	7.7
Q_{45} - 1 pole		$1.6 \cdot 10^{-3}$	0.1	$180 \cdot 10^{-3}$	0.04	0.5	324	2.3	14675	7.7
focus		$0.5 \cdot 10^{-3}$								

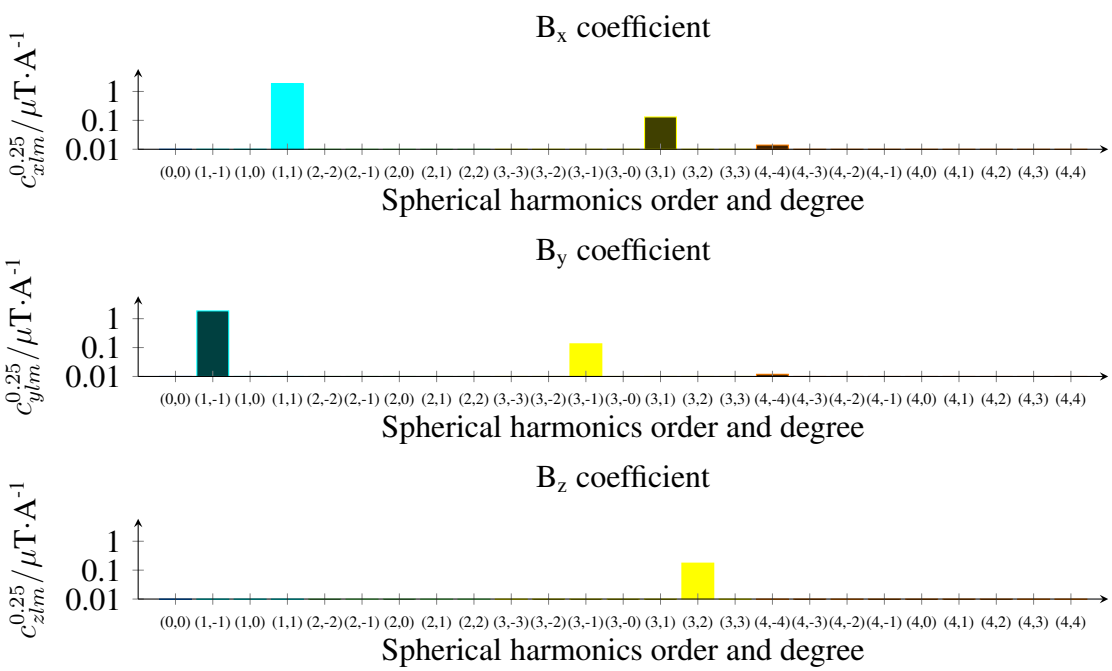

Figure B.12: Simulated SHSE for the human-sized quadrupole at 0° up to degree $l = 10$ and order $m = 10$. Darker filling color indicates a negative coefficient.

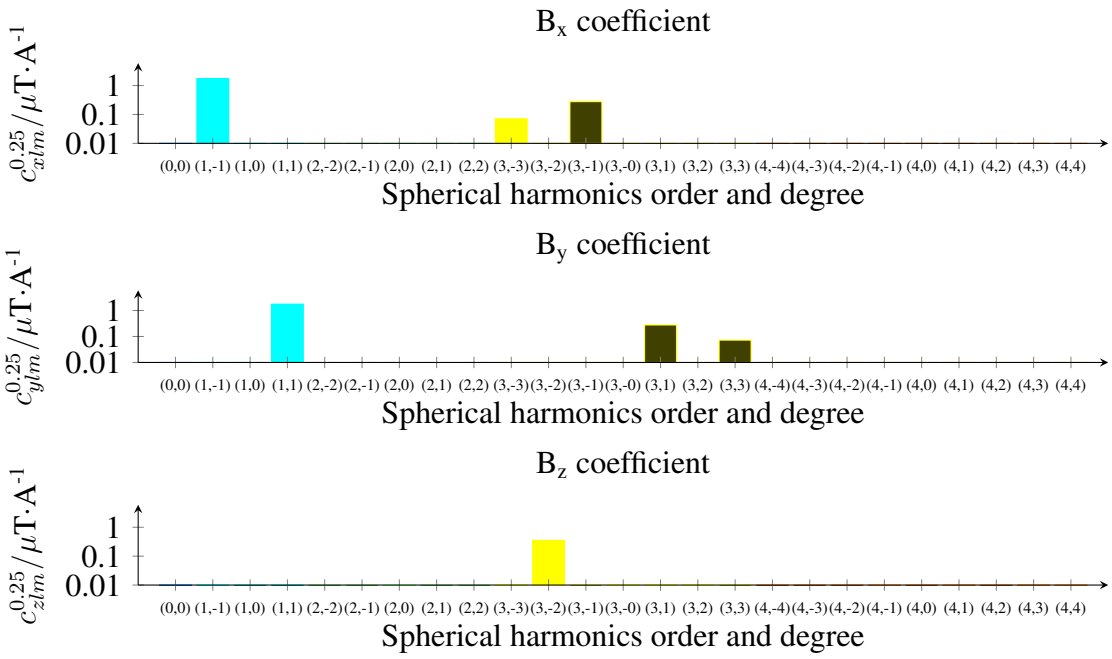

Figure B.13: Simulated SHSE for the human-sized quadrupole at 45° up to degree $l = 10$ and order $m = 10$. Darker filling color indicates a negative coefficient.

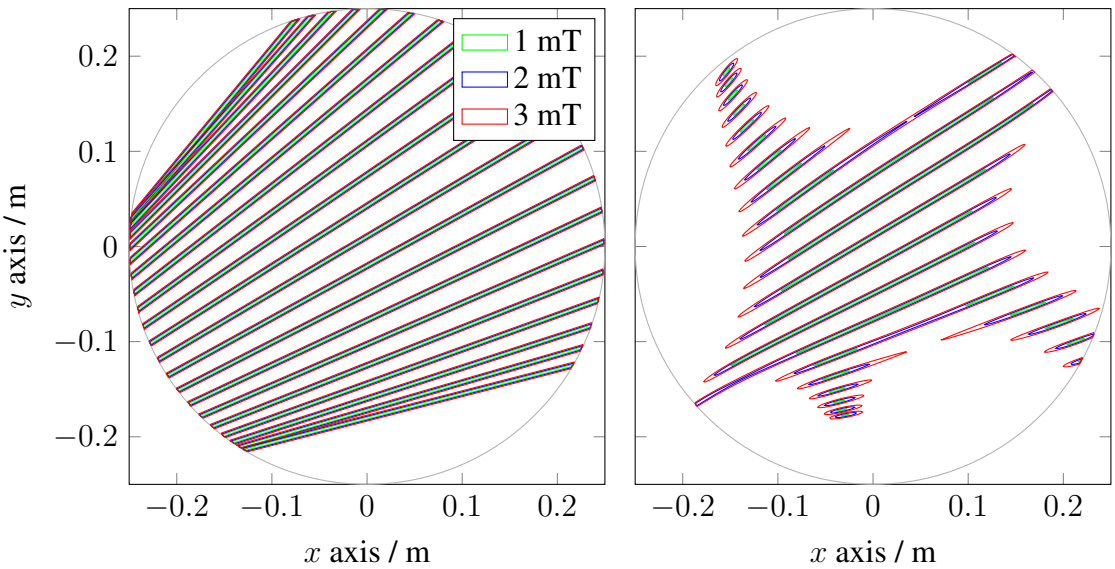

Figure B.14: Shape of the LFVs of the human-sized scanner presented in Section 6.2 for ideal magnetic fields in (a) and in (b) for the actual model which includes SHCs of higher order. The same time points are chosen for both representation, namely starting from 80.5 ms to 85.5 ms in step of 2.5 ms.

C

nMIEFA for MPI coils

In this appendix, the induced electrical field amplitudes for different coils used in MPI is displayed. The relative positions between the human model and the current carrying surface have been chosen so that the position at which the HMIEFA occurs can be analysed, and the distribution of the induced electrical field can be evaluated. This is done to gain a feeling about the importance of the geometry of the patient.

In Figures 5.4 and 5.5, the results for a x-drive coil are presented.

In Figures C.1 and C.2, the results for a y-drive coil are presented.

In Figures C.3 and C.4, the results for a z-drive coil are presented.

In Figures C.5 and C.6, the results for a quadrupole Q_0 are presented.

In Figures C.7 and C.8, the results for a quadrupole Q_0 are presented.

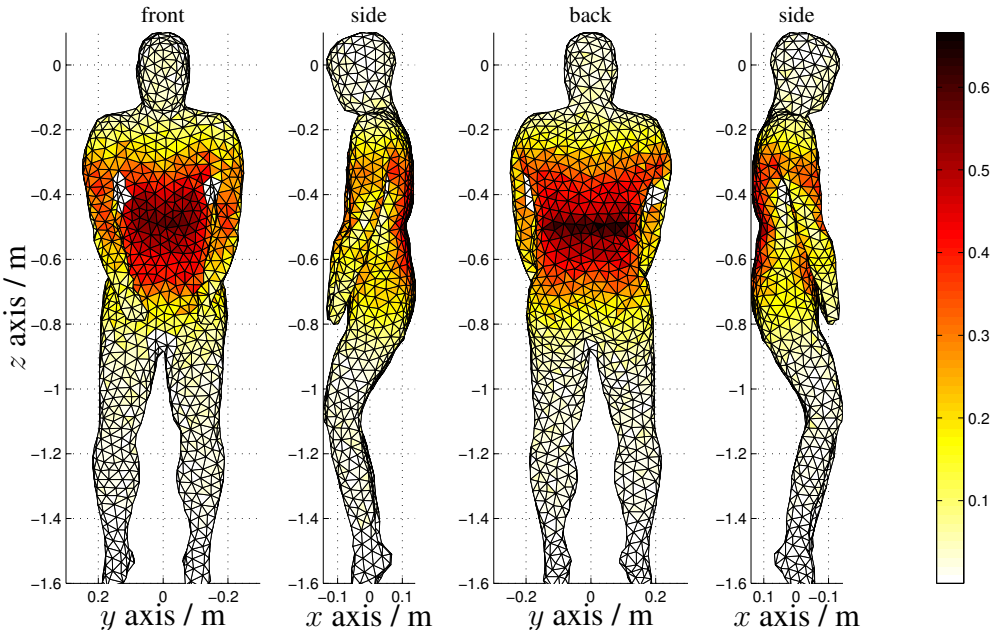

Figure C.1: nMIEFA of the y-drive coil on an MRI-based model. The represented relative position is the one leading to the nHMIEFA.

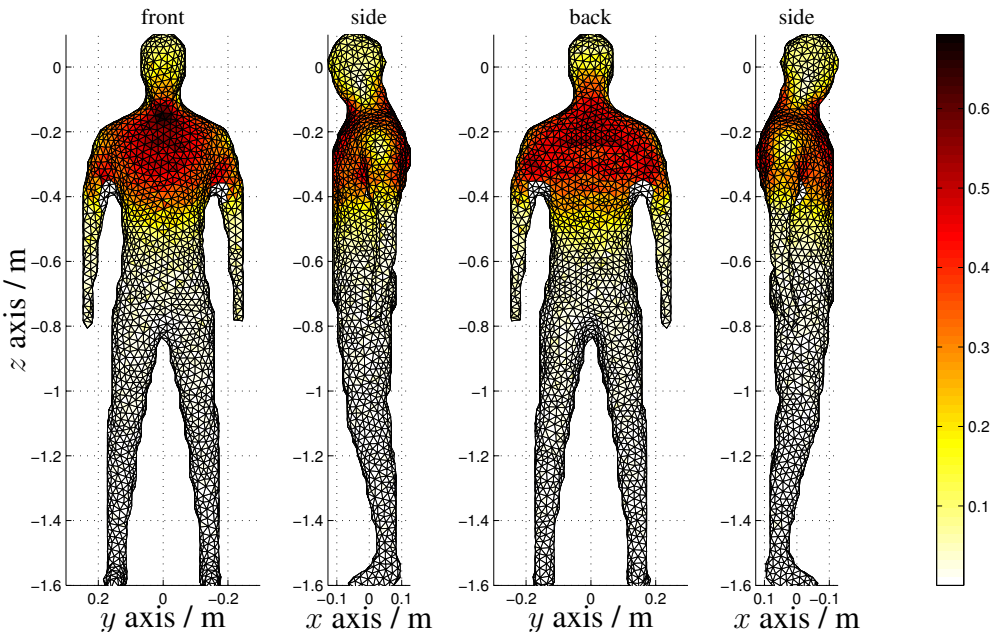

Figure C.2: nMIEFA of the y-drive coil on a photo based model. The represented relative position is the one leading to the nHMIEFA.

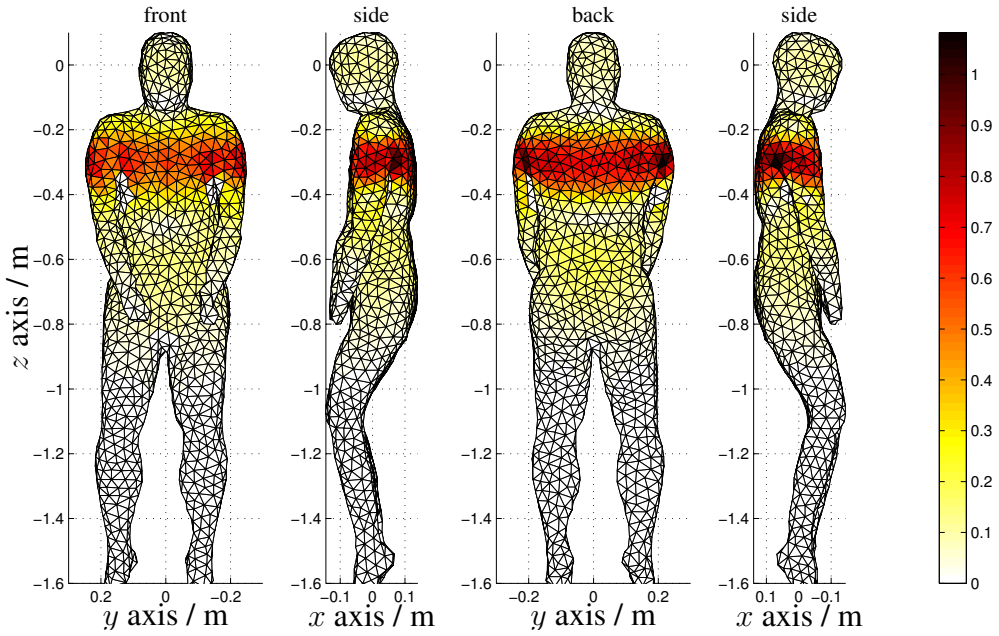

Figure C.3: nMIEFA of the z-drive coil on an MRI-based model. The represented relative position is the one leading to the nHMIEFA.

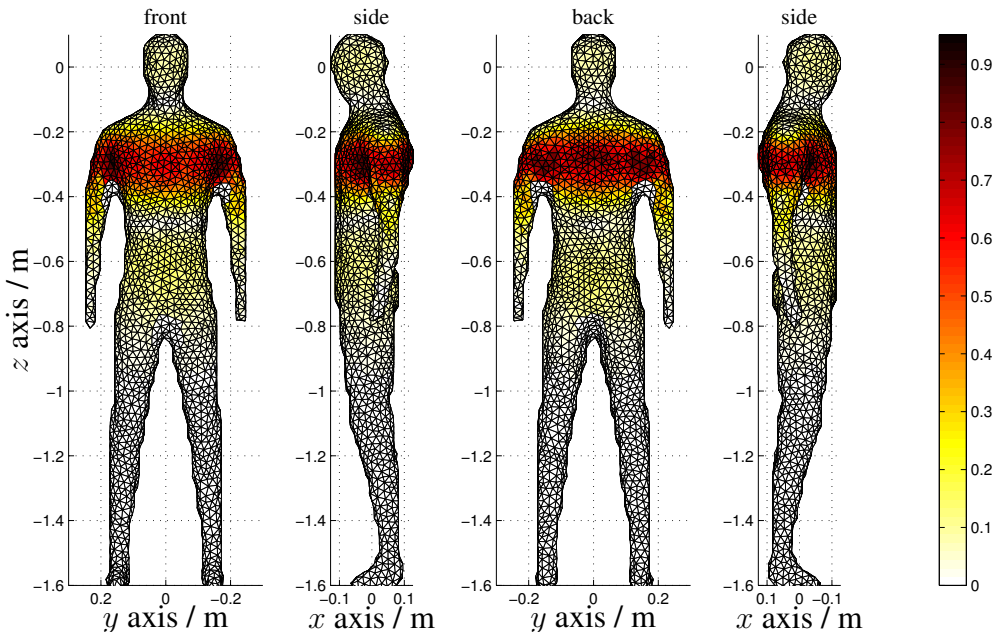

Figure C.4: nMIEFA of the z-drive coil on a photo-based model. The represented relative position is the one leading to the nHMIEFA.

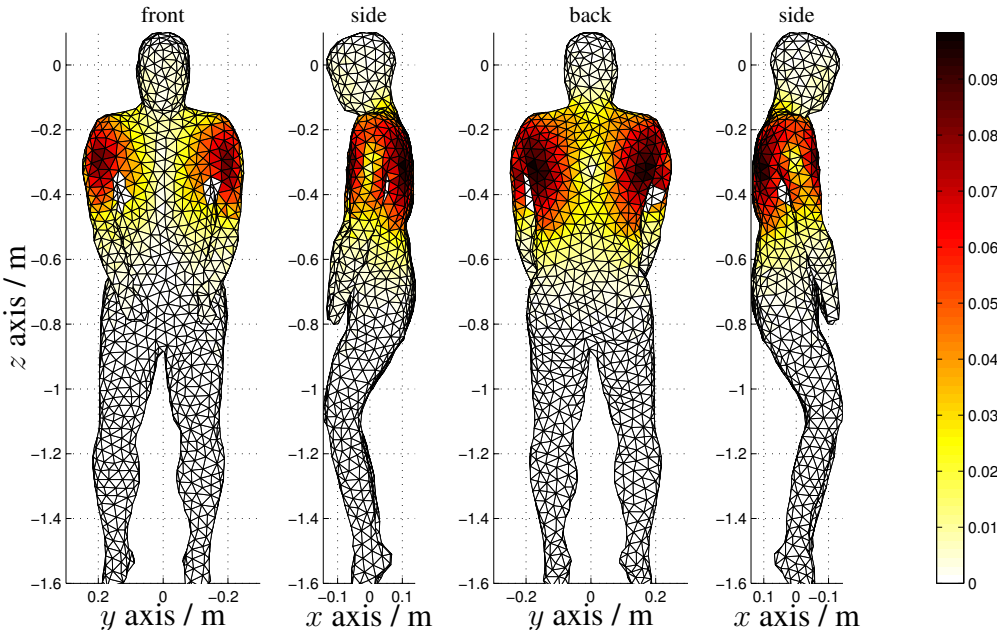

Figure C.5: nMIEFA of the Q_0 coil on an MRI-based model. The represented relative position is the one leading to the nHMIEFA.

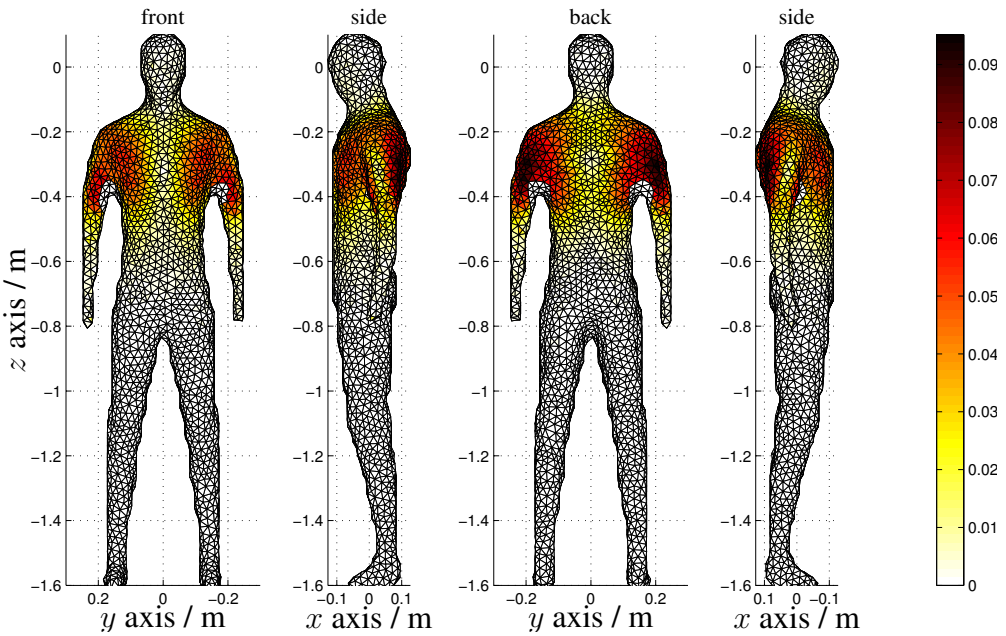

Figure C.6: nMIEFA of the Q_0 coil on a photo-based model. The represented relative position is the one leading to the nHMIEFA.

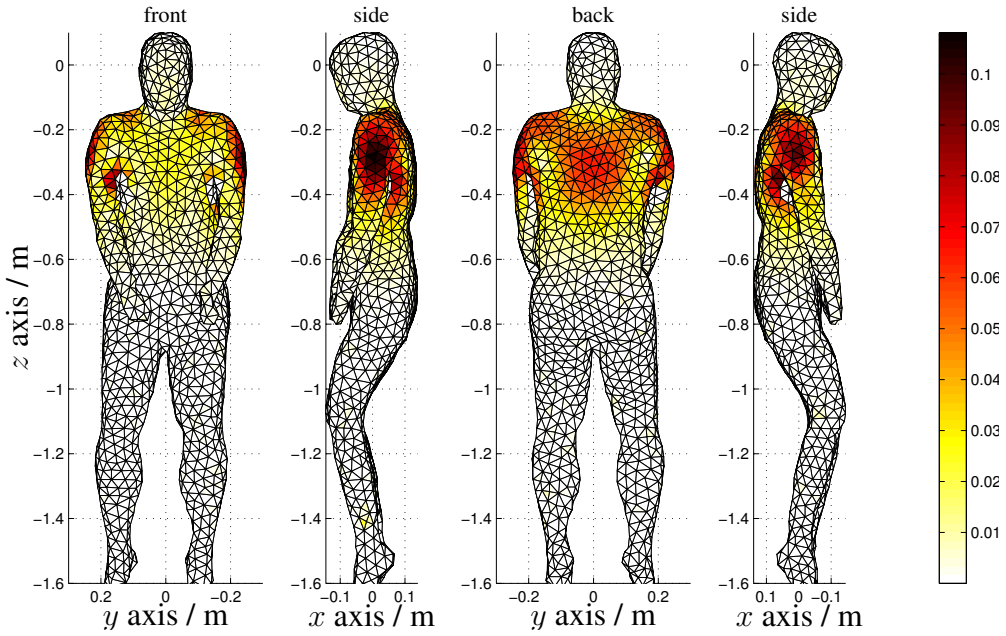

Figure C.7: nMIEFA of the Q_{45} coil on an MRI-based model. The represented relative position is the one leading to the nHMIEFA.

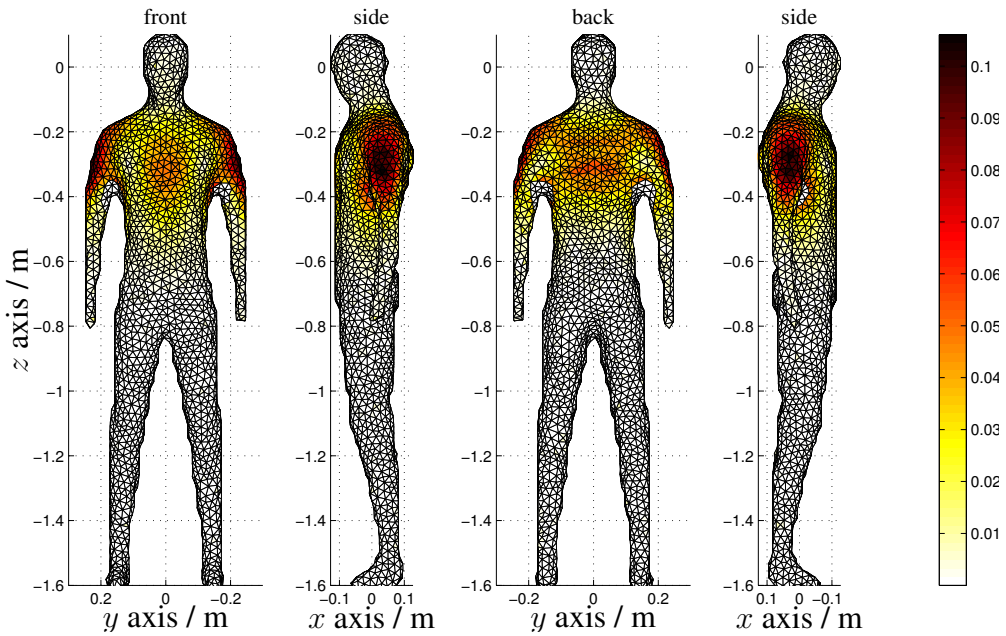

Figure C.8: nMIEFA of the Q_{45} coil on a photo-based model. The represented relative position is the one leading to the nHMIEFA.

D

nMIEFA for MRI coils

In this appendix, the normalised maximal induced electrical field amplitude (nMIEFA) curves of the three MRI coils are presented. Thus, it can be evaluated, where along the z axis, the stimulation may occur and at which relative position the induced electrical field amplitude is maximal. All three curves are presented in Figure D.1.

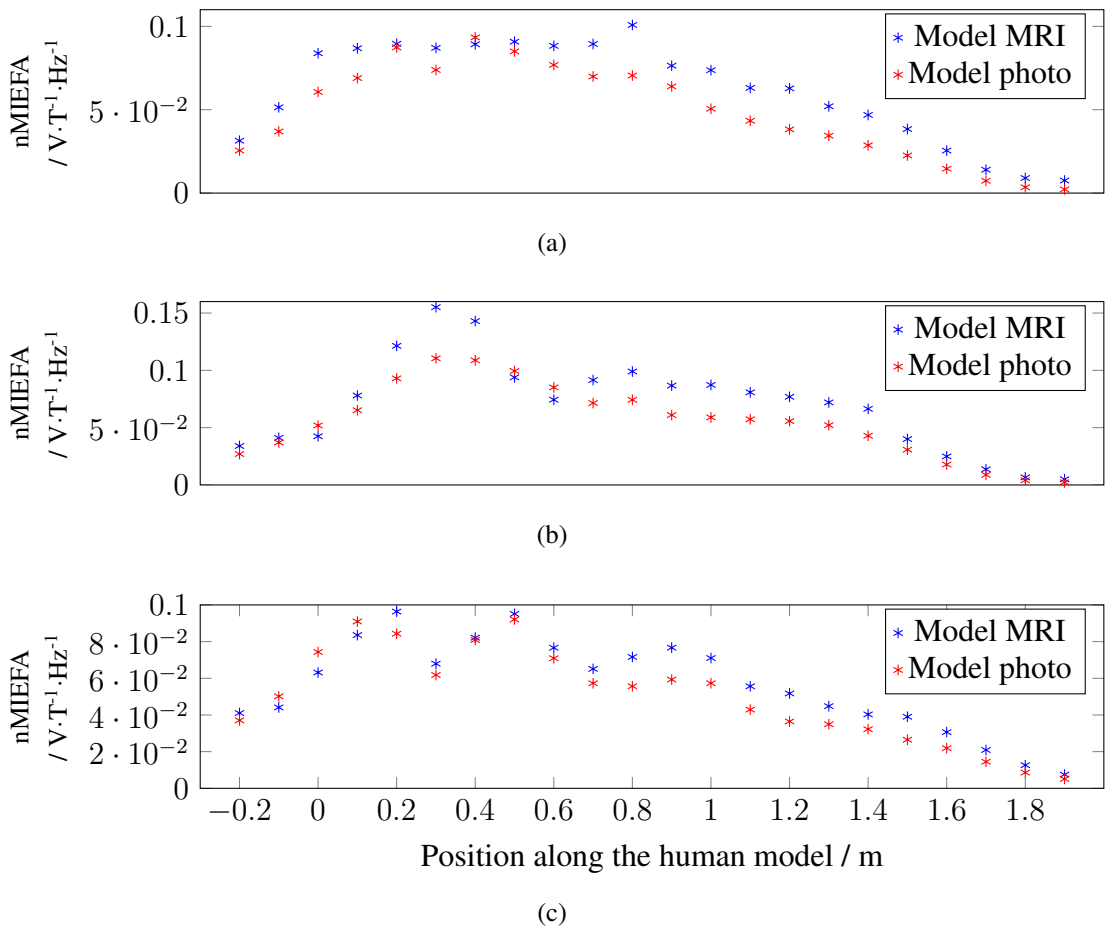

Figure D.1: nMIEFA for different field topologies used in MRI. (a) x-gradient coil. (b) y-gradient coil. (c) z-gradient coil.

E

MPI-simulation framework

In order to evaluate new ideas, the basic equations presented in this work have been implemented or imported from an external library to form a basic kit for MPI simulations. In 18 steps, the simulation of an SF and an MPI signal associated with a phantom is done. These functions have been implemented in Matlab (7.11.0, Mathworks, USA) and are available at `http://www.imt.uni-luebeck.de/` and `https://github.com/gBringout/BasicMPI`.

Those steps are detailed in the following subsections. Some example files are available: *SignalGeneration.m* to simulate a basic 0D spectrometer, *SignalEncoding.m* to simulate a basic 0D spectrometer with an offset field to make the spatial encoding, and *Reco2D IdealFFL.m* to simulate a 2D FFL ISIC. Other examples are also available.

E.1 Access paths and external dependencies

The first step is to defines the access paths to the other packages. These are typically the *sphericalHarmonics* [O3] and *ScannerDesign* packages.

The functions used for the reconstruction are directly included in the core functions pf the *BasicMPI* package.

E.2 Scanner details

The second step is to load the scanner coil model. Each coil model is made of at least the SHCs, the radius in which they are defined and the nominal current used for the coil. The commonly used structures are named after the coil function or topology and direction, as `Drive_X` and `Drive_Y` for the drive fields in x and y direction, `Selection_Z` for a selection field or `Q_0` and `Q_45` for two different orientations of quadrupole.

E.3 Systems parameters

The third step is used to define all the other system parameters, as the spatial resolution of the phantom and the SF, the used frequencies, time vector, sampling frequencies, noise parameters etc. This is highly dependent on the scanner which has to be modelled and the way it has to be modelled.

The choice of most of those parameters are interdependent. For example, the choice of the excitation frequencies, sampling frequencies and time points have to be adequate in order to properly resolve the spectrum. This could comprise the Shannon-Nyquist theorem and the MPI-signal spectrum resolution, as stated by the relation (2.29). This has to be ensured by the user. No verification is done on the input data.

The simulation volume and resolution are also defined here. The resolution of the phantom and the SF have to be kept different to avoid any inverse crime [20], with the highest resolution used for the phantom.

Special care has to be taken to choose the simulation volume, resolution and time length of a simulation, as the whole process can easily take several hundreds of gigabyte in memory space. For example, each of the 25 simulations have required to obtain Figure 6.13 required 900 GB of RAM.

It is of a common practice to build simulation which uses a particle diameter of 30 nm, which is a good model for the tracer Resovist under an excitation signal of around 25 kHz [32].

A noise resistance of $R_s = 185 \cdot 10^{-6}\ \Omega$ is foreseen as the lower limit for the resistance noise generated by a human-sized scanner [31].

The different parameters to truncate the SF are also defined there. An $\mathrm{SNR}_{\mathrm{S}}^{(3)}$ limit of 6 is a good starting point. A first picture could be obtained with the Kaczmarz method in 3 to 50 iterations.

E.4 Magnetic flux-density for the SF

The fourth step is to calculate the magnetic flux-density for the required volume and resolution. This is done using the spherical harmonic coefficient (SHC) associated to the scanner and the relation (2.12).

E.5 MPI sequence

In this section, the time-varying amplitudes applied to the different coils are defined. This is done as series of coefficients, which will then be multiplied by the magnetic flux-density of the different coils system. This can be seen as the sequence definition and is specific to each scanner.

As we are going to calculate a derivative, two similar vectors of coefficients are created for each amplitude. One at the time t and one at time $t + \mathrm{d}t$. A value $\mathrm{d}t = 10$ ns is used by default. This has been validated by simulating the measurement presented in [29].

E.6 Time-varying magnetic flux-density for the SF

In this section, the time-varying magnetic flux-density matrices used for the SF are created. This is memory and time consuming for large simulations. The absolute value of the magnetic flux density is also calculated to facilitate the calculation of the magnetisation later on.

E.7 Time-varying magnetic flux-density verification

In this section, the magnetic flux-density is displayed in a 2D plane for all time t, to check the LFV movement. Figures as Figures 2.11 and 3.6 can be created at this step. This step is disabled by default to improve the speed of the whole simulation.

E.8 Time-varying magnetisation for the SF

In this section, the time-varying magnetisation is evaluated for each point in space for the SF. It is done using the Langevin model described by equation (2.36) and the tracer concentration defined at step 3.

Note that the magnetic flux-density matrix is used to store the obtained values, in order to save memory. If the computer used for the simulation has enough memory, the magnetisation can be saved in another matrix.

E.9 Induced voltage and SF calculation

In this section, the induced voltage for the SF is calculated using equation (2.49). At this stage, the noise is added. It is modelled as white noise according to Johnson's model (2.72) and values given in [31], which are adapted to the actual bandwidth of the simulation. Here, the SF is calculated as the DFT of $\hat{u}^{(3)}$ defined by equation (2.31). The Matlab command *fft* is used for this purpose. Thus $\hat{\underline{\underline{S}}}$ is obtained.

E.10 Create the phantom

In this section, the phantom is defined as a matrix with positive values, representing the tracer concentration. The covered FOV is exactly the same as for the SF; only the resolution differs. It is common to use simple geometric Figures to assess the image reconstruction. The phantom is then filtered to be sure that all the particles are inside the spherical domain where the fields are defined.

E.11 Magnetic flux-density for the phantom

In this section, the same processing is done for the phantom as it was done for the SF in Section E.4.

E.12 Time-varying flux-density for the phantom

In this section, the same processing is done for the phantom as it was done for the SF in in Section E.6.

E.13 Time-varying magnetisation for the phantom

In this section, the same processing is done for the phantom as it was done for the SF in Section E.8.

E.14 Time-varying magnetisation of the phantom

In this section, the time-varying magnetisation is multiplied by the phantom relative tracer distribution to approximate the response of such a phantom.

E.15 Induced voltage and MPI-signal calculation

As in Section E.9, the induced voltage is calculated using equation (2.49). Additionally, the amplitude spectrum (AS)and the power spectrum (PS) are calculated.

E.16 Signal to noise ratio

In this section, an empty measurement is simulated and the $\mathrm{SNR}_{\mathrm{S}}^{(4)}$ values are calculated for the MPI signal on each channels.

E.17 Signal truncation

In this section, the MPI signals and the SF are truncated. All the FCs situated in a given bandwidth, typically for this work between $1.8\,f_0$ and $20\,f_0$, are kept, as explained in Section 2.3.9. All FCs with an $\mathrm{SNR}_{\mathrm{S}}^{(4)}$ lower than a given threshold are removed. The thresholds commonly used are quite low, in the order of 5 to 10 [20]. The truncated matrices $\vec{\hat{u}}^{\dagger}$ and $\underline{\underline{\hat{S}}}^{\dagger}$ are here obtained.

E.18 Reconstruction

In this section, the channel are assembled and the tracer distribution is reconstructed as described in Section 2.3.9. Here, a modified Kaczmarz algorithm, also known as ART method, is used, as it provides good performance [20]. The implementation from [57, 47] is used, with the addition of a forced non-negative constrain, implemented by setting to zero any negative results at each iteration.

Another approach has to be taken to form the sinogram as displayed in Figure 3.3. This is explained in [5].

F

Coil design framework

The implementation of the coil design techniques presented in this work is done in Matlab (7.11.0, Mathworks, USA) and is available at http://www.imt.uni-luebeck.de/ and https://github.com/gBringout/CoilDesign.

The main work flow is divided into 8 steps. Each of them are here detailed.

F.1 Access paths and external dependencies

The first step is to defines the access paths to the external dependencies as the spherical harmonic calculation toolbox and the external toolboxes used for the optimisation [57, 116, 117, 119, 118].

F.2 Define the coil-design properties

All the information specific to each design is defined in separate files. One example for the design of a drive coil is given in the files */streamBEM/examples/IWMPI Drive.m*. Other examples are available.

First, the meshes are created using an external software. For this work, Blender (Blender

2.69.0, Blender foundation, the Netherlands) is used to create the meshes and export them as .obj files.

The meshes are then loaded as three matrices with the node positions, triangle definitions and relations between both.

The number of target points, their position, the target field topology and the magnetic flux-density amplitude on those points are also created here.

The physical properties such as the surface thickness, the width and height of the wire used to discretise the stream function and the surface resistivity are then specified.

Then, the type of optimisation and the required matrix are set. Finally, the points used to display the magnetic flux-density to visually check the topology are fixed.

F.3 Pre-processing of the meshes

The meshes are pre-processed to facilitate later simplification and to calculate required derived quantities. Nodes belonging to the mesh boundaries are sorted in sets which are stored on top of the different vectors and matrices. The calculated derived quantities include the air of triangles, their barycentre, basis function $\vec{v}_{nj}$, points used for numerical integration and links between nodes and triangles. All the quantities are calculated using a right-hand orientation, with the coordinate centre taken as the origin of the mesh.

F.4 Calculation of the matrices

The required matrices ($\underline{\underline{R}}$, $\underline{\underline{L}}$ etc.) are then evaluated. Depending on the design, the magnetic flux-density matrices $\underline{\underline{B}}_i$ are assembled.

F.5 Normalisation of the set of basis functions

To normalise the set of basis functions, only one node per mesh sub-boundary is kept. Thanks to the pre-processing step, this is easily done by simply suppressing most of the first line and first column of the matrices.

F.6 Resolution of the optimisation problem

The chosen optimisation technique is applied to the problem and the vector $\vec{s}$ is obtained. To reverse the normalisation, it is then padded with zero to obtain a vector with the correct size.

F.7 Discretisation in wire centroids

The meshes and associated vector $\vec{s}$ are used to obtain the wire loops. Those are defined as vectors with an additional orientation parameter, to be able to invert easily the current flowing-direction, thus influencing the magnetic flux-density calculation.

F.8 Characterisation

Different properties, such as the SHSE of the produced magnetic field, the coil efficiency, inductance, resistance are evaluated on the stream function $\vec{s}$, the wire model or the calculated magnetic flux-density.

Nomenclature

b_i	Measured i^{th} component of the magnetic flux-density, see equation (2.15)	T
c	Tracer concentration, see equation (2.36)	mol(Fe)·l^{-1}
c_k	Weighting factor for a numerical integration, see equation (4.34)	
c^R_{ilm}	Coefficients in the ith direction of the normed real spherical surface harmonics Y_{lm} defined on a sphere of Radius R, see equation (2.12)	
d	Thickness of a surface, see equation (4.10)	m
d_{coil}	Diameter of a cylindrical coil, see equation (4.70)	m
d_{np}	Diameter of the core of a single nano-particle, see equation (2.38)	m
f_0	Excitation frequency for an MPI signal. Typically 25 kHz in this work, see equation (2.35)	Hz
f_{B}	Base frequency used to generate a Lissajous figure, see equation (2.48)	Hz
f_i	Frequency applied for the amplitude modulation of the magnetic field generated by a drive coil i, see equation (2.42)	Hz
$f_{\text{FF}x}$	Frequency linked to the x component of a Lissajous figure used by a focus field , see equation (6.8)	Hz
$f_{\text{FF}y}$	Frequency linked to the y component of a Lissajous figure used by a focus field , see equation (6.9)	Hz
f_{Ny}	Nyquist frequency, see equation (2.27)	Hz
f_{s}	Sampling frequency, see equation (2.24)	Hz
i	Components of a vector in a Cartesian coordinate system, see equation (2.12)	

j	Natural number, see equation (2.16)	
k	Natural number, see equation (2.16)	
k_{B}	Boltzmann constant $k_{\mathrm{B}} \approx 1.38 \cdot 10^{23}$, see equation (2.37)	J·K^{-1}
l	Degree of the associated Legendre polynomial, see equation (2.12)	
m	Order of the associated Legendre polynomial, see equation (2.12)	
n	Natural number, see equation (2.23)	
n	Order used in the multipole series expansion, see equation (4.71)	
n_γ	Number of projections acquired for a 180 ° rotation of the line in an FFL scanner, see equation (3.1)	
n_{s}	Total number of sampling points in an MPI-signal acquisition, see equation (3.2)	
n_i	Mixing power associated with the frequency applied to the i-drive coil, see equation (2.58)	
$n_{\mathrm{FF}x}$	Integer defined as the ratio of the frequency $f_{\mathrm{FF}x}$ divided by Δf, see equation (6.8)	
$n_{\mathrm{pp}\gamma}$	Number of points contained in each FFL projection, see equation (3.3)	
n_θ	Integer defined as the ratio of the frequency f_θ divided by Δf, see equation (6.10)	
$p_{\mathrm{FF}i}$	Scalar function describing the i position toward which the line is translated using focus fields, see equation (3.38)	
q_1	Maximum pressure applied to the screws holding the housing before first deformation, see equation (6.5)	Pa
q_2	Maximum pressure applied to the exterior of a thin-walled cylinder before first deformation, see equation (6.6)	Pa
q_3	Maximum pressure applied to the interior of a thin-walled cylinder before first deformation, see equation (6.7)	Pa
r_0	Radius of the innermost free circle centred at the centre of the magnet, see equation (4.72)	m
$\hat{s}$	Point response acquired via channel q, see equation (2.50)	

$\hat{s}$	System functions element for channel q and FC k, see equation (2.50)	
s_n	Stream-function value on the nth node of a surface, see equation (4.13)	
t	Thickness of a cylinder, see equation (6.6)	m
t	Time, see equation (2.2)	s
t_n	Discrete point in time, see equation (2.23)	s
u	Continuous-time voltage signal, see equation (2.23)	V
$\bar{u}$	Discrete voltage signal series, see equation (2.23)	V
$\bar{u}_n$	n^{th} discrete voltage measurement, see equation (2.23)	V
$\bar{u}_{\text{noise}}$	Discrete RMS voltage produce by a noise source, see equation (2.72)	V
$\hat{u}$	Fourier coefficient series, see equation (2.26)	
$\hat{u}^{(2)}$	Scaled Fourier coefficient series, see equation (2.30)	
$\hat{u}_k^{(2)}$	k^{th} scaled Fourier coefficient, see equation (2.30)	
$\hat{u}^{(3)}$	One-sided scaled Fourier coefficient series, see equation (2.31)	
$\hat{u}_k^{(3)}$	k^{th} one-sided scaled Fourier coefficient, see equation (2.31)	
$\hat{u}_k$	k^{th} Fourier coefficient, see equation (2.26)	
u_i	Position used to evaluate the weighting factor w_i of the Gauss-Legendre quadrature, see equation (4.35)	
u_k	First coordinate on the unit triangle corresponding to the weighting factor c_k, see equation (4.34)	
v_k	Second coordinate on the unit triangle corresponding to the weighting factor c_k, see equation (4.34)	
w_i	Weighting factor for a numerical integration associated with the Gauss-Legendre quadrature, see equation (4.35)	
i	Imaginary unit, defined as $\text{i}^2 = -1$, see equation (2.26)	
A_{tri}	Surface of a triangular element, see equation (4.18)	m^2

A_{noise}	Power of the noise, see equation (2.75)	V
A_{signal}	Amplitude of the signal, see equation (2.75)	V
ASD_k	k^{th} coefficient of the ASD of a signal, see equation (2.35)	$\text{V}\cdot\text{Hz}^{-1/2}$
AS_k	k^{th} coefficient of the AS of a signal, see equation (2.34)	V
BW	Bandwidth used during a measurement, see equation (2.72)	Hz
B_i	i component of the magnetic flux-density $\vec{B}$, see equation (3.14)	T
$B_{in}(\vec{r}_{\text{t}})$	Magnetic flux-density in direction i produced at point $\vec{r}_{\text{t}}$ by the stream function at the mesh node n, see equation (4.24)	T
C_n	Coefficient used for the definition of the multipole series expansion of order n, see equation (4.71)	$\text{T}\cdot\text{m}^{-(n-1)}$
E	Young's modulus or tensile modulus of a material, see equation (6.6)	Pa
E_{stored}	Stored energy of a device, see equation (4.5)	J
$G_{i,j}$	Coefficient of the matrix $\underline{\underline{G}}$ from the ith line and j^{th} column, see equation (3.29)	
I	Current amplitude, see equation (2.17)	A
I_n	Current density associated to the basis function n, see equation (4.3)	$\text{A}\cdot\text{m}^{-2}$
K	Number of triangular element on a mesh, see equation (4.32)	
K_l^m	Normalisation factor for the spherical surface harmonics, see equation (2.13)	
L	Self-inductance of a coil, see equation (4.5)	H
$\mathscr{L}J$	Laplacian of the function J, see equation (4.9)	
M	Number of spatial positions covered by an acquisition, see equation (2.49)	
M	Number of spatial positions covered by an acquisition, see equation (2.51)	
M_{s}	Magnetisation at saturation of a material, see equation (2.36)	$\text{A}\cdot\text{m}^{-1}$
M_{mn}	Mutual inductance between basis function m and n, see equation (4.28)	H
M_{mn}	Mutual inductance between basis function m and n, see equation (4.6)	H
N	Number of nodes in a mesh, see equation (4.13)	

N_{D}	Natural number defining the density of a Lissajous trajectory, see equation (2.45)	
N_t	Number of FC in the truncated MPI signal, see equation (2.78)	
N_{loops}	Number of loops used to discretise the stream function, see equation (4.46)	
N_{s}	Number of sampled points in a signal, see equation (2.25)	
N_θ	Number of points taken in the θ direction on a sphere, see equation (2.16)	
N_φ	Number of points taken in the φ direction on a sphere, see equation (2.16)	
P_l^m	Associated Legendre polynomials of degree l and order m, see equation (2.13)	
P_{dis}	Dissipated power of a device, see equation (4.7)	W
P_{noise}	Power contained in the noise, see equation (2.74)	W
P_{signal}	Power contained in the signal, see equation (2.74)	W
PSD_k	k^{th} coefficient of the PSD of a signal, see equation (2.33)	$\mathrm{V}^2\cdot\mathrm{Hz}^{-1}$
PS_k	k^{th} coefficient of the PSD of a signal, see equation (2.32)	$\mathrm{V}^2\cdot\mathrm{Hz}^{-1}$
Q	Number of receive channels included in a scanner, see equation (2.49)	
R	Radius of a sphere, see equation (2.12)	m
R	Resistance of a coil, see equation (4.7)	Ω
R_{mn}	Mutual resistance between basis function m and n, see equation (4.8)	H
S	Domain defined on a sphere, see equation (2.15)	
T	Temperature, see equation (2.37)	K
T_{Rl}	Repetition time for a Lissajous curve, see equation (6.12)	s
T_{Rs}	Repetition time for a sequence, see equation (2.46)	s
T_{u}	Unit triangle, see equation (4.34)	
T_{a}	Sampling interval, see equation (2.25)	s
U_{lk}	Element of the single layer matrix $\underline{\underline{U}}$ for indices l and k, see equation (5.22)	
V_n	RMS peak amplitude of the nth harmonics, see equation (2.64)	V

V_{lki}	Element of the $\underline{\underline{Y}}$ for indices l and k, see equation (5.29)	
V_{lk}	Element of the double layer matrix $\underline{\underline{V}}$ for indices l and k, see equation (5.23)	
W_n	Number of triangular element associated with node n, see equation (4.19)	
X_{lki}	Element of the matrix $\underline{\underline{X}}$ for indices l and k., see equation (5.28)	
Y_{lm}	Spherical surface harmonic of degree l and order m, see equation (2.12)	
δ	Skin depth, see equation (2.6)	m
δ_{lk}	Kronecker's delta function for l and k, see equation (5.23)	
ϵ	Electrical permittivity, see equation (2.4)	$F \cdot m^{-1}$
η_{coil}	Coil efficiency, see equation (2.39)	$T \cdot m^{-l} \cdot A^{-1}$
λ	Regularisation parameter, see equation (4.44)	
μ	Expectation value of the signal amplitude, see equation (2.76)	V
μ	Magnetic permeability, see equation (2.4)	$T \cdot A \cdot m^{-1}$
μ_0	Magnetic permeability in vacuum, see equation (2.17)	$T \cdot A \cdot m^{-1}$
μ_s	Magnetic moment at saturation of a single particle, see equation (2.37)	$A \cdot m^2$
ν	Poisson's ratio for a material, see equation (6.6)	
ω	Angular frequency, see equation (2.6)	$rad \cdot s^{-1}$
ω_j^θ	Weight used for the numerical integration of a function in the θ direction, see equation (2.16)	
ω_k^φ	Weight used for the numerical integration of a function in the φ direction, see equation (2.16)	
ϕ_e	Electric scalar potential field, see equation (2.21)	$J \cdot C^{-1} = V$
ψ	Stream function, see equation (4.11)	
ρ	Radial distance, see equation (2.12)	m
ρ_c	Charge density, see equation (2.1)	$C \cdot m^{-3}$
ρ_e	Electrical resistivity, see equation (2.6)	$\Omega \cdot m$

σ	Standard deviation of the noise, see equation (2.76)	V
σ_2	Transverse tensile strength for a materials, see equation (6.7)	Pa
θ	Polar angle, see equation (2.12)	Radian
φ	Azimuthal angle, see equation (2.12)	Radian
$\vec{r}_p$	Position p in the imaging volume Ω, see equation (2.49)	
$\widehat{\psi}_n$	Basis function at the mesh node n associated to the stream function ψ, see equation (4.13)	
Δf	The spectrum resolution, see equation (2.28)	Hz
Δt	Sampling interval, see equation (2.23)	s
Δ_s	Level difference between two contour of the stream function, see equation (4.46)	
Ω	Imaging volume, see equation (2.49)	
$\vec{e}_{\vec{B}}$	Unit vector in $\vec{B}$ direction , see equation (2.36)	
$\vec{j}$	Surface current density, see equation (4.10)	$A \cdot m^{-1}$
$\vec{j}_k$	Surface current density on the kth triangle of a surface, see equation (4.17)	$A \cdot m^{-1}$
$\vec{l}$	Length element, see equation (2.17)	m
$\vec{p}_q$	Sensitivity of the receive coil q, see equation (2.19)	$T \cdot A^{-1}$
$\vec{r}$	Coordinate vector, see equation (2.12)	m
$\vec{r}^{\text{FFL}}$	Coordinate vector in the FFL coordinate system, see equation (3.9)	m
$\vec{r}^{\text{global}}$	Coordinate vector in the global coordinate system, see equation (3.7)	m
$\vec{r}_{\text{s}}$	Coordinate of a source element, see equation (2.17)	m
$\vec{r}_{\text{t}}$	Coordinate of a target element, see equation (2.17)	m
$\vec{s}$	Stream-function vector, see equation (4.14)	
$\vec{s}_{\text{c}}(t)$	Time dependent stream-function value associated to a coil, see equation (4.50)	
$\vec{s}_{\text{i}}(t)$	Time dependent stream-function value associated with an induced surface, see equation (4.51)	

$\vec{\hat{u}}^{\dagger}$ Fourier coefficient of the truncated MPI signal acquired in a scanner, see equation (2.78)

$\vec{v}_{nj}$ Basis function associated with node n and the jth triangle attached to it, see equation (4.19)

$\vec{A}$ Magnetic vector potential field, see equation (2.21) V·s·m^{-1}

$\vec{A}^n$ Component of the magnetic vector potential time derivative in the direction $\vec{n}$, see equation (5.25)

$\vec{A}_i^t$ Time dependent magnetic vector potential in the direction i, see equation (5.32)

$\vec{A}_n(\vec{r}_{\text{t}})$ Magnetic vector potential produced at point $\vec{r}_{\text{t}}$ by stream function at the mesh node n, see equation (4.20) V·s·m^{-1}

$\vec{A}_n(\vec{r}_{\text{t}})$ Magnetic vector potential produced at point $\vec{r}_{\text{t}}$ by the stream function at the mesh node n, see equation (4.21) V·s·m^{-1}

$\vec{A}^t$ Time-varying magnetic vector potential, see equation (5.6)

$\vec{B}$ Magnetic flux-density, see equation (2.3) T

$\widehat{\vec{B}}_n$ Magnetic field $\vec{B}_n$ using the basis function $\widehat{\vec{J}}_n$, see equation (4.6)

$\vec{B}_n(\vec{r}_{\text{t}})$ Magnetic flux-density produced at point $\vec{r}_{\text{t}}$ by the stream function at the mesh node n, see equation (4.23) T

$\vec{B}_{\text{global}}$ Magnetic flux-density in the global coordinate system, see equation (3.5) T

$\vec{D}$ Displacement, see equation (2.1) C·m^{-2}

$\vec{E}$ Electric field, see equation (2.3) V·m^{-1}

$\vec{H}$ Magnetic field, see equation (2.2) A·m^{-1}

$\vec{J}$ Current density, see equation (2.2) A·m^{-2}

$\widehat{\vec{J}}_n$ Set of independent basis functions used to express the current density, see equation (4.3)

$\vec{M}$ Magnetisation vector, see equation (2.18) A·m^{-1}

$\vec{\lambda}$ Fundamental solution of Laplace's equation in 3D for a potential problem, see equation (5.11)

$\vec{\phi}_e$	Electrical scalar potential on a mesh, see equation (5.25)	V
$\underline{\underline{A}}_i$	Magnetic vector potential matrix for the direction i, see equation (4.22)	$\mathrm{V{\cdot}s{\cdot}m^{-1}}$
$\underline{\underline{B}}_i$	Magnetic flux-density matrix for the direction i, see equation (4.27)	T
$\underline{\underline{D}}$	Transformation representing a translation, see equation (3.33)	
$\underline{\underline{G}}_{\mathrm{global}}$	Transformation matrix for a rotated FFL in a global coordinate system, see equation (3.5)	
$\underline{\underline{J}}$	Jacobian matrix, see equation (3.14)	
$\underline{\underline{L}}_S$	Matrix of the Laplacian of a mesh, see equation (4.33)	
$\underline{\underline{M}}$	Mutual inductance matrix, see equation (4.29)	
$\underline{\underline{M}}_{\mathrm{ci}}$	Mutual inductance matrix between two separated meshes, see equation (4.48)	
$\underline{\underline{M}}_{\mathrm{c}}$	Mutual inductance matrix associated with a coil mesh, see equation (4.48)	
$\underline{\underline{M}}_{\mathrm{i}}$	Mutual inductance matrix associated with a mesh of a surface with induced current, see equation (4.48)	
$\underline{\underline{Q}}$	Matrix former by the eigenvectors of a matrix, see equation (4.54)	
$\underline{\underline{R}}$	Mutual resistance matrix, see equation (4.31)	
$\underline{\underline{R}}^{-\theta}$	Transformation matrix for a rotation in the clockwise direction in a right-handed coordinate system, see equation (3.7)	
$\underline{\underline{R}}^{\theta}$	Transformation matrix for a rotation in the counterclockwise direction in a right-handed coordinate system, see equation (3.6)	
$\underline{\underline{R}}_{\mathrm{c}}$	Mutual resistance matrix associated with a coil mesh, see equation (4.49)	
$\underline{\underline{R}}_{\mathrm{i}}$	Mutual resistance matrix associated with a mesh of a surface with induced current, see equation (4.49)	
$\underline{\underline{\hat{S}}}$	System matrix associated with an MPI scanner, see equation (2.51)	
$\underline{\underline{\hat{S}}}^{\dagger\mathrm{H}}$	Complex conjugate transpose of $\underline{\underline{\hat{S}}}^{\dagger}$, see equation (2.79)	
$\underline{\underline{\hat{S}}}^{\dagger}$	Truncated system function associated with an MPI scanner, see equation (2.78)	
$\underline{\underline{T}}$	Transformation matrix, see equation (3.13)	

$\underline{\underline{T}}^\top$ Transpose of a transformation matrix $\underline{\underline{T}}$, see equation (3.13)

$\underline{\underline{U}}$ Single layer matrix, see equation (5.25)

$\underline{\underline{V}}$ Double layer matrix, see equation (5.25)

$\underline{\underline{W}}$ Weighting matrix used for the MPI-image reconstruction, see equation (2.79)

$\underline{\underline{X}}$ Gradient of the single-layer matrix, see equation (5.30)

$\underline{\underline{Y}}$ Gradient of the double-layer matrix, see equation (5.30)

$\underline{\underline{Z}}$ Matrix used for the calculation of the electrical potential gradient on a surface, see equation (5.31)

$\underline{\underline{\Gamma}}$ Tikhonov matrix used for regularisation, see equation (4.44)

$\underline{\underline{\Lambda}}$ Diagonal matrix formed by the eigenvalues λ, see equation (4.54)

List of abbreviations

AS amplitude spectrum

ASD amplitude spectral density

ART algebraic reconstruction technique

BEM boundary element method

CS coordinate system

CT computed tomography

DCT discrete cosine transform

DFT discrete Fourier transform

FBP filtered back-projection

FC Fourier coefficient

FEM finite element method

FFL field-free line

FFP field-free point

FOV field of view

HMIEFA highest maximal induced electrical field amplitude

ISIC idealised scanner made of idealised coils

LFV low-field volume

LNA low-noise amplifier

MC multipole coefficient

MIEFA maximal induced electrical field amplitude

MPI magnetic particle imaging

MRI magnetic resonance imaging

MSE multipole series expansion

nHMIEFA normalised highest maximal induced electrical field amplitude

nMIEFA normalised maximal induced electrical field amplitude

PNS peripheral nerve stimulation

PS power spectrum

PSD power spectral density

QPQC quadratic programming problem with quadratic constrains

RMS root mean square

SAR specific absorption rate

SF system function

SHC spherical harmonic coefficient

SPION superparamagnetic iron oxide nanoparticle

SNR signal to noise ratio

SHSE spherical harmonic series expansion

THD total harmonic distortion

tSF truncated system function